Departamento de Superficies y Recubrimientos

Instituto de Ciencia de Materiales de Madrid

Consejo Superior de Investigaciones Científicas

Structure and Electronic Properties of Different Adsorbates on the rutile TiO_2 (110) surfaces

Memoria presentada para optar al grado

de Doctor en Ciencias Físicas por

Carlos Sánchez Sánchez

Dirigida por **Dra. Mª Francisca López Fagúndez** y **Dr. J. Ángel Martín Gago**

Tutor: **Prof. Enrique García Michel**

Madrid, marzo de 2011

Departamento de Física de la Materia Condensada

Universidad Autónoma de Madrid

A mi familia y especialmente a ti, Sandra

Agradecimientos

En primer lugar, y como no podía ser menos, tengo que agradecer a mis directores de tesis, la Dra. Paqui López y el Dr. J. A. Martín Gago, todo su apoyo, esfuerzo y comprensión durante estos casi cinco años de tesis. Como es lógico, sin vuestra ayuda nunca habría podido llegar hasta este punto.

En segundo lugar, me gustaría agradecer a todos mis compañeros (y antiguos compañeros) del grupo ESISNA, su inestimable ayuda para que esta tesis llegara a buen puerto. Gracias al Dr. Javier Méndez, por su ayuda en el laboratorio, sobre todo cuando el STM no quería funcionar y yo no sabía por qué. Al Dr. Pedro de Andrés, al Dr. Pavel Jelinek, al Dr. César González y a la Dra. María Blanco por sus contribuciones teóricas sin las cuales esta tesis habría quedado algo "coja". Al ya doctor, Gonzalo Otero, por haberme introducido en el mundo del STM y del UHV, y haberme enseñado tus "trucos" para hacer funcionar la campana. Al Dr. Renaud Caillard, por tu ayuda y por los buenos momentos que hemos pasado en el "labo". A la ya también doctora Lucía Álvarez, por tu ayuda y buen humor, y por las casadiellas que traías de tu tierra! A Anna Lisa Pinardi, Annita, por haberme ayudado y hecho compañía en el laboratorio. Y finalmente, a la Dra. Celia Rogero, por tu ayuda cuando he tenido alguna duda, sobre todo con las porfirinas. Y por supuesto, a la gente del CAB, Jesús, Pablo, Martin, Elena y Eva por haberme aceptado durante algunos meses en vuestros laboratorios, especialmente a Jesús, por no echarme por *Destroyer*. A todos vosotros, GRACIAS!

En tercer lugar, a todos los miembros de ALOISA, por haberme acogido durante tres meses y haberme hecho sentir como en casa, así como por su ayuda en las numerosas visitas al sincrotrón. Especialmente, gracias a Valeria Lanzilotto y al Dr. Luca Floreano, por su gran ayuda. Grazie mille!

También me gustaría dar las gracias a la Dra. Elisa Román, por su ayuda en los inicios de esta tesis con el complejo mundo de la preparación del TiO_2. Así mismo me gustaría agradecer al Prof. Aebi, al Dr. Garnier y al Dr. Despont toda su ayuda durante las tres semanas que pasé en su laboratorio de Neuchatel (Suiza).

Y por supuesto, gracias a todos aquellos que han hecho mi estancia en el ICMM mucho más amena y placentera, sobre todo en las comidas: Lidia, Elvira, Mercedes, Manu, María, Elena, César, Anna, etc. Si me olvido de alguien, por favor, no me lo tengáis en cuenta.

A mis amigos de toda la vida, Héctor, Pati, Alex, Rocío y Dani, por ayudarme a desconectar durante los fines de semana y hacer más llevaderos estos años. Muchas gracias.

Muchas gracias también a mis cuñados, Mónica e Iván, y como no a mi pequeña sobrinilla, Julia, y al recién llegado Dani! Para mí, ya formáis parte de mi familia.

Finalmente, y para mí los más importantes, le quiero dar las gracias a mi familia por estar siempre ahí, pase lo que pase, para ayudarme y darme su apoyo en los buenos y en los malos momentos. Me refiero a mis abuelos, mis padres y mi hermano. Sin duda, todo lo que soy y a lo que he llegado se lo debo a ellos. Os quiero.

Y como no, a Sandra, la persona más especial en mi vida, y la que más ha tenido que aguantarme durante tantos años. Sin ti, nada habría sido igual. Te quiero.

Contents

Resumen

El dióxido de titanio está presente en muchos aspectos de nuestras vidas. Es posible encontrarlo en diferentes productos de uso cotidiano como pinturas, pasta de dientes, papel, cosméticos, cremas solares, comida, etc., así como material de base en muchas aplicaciones tecnológicas tales como la catálisis heterogénea, fotocatálisis, células solares, etc. Debido al amplio abanico de posibles aplicaciones que existen sobre este material, es de gran importancia entender sus propiedades mediante un estudio exhaustivo de su estructura atómica y electrónica.

Por otro lado, las moléculas orgánicas han surgido como sustitutos potenciales del silicio en la electrónica del futuro. Presentan propiedades críticas para este fin, tales como su carácter donor-aceptor o su posibilidad de transferir carga, ambas fundamentales para el desarrollo de componentes electrónicos como rectificadores, transistores, etc. Todas estas cualidades hacen de la electrónica molecular un prometedor candidato para sustituir al silicio en la tecnología del futuro.

Así, la combinación de ambos, óxido de titanio y moléculas orgánicas, forma un sistema muy interesante en diferentes campos del conocimiento tanto fundamental como tecnológicos. En esta tesis hemos estudiado la interacción de diferentes adsorbatos, orgánicos e inorgánicos, con las superficies limpias del TiO_2 (110), utilizando para ello técnicas y protocolos experimentales característicos de la física de superficies. Todo ello incluye el uso de equipos de ultra-alto vacío (UHV), así como técnicas como la microscopia de efecto túnel (STM), la difracción de electrones de baja energía (LEED), la fotoemisión de rayos X (XPS), la absorción de rayos X (NEXAFS), la difracción de fotoelectrones

(XPD), etc. Hemos dividido este trabajo en dos partes relacionadas con las dos principales superficies que presenta esta cara, la (1x1) y la (1x2).

Primero, hemos analizado la influencia de la punta de STM a la hora de realizar una correcta interpretación de las imágenes de resolución atómica de la superficie (1x1) limpia. Gracias a este estudio hemos sido capaces de explicar y reproducir la mayoría de las imágenes más habituales de esta superficie considerando la adsorción de uno o dos átomos de oxígeno en el vértice de la punta. Aún más, hemos conseguido reproducir incluso la manera en que los principales defectos que presenta esta superficie se observan mediante STM.

En segundo lugar, hemos estudiado las superestructuras que forman diferentes moléculas orgánicas (C_{60}, pentaceno, $C_{60}H_{30}$ y protoporfirina IX), así como la interacción del substrato con las mismas. Tanto el C_{60} como el pentaceno y el $C_{60}H_{30}$ presentan una interacción muy débil con el substrato, mientras que las protoporfirinas interaccionan fuertemente a través de sus átomos de nitrógeno. También nos hemos interesado en el estudio de la estabilidad térmica de dichas capas moleculares. Para ello hemos realizado diferentes experimentos en los que el sistema se ha ido calentando a diversas temperaturas hasta llegar a su desorción.

En lo referente a la reconstrucción superficial (1x2), hemos centrado nuestros esfuerzos en tratar de resolver tres cuestiones básicas. Primero, hemos estudiado la formación de la superficie (1x2) así como la influencia de la temperatura y la duración de los ciclos de calentamiento en la calidad de la superficie final. Hemos visto que las cadenas de la (1x2) se forman encima de las filas de Ti_{5f} de la superficie (1x1), pudiendo encontrar *single* y *cross-links* desde las primeras fases del crecimiento. Hemos demostrado que se necesitan ciclos de calentamiento de 60 minutos de duración y 1100 K para obtener superficies de buena calidad.

Una vez que tenemos un procedimiento para obtener una buena superficie (1x2), hemos estudiado su estructura electrónica en detalle. Hemos realizado medidas ARUPS de la región del gap y de la banda de valencia donde hemos encontrado una banda dispersiva que se extiende a lo largo de la dirección [001] del substrato y que está asociada al mismo. Hemos probado la existencia de una doble contribución en el llamado “pico de defectos” que aparece en la

zona ocupada del gap. Una es debida a los defectos del volumen (principalmente vacantes de oxígeno) y la otra a la reconstrucción superficial.

Finalmente, hemos estudiado los primero estadios del crecimiento de platino sobre esta superficie. Hemos observado la formación de clusters de Pt situados encima de la filas Ti_2O_3 de la reconstrucción (1x2). El calentamiento del sistema produce una aglomeración de material, con una nucleación preferente en los single y cross-links de la superficie.

Abstract

Titanium dioxide is present in many ways in our daily lives. It is possible to find it in paints, toothpaste, papers, cosmetics, drugs, sun creams, food, etc, and in many other technological applications such as heterogeneous catalysis, photocatalysis, solar cells, etc. Due to all its applications, it is of crucial importance to understand its properties through a deep study of its atomic and electronic structures.

On the other hand, organic molecules have revealed as encouraging substitutes of silicon in future electronics. They present donor – acceptor properties, fundamental for the development of electronic components such as rectifiers, transistors, etc. Additionally, they are cheap, very stable and easy to handle. All these qualities make of molecular electronics a very promising candidate to relieve Si in future technology.

Thus, the combination of both, titania and organic molecules, seems to be a hopeful system with many potential applications in diverse fields. For this reason, an exhaustive study of the interaction of organic and inorganic adsorbates with TiO_2 is of crucial importance, both from the fundamental and technological point of view.

In this thesis, we have studied the interaction of different adsorbates, both organic and inorganic, with the clean surfaces of rutile TiO_2 (110). For this purpose we have made use of different techniques and experimental protocols characteristic of surface science. It includes the use of ultra-high vacuum (UHV) equipments and techniques such as scanning tunneling microscopy (STM), low energy electron diffraction (LEED), X-ray photoemission spectroscopy (XPS), near edge X-ray absorption fine structure (NEXAFS), X-ray photoelectron diffraction (XPD), etc. We have divided this work in two parts related to the two main surfaces present in rutile TiO_2 (110), the bulk-like (1x1) and the reconstructed (1x2) surfaces.

First of all, we have analyzed the influence of the STM tip in the interpretation of the atomic-resolution images usually obtained during the measurement of the clean (1x1) surface. We have been able to explain the majority of these images by considering the adsorption of one or two oxygen atoms in the tip apex. Furthermore, we have successfully reproduced the main surface defects.

Using the (1x1) surface as a template, we have studied which are the superstructures formed by different organic molecules (C_{60}, pentacene, $C_{60}H_{30}$ and protoporphyrin IX), as well as their interaction with the surface. C_{60}, pentacene and $C_{60}H_{30}$ show a very low interaction with the substrate at room temperature, whereas porphyrins interact strongly through their N atoms. We have also addressed the issue of the thermal stability of the molecular layers. For this purpose we have performed annealing experiments at different temperatures until molecular desorption is observed.

Regarding the (1x2) surface reconstruction, we have focused our efforts in trying to solve three open questions. First, we have studied the formation of the (1x2) reconstruction as well as the influence of temperature and annealing duration in the final surface quality. We have seen that the (1x2) rows are formed on top of the (1x1) Ti_{5f} rows, being possible to find single and cross-links since the very beginning of the growth. Annealing cycles of 1100 K and 60 minutes long are necessary to get a good (1x2) surface.

Once a good (1x2) surface is formed, we have studied in detail its electronic structure. We have performed ARUPS measurements of the band-gap region and the valence band, where we have found a dispersive band extending along the [001] surface direction, associated to the bulk. Regarding the occupied states region in the gap, we have shown a double contribution to the defects electronic state appearing at a binding energy of approximately 0.8 eV. One is associated to the bulk defects (mainly oxygen vacancies) and the other one to the Ti^{3+} states present at the surface reconstruction rows.

Finally, we have studied the initial stages of the Pt growth on this surface. We have observed the formation of Pt clusters located on top of the Ti_2O_3 rows. Annealing the system yields the agglomeration of Pt clusters, with a more frequent nucleation at the single and cross-links of the surface.

1. Introduction

Surface physics is a science which studies the physical and chemical phenomena taking place at the interface of two phases involving the three main states of matter: solid, liquid and gas. Most of the studies have been focused so far in the understanding of the interface between a solid and the vacuum, i.e. the study of the last atomic layers of a solid, what we call the surface. Surfaces play a key role in material science as they are responsible for the catalytic, adhesion, friction, corrosion… properties. Additionally, new electronic properties characteristic of the surface and different from those of the bulk may appear as a consequence of the symmetry rupture taking place at them.

Although we can consider the development of *ultra-high vacuum* (UHV) systems in 1960´s as the starting point of modern surface science, it has been present in history since thousands of years ago. For example, there are evidences of the use of lubricants five thousand years ago in Egypt [1]. However, we have to wait until the 15th century to find the first documentation related to a scientific approach to the friction phenomenon carried out by Leonardo da Vinci (see figure 1.1)[2-4]. These early studies were not pursued and it was not until the end of the 17th century when Guillaume Amontons rediscovered da Vinci´s friction laws and formulated the first empirical friction law [5]. Since then, many other important discoveries related to surfaces and interfaces have taken place, like the explanation of surface tension in liquids (1805) by Laplace [6], the appearance of surface thermodynamics (1877) by J. W. Gibbs [7,8], the contributions by Irving Langmuir (20th century) [9], the discovery of low energy electrons diffraction by Davidson and Germer (1927) [10], the theory of the surface electronic states by Shockley and Tamm (1930´s) [11,12], the invention of the transistor by Shockley, Brattain and Bardeen (1949) [13] … However, the major progresses in surface science, in the sense of understanding the new atomic and electronic properties originated at surfaces and interfaces, have taken place with the appearance of the UHV technologies. In this way, development of modern surface science techniques such as *scanning probe microscopies* (SPM), *photoemission spectroscopies* and *diffraction*, together with reliable *theoretical* methods has allowed us to go one step further in the description of the surface processes.

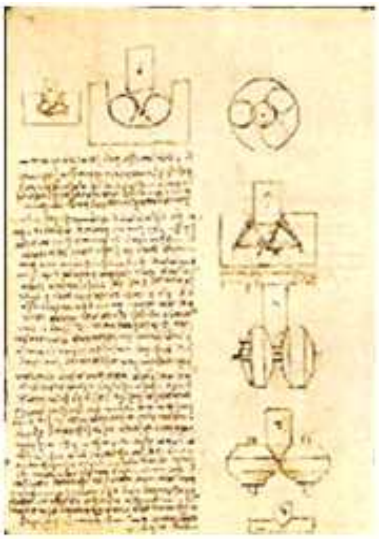

Figure 1.1- *Original sketches of different antifriction bearings designed by Leonardo da Vinci.* On it we can see four different types of antifriction bearings: three-ball bearings, cones, shaped spheres and a straightforward depression. Obtained from [4].

Understanding the surface atomistic processes taking place during the interaction of surfaces with the surrounding media is not an easy task. For this reason, drastic simplifications are necessary. The simplest system we can consider is an ideally perfectly clean and ordered surface, as it is the case of single crystals. Additionally, to study the intrinsic properties of materials, we need an atomically clean surface in order to be able to extract contributions exclusively from the system we are interested in. Two important consequences are derived from this fact. First, that this is only possible under controlled UHV conditions as otherwise, at a pressure of 10^{-6} mbar, we would have one layer of contamination on the surface just in about one second. For this reason, the real take off of surface science began with the development of the UHV systems. Second, that it provides model experiments where it is possible to test fundamental properties of chemistry at an atomistic level.

Since then, an enormous amount of surface science studies have been carried out on a huge variety of systems covering metallic, semiconducting and insulating materials. Probably metal single crystals represent the most simple and perfect systems that can be studied. They present almost atomically

perfect structures with surface atoms usually sitting very close to their bulk-like positions, although in some cases it is possible to find modifications of the surface atomic structure (*reconstruction*) (see figure 1.2). As they are the simplest systems, they have been extensively studied since the very beginning of modern surface science. However, nowadays, more complex, "real" and technologically relevant systems such as semiconductors and insulating materials are devoting the scientific efforts. As an example, metal oxides are attracting a lot of attention not only because of their potential technological applications but also from the fundamental point of view. These materials are characterized by the presence of a non-negligible amount of defects, making them more "real" materials. This approach towards more realistic solids has a cost in their complexity. Usually, metal oxides present complicated surface structures and different reconstructions, which may vary inside the same substrate depending on different parameters such as the reduction level.

Among metal oxides, titanium dioxide is considered the prototype one for surface science studies [14]. It presents a very good surface quality and it is possible to reduce it easily, avoiding charging problems and making it suitable for being studied by surface science techniques.

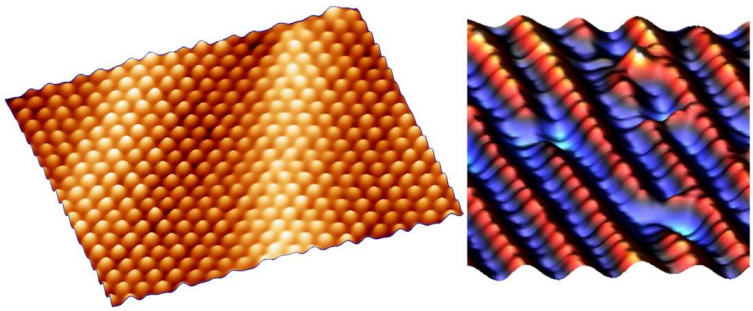

Figure 1.2.- *Artistic 3-dimensional representation of two atomic resolution STM images*. On the left, STM image of the Au (111) surface. Each round feature corresponds to a Au atom. Surface atoms reconstruct in a "herring-bone" structure. As we can see, there are no defects at the atomic scale, something characteristic of metal surfaces. On the right, the rutile TiO_2 (110)-(1x1) surface. In this case, surface atoms stay in their bulk-like positions. We can find several different defects on this surface, like depressions on the red rows or bright features on top of the blue lines. Metal oxide surfaces usually present a non-negligible amount of defects.

From the technological point of view, TiO_2 presents numerous applications in different technological areas such as heterogeneous catalysis, as a photocatalyst, in solar cells for the production of hydrogen and electric energy, as gas sensor, as white pigment, in electric devices, medicine, etc [14]. All these potential applications, as well as many others not mentioned, make TiO_2 an extremely interesting material to be studied. Nowadays, probably two of the most interesting applications of titania are heterogeneous catalysis and electronics.

Heterogeneous catalysis normally makes use of the deposition of metals on oxides supports. For this reason many different noble metals such as Pt, Au, Ag, etc. have been deposited on TiO_2 and studied as model systems for other oxides [14]. It has also been used as a model system to study the important *"strong metal-support interaction"* (SMSI) taking place in heterogeneous catalysis [15,16]. SMSI refers to the catalytic activity changes taking place when group VIII metals supported on reducible oxides are reduced at elevated temperatures. In particular, the Pt / TiO_2 system can be considered a model system for heterogeneous catalysis studies and it has been extensively studied [15, 17-25].

Regarding electronics, SiO_2 MOSFET devices are reaching their miniaturization limits and metal oxides, and particularly TiO_2 with its high dielectric constant (between 86 and 170 [14]), have revealed as a suitable material for substituting SiO_2 in dielectric gates. TiO_2 is also a promising material for spintronics applications. Although titania itself is not magnetic, when anatase TiO_2 films are doped with Co they become ferromagnetic [14].

The technological strategy followed until these days is the so-called *top-down* approach, consisting in a continuous miniaturization of the size of the electronic components in order to increase their density. This decrease in the component dimensions has followed the so-called Moore´s law but a new strategy is needed in order to extend it beyond the foreseen limits. This new strategy is thought to be *molecular electronics* that it is based in the *bottom-up* approach, consisting in using nanometric molecules as building blocks for the construction of new electronic devices. This is possible thanks to the well-localized molecular orbitals and to the charge transfer process within the molecules. Several organic molecules such as C_{60}, C nanotubes, acenes,

phthalocyanine, polymers, etc. present conductive properties suitable for molecular electronics. The possibility of organic molecules to get or lose charge when interacting with other systems (the acceptor – donor character) makes them promising building blocks for the construction of electronic devices. As an example, we indicate the expected electronic character of some of the most common organic molecules proposed to be used in molecular electronics in table 1.I. Moreover, some of these molecules tend to self-assemble and self-organize forming ordered structures. Additionally, today´s organic chemistry allows us to have a complete control in the fabrication of new functional organic molecules. In this way, changing the functional groups present in the molecules allows us to tune their properties and to fabricate molecules with the desired functionality. Thus, it is of crucial importance to understand the molecule – substrate interaction in order to offer new systems valuable for molecular electronics technology.

Acceptor	C_{60}	PTCDA	
Donor	Porphyrin	Phtalocyanine	Pentacene

Table 1.I.- *Examples of donor – acceptor organic molecules.*

The combination of both TiO_2 substrates and organic molecular layers is a promising candidate for the development of new devices in molecular electronics. In fact, they have already been successfully combined for the construction of high efficiency solar cells [26-28], transistors [29], rectifiers [30], etc. Thus, it is interesting for these new applications to study and understand the interaction between organic molecules and the TiO_2 surface.

Additionally, we are dealing with a complex system as TiO_2, in which many other fundamental questions remain unclear. Regarding the (1x1) surface, it is still missing an exhaustive study on the interpretation of the wide spectrum of atomic-resolved STM images daily observed and reported in literature. On the other hand, many other aspects related to the (1x2) surface reconstruction need to be clarified, as this surface termination has been the subject of much

less investigations. For example, a complete study of its electronic structure is still missing.

In this thesis we focus on the study of the interaction of different adsorbates such as noble metals (platinum) and organic molecules (C_{60}, pentacene, $C_{60}H_{30}$ and protoporphyrin IX, see figure 1.3) with the rutile TiO_2 (110)-(1x1) and (1x2) surfaces.

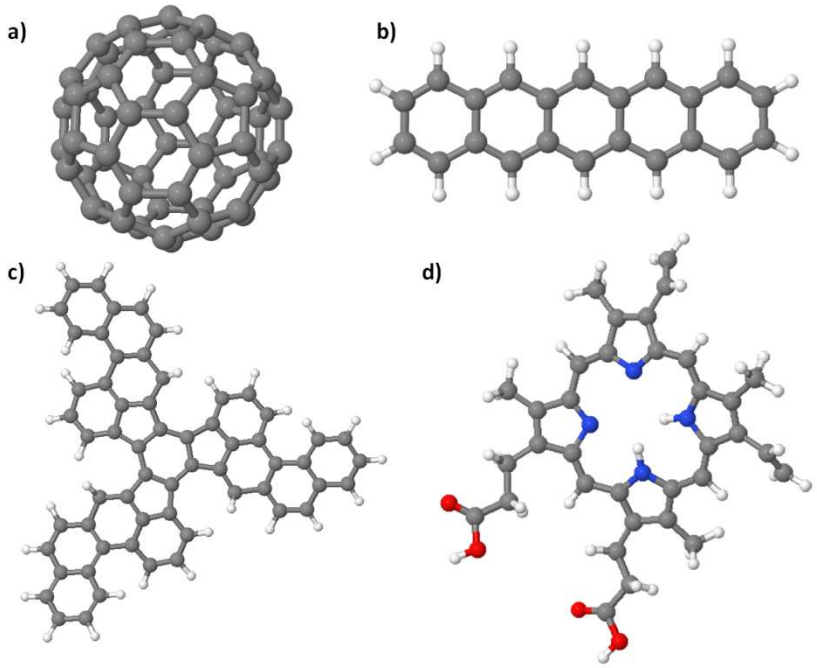

Figure 1.3.- *Schematic ball-and-stick representation of the four different organic molecules used during this thesis*. a) C_{60} molecule. Organic molecule composed by 60 carbon atoms (grey balls) arranged forming hexagons and pentagons and giving rise to a spherical molecule similar to a football ball. b) Pentacene molecule. Organic molecule composed by 22 carbon atoms forming 5 benzene rings fused in one of their sides. The molecule is surrounded by 14 hydrogen atoms (white balls). c) $C_{60}H_{30}$ molecule. Aromatic flat precursor of C_{60} formed by 60 carbon atoms and 30 hydrogen atoms arranged in hexagons and pentagons. When the molecule is cyclodehydrogenated it spontaneously folds forming a C_{60} molecule. d) H_2PPIX molecule. Organic molecule formed by 34 carbon atoms, 34 hydrogen atoms, 4 oxygen atoms and 4 nitrogen atoms arranged as it is shown in the figure. It belongs to the porphyrin family. Colors code: hydrogen (white), carbon (grey), nitrogen (blue) and oxygen (red) atoms.

We have organized this thesis into five main chapters, trying to cover the previously described points:

- **Chapter 1:** *Introduction and motivation of this thesis*. We present a general scientific background and the motivation of this work.
- **Chapter 2:** *The TiO_2 substrate*. In this chapter we explain the main structural characteristics and electronic properties of the two main surfaces of the rutile TiO_2 (110) face.
- **Chapter 3:** *Methods*. In this chapter we briefly explain the most important aspects of each experimental technique and theoretical methods used for the realization of this thesis, together with examples associated to the clean TiO_2 surface. We also comment the main considerations about the substrate preparation and adsorbates evaporation, as well as a description of the main UHV chambers used.
- **Chapter 4:** *The rutile TiO_2 (110)-(1x1) surface*. In this chapter, which is divided into five sections, we explain all the experiments carried out using this surface as a template. We describe the interaction of C_{60}, pentacene, $C_{60}H_{30}$ and protoporphyrin IX with the (1x1) surface, making also a comparative electronic study among all of them; we analyze the influence of the STM tip in the interpretation of the STM images.
- **Chapter 5:** *The rutile TiO_2 (110)-(1x2) reconstructed surface*. This chapter is divided into three sections where we study the electronic structure of the clean (1x2) surface, the interaction of Pt atoms with this surface and the phase transition between the (1x1) and the (1x2) surfaces.
- **Chapter 6:** *Conclusions*. In this final chapter we summarize the main findings of the present thesis.

2. The substrate: titanium dioxide

Solid state materials interact with the surrounding media through their outermost layers, the surface. The intrinsic characteristics of this region, such as the geometrical disposition of atoms, the electronic surface states, the presence of defects, etc. determine their relationship with the environment and, subsequently, their properties. As an example, surface defects play a very important role in surface catalysis as they usually confer special local properties different from those of the bulk or even of the rest of the surface. Therefore, it is crucial to know the surface atomic and electronic properties and the way defects can affect them.

In this chapter we explain the most important and characteristic properties of a clean titanium dioxide surface. We discuss its atomic and electronic structures together with the role played by surface defects in single-crystal TiO_2. We exclusively focus on its most studied face: rutile TiO_2 (110).

2.1. Atomic structure of the rutile TiO_2 (110) face

This transition metal oxide is present in nature in three different atomic structures: rutile, anatase and brookite. First two exhibit a tetragonal crystallographic structure while the third one is orthorhombic [14]. Among all of them, rutile is the most common one in nature as it presents the most stable structure [31]. For this reason, rutile is also the most studied one in surface science although in the last decade anatase has also attracted high scientific interest [32,33]. For the realization of this thesis we have focused on the rutile structure.

Rutile titanium dioxide presents a tetragonal structure as the one shown in figure 2.1. Its unit cell (a = b = 4.584 Å, c = 2.953 Å [34]) is formed by one Ti atom surrounded by six O atoms distributed in a distorted octahedral disposition. As all single-crystals it can present several faces, being the (110) the most stable one, as reported from first-principle calculations of the Wulff construction for TiO_2 [35]. There are at least three known terminations for this face: the (1x1), the (1x2) and the (1x3). The most used and studied ones in surface science, and in this thesis, are the (1x1) and (1x2).

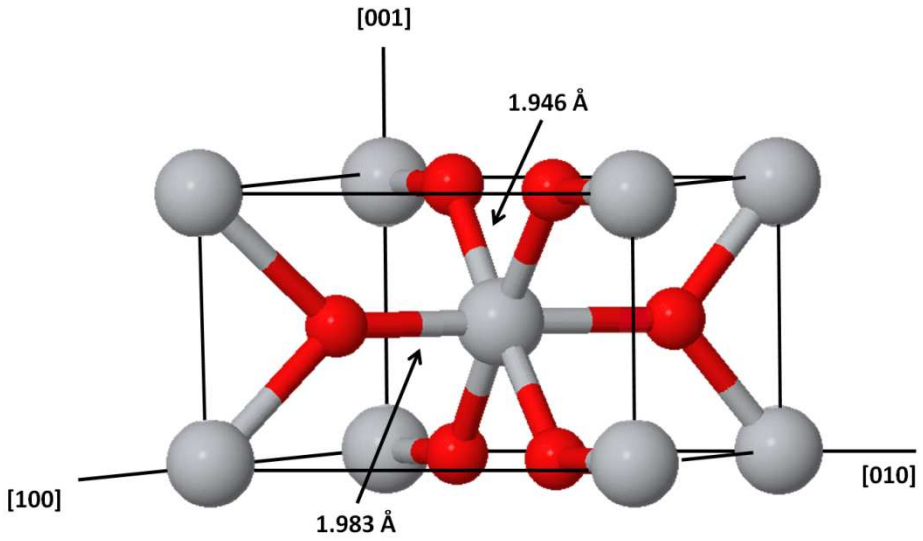

Figure 2.1.- *Ball-and-stick model of the rutile TiO_2 unit cell.* In this figure we can see the spatial distribution of the Ti atoms (grey big circles) and the O atoms (small red circles) when arranged in a tetragonal structure like the one in rutile TiO_2.

2.1.1. The (1x1) surface or bulk-like structure: it is the one obtained for stoichiometric or slightly reduced crystals, as it is the result of the bulk truncation, but introducing some relaxations, as recently corroborated by LEED-IV and surface X-ray diffraction measurements [36-38]. It is the easiest one to be obtained as it is stable at low temperature, where the concentration of surface defects is still low (below 10%) [39]. Figure 2.2 shows a schematic 3-dimensional representation of this surface resulting from a density functional theory (DFT) optimization. We can see that it is formed by two-fold oxygen atom rows which are protruding from the surface by approximately 1.5 Å (also known as *bridging oxygen atoms*, O_{br}) [37] and in-plane five-fold titanium rows (Ti_{5f}) both running along the [001] surface direction. We have also marked in the image the so-called six-fold titanium atoms (Ti_{6f}), which are those under the O_{br} atoms. Interestingly, the surface forms a small ripple as Ti_{5f} atoms displace downwards, towards the bulk, by approximately 0.1 – 0.2 Å.

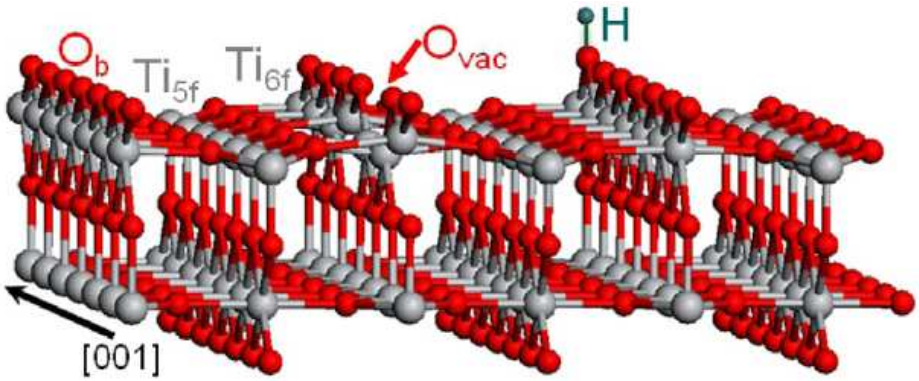

Figure 2.2.- *Ball-and-stick optimized 3-dimensional representation for the TiO_2 (110)-(1x1) surface*. This model is the result of the geometrical optimization of a (1x1) surface with one O_{vac} included (marked with a red arrow). The H atom (marked in green) is just included to complete the most common surface defects described in the text. Large grey balls correspond to Ti atoms while small red balls correspond to O atoms. In this model we can see the in-plane five-fold Ti atoms (Ti_{5f}) extending along the [001] direction together with the six-fold Ti atoms (Ti_{6f}) located below the two-fold bridging-oxygen atoms (O_{br}).

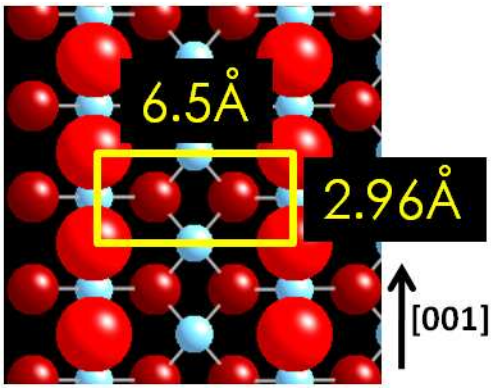

Figure 2.3.- *Schematic ball-and-stick representation of the TiO_2 (110)-(1x1) surface unit cell*. Top view of the (1x1) surface. Blue small circles correspond to Ti atoms while oxygen atoms are represented in red (big circles for O_{br} and smaller ones for O atoms in the plane). We have marked in yellow the unit cell for the (1x1) surface, together with the periodicities along both surface directions.

This face is characterized by a rectangular surface unit cell, as depicted in figure 2.3. The unit cell periodicity is 2.96 Å and 6.5 Å along the [001] and the [1-10] surface directions, respectively. It also presents steps whose height is approximately 3.2 Å. This value corresponds to the separation between two consecutive Ti planes measured along the [110] direction.

As a metal oxide, it is very common to find defects in this material. These can be of very different nature like step edges, oxygen vacancies, interstitial titanium atoms, OH groups or crystallographic shear planes [14]. But probably, the most interesting ones from the reactivity point of view are oxygen vacancies (O_{vac}). They appear mainly during the *in-situ* preparation of TiO_2 through the standard procedure consisting of repeated cycles of sputtering and annealing under UHV conditions. The most typical reduction process is annealing the sample at high temperature (between 800 K and 1150 K). This process will increase the number of O_{vac} up to a concentration of approximately 10^{-18} cm^{-3} [40]. However it has also been shown that when we perform the Ar^+ sputtering cycles during the sample preparation we preferentially remove the surface oxygen atoms [41-43]. This is due to their higher cross-section towards Ar ions compared with the one of Ti atoms, and it will produce an increase in the concentration of defects. At this point TiO_2 will no longer behave as an insulating material but as an n-type semiconductor. Besides, a very characteristic change in the color of the crystal will take place as it will pass from a transparent yellow to a deep blue, as shown in figure 2.4 [14]. But this is not the unique effect of O_{vac}´s. When we remove an O atom, it leaves two extra electrons which will be shared by the surrounding Ti atoms making this vacancy a very reactive site [44]. This reactivity will give rise to other kind of defects as OH groups. They usually come from the dissociation of residual water molecules on one of these O_{vac}. Both of them are also shown in figure 2.2.

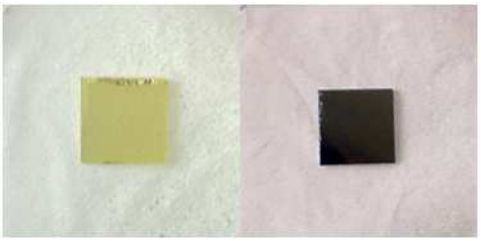

Figure 2.4.- *Two pictures for two different reduction levels of the TiO_2 samples*. On the left side, we have the photo of a new stoichiometric TiO_2 sample as received from the supplier. It has transparent yellow color because defects have not been created on it. On the right side, we show the picture of a heavily reduced TiO_2 sample after several sputtering and annealing cycles in UHV. As we can observe, the color has changed to a dark blue and it is no longer transparent.

2.1.2. The (1x2) surface reconstruction: This is the characteristic surface for heavily reduced substrates (O_{vac} concentration higher than 10%). It is stable at high temperature and it is characterized by a redistribution of the outermost atoms of the substrate. This is a consequence of the fact that the bulk is so heavily reduced that it cannot maintain a TiO_2 stoichiometry on the surface so it is forced to adopt a more reduced one [14]. There has been a lot of controversy during the last decades about the correct identification of this surface reconstruction. Up to four different models have been proposed: the "missing row model" [45], the "added row model" [46] and two variations of the "missing unit model", one with a Ti_3O_5 stoichiometry [47] and another one with Ti_3O_6 stoichiometry [48]. Nowadays the most accepted model is the Ti_2O_3 added row one. But still two different possibilities appear. On the one hand we have the model proposed by Blanco-Rey *et al.* [49,50] in which they suggest a Ti_2O_3 added row model where Ti atoms are in interstitial *iv* positions (keeping the notation used in ref. [51]). On the other hand, we have the model proposed by Park *et al*. [52] where Ti atoms adopt interstitial *ih* positions. This last model has been recently corroborated by high-resolution transmission electron microscopy (HR-TEM) measurements where they are able to "see" the outermost atoms of the (1x2) surface reconstruction [53].

In any case, this Ti_2O_3 model is the most accepted one among the community. A schematic representation of the model proposed by Blanco-Rey *et al.* is

given in figure 2.5. As we can see in this figure, the last layer morphology is completely changed with respect to the one exhibited in the (1x1) surface. New Ti(*iv*)$_2$O$_3$ strands running along the [001] direction appear. The unit cell for this surface reconstruction presents a double periodicity along the [1-10] direction (2.96 Å x 13 Å). The Ti atoms of the reconstruction rows protrude from the Ti atoms of the layer beneath by approximately 3.4 Å. We also find a surface ripple as the Ti_{5f} atoms move inwards by about 0.46 Å (more than twice the value for the (1x1) surface).

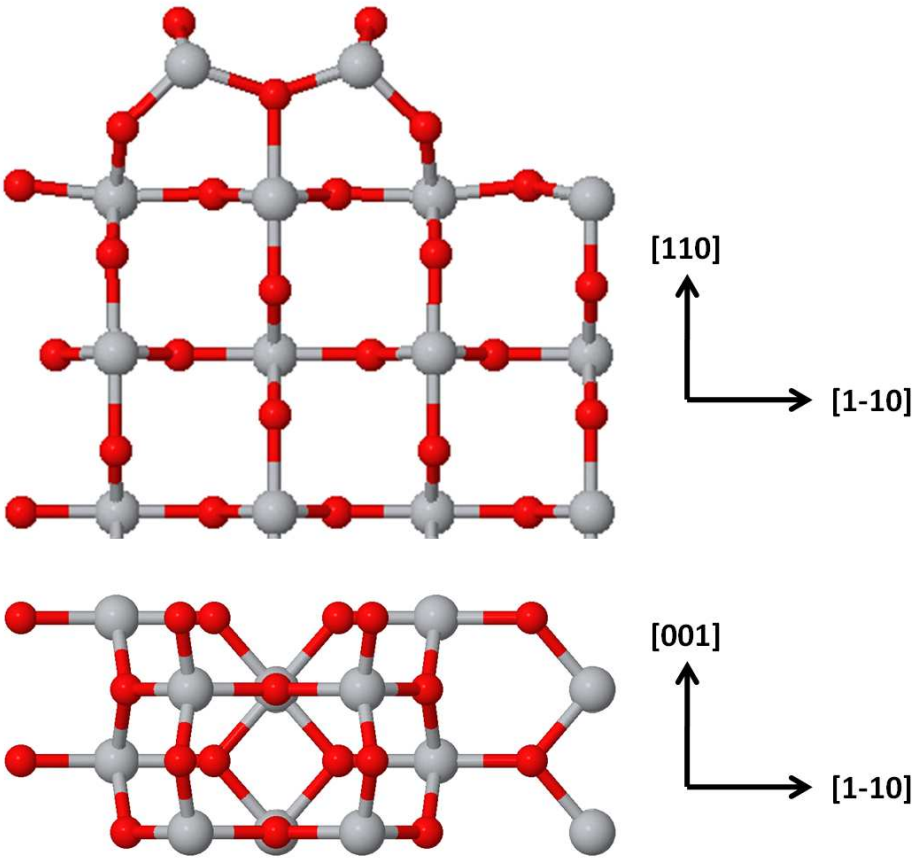

Figure 2.5.- *Ball-and-stick model for the TiO_2 (110)-(1x2) surface reconstruction*. In the upper part we have the side view along the [001] direction of the Ti(*iv*)$_2$O$_3$ added row structure. The periodicity along the [1-10] direction is doubled. Lower part: Top view of the same structure. Represented with the XCrySDen program [54].

Obviously, this high temperature phase is not defect free. Apart from the possibility of removing O atoms from the last layer, we can find two new and characteristic defects in this (1x2) surface reconstruction, as it is evident from the STM images shown in figure 2.6: *single-links (SL)* and *cross-links (CL)*. There are three models for these features which correspond to the three main (1x2) structural models proposed in literature. First of all, we have the model proposed by Takakusagi *et al*. [55,56] where these features are associated to TiO_2 and Ti_2O_3 units, respectively, which diffuse on the surface until they are trapped by two neighboring Ti_2O_3 rows. This gives rise to the formation of rows running along the [1-10] direction, interrupting the characteristic rows of the reconstruction, as can be seen in figure 2.7. Secondly we have the model proposed by Bennet *et al*. [48,57]. In this model, the starting point is quite different as they consider a Ti_3O_6 model for the (1x2) surface reconstruction. Under these conditions, SL and CL would be formed when the troughs of the reconstruction start to be filled by oxygen atoms with Ti ions moving out of the strings to bridge them. SL would be just one half of this new feature (see figure 2.8). Finally, we have the model proposed by Szabo *et al*. [58-60] in which they adapt the explanation of these SL and CL to the missing row model they use for the (1x2) reconstruction. In this case they attribute the CL to TiO_2 units placed in their next layer positions (figure 2.9). Taking into account that it has been proved recently that the most convincing model for the (1x2) reconstruction is the Ti_2O_3 added row one, we can conclude that the most feasible structure for SL and CL is the one given in references [55] and [56].

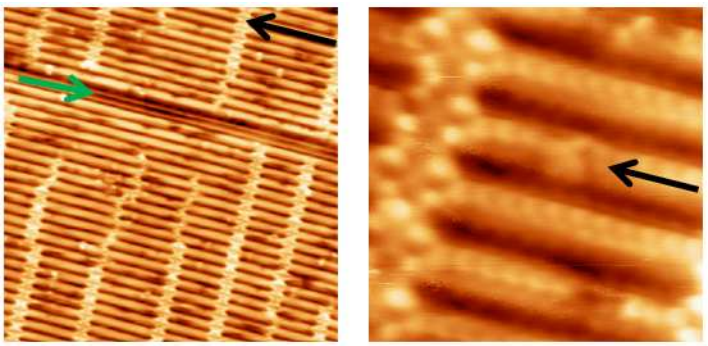

Figure 2.6.- *Scanning tunneling microscopy (STM) images of the TiO_2 (110)-(1x2) reconstruction.* **Left panel:** Constant Current Mode (CCM) image of the reconstructed (1x2) surface. Bright rows

running along the [001] direction (black arrows) correspond to Ti_2O_3 rows. The separation between these rows is 13 Å. Bright cross-shaped features running along the [1-10] direction are known as *cross-links* (CL). At the end of some of these CL rows (center of the image) we can observe smaller snake-shaped bright features called *single-links* (SL). We can also see the underlying (1x1) structure composed by narrower bright rows running along the [001] direction (green arrow). For this structure the separation between bright rows is 6.5 Å. STM image size: (50 nm x 50 nm). **Right panel:** CCM STM image of some of these CL. These cross-shaped features present four bright maxima located at the corners of the CL. There are two lower intensity maxima located in the center of this imaginary rectangle, aligned along the [001] direction, in good agreement with the model proposed by Takakusagi *et al.* [55]. Size: (8 nm x 8 nm). STM parameters for both images: I = 0.1 nA, V = 1.2V.

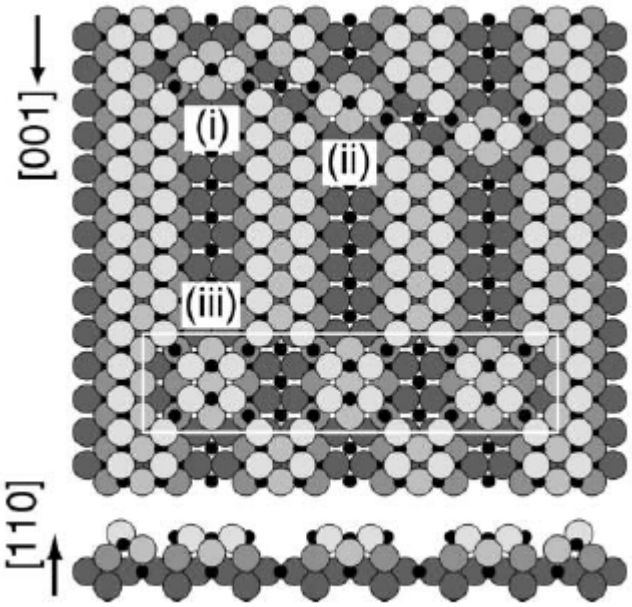

Figure 2.7.- *Schematic representation of the Ti_2O_3 models for SL and CL proposed by Takakusagi et al.* [55]. In this model small black circles correspond to Ti atoms while large grey circles are O atoms. Brighter means higher in topography. In the upper part of the figure we can see the model proposed for the SL. In this case, they would be formed by TiO_2 units trapped in between two Ti_2O_3 reconstruction rows. They induced a local rearrangement of the Ti_2O_3 rows atoms. In the lower part we have the model for the CL. In this case, the trapped unit is a Ti_2O_3 "molecule" which also induces a major local rearrangement of the rows atoms close to it. Six Ti atoms contribute to the cross-shaped appearance observed by STM.

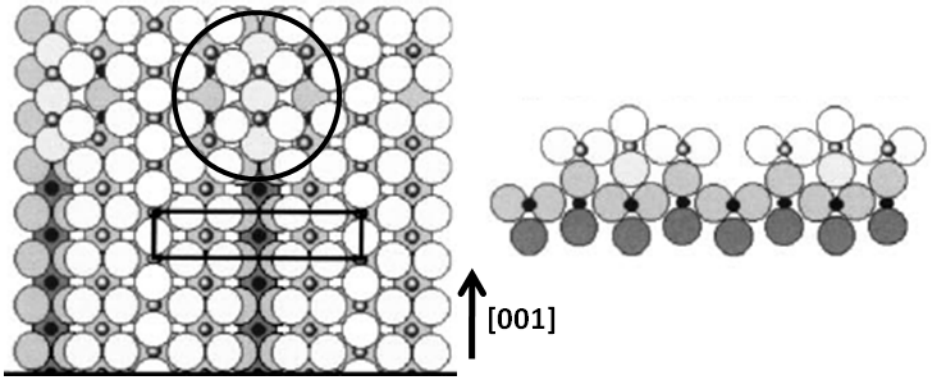

Figure 2.8.- Schematic *representation of CL in the Ti_3O_6 model for the (1x2) reconstruction*. **Left side:** top view of the Ti_3O_6 model for the TiO_2 (110)-(1x2) surface proposed by Bennet *et al*. [48,57]. The unit cell for this structure is marked with a black rectangle. The model for the CL is marked with a black circle. In this case the CL appears by filling the troughs of the Ti_3O_6 rows. **Right side:** lateral view of the Ti_3O_6 model along the [001] direction. In both cases small circles correspond to Ti atoms and large ones to O atoms. Dark means deeper into the substrate.

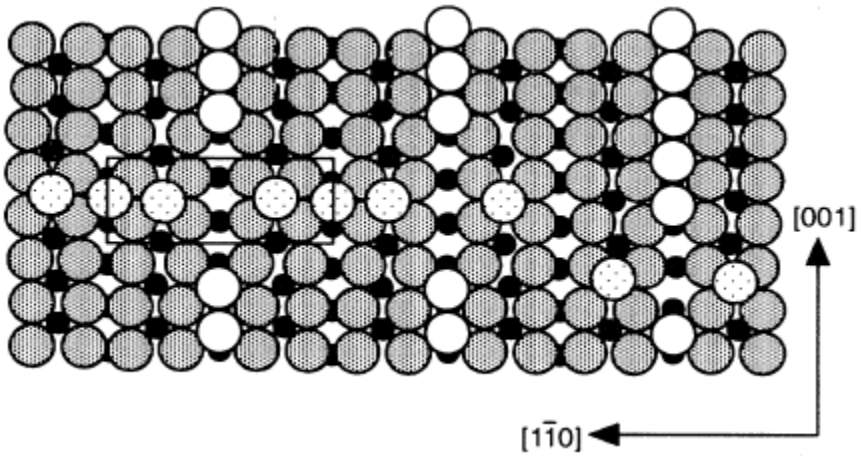

Figure 2.9.- *Schematic representation of the CL model proposed by Murray et al.* [60]. In this top view it is depicted the CL model proposed for a missing row (1x2) surface. Again, small circles correspond to Ti atoms and large ones to O atoms. Dark means deeper into the substrate.

2.2. Electronic structure of the rutile TiO_2 (110) face

Titanium dioxide is an ionic solid formed by Ti^{4+} and O^{2-} ions. As a metal oxide, when stoichiometric, we can consider it to be an insulating material or at least a wide band-gap semiconductor as the difference between the valence band (VB) upper edge and the conduction band (CB) lower edge is around 3.1 eV [61,62]. Experimental and theoretical investigations have revealed that the CB has mainly a Ti character (Ti 3d) while the VB is in its majority coming from the oxygen atoms present in the material (O 2p) as one could expect for an ionic system. However, when analyzing in detail the VB we observe that it is more complex than that. Resonant photoemission experiments and theoretical calculations have proved that inside this band we can find hybridization between the O 2p states and the Ti 3d ones [62,63]. In this way, the lower binding energy (BE) region located around 4-5 eV, also known as *non-bonding* region, is predominately due to the O 2p states, while the higher BE region (*bonding* region), located around 7-8 eV, is a combination of O 2p and Ti 3d orbitals, hybridized ([62,63] and references therein).

We have seen that it is common to find defects in the form of O_{vac} (and interstitial Ti in a lesser extent) coming from the substrate preparation procedure in UHV. When an O_{vac} is formed (either in bulk or surface), two extra electrons remain on the substrate. These electrons will be distributed among several Ti atoms surrounding this vacancy [44], thus partially filling the Ti 3d states and changing their electronic state from a Ti^{4+} to a Ti^{3+}. These partial filling of the band will give rise to a new electronic state in the band-gap region, as evidenced experimentally and theoretically [14]. This new state located approximately 0.8 eV below the Fermi level is a clear fingerprint of the presence of defects in non-stoichiometric surfaces, such as the (1x2) surface reconstruction (see figure 2.10).

Apart from this, the whole shape of the VB changes. The peak at around 5.5 eV remains almost unaltered but peaks at 4 eV and 7.8 eV suffer an important intensity increase after the 1x1 → 1x2 phase transition. Both changes can be assigned to variations in the local electronic structure as a consequence of the higher reduction level of the substrate for the (1x2) structure and the local atomic rearrangement taking place at the surface. But this is not the unique modification of the electronic structure due to these defects. It also appears a

small shoulder in the low BE region of the Ti 2p core level photoemission spectrum. Again, this shoulder is due to the presence of Ti^{3+} states in the substrate (see, for example, ref. [14] and [64]).

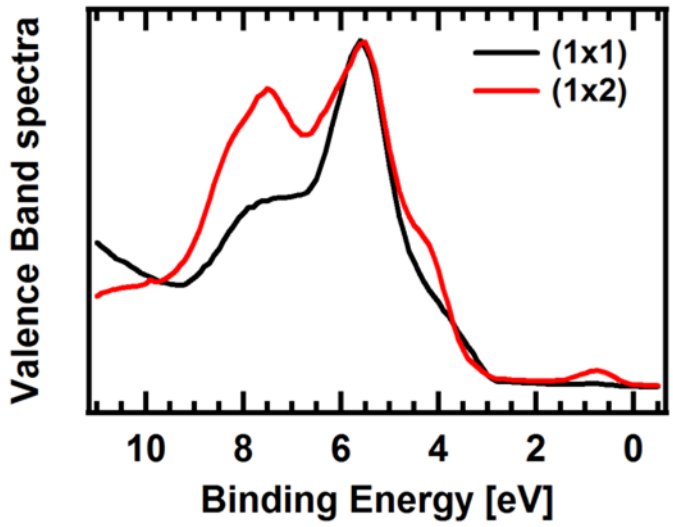

Figure 2.10.- *Comparison of the Ultraviolet photoemission spectroscopy (UPS) spectra for the (1x1) and the (1x2) surfaces.* It is represented the valance band spectra for both surfaces. Important changes take place after the phase transition from the (1x1) surface to the (1x2) surface. A new peak associated to Ti^{3+} states appears in the band-gap region at around 0.8 eV below the Fermi edge. Also the upper edge of the VB and the high BE region suffer substantial modifications. It was measured with a HeI (hv = 21.22 eV) lamp.

3. Methods

Surface Science has undergone a very important advance in the last decades thanks to the improvement and development of a wide variety of experimental techniques and theoretical methods, together with a crucial improvement of the technological means which have allowed scientists to achieve the essential ultra-high vacuum (UHV) conditions for surface science studies.

We can classify surface science experimental techniques into three big families attending to their nature: microscopies, spectroscopies and structural techniques.

***Microscopies**, such as Scanning Electron Microscopy (SEM), Transmission Electron Microscopy (TEM), Photoemission Electron Microscopy (PEEM) and, mainly, Scanning Probe Microscopies (SPM) provide us morphological and topographical information although, in some cases, we can also obtain spectroscopic information (Scanning Tunneling Spectroscopy (STS)). But probably the most important contribution of microscopies is the local character of the information we get from them. This is of major importance as it allows us to study individual processes like the effect of punctual defects on the reactivity of a material. This kind of techniques also present disadvantages like the influence of the uncontrollable state of the probe on the interpretation of the results, which is never straightforward and particularly difficult for oxide surfaces.*

***Spectroscopies**, such as Auger Electron Spectroscopy (AES), Ultra-violet / X-ray Photoelectron Spectroscopy (UPS / XPS), Near Edge X-ray Absorption Fine Structure (NEXAFS), Surface Extended X-ray Absorption Fine Structure (SEXAFS), Resonant Photoemission Spectroscopy (RPES), Reflection Absorption Infrared Spectroscopy (RAIRS), etc. give us information about the electronic structure and chemical state of the atoms present in the system under investigation. The interesting point of these techniques is that we can understand, for example, the way one adsorbate is bonded to a certain surface. Their biggest drawback is the necessity of conductive or at least semiconducting samples and, in some cases, the requirement of synchrotron radiation.*

***Structural techniques**, such as Low Energy Electron Diffraction (LEED), X-ray Photoelectron Diffraction (XPD), X-ray Diffraction (XRD), X-ray Standing Waves (XSW), etc. take advantage of the ondulatory behavior of electrons and*

photons to extract information about the crystallographic structure and chemical composition of the system we are studying, whether we are interested in the bulk or in the surface region. The major problem of this family of techniques is that for most of them, you need long range order to get information from your system.

So to fully characterize a system it is mandatory to combine several of these techniques, from different families, with the aim of obtaining complementary information.

In this chapter we summarize and discuss the basic concepts of some of these experimental techniques we have used during the realization of this thesis. The chapter will be organized as follows: first, we explain all the experimental techniques used through the presentation of some examples related to the clean substrate utilized during the thesis: TiO_2. Readers interested in a deeper comprehension of any of these techniques will be forwarded to more complete review works already existing in the literature. Secondly, we briefly explain the theoretical and simulation methods used to complement and corroborate the experimental data obtained. Then, we comment the experimental protocols followed during the realization of this work related to the sample preparation and the organic/inorganic material deposition procedures. Finally, we describe the experimental systems used in this work.

3.1. Scanning Tunneling Microscopy (STM)

This technique has been the keystone of this thesis as it has been used for the study of most of the systems analyzed in this work [65,66]. It was invented in 1982 by G. Binnig and H. Röhrer while working for IBM Research Laboratory in Zürich (Switzerland) [67,68]. It consists in scanning the surface with a metallic tip separated from it by some angstroms. While doing this movement, the tunneling current between the surface and the tip is recorded as a function of the tip position relative to the sample.

This technique is based in the quantum *tunneling effect*. In classical mechanics a particle with a certain kinetic energy E_k cannot pass through a potential barrier of energy E, where $E > E_k$. Thanks to the particle-wave duality of

electrons and photons, the probability for a particle to go through a potential barrier of energy higher than the kinetic energy of the considered particle is not zero. There exists a non-zero probability for the particle to *tunnel* through the barrier, given by the square-modulus of its wave function obtained as a solution of the time-independent Schrödinger equation in one dimension [69].

$$Tunneling\ probability\ \propto |\Psi(0)|^2 e^{-2\kappa z} \quad \textbf{(1)}$$

where $\Psi(0)$ is the evaluation of the wave function at z = 0 and κ is the wave number and it is proportional to the energy difference between the barrier energy and the particle kinetic energy given by:

$$\kappa = \frac{\sqrt{2m\,(E-E_k)}}{\hbar} \quad \textbf{(2)}$$

where m is the electron mass and $\hbar$ is proportional to the Planck´s constant.

So, the exponential term in **(1)** is due to the attenuation of the amplitude suffered by the particle inside the potential barrier. In this way we can see that the higher the difference between the barrier energy and the particle energy, the lower the probability of tunneling. The same inverse relationship is observed for the width of the barrier.

But in practice a more accurate model is necessary. Nowadays, the most used model is the so-called *Bardeen approach* [70] which consists in considering the overlapping between the tip and the sample wave functions. Just as a summary, this model predicts a tunneling current proportional to the density of states (DOS) of the tip and the sample, close to the Fermi edge as it can be inferred from equation **(3)**:

$$I = \frac{4\pi e}{\hbar} \int_0^{eV} \rho_s\,(E_F - eV + \varepsilon)\,\rho_t\,(E_F + \varepsilon)\,|M|^2\,d\varepsilon \quad \textbf{(3)}$$

where ρ_s is the sample DOS, ρ_t is the tip DOS, eV is the sample bias and M is the tunneling matrix element which is related to the overlapping between sample and tip.

From the experimental point of view, STM consists of a conductive tip, usually made of W or Pt/Ir, mounted on a piezoelectric support, and a sample where the bias is applied. The tip is approached to the surface of the sample until a

tunneling current is measured, typically 5 Å. At this moment we are under tunneling conditions. In order to obtain an image, we move the tip above the surface making a scanning movement from left to right and up and down, and vice versa. There are two possible tunneling modes: constant current mode (CCM) and constant height mode (CHM). In the first one we scan the surface while the tunneling current is kept constant through a feedback loop. In this way we can measure the variation in the z piezoelectric obtaining a topography image. This is the most extended mode and it is the one used for this thesis. In the second mode, we keep the distance between tip and sample constant during the image acquisition while we measure the variation in the tunneling current obtaining a current image. In this case the feedback is off. In both cases, the measured parameter goes to the acquisition program in the computer after several transformations and amplifications. A schematic representation of this cycle is shown in figure 3.1.

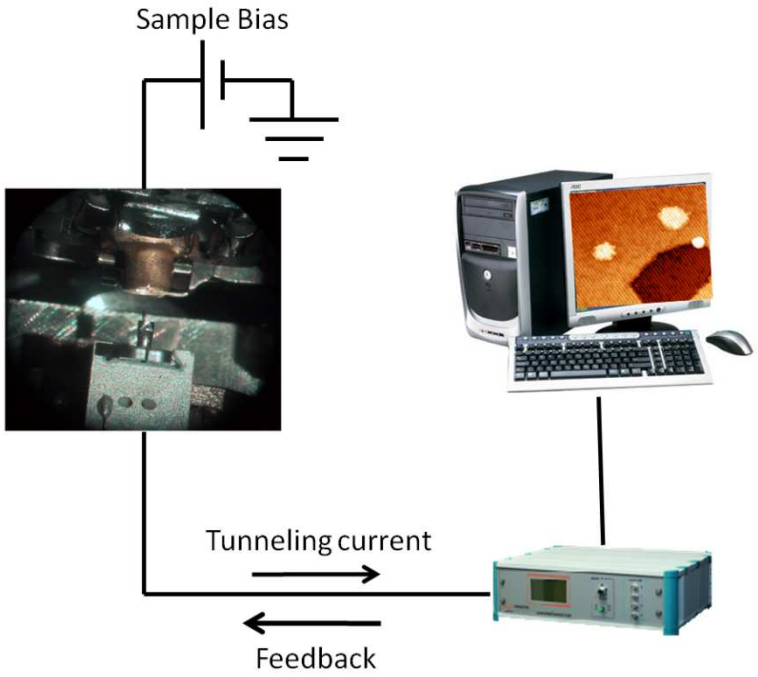

Figure 3.1.- *Schematic representation of the STM system*. In this figure we can see a very simplified view of how the STM measurement cycle works. The tunneling current travels from the tip to the STM electronics (Dulcinea, Nanotec) and from it to the acquisition software (WSxM, Nanotec) in the computer where the STM image is formed.

The strength of this technique stems in the extremely high lateral and height resolution, in the order of tenths of an angstrom, which allows the visualization of individual atoms. This is possible thanks to the exponential variation of the tunneling current with the tip-sample distance and to the extremely fine movement of the piezoelectric materials which perform the scanning. But this technique also presents disadvantages. The biggest one is that it cannot be used to image insulating materials as in this case it would be impossible to detect any tunneling current due to the big energy gap of this kind of materials. Another problem which can be overcome is the difficulty in the acquisition and interpretation of STM images. The interpretation of STM images is, in the majority of the cases, not straightforward as not only topography is influencing the image but, as already said before, we have a very important contribution of the local density of states (LDOS) of the system formed by the tip and the sample. This means that STM images are a convolution of the surface topography and the tip and sample LDOS. It is also very common (mainly in oxide surfaces) to have some contamination adsorbed at the tip apex. This contamination will influence the STM images as it will change the LDOS of the tip. In these cases it is important to perform theoretical simulations in order to properly interpret the images. A very clarifying example will be given in chapter 4.1.

Regarding the acquisition, we have to take into account that in order to obtain atomic resolution we need a tip ideally finished in one atom. In the majority of cases this is not so and we have a rough tip with many atoms at the apex that contribute to the tunneling current, losing the resolution. To try to overcome these typical problems we have developed a procedure to prepare the tip *in-situ*, inside the UHV system. This procedure will be explained in detail later.

In our case, we have used a commercial room-temperature (RT) STM from Omicron together with a commercial electronics from Nanotec. In this STM the tip and the sample are mounted on an anti-vibrational support in order to avoid the propagation of the equipment vibrations which would considerably affect the acquisition. We must take into account that the tip-sample distance is in the order of some angstroms so any vibration can destroy the STM measurement. This anti-vibrational stage is formed by a plate holding from some springs and stabilized by several magnets as we can see in figure 3.2.

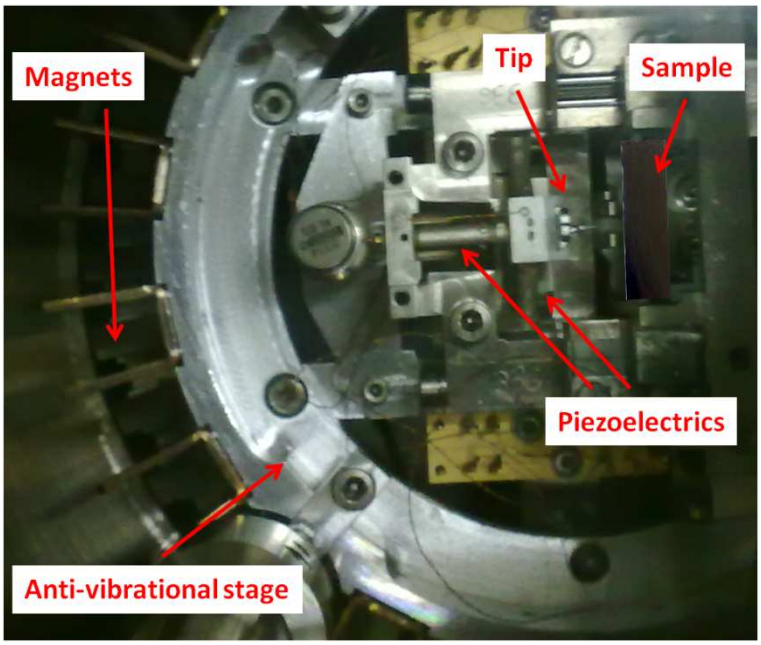

Figure 3.2.- *Picture of the STM system*. We can see the different parts that compose the UHV STM. The tip is fixed to a tripod made of a piezoelectric material, facing the sample. Both the sample and the tip are mounted on an anti-vibrational support stabilized by several magnets.

We have used electrochemically etched W tips. We have done them by immersion of a 0.25 mm thick W filament (99.999% purity) in a 2.5 M KOH aqueous solution membrane supported on a stainless steel hoop, as shown in figure 3.3. Then we apply a voltage between the hoop and the filament, typically 10 V, starting the creation of K^+ ions that are attracted towards the W filament and dissolve it giving the filament a sharp shape. Once we have a macroscopically sharp tip, we complete the process by cleaning it under UHV conditions. When the tip is inside the UHV chamber, we clean it by high temperature annealing through direct heating of the tip (around 900 K for two minutes and a flash to 1200 K) in the presence of a negative high voltage

(-2kV) to favor the extraction of ions from the tip. With this annealing we remove the majority of the contamination present in the tip. In order to completely clean the tip and to sharpen it as much as possible, we perform a Ne^+ bombardment. This is done by approaching the tip up to some millimeters from a ball where we apply a variable positive voltage until the tip emits electrons. At this moment we introduce Ne into the chamber until a pressure of 10^{-5} mbar is reached. The Ne atoms which pass through this voltage will be ionized and accelerated towards the tip, cleaning it and improving its shape.

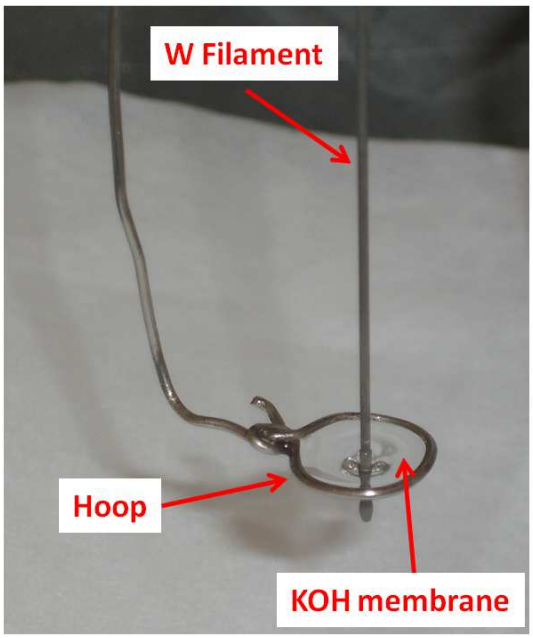

Figure 3.3.- *Picture of the chemical-etching process for the tip preparation*. In this figure we can see how the etching apparatus looks like. On one side we have a stainless steel hoop which supports the KOH membrane. On the other side we have the W filament we will use for the tip. When we immerse it in the KOH membrane and apply a voltage, the K^+ ions will dissolve the W filament giving it a sharp shape. This tip will have to be prepared *in-situ* again in order to completely remove all the contamination.

All the STM images shown in this thesis have been measured with positive voltages applied on the sample and have been processed with the WSxM software from Nanotec [71].

As an illustrative example of the kind of information obtained with the STM we show in figure 3.4 two STM images of the clean (1x1) and (1x2) surfaces of rutile TiO_2 (110). Figure 3.4 a) shows the clean (1x1) surface. On it we can see bright rows running along the [001] direction (indicated by a blue arrow). These bright rows correspond to the in-plane five-fold Ti atoms (Ti_{5f}) and not to the protruding oxygen rows as one could expect according to the topography [72,73] (see figure 2.2). This is a clear evidence of the intricate interpretation of STM images. Bright rows correspond to Ti_{5f} because the TiO_2 (110)-(1x1) conduction band is mainly due to the Ti_{5f} atoms, as it will be shown later in figure 3.15. When we use positive voltages applied on the sample, we are probing the CB of TiO_2, "watching" these atoms with the STM. It is another example of the importance of the LDOS of the tip and the sample. These bright rows are formed by individual bright maxima which correspond to individual Ti_{5f} atoms with a 3 Å periodicity along the rows ([001] direction), as expected. The separation between Ti rows is in good agreement with the theoretical value of 6.5 Å. In this figure we can also observe an example of the power of this technique as we are able to distinguish individual defects like the one surrounded by a green circle. As it will be explained in future chapters, this defect can be an O_{vac} or an OH group. Figure 3.4 b) shows the clean (1x2) reconstructed surface. We can see one terrace larger than a 1000 Å with bright rows running along the [001] direction (blue arrow). These bright rows correspond to the Ti^{3+} atoms which form the Ti_2O_3 rows of the reconstruction [14]. The periodicity along the perpendicular direction to the rows is approximately 13 Å as it corresponds to this surface. We can also see some punctual defects in the form of "holes". They are surface areas which did not reconstruct, probably due to the presence of sub-superficial defects or just because of a lack of temperature or time during the annealing.

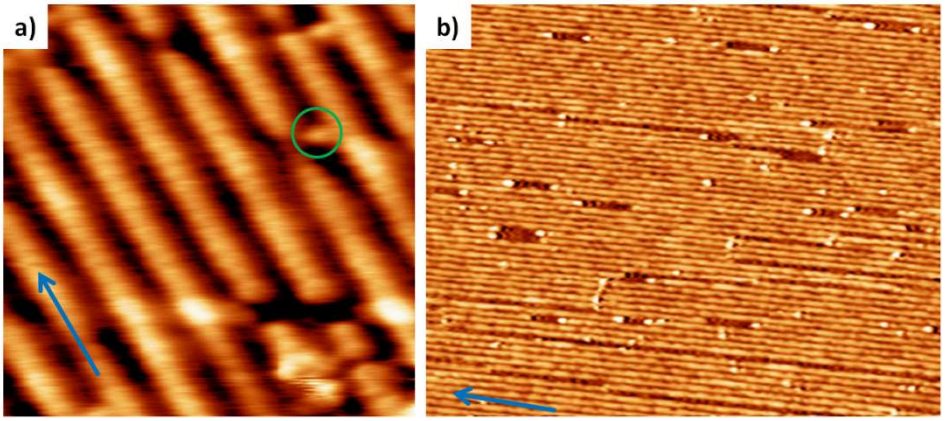

Figure 3.4.- *High-resolution STM images for the (1x1) and (1x2) surfaces*. **a)** Atomic resolution STM image of the clean TiO_2 (110)-(1x1) surface. Bright rows correspond to Ti_{5f} rows, which extend along the [001] direction (blue arrow). Point-defects are also visible, like the O_{vac} marked with a green circle. STM parameters: (50 Å x 50 Å), I = 0.17 nA, V = 1.5 V. **b)** STM image for the clean TiO_2 (110)-(1x2) surface. Bright rows running along the [001] direction (blue arrow) correspond to the Ti_2O_3 rows of the reconstruction. Some holes appear in the image. They are non-reconstructed areas probably due to low temperature or short time during the annealing. STM parameters: (1200 Å x 960 Å), I = 0.23 nA, V = 1.6 V.

3.2. Low Energy Electron Diffraction (LEED)

This technique belongs to the family of diffraction techniques. A LEED experiment consists of using a low energy electron beam (typically in the range 20 – 1000 eV) to probe the reciprocal space. These electrons, after interfering with the ordered layers present at the surface, are collected in a fluorescent screen where we obtain a diffraction pattern. There are two reasons for the use of electrons in this energy range. The first reason is that the electrons need to have a wavelength (λ) similar or smaller than the lattice parameter (a) of the system under study ($\lambda \leq a$) to interfere with the ordered layers at the surface. The second one is that we want to be *surface sensitive*, that is, we want to get information about the last layers (typically 10 – 30 Å). As we are working with electrons we have to consider their inelastic mean free path inside solids that it is between 10 and 50 Å for this energy range [74].

The theoretical basis behind this technique is based on the ondulatory behavior of particles. If we consider an electron with a well-defined energy, its wavelength is given by the de Broglie relation:

$$\lambda = \frac{h}{p} = \frac{h}{\sqrt{2mE_k}} \quad \textbf{(4)}$$

where p is the electron momentum that can be related to the electron kinetic energy (E_k). If we consider the usual units used when working with electrons, i.e. kinetic energies given in electron volts, equation **(4)** can be expressed as:

$$\lambda = \frac{12.21}{\sqrt{E_k}} \quad \textbf{(5)}$$

where E_k is given in eV and λ is expressed in $\mathring{A}$.

There are two ways in which LEED can be used: qualitatively and quantitatively. The first one is based on the simple inspection of the diffraction patterns, i.e. in studying the patterns formed, the spots width and their total intensity together with the incoherent background. With this study we can obtain information about the periodicities present in the surface, the presence of domains and their size (correlation length) and about the presence of defects or not ordered areas. In this work we have used this mode for our studies. The second and much more complex way is based on the quantitative analysis of the LEED I-V curves. With it we can obtain structural information about the position of atoms inside a unit cell [49,50]. In first approximation, the interlayer distances can be obtained from kinematical analysis of the more intense peaks. A full structural determination requires a dynamical treatment of the data, including multiple scattering calculations. Due to the complexity of these methods, we are not going to enter into details. For people interested in a deeper knowledge about this mode and the technique we give some references [75,76].

We show a schematic representation of a LEED apparatus set-up in figure 3.5. It is composed by a fluorescent screen where electrons are collected and the diffraction pattern is formed; some grids (in our case three), which are used to repeal the inelastic secondary electrons through the application of different potentials; and an electron gun which produces an electron beam that is collimated and accelerated towards the sample.

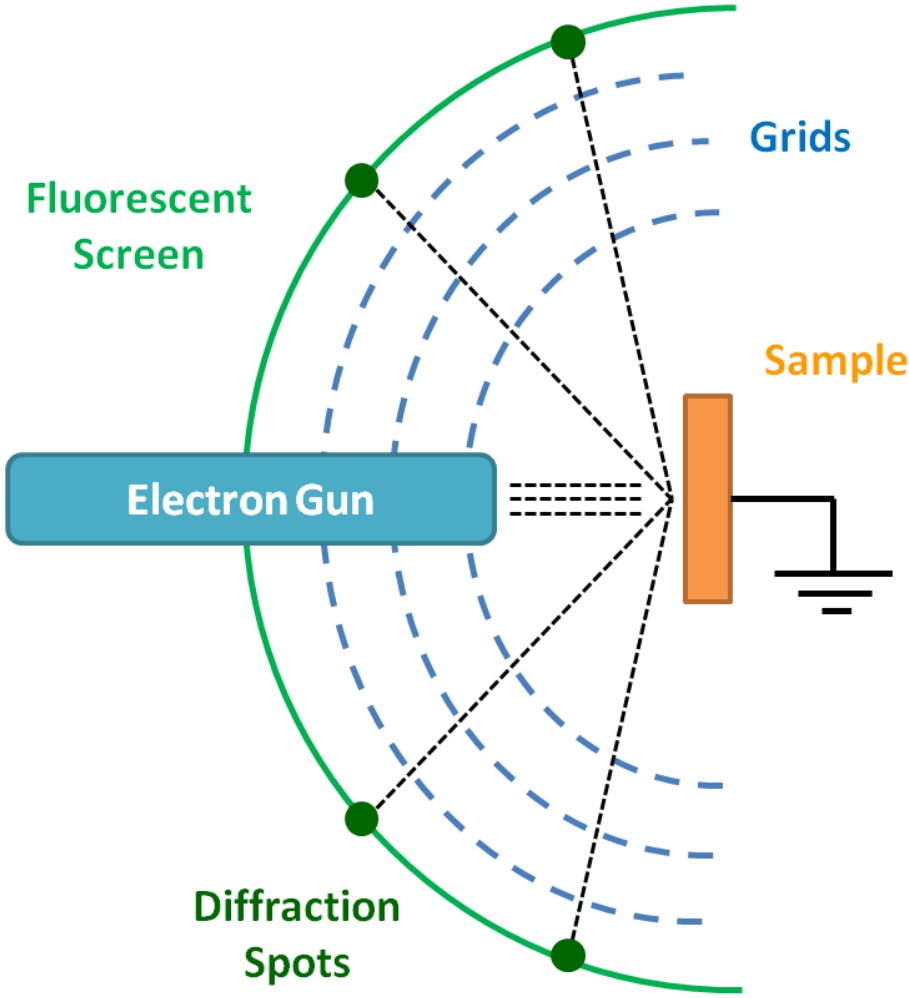

Figure 3.5.- *Schematic representation of an experimental LEED set-up.* The sample is irradiated with low energy electrons which diffract on the surface producing constructive interference spots which are accelerated towards a fluorescent screen. Grids are polarized in order to reduce the flux of inelastically diffracted electrons (secondary electrons).

As an example, we show the LEED pattern for the clean TiO_2 (110)-(1x1) surface (figure 3.6). In this figure we can observe 19 spots which correspond to the different diffraction orders. These spots represent the different Brillouin

zones, i.e. the unit cell of the reciprocal space which is inversely related to the real space [77]. Just with a quick inspection of the LEED pattern we can extract some information. First of all, we see that we have a rectangular unit cell in the reciprocal space which corresponds to a rectangular unit cell also in the real space, but rotated 90°. The ratio between the distance of spot (1,0) and (0,1) gives us the relationship between the lattice parameters in both directions, in this case ~ 2.21, in good agreement with the one obtained from the crystallographic distances (~ 2.19 as it can be extracted from figure 2.3). We also see that we have sharp round spots and only one domain. This is an indication of a well formed surface. Finally the fact of having a low intensity background means that we have a well ordered structure with a very small amount of defects.

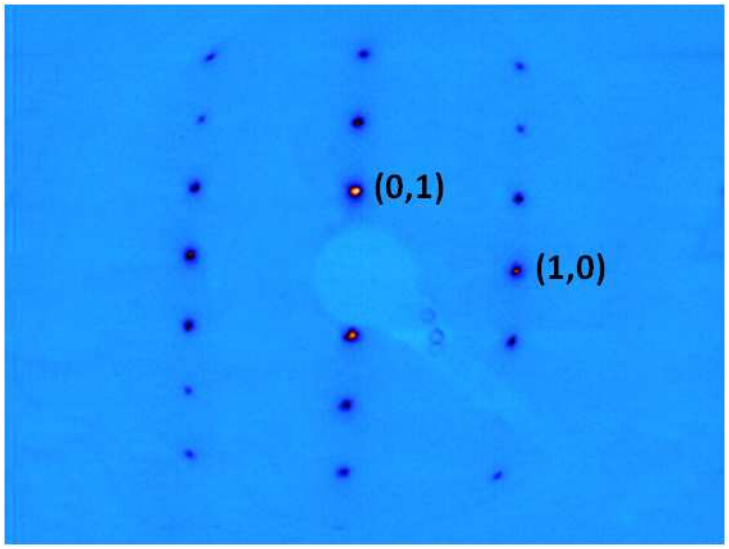

Figure 3.6.- *LEED pattern for the clean TiO_2 (110)-(1x1) surface*. Spots correspond to the reciprocal space of this surface. We observe a rectangular structure in agreement with the expected one for a rectangular unit cell in the real space (see figure 2.3). This LEED pattern was taken at 109 eV.

3.3. Ultra-violet / X-ray Photoelectron Spectroscopy (UPS / XPS)

This spectroscopic technique is based on the *photoelectric effect* discovered by H. Hertz in 1887, explained by A. Einstein in 1905 and considered one of the starting points of quantum physics.

It can be described in the following way: a sample is irradiated with monochromatic photons whose energy is in the range between ultra-violet (UPS) and hard X-ray (XPS) radiation. Some of these photons are going to be absorbed by the atoms producing an excitation induced by the extraction of the electron, which is emitted into the vacuum with a kinetic energy given by the expression:

$$E_{kin} = h\nu - E_B - \varphi \qquad \textbf{(9)}$$

where E_{kin} is the kinetic energy of the emitted electron, $h\nu$ is the photon energy, E_B is the binding energy of the emitted electron and φ is the sample work function. Figure 3.7 shows a scheme of the process.

Then, we measure the number of photoelectrons detected at the analyzer (photoelectron intensity) as a function of their kinetic energy. This kinetic energy is transformed into binding energy, which is characteristic of the energy level of each atomic species and of the chemical environment [78,79]. The measured photoelectron intensity is mainly conditioned by three parameters: the photoionization cross-section of the element under study, the mean free path of the photoelectrons and the distribution of the atomic species on the substrate. This relationship is given by:

$$I = \frac{J_I\, \sigma_A(h\nu_I)\, L_A^Z(\gamma_e, h\nu_I)}{\cos\theta_I}\, \frac{\Omega_d}{4\pi} \int_0^d N(x)\, e^{-\frac{x}{\lambda \cos\theta_d}}\, dx \qquad \textbf{(10)}$$

where J_I is the number of incident photons, σ_A is the photoionization cross-section of element A, $L_A{}^Z$ is the emission asymmetry factor, Ω_d is the detection solid angle, d is the distance from the surface to the bulk along we integrate the emitters density, $N(x)$ is the emitters density (atomic density of the surface), x is the position, θ is the incident or detection angle depending on the suffix and λ is the photoelectron mean free path. The suffix d makes reference to the detection while the suffix I is relative to the incident beam.

Depending on the photon energy used to excite the atom we will probe different energy levels. If we use UV radiation we will extract electrons from the valence band region (UPS) while if we use X-ray radiation we will excite electrons from the core levels of the atoms (XPS). Another variation of PhotoElectron Spectroscopies (PES), that it is the generic name given to this kind of techniques, is the Angle-Resolved Ultra-violet Photoelectron Spectroscopy (ARUPS). It consists of measuring the distribution of the emitted photoelectrons in the reciprocal space of the sample under study. This is done by measuring the kinetic energy and the direction (momentum) of the photoelectrons obtaining a reciprocal space or band mapping as a function of the momentum parallel to the surface ($k_{\parallel}$). In this way we will obtain a very detailed description of the electronic structure.

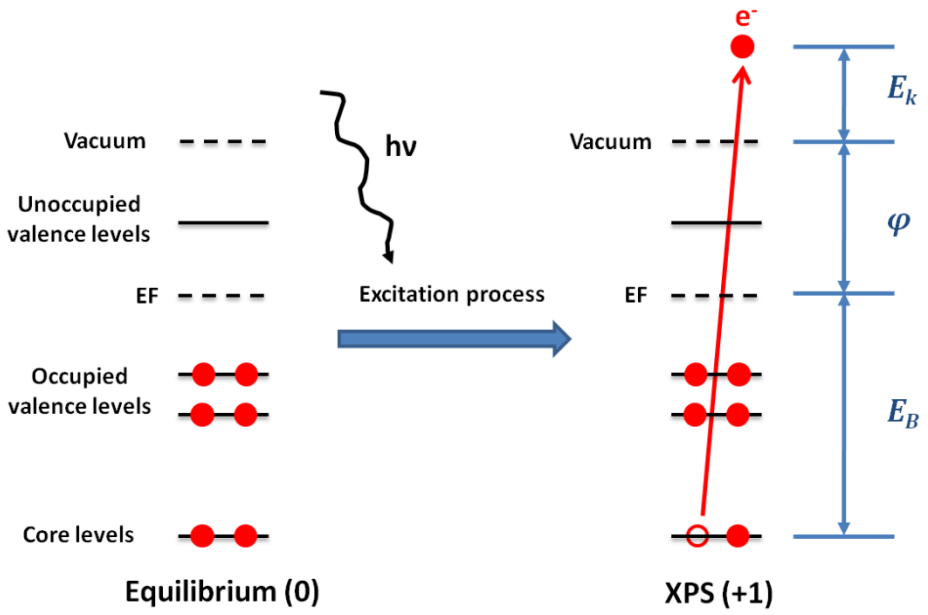

Figure 3.7.- *Schematic representation of the photoelectric effect*. Starting from an atom in equilibrium, when we irradiate it with photons whose energy is above the ionization threshold, a photon can be absorbed and its energy transferred to an electron in a core level / valence band state. This electron will have enough energy to escape from the atom so we will be able to detect it and to measure its kinetic energy in order to get spectroscopic information.

We can use these techniques in any conventional laboratory through the use of X-rays and ultra-violet sources such as Mg K_α ($h\nu$ = 1253.6 eV) or Al K_α ($h\nu$ = 1486.6 eV) for the X-rays production and HeI (21.22 eV) or HeII (40.8 eV) for the ultra-violet radiation and an electron analyzer. The biggest disadvantage of X-ray sources is that their brightness (proportional to the photon flux) is not very high (~ 10^6 – 10^{10} photons s^{-1} mm^{-2} mr^{-2} (0.1 % bandwidth)$^{-1}$). This low brightness will affect the resolution of our measurements. Typical values for the resolution in a standard laboratory are around 0.7 and 0.1 eV for X-ray and UV, respectively. If we need a more precise measurement it is convenient the use of synchrotron radiation [80], where the brightness is in the range of 10^{14} – 10^{20} photons s^{-1} mm^{-2} mr^{-2} (0.1 % bandwidth)$^{-1}$. In this way we can obtain an energy resolution in the range of some meV. Another big advantage of synchrotron radiation is the tunnability, that is, the possibility of changing the photon energy in a continuous range. This is crucial for others techniques such as NEXAFS, as we will discuss in the next section.

For the XPS fitting, we have used Lorentzian / Voigt peaks with a typical fixed FWHM in the range of 0.1 - 0.3 eV, depending on the element, allowing the variation of the Gaussian broadening with typical values in the range of 0.5 – 1.5 eV. Unless explicitly mentioned, we have utilized the lower number of components capable to properly fit the experimental data. A Shirley type background has been considered in all the spectra. C1s and valence band spectra have been calibrated to the defects peak binding energy (~ 0.8 eV) while for O1s and Ti2p core levels we have used the O1s peak at ~ 530.7 eV. We have utilized two fitting programs throughout the thesis: a home-made Igor macro (developed by Francesco Bruno, ALOISA beamline, Laboratorio TASC, CNR-IOM) and the XPSPEAK 4.1 program.

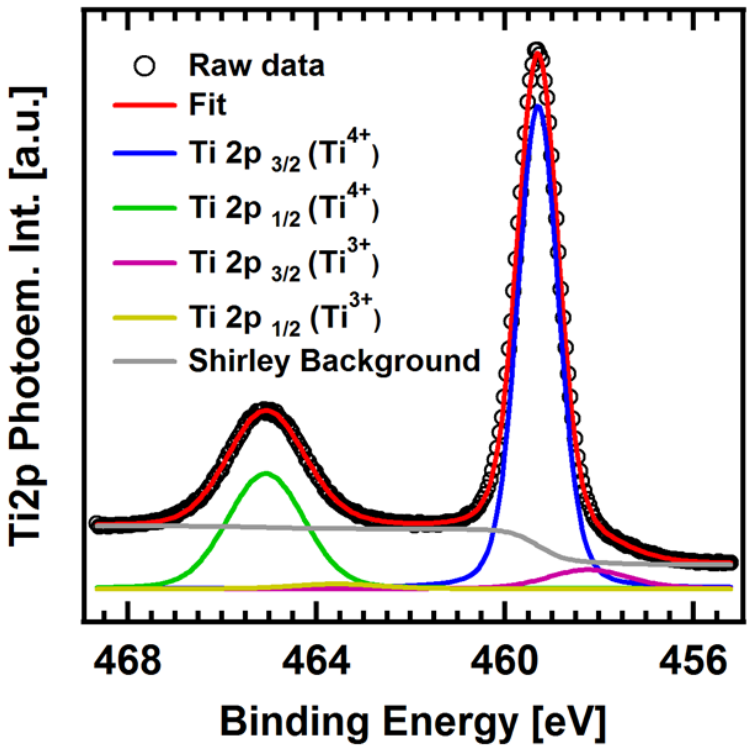

Figure 3.8.- *Example of the Ti 2p XPS spectrum for the clean TiO_2 (110)-(1x1) surface*. In this figure we can see the emission from the Ti $2p_{3/2}$ and Ti $2p_{1/2}$ states. The main peaks correspond to the titanium atoms in their "normal" oxidation state inside TiO_2 (Ti^{4+}). The small peaks correspond to the titanium atoms with an oxidation state Ti^{3+} as a consequence of having trapped extra charge coming from defects. The photon energy used for this spectrum is 650 eV.

In a UPS / XPS spectrum we represent the photoemission intensity with respect to the binding energy of the photoelectrons detected. We show an example in figure 3.8. It corresponds to the emission of the Ti 2p states of the clean TiO_2 (110)-(1x1) surface. We can observe two main peaks at BE = 459.3 eV and BE = 465 eV which correspond to the emission from the Ti $2p_{3/2}$ and Ti $2p_{1/2}$, respectively. These peaks are related to the titanium atoms in a fully oxidized 4+ state, that is, the ones with no extra charge due to the presence of an O_{vac}. The Ti^{3+} states related to defects give rise to the two small peaks located at a BE = 458.2 eV and BE = 463.3 eV.

3.4. Auger Electron Spectroscopy (AES)

Auger Electron Spectroscopy can be regarded as a three step process in which three electrons are involved. In the first step an atom is irradiated with photons (XPS) or electrons, which are going to be absorbed by the atom. Their energy is transmitted to an electron producing an excitation in the atom. In this technique, we are not interested in the photoelectrons emitted (like in XPS, for example) but in the ones emitted during the de-excitation process. After the excitation of the atom there is a hole in a core level state. This excited state is not stable and the atom will release energy through a de-excitation process, i.e. by the decay of an electron from a higher energy level (second step). This decay can be two-fold: through the emission of a photon (*Fluorescence or radiative decay*) or the emission of an electron (*Auger or non-radiative decay*). In our case we are interested in the second de-excitation process which, furthermore, presents a much higher cross-section for atoms with Z < 90. The difference in energy between both states is then transmitted to another electron from an energy level closer to the Fermi level that is then emitted into vacuum (third step) with a kinetic energy given, in first approximation, by:

$$E_{kin} \cong E_K - E_{L_1} - E_{L_2} \quad \textbf{(7)}$$

where E_K, E_{L1} and E_{L2} are the energies of the K, L_1 and L_2 levels. A schematic representation of the Auger process can be observed in figure 3.9.

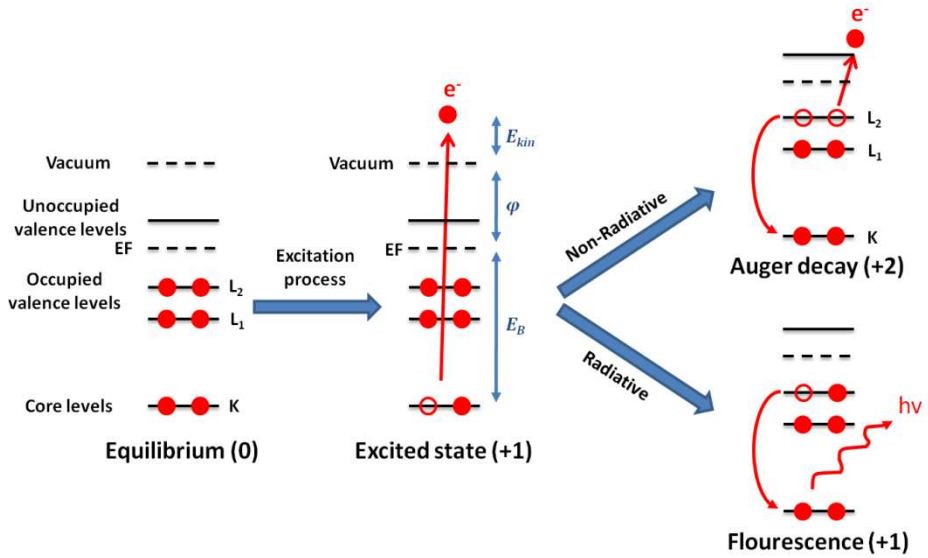

Figure 3.9.- *Schematic representation of the three steps involved in the AES process*. On the left, we can observe the target atom in its ground state before the ionization. In the middle we can see the excitation process in which one core level electron is ejected from the sample after the absorption of a photon/electron. The atom is now in an excited state. On the right we can see the de-excitation process that can be radiative or non-radiative. In the case of the Auger de-excitation (non-radiative) one electron from a higher energy level occupies the hole and a third electron is emitted thanks to the energy released during the de-excitation process. In the final state the atom is doubly ionized as two electrons have been emitted during the whole process.

This expression is a first approximation as it does not take into account energy relaxations due to the loss of an electron when the atom is in the excited state [78,81].

The emitted electrons are collected by an electron analyzer where their kinetic energy is measured. This kinetic energy is a fingerprint of the atomic species present in the surface of the sample under study.

This technique is very useful as it gives us chemical information like the species present in the sample surface and their interaction. Besides it can be done in any conventional laboratory. It presents a high surface sensitivity as we are detecting electrons with energies in the range of some hundreds of eV, whose

inelastic mean free path is lower than 50 Å as we have seen in the previous section.

As an example, figure 3.10 shows an AES spectrum for the clean TiO_2. On it we can see three Auger peaks which correspond to the Ti *LMM*, Ti *LMV* and O *KLL* transitions, where the letters *K, L, M* and *V* make reference to the energy levels involved in the Auger transitions (*K*: quantum number = 1; *L*: quantum number = 2; *M*: quantum number = 3; and *V*: valence band). Analyzing the intensities of the Auger peaks we can obtain quantitative information like, for example, the stoichiometry of the sample. In this thesis we have used AES spectroscopy as a qualitative technique just to check if the sample surface was clean. In figure 3.10, no carbon is observed (E_{kin} ≈ 270 eV) so we can conclude that the sample surface is clean (up to the resolution of our AES system, ~ 0.1 ML).

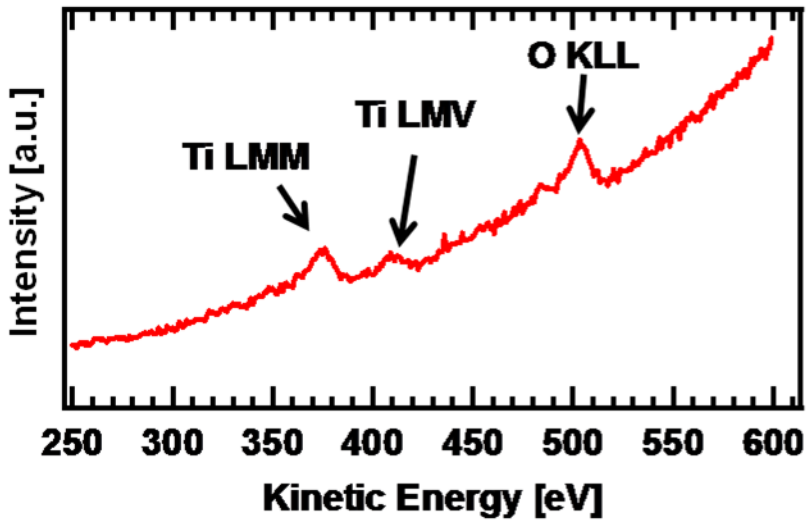

Figure 3.10.- *AES spectrum for the clean TiO_2 (110)-(1x2) reconstruction.* In this wide scan we can see three peaks corresponding to two Auer transitions of the Ti atoms (*LMM* and *LMV*) and one related to the oxygen atoms (*KLL*). The sample is clean as no other Auger peaks associated with other atomic species are observed.

3.5. Near-Edge X-ray Absorption Fine Structure (NEXAFS)

This spectroscopic technique developed in the 1980´s has become one of the most widely used experimental techniques for the study of the electronic and crystallographic structures of low-z molecules (those containing H, C, N, O and F) bonded to surfaces. It makes use of the specificity of the absorption edges of the different atomic species to probe the intra-molecular neighbors making possible the detection of specific bonds in molecules (like C-C, C=C, C-H, etc.), the determination of the length of the bonds, the investigation of the orientation of the molecules and the determination of the molecular orbitals involved in the chemical bond to the surface.

It consists of the irradiation of the sample with photons (usually linearly polarized) and studying their absorption as a function of the incident photon energy [82]. When a photon is absorbed by an atom it produces an excitation in it. This excitation can be an ionization, if the excited electron is ejected from it ($h\nu$ > *Ionization Potential* (IP)), or just an excitation to a bound state ($h\nu$ < IP). If it produces an excitation to a bound state, this unstable state will decay through an Auger process giving rise to the emission of an electron. We can thus operate the NEXAFS experiment in different modes depending on the electrons we detect: Auger Electron Yield (AEY) when we detect only the Auger electrons present at a fixed kinetic energy, Partial Electron Yield (PEY) when we detect all the electrons (elastic and inelastic ones) above certain threshold energy, and the Total Electron Yield (TEY) where we detect all electrons independently of their kinetic energy or creation process.

Molecular orbitals usually present a strong directional character. This directionality can be used to study the molecular orientation as resonance intensities exhibit a dramatic angular dependence when probed with linearly polarized photons. This dependence is a function of the dot product of the electric field of the incoming photon and the orientation of the probed molecular orbital. For the special case in which the incoming electric field is parallel / perpendicular to the orbital under study, the dot product will be maximum / zero. We can define two special cases depending on the relative orientation of the electric field and the surface of the system. If the electric field is parallel / perpendicular to the surface, it is said we are under *s-polarization* and *p-polarization* conditions, respectively. A schematic

representation is shown in figure 3.11. For the particular case of a π-plane transition symmetry and a two-fold surface symmetry, the angle between the molecular orbital and the surface, γ, can be obtained from the ratio between the two opposite polarizations. This ratio depends on γ in the following way [82]:

$$\frac{I_{s-pol}}{I_{p-pol}} \propto tan^2\gamma \qquad \textbf{(11)}$$

where $I_{s\text{-}pol}$ and $I_{p\text{-}pol}$ are the intensities of the NEXAFS peaks associated to π transitions in s and p-polarization conditions, respectively.

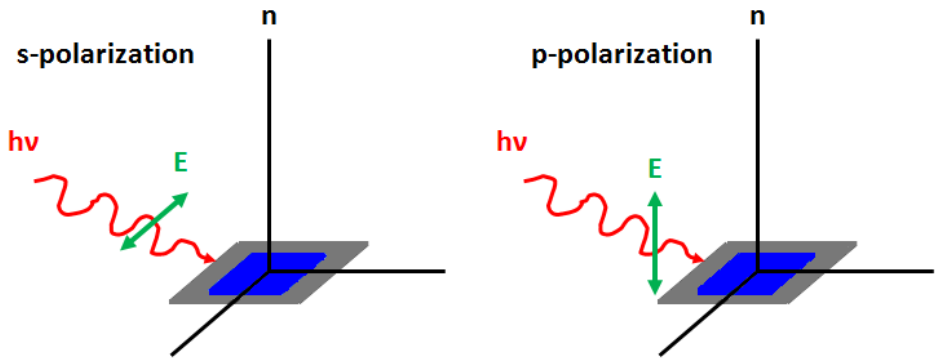

Figure 3.11.- *Schematic representation of the s and p-polarizations.* As we can see in the left panel, when the electric field of the incoming photon is parallel to the surface we are studying, we are in the so-called s-polarization geometry. If the electric field is perpendicular to it (right panel), we have p-polarization.

There is another general methodology to estimate the tilt angle consisting of fitting the intensity of the peaks in the π region versus the angle [82].

Thus, if we perform a NEXAFS measurement varying the relative orientation of the electric field of the incoming linearly polarized photon beam with respect to the surface we can obtain the tilt angle (γ) of the molecule. We just have to plot the intensity variation of the π transitions versus the angle between the beam and the surface and fit them with the expression given in ref. [82].

In our case, all the NEXAFS spectra shown here have been measured at the ALOISA beamline at Elettra synchrotron (Trieste, Italy). In all cases we have measured the NEXAFS spectra at the C K-shell ionization threshold by rotating the sample around the photon beam axis, which corresponds to a polar scan. We used the PEY mode with an electrostatic high-pass filter set at -230 eV in order to reject the inelastic secondary electrons. The photon energy was calibrated using the C absorption feature at I_0, obtaining a precision of 0.01 eV.

3.6. X-ray Photoelectron Diffraction (XPD)

X-ray photoelectron diffraction is a very powerful technique for the determination of surface structures at the atomic scale [83-87]. This technique is based on the fact that photoelectrons may suffer elastic scattering processes during their way out of the crystal, being possible to observe diffraction patterns due to the interference between the direct and scattered waves. It presents two major advantages with respect to other diffraction techniques such as LEED or x-ray diffraction (XRD): it is element specific since it is usually possible to find a kinetic energy specific of the element under investigation, and it is local, i.e. it probes the short-range order around the selected emitter giving us information about its neighboring atoms.

The physical process behind XPD is the elastic electron scattering. When we irradiate an atom with photons of enough energy to extract one electron from it, this electron can be ejected through two ways: it can propagate directly into vacuum or it can undergo a number of elastic scatterings with the neighboring atoms of the emitter. Electrons coming from these two paths can interfere giving rise to a diffraction pattern which is very sensitive to the relative atomic positions. If we measure the variation of this photoelectron intensity either with the photon energy or the emission angle we will be able to determine the atomic structure around the emitter atoms. In the case of angle-resolved XPD, if we use the so-called *forward-focusing* regime, i.e. when the photoelectrons kinetic energy is above 500 eV, the majority of the intensity will be emitted in

the same direction of the scattering atoms, making much easier the interpretation of the XPD patterns (see figure 3.12).

Once we have measured the experimental XPD diffraction pattern it is mandatory to carry out multiple scattering calculations in order to be able to correctly interpret the obtained results. These calculations give rise to a simulated diffraction pattern which can be compared with the experimental one in order to determine the exact position of the atoms of the system under investigation. This comparison is usually done through a reliability-factor (*R-factor*).

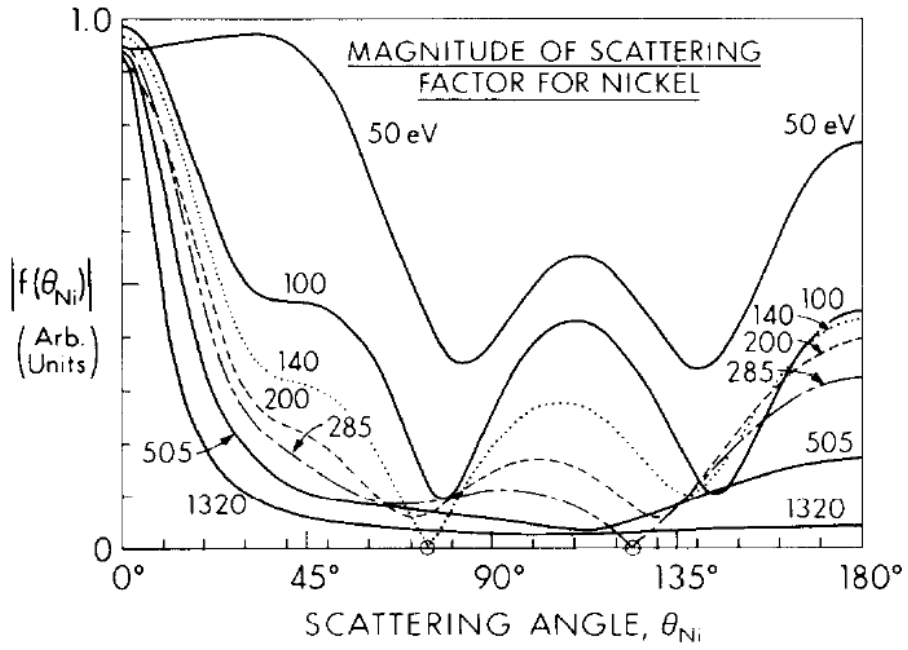

Figure 3.12.- *Representation of the scattering factor amplitudes*. It is represented the scattering factor amplitudes as a function of the scattering angle for the case of Nickel. As we can see, from an electron kinetic energy of 500 eV the predominant scattering angle is 0° (forward-focusing regime). Taken from ref. [83].

In our case, we have carried out all the XPD measurements on molecular systems at the ALOISA beamline at Elettra synchrotron (Trieste, Italy) while those on the clean TiO_2 were done at the Institut de Physique at the Neuchatel University (Neuchatel, Switzerland). In both cases we measured the photoelectron intensity as a function of the emission angle. For the representation of the obtained data, we displayed the *chi-function* (χ) which is defined as:

$$\chi(\theta,\varphi) = \frac{I(\theta,\varphi) - I_0(\theta,\varphi)}{I_0(\theta,\varphi)} \quad \textbf{(12)}$$

where $I(\theta,\varphi)$ is the photoemission intensity at the angles θ and φ and $I_0(\theta,\varphi)$ is the background intensity obtained as the azimuthal average for each polar angle. This chi-function is related to the oscillatory part of the photoemission intensity, i.e. the anisotropy.

For the simulations we have used the Electron Diffraction in Atomic Clusters (EDAC) program [88]. Table 1 exhibits the typical parameters we have used for the C1s XPD patterns such as the *inner potential* (V_0), the *cluster surface*, the *inelastic mean free path* (λ) and the *maximum value of the orbital angular momentum number* (l_{max}). The V_0 is the parameter used to indicate the energy difference between the vacuum level and the muffin-tin zero while the *cluster surface* is the value of z below which the photoelectron can suffer inelastic losses.

Inner Potential (V_0)	**Cluster surface**	**Inelastic mean free path (λ)**	**l_{max}**
5 eV	2.3 Å	30 Å	12

Table 3.I.- *XPD parameters table*. In this table we show the values used for the simulations for the most important parameters. We have chosen these values after several verifications.

All the values shown in this table have been tested and the “best” ones have been used, considering as the “best” ones those which gave a more “physical” and “real”result.

Once we have both the experimental results and the theoretical simulations we compare them through a reliability-factor (*R-factor*) defined as:

$$R - factor = \frac{\left(\chi_t - \alpha\, \chi_{exp}\right)^2}{\chi_t^2 + \left(\alpha\, \chi_{exp}\right)^2} \qquad \textbf{(13)}$$

where the suffix t makes reference to the theoretical simulation, the suffix exp to the experimental data and α is a scaling factor.

In figure 3.13 we show an experimental angular XPD pattern for the Ti 2p photoemission peak in the clean TiO_2 (110)-(1x2) surface. In this pattern, the center means normal emission while the border is grazing emission. A radial line is a polar scan while a circumference is an azimuthal scan. In the intensity scale, brighter means more intense. This pattern was taken in the forward-focusing regime so each bright feature corresponds to the direction in which the emitter (Ti) has a neighbor (O or Ti). We would need to perform a simulation for the surface structure pattern in order to be able to identify all the bright features present on it. However, when we compare this pattern with the one obtained for the bulk-like (1x1) structure, we do not appreciate characteristic features associated to the (1x2) reconstruction. This is so because the signal from the bulk is much stronger than that from the surface.

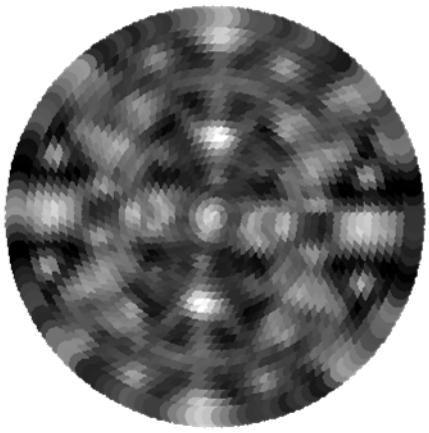

Figure 3.13.- *XPD pattern for the Ti 2p core level*. In this figure we show the electron diffraction pattern obtained for the Ti 2p state in the TiO_2 (110)-(1x2) surface. In the intensity scale, brighter means more intense. It has been taken in the forward-focusing regime with a photon energy of 1253.6 eV (Mg Kα) and a kinetic energy of 794 eV.

3.7. Helium Atom Scattering (HAS)

Helium atom scattering is a diffraction technique which uses He atoms to probe the size and orientation of the surface unit cell and even the geometrical arrangement of the surface atoms through the study of the surface corrugations obtained from the analysis of the diffraction intensities [89,90]. Thanks to the extremely low energy of the atoms (10 - 300 meV) used as a probe we obtain real surface information in a non-destructive way and it is valid for all type of materials whether they are metals, semiconductors or even insulators. The diffraction is done thanks to the de Broglie wavelengths of the incoming atoms since at these energies they present a wavelength in the order of some Å. It is an extremely sensitive technique as it is able to identify the presence of impurities even at a concentration of ~ 0.001 ML.

The basis of this technique is the He – surface interaction potential. As the He atoms approach the surface they suffer two different interactions depending on their distance to it. In a first step, they are attracted due to the van der

Waals forces. As they get closer to the surface they start being repelled due to the overlap of the He and surface electronic wavefunctions, which will force the He atoms to be diffracted.

In our case, we performed the HAS measurements at the branchline of the ALOISA beamline at Elettra synchrotron (Trieste, Italy). We operated the He beam while cooling down the nozzle at liquid nitrogen (LN_2) temperature. This yields a beam wavevector of 6.074 $Å^{-1}$, which is equivalent to a He beam energy of ~ 19 meV.

3.8. Sample preparation

For our experiments we have used square commercial TiO_2 (110) samples from Mateck. The typical size of the samples we have used is 10 x 10 x 1 mm^3 although other sizes and shapes have been tried. We have chosen these dimensions from a practical point of view. Square samples are easier to handle and 10 mm side is the biggest size we can accommodate in our STM equipment. The election of the thickness is a compromise between two factors that must be taken into account: the rupture resistance of the crystal and the reduction speed. We have seen that samples with a thickness of 0.5 mm are easily reduced, what it can be an important factor if you are interested in working with the (1x2) surface, but they present a big withdraw as they are very fragile so it is very easy to break them during the annealing cycles as they tend to expand. If these samples are going to be used, special attention must be taken during the mounting of the sample. On the other hand, if we choose a 1 mm thick sample we can be confident that it will not break during the annealing cycles but we will have problems to get the (1x2) surface as it will take a lot of time to get the necessary reduction of the bulk.

Preparing titanium dioxide is a triple aim purpose. First we have to clean all possible contaminants present at the surface and bulk. Secondly we have to produce a high quality surface in order to be able to perform the desired experiments. Thirdly, we want to reduce the substrate in order to be able to use surface science techniques. The procedure for removing all the contaminants from the substrate is quite simple although some considerations

must be taken into account, as the procedure will be slightly different depending on the surface structure we are interested in.

3.8.1. *Preparation of the TiO_2 (110)-(1x1) surface*: we will explain the whole procedure for the preparation of this surface taking a new sample as the starting point. We do all the preparation process *in-situ*, i.e. inside the UHV chamber. The first thing to do is the outgassing of the sample. This process is time-consuming as it is convenient to do it under a controlled atmosphere, i.e. with a maximum pressure of low 10^{-7} mbar inside the chamber. We have to increase the sample temperature until we reach the one we will use during the annealing cycles (approximately 1000 – 1100 K). The purpose of this annealing is to remove all the typical impurities present in a sample when it has been exposed to air (water, nitrogen, carbon, etc.) apart from the ones characteristic of titanium dioxide which come from the fabrication process and are segregated into the surface during the annealing cycles (calcium, potassium, etc.). We will continue with the annealing until the pressure in the UHV chamber decreases to low 10^{-8} mbar. In this way we will be sure that pressure will remain low during the future annealing cycles. Once it is outgassed, we perform sputtering and annealing cycles. The first sputtering cycle will be done at high energy (typically 1.5 keV) and we will decrease it as we advance in the number of cycles, finishing always with a 0.5 keV sputtering. This is done in this way because the initial sputtering cycles will completely destroy the surface as they must remove a lot of contamination while for the last ones we want a soft sputtering in order not to create a big corrugation on the surface so it will be easier to get a high quality surface. Always after a sputtering cycle we do an annealing one to recover the quality of the surface and to help to evaporate the possible impurities still present on it (for example, Ar). The duration of these annealing cycles is usually 10 – 15 minutes. If the sample is new we may need up to six – seven complete cycles until getting a clean good-quality surface. Once we have it, we do not need to sputter every day if we do not deposit anything on it. Just a refreshing annealing is necessary before starting a new experiment. If some organic / inorganic material is deposited on the surface, at least three sputtering / annealing cycles are necessary, two of them done at high energy. The

cleanness of the sample is checked by AES and STM while the quality of the surface is checked by LEED and STM.

3.8.2. *Preparation of the TiO_2 (110)-(1x2) surface*: usually we obtain this surface spontaneously after several months working on the (1x1). The important point for obtaining a good (1x2) surface is the annealing temperature and the annealing duration. We need to reach 1100 K for several minutes (at least cycles of 60 minutes) in order to be able to form a complete (1x2) surface. If we do not reach this temperature or if the annealing is too short, we will have a coexistence of both, the (1x1) and the (1x2) surfaces, as it will be shown in section 5.1. The preparation procedure after the deposition of organic / inorganic material is the same as for the (1x1) surface. The surface quality, given by the size of the terraces and the density of surface defects (different from O_{vac}´s) will also depend on the pressure inside the UHV chamber during the annealing cycles. A pressure lower than 10^{-8} mbar is desirable to get a good quality surface.

3.9. Organic / inorganic material deposition

During this thesis we have deposited two types of substances on both surfaces: organic molecules and platinum.

3.9.1. *Organic molecules*: we have deposited four different organic molecules on the TiO_2 (110)-(1x1) surface: C_{60} (98 % purity, Sigma-Aldrich), pentacene (99.5 % purity, Sigma-Aldrich), $C_{60}H_{30}$ (synthesized by Dra. Berta Gómez Lor (ICMM-CSIC)) and protoporphyrin IX (95 %, Sigma-Aldrich). All of them have been deposited from home-made tantalum envelopes spot-welded to two stainless steel rods fixed to a feedthrough. We also spot-welded a K-type thermocouple to the Ta envelope in order to be able to measure the deposition temperature. The envelopes are heated by circulating a current through them. In general, the distance between the sample and the evaporator during the deposition was around 5 – 7 cm. Typical currents are between 5 and 13 A.

The evaporation temperatures for the different molecules are shown in table 3.II. As we can see, temperatures are quite different so we have to pay special attention during the mounting of the evaporators in order not to overcome the maximum temperature for pentacene during the bake-out of the chamber to avoid their decomposition or the emptying of the evaporator.

Molecule	C_{60}	Pentacene	$C_{60}H_{30}$	Protoporphyrin
Temperature	700 – 750 K	450 – 470 K	650 – 670 K	550 – 580 K

Table 3.II.- *Evaporation temperatures for organic molecules*. This table shows the evaporation temperature ranges in which the organic molecules used during this thesis have been evaporated. Special care must be taken with pentacene to avoid their evaporation during the bake-out.

In the experiments carried out at the ICMM we have calibrated the evaporation rate with the STM. In the other cases, we used a quartz microbalance for an estimation of the evaporation rate as we had no access to a STM system.

A very important point that must be taken into account when working with organic molecules is their outgassing. It is extremely important to remove all the possible contaminants present in the molecular powder before doing the experiments. We have always outgassed the molecules by annealing them at least at the evaporation temperature until we observed a stabilization of the pressure. This is particularly important in the case of $C_{60}H_{30}$ as they are home-made and they did not undergo strong purification process.

3.9.2. Platinum deposition: we have deposited Pt by direct heating of a Pt wire (99.99% purity, Mateck) fixed to a feedthrough with Be barrels. We have used a home-made Ta shutter with a hole (2 mm diameter) to focus the evaporation. The evaporator was also outgassed by annealing it up to the evaporation temperature. The distance between the evaporator and the sample during the deposition was 10 cm approximately. Typically, we have used a current of about 10 A to evaporate it.

3.10. Experimental systems

During the realization of this thesis we have used up to four different experimental systems. The majority of the thesis experiments have been done in the ESISNA group UHV system located at the Instituto de Ciencia de Materiales de Madrid (ICMM-CSIC) [91]. It is equipped with a room temperature STM, LEED-IV, AES, evaporators, QMS, sputtering and heating system, etc. as it can be seen in the picture of figure 3.14. In this chamber we have done all the STM, LEED and AES measurements presented in this thesis.

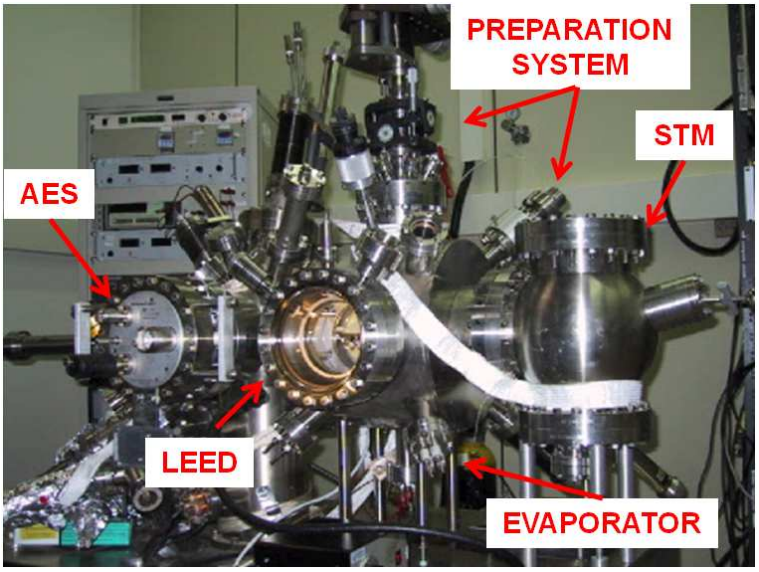

Figure 3.14.- *Experimental system at the ESISNA group (ICMM-CSIC)*. As we can see, this home-made UHV chamber is equipped with three main experimental techniques: RT-STM, LEED-IV and AES. Apart from this, it is also equipped with a Quartz microbalance, QMS, evaporators and a preparation system composed by a sputtering gun and a heating system (electron bombardment). The base pressure is 1 10^{-10} mbar.

As it has been mentioned before, apart from the experimental techniques available at our laboratory, we have used some other techniques in order to get complementary information necessary for the complete study of our systems. For this reason we have established a collaboration with the

members of the ALOISA beamline at Elettra synchrotron (Trieste, Italy). This collaboration has allowed us to travel in several occasions to their installations to perform the majority of the spectroscopic and diffraction measurements. All the UPS, XPS, NEXAFS, XPD and HAS measurements related to molecular deposition on TiO_2 have been done at ALOISA beamline [92].

The spectroscopic and diffraction measurements related to the determination of the electronic structure of the TiO_2 (110)-(1x2) surface where done in two different experimental chambers. The ARUPS and XPD measurements were done at the group of Prof. P. Aebi at the Institut de Phisique of the Neuchatel University (Neuchatel, Switzerland) while the UPS measurements for the determination of the double contribution in the defects peak were done at the Spectroscopy and Microscopy on Surfaces (SMS) system in the Centro de Astrobiologia (CSIC-INTA).

3.11. Density Functional Theory (DFT)

To study the electronic structure from a theoretical point of view it is mandatory to determine the optimized geometrical structure of the system under investigation. This means solving the Schrödinger equation for a many-body system as it is the case of a solid. DFT proposes a new approach for the determination of the electronic structure of many-body systems through the optimization of the charge density functional, which is related to the total energy of the system [93]. Once we have obtained the ground state of our system we can calculate the forces actuating on the atoms and, consequently, the equilibrium positions of the atoms.

For this thesis, we have performed DFT calculations for the determination of the optimized structures of different systems, together with the simulation of STM images. We have used two codes for these calculations: CASTEP [94,95], which is based in the use of a plane-wave basis, and FIREBALL [96-98], which uses an atomic-like localized orbitals basis [99]. The biggest difference between both methods is the accuracy and computational cost. CASTEP is a more accurate method although it is much more expensive from the

computational point of view. On the other hand, FIREBALL is less accurate but it is much faster.

For the calculation of the tunneling current in the STM simulations we have used the Keldysh-Green function formalism [100,101]. The procedure is optimizing separately the electronic structure of the tip and the surface and then calculating the tunneling current taking into account the hopping probability between tip and sample. In this way, the tunneling current is described by equation **(14)**.

$$J = \frac{4\pi e}{\hbar} \int_{E_F}^{E_F+eV} T_r[T_{TS}\, \rho_{SS}(E)\, D_{SS}^{R}\, T_{ST}\, \rho_{TT}(E-eV)\, D_{TT}^{A}]\, dE \qquad \textbf{(14)}$$

where J is the tunneling current, T_r is the trace of the matrix expressed in square brackets, $T_{TS/ST}$ is the hopping probability between tip and sample and vice versa, $\rho_{SS/TT}$ is the sample / tip density of states and $D_{SS/TT}$ is related with the probability of multiple scattering of the electrons between tip and sample.

The Hamiltonians necessaries for the calculation of each term expressed in equation **(14)** are obtained using the DFT-LDA FIREBALL code, where LDA is the acronym of the Local-Density Approximation. This approximation consists in considering the electronic density as a homogeneous electron gas, i.e. as a non-interacting electron gas.

As an example of the possibilities of DFT calculations, in figure 3.15 we present the theoretical DOS for the clean TiO_2 (110)-(1x1) surface close to the Fermi level. We can observe that the main contribution to the VB is coming from the bridging oxygen atoms (O_{br}) although some contribution from six-fold Ti (Ti_{6f}) atoms is observed. This is due to the hybridization between these two atoms. On the other hand, the CB is due to the Ti atoms, mainly the 3d state of five-fold Ti (Ti_{5f}) atoms. This is the reason why the bright rows observed in STM images correspond to the Ti_{5f} atoms and not to the O_{br} atoms, as we explained in section 3.1.

The theoretical calculations shown in this thesis have been performed by Dr. Pedro de Andrés, Dr. Maria Blanco-Rey and Dr. César González, members or former members of the ESISNA group, and by Dr. Pavel Jelinek, from the Institute of Physics (Prague).

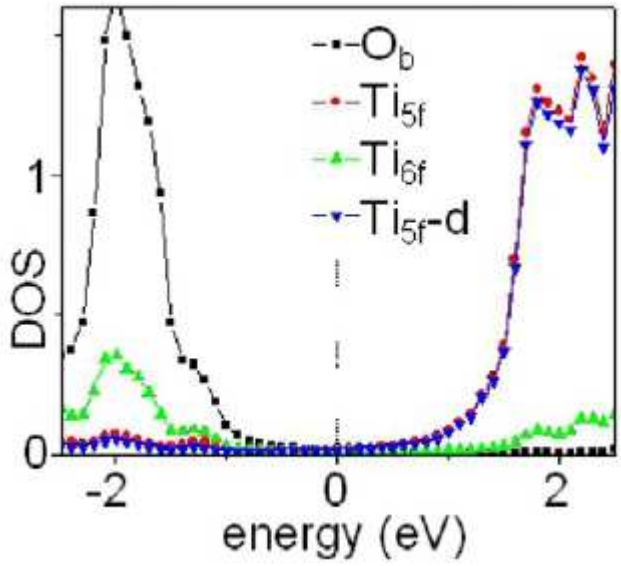

Figure 3.15.- *Calculated density of states (DOS) of the rutile TiO_2 (110)-(1x1) surface*. The DOS is represented decomposed into its orbital contributions. As we can see, the conduction band presents a predominant Ti character while the main contribution to the valence band comes, mainly, from the O atoms.

4. The rutile TiO_2 (110)-(1x1) surface

In this chapter we show the results obtained for different experiments carried out on the rutile TiO_2 (110)-(1x1) surface. We can divide them in two groups: one related to the clean surface, where we have studied the influence of the tip state in the interpretation of the atomic-resolution STM images; and the second one, where we have investigated the interaction of four different organic molecules (C_{60}, pentacene, $C_{60}H_{30}$ and protoporphyrin IX) with this surface.

The scheme we are going to follow along this chapter is the following: we start analyzing the atomic-resolution STM images of the clean surface. Then we study the interaction of the different organic molecules mentioned above, separately. Finally, we perform a comparative study of the four different molecules, focusing the discussion on their interaction with the TiO_2 surface.

4.1. Influence of the tip state in the interpretation of atomic-resolved STM images on the rutile TiO_2 (110)-(1x1) surface

Titanium dioxide presents punctual defects on its surface. The most common and interesting ones are bridging oxygen vacancies (O_{vac}) as they are responsible of the majority of the catalytic properties of this surface. As an example, we can mention the catalytic role of O_{vac} in the dissociation of residual gas water molecules into OH groups which "heal" the corresponding O_{vac} giving rise to the second main defects of this surface [14,102-104]*. The local character of these defects makes STM a very interesting technique to study their influence on different surface processes that can be catalyzed by them* [105-107]*. As this influence can be different depending on the type of defect, it is important to correctly identify O_{vac} and OH species on STM images of this surface. But their appearance at the STM is still not clear. In addition, the interpretation of the STM images on TiO_2 surfaces is complex due to its peculiar electronic structure so the total comprehension of the images is still an open question* [108-111]*. When analyzing an STM image it is common to find bright features between the Ti rows or depressions within them. These features are associated to point-defects. These are also observed in the case of AFM where the images are not so affected by the electronic features, attracting renewed interest in the last years* [112-114]*. Apart from the interpretation of the STM images associated to defects, new efforts have been recently devoted to the interpretation of the influence of the tip nature when imaging the TiO_2 surface with an AFM* [114-117]*.*

It is well known that the interpretation of STM images is never straightforward and unexpected features usually appear on them. A fully understanding of the images requires a combination of experimental data with theoretical simulations. Simulating systems where many atoms are involved is not a simple task as both the tip and the surface should be included in the calculation [118-120]*. In an idealistic model we can consider the tip as a group of atoms, usually tungsten, arranged in a pyramidal structure in such a way that the practical totality of the tunneling current goes through the atoms closer to the surface (tip apex). However, during an experimental STM session is very common to experience structural changes of the tip as it is some angstroms far from the surface and the interaction is not negligible. This is even more notorious in substrates like TiO_2 where the bridging oxygen atoms (O_{br}) are slightly bonded to the surface and can be easily removed from it and transferred to the tip* [14,115]*. The types of changes that a tip could suffer can go from a simple*

reorientation of the atoms at the apex to the adsorption of a foreign atom coming from the surface. In this sense, it has been suggested the formation of exotic functional groups at the tip apex such as Ti_3O_5 *groups* [114,116]. *A common tip contaminant is oxygen. It has been proved on different environments that the adsorption of oxygen atoms at the tip apex can produce the appearance of artifacts in the STM images such as contrast inversion* [118,119]. *Due to the relevance of the tip effects on the experimental images recorded on this surface, many theoretical studies based on the simulation of AFM images with Si tips have been performed* [114-117]. *On the contrary, the amount of theoretical work carried out on the simulation of STM images using W tips is still insufficient* [108,109].

For the particular case of the clean rutile TiO_2 *(110)-(1x1) surface, there are different types of atomic-resolved STM images published in the literature* [39,58,121,122]. *As an example, some groups have observed wide bright rows composed of elliptical features with their long axis oriented along the [1-10] direction* [39,58]. *This effect has also been detected recently by AFM* [112,116]. *Several explanations have been given for these features but a complete study is still missing.*

In this section we show how with the combination of theoretical STM simulations and experimental STM images we are able to explain the appearance of the STM images based on the influence of the tip apex nature. We demonstrate that it is feasible to identify the state of the tip by a careful inspection of the STM images. Our STM study allows us to identify features on the TiO_2 *(110)-(1x1) surface, and in particular we can distinguish between point defects scanned with a clean W tip and those scanned with a contaminated one, whether with one or two oxygen atoms at the apex.*

4.1.1. Previous theoretical considerations

As we already mentioned in the *Methods* chapter (section 3.11) we have used the FIREBALL code [97,98] to carry out the DFT calculations. The exchange-correlation potential has been calculated using the local-density approximation (LDA) and a basis of numerical atomic orbitals with appropriate special cutoffs, adequate for the formalism that we have used for the STM simulations [99,123]. All the basis sets and cut-off radii that we have used for these simulations have been checked previously in other works. In table 4.1.I we show the basis sets and cut-off radii employed in this work for the different elements used. As an example, the Ti and O radii have been successfully used in the description of the bulk and the surface of TiO_2 [115,124].

Element	Basis	S	P	d
H	Double	2.01		
O	Double	1.75	2.01	
Ti	Single	3.28	3.54	3.02
W	Single	2.49	2.75	2.38
C	Single	2.38	2.38	

Table 4.1.I.- *Basis sets and spatial cut-off radii (angstroms) for the different atoms involved in the tip and TiO_2 relaxation.*

The W radii have been also tested in the Si (111) (4x1)-In system obtaining a satisfactory result [125]. Regarding the optimization of the rutile TiO_2 (110) surface we have used a three tri-layer slab with a (1x1) periodicity for the clean surface, and (4x3) or (7x3) two-dimensional unit cells when we have introduced any defect. The reason for these unit cell dimensions is that in this way we could avoid interactions across periodic images. For all the optimization processes we kept the last layer (the deepest one) fixed taking as a reference the bulk-like optimized positions. The criterion used to consider that a structure has reached convergence is that the total energy has changed by less than 10^{-6} eV / atom in three consecutive iterations and that the maximum force on these atomic configurations has fallen below 0.05 eV $Å^{-1}$.

For the case of the tip, we have modeled it as a pyramid-like cluster formed by more than one hundred W atoms terminated in (100) planes and we have fully relaxed them using the same criteria explained above. In order to be able to reproduce the experimental STM images we have used up to 17 different tips where we have changed the geometrical and chemical termination. This has been done by introducing foreign atoms (H, O or C) which may be transferred from the surface or the residual gas to the tip apex during the STM measurement. The complete set of tips that we have tested for the simulations is shown in figure 4.1.1. Here we can see a side-view of sixteen of the seventeen tips used (the seventeenth tip is just the so-called **C** tip but rotated 90°). As it can be observed, we have proved tips contaminated with one or two different atoms whether adsorbed on the apex or even replacing it. Among all of them we have chosen the simplest four tips capable to reproduce correctly the experimental results. They are shown at the bottom of figure 4.1.1 and, more in detail, in figure 4.1.2 a). We have called them **A** (clean W), **B** (one O atom replacing the W apex), **C** (two O atoms adsorbed at near-bridge positions) and **D** (one O atom adsorbed below the W apex) tips.

Our goal has been to test the effect on the tunneling images of different tip coordination and symmetries, as well as the chemical substitution of some key atoms. In order to have a reference system we will compare all the results obtained for the different tips with those obtained with a “standard” clean W tip (**A** tip).

In the case of the **B** tip, when an O atom replaces the original W apex, our calculations show that all the high symmetry adsorption sites are equally stable as the energy is similar in all cases. However, when the **B** tip adsorbs an extra O atom forming the so-called **C** tip, a charge transfer from the W atoms to the O atoms produces an electrostatic repulsion between both adsorbates. This repulsion will force the O atoms to displace their equilibrium positions to near-bridge ones (**C** tip).

Among all the tip models we have calculated, the **A**, **B**, **C** and **D** tips represent the simplest possible set of configurations which are able to explain the features observed by the STM. A closer view of all of them can be observed in figure 4.1.2 a).

The Keldysh-Green function formalism [100,126] that we have used for the simulation of the STM images allows us to relax the tip and the surface separately obtaining in this way the Hamiltonians for the isolated tip and surface subsystems. The procedure we have followed consists of using these Hamiltonians to compute the Green´s function that describes the propagation of the electrons. Then we switch on an interaction Hamiltonian that will allow us to compute the tunneling current flowing between tip and sample even under strong interaction and non-equilibrium conditions (e.g. a large and finite voltage between tip and sample).

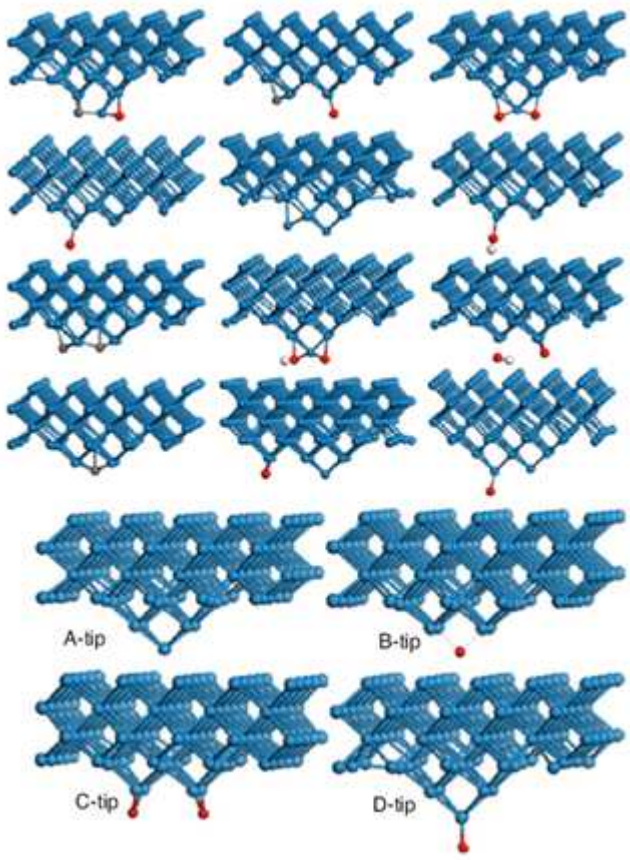

Figure 4.1.1.- *Geometrical structure of all the tips checked for the simulations.* We present the optimized tips used for the STM simulations. The four most relevant ones at the bottom. Color code: W (blue), O (red), C (grey) and H (white).

In principle, this theory can account for the possible deformation of the sample due to its interaction with the tip but the computational price that we would have to pay for a self-consistent geometrical optimization is too large. For this reason we restricted ourselves to the approximation where the tip and sample interaction is not high enough to produce elastic deformations or displacements of atoms. We think this is a good approximation, except perhaps for the case of the giant corrugation images that we consider beyond our theoretical computational means.

We have computed the simulated tunneling intensities either in the constant current (CCM) or in the constant height (CHM) modes. We have observed that both modes yield the same qualitative simulated STM images so we have used the CHM mode as it is not so time-demanding from a computational point of view. On the other hand, the CCM mode is better to compute the corrugations along a given scan line as it gives us directly the physical magnitude and a more accurate value.

In order to show the influence of the O atoms present in **B**, **C** and **D** tips on the density of states (DOS) of the tip, we exhibit in figure 4.1.2 b) the curves associated to the DOS of the different tips decomposed into their orbital contributions. In this figure we see how the presence of O atoms on the tip can influence the STM images. As we explained in equation **(3)**, section 3.1, the tunneling current depends on the tip DOS and it is extremely influenced by the tip termination. This behavior will be discussed later.

Finally, we have performed all the theoretical calculations at T = 0 K, using sharp Fermi-Dirac distribution functions. This is a good approximation for room temperature and a constant bias [127]. However, we have added to the energy a phenomenological imaginary part of about 2 k_BT (T = 300 K) in order to improve the convergence of the Green´s functions and round density of states. We have checked that our conclusions do not depend on this parameter by re-calculating selected cases for half its value. A detailed explanation of the calculation methodology can be found in [128].

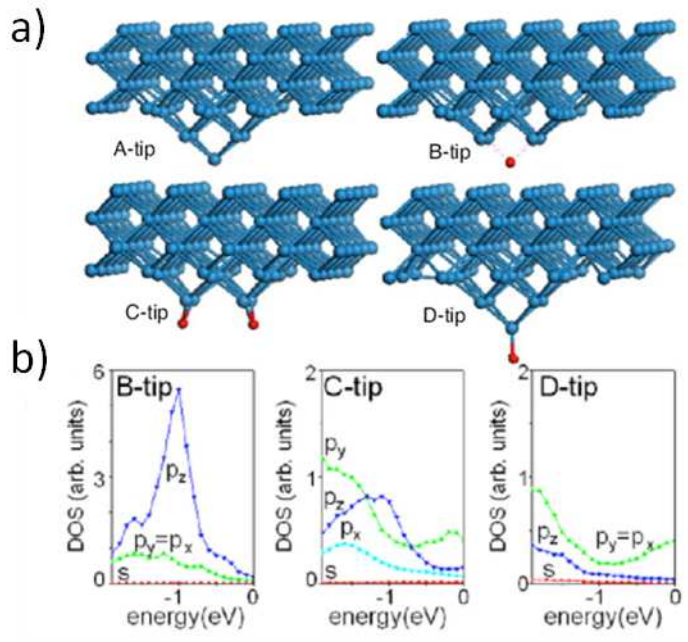

Figure 4.1.2.- *Geometrical structure and DOS of the main tips used for the simulations.* a) Most relevant optimized tips used for the STM simulations. They are labeled as: **A** tip, clean W tip made of a pyramidal 105-atom cluster terminated in a (100) plane; **B** tip, terminated in a single O atom substituting the W apex; **C** tip, double tip obtained by adsorption of a couple of O atoms on near-bridge positions; **D** tip, a single O atom adsorbed below the W apex. b) DOS for the O-apex atom in the B, C and D tips, decomposed into the orbital contributions. The Fermi level is at the origin of energies for each tip. Color code: W (blue) and O (red).

4.1.2. Interpretation of the STM images for the clean TiO_2 (110)-(1x1) surface

In figure 4.1.3 a) we show the schematic representation of the rutile TiO_2 (110)-(1x1) surface. As already mentioned in chapter 2, this figure is the result of the geometrical optimization of the surface, including a vacancy at the O_{br} position, using the theoretical procedure explained above. The other typical defect, the OH group, is just included in order to have a more complete visual description of the different defects. Although the model is the result of the

optimization of a three tri-layer slab, we just show two of them to simplify the image. Before using this model for the STM simulations, it is important to corroborate that the theoretical structure obtained from DFT calculations is similar to the one determined experimentally. In that sense, we have compared our theoretical structure with the one obtained by Lindsay et al. after the quantitative analysis of their LEED-IV and SXRD results [36-38]. For example, they find an inwards relaxation of the in-plane Ti_{5f} atoms of 0.44 Å with respect to the Ti_{6f} atoms while the value we obtain theoretically is 0.41 Å. We also achieve a good agreement in the O_{br}-Ti_{5f} distance (1.45 (theoretical) vs 1.5 Å (experimental)).

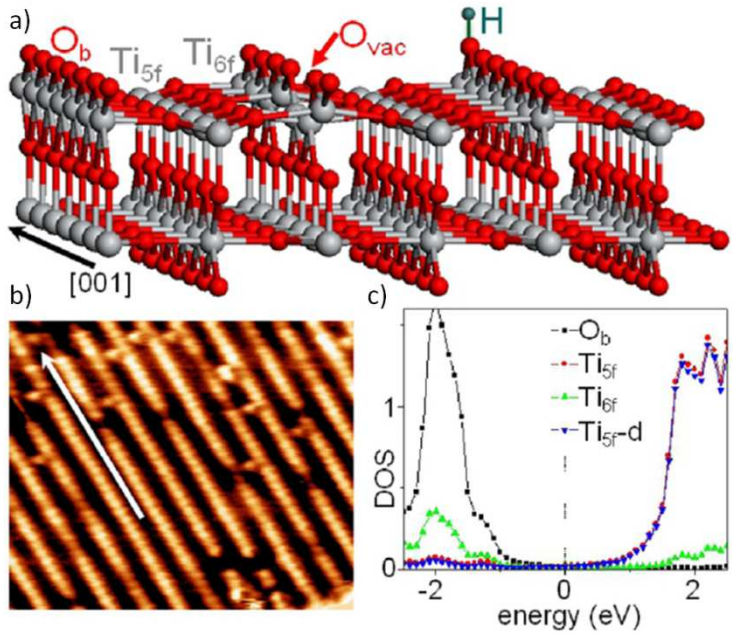

Figure 4.1.3.- *The clean rutile TiO_2 (110)-(1x1) surface.* a) Ball-and-stick representation of the DFT optimized structure of the TiO_2 (110)-(1x1) surface. Large gray and small red spheres represent the titanium and oxygen atoms, respectively. We have labeled the two-fold coordinated bridging O (O_{br}) and five-fold and six-fold coordinated Ti atoms (Ti_{5f} and Ti_{6f}, respectively). We also show oxygen vacancies (O_{vac}) and OH groups defects. The [001] crystallographic direction is indicated by a black arrow. b) Experimental atomic resolution STM image for this surface. The [001] direction is indicated by a white arrow. STM parameters: (80 Å x 67 Å), I = 0.17 nA, V = 1.5 V. c) Computed total DOS on O_{br}, Ti_{5f}, $Ti_{5f\text{-}3d}$ and Ti_{6f} showing their relative expected contribution to the STM image. For Ti atoms, exclusively d-orbitals are shown.

We can conclude that our calculated structure is valid due to the good agreement with the experimental one. Figure 4.1.3 b) shows an atomic-resolution STM image of the clean TiO_2 (110)-(1x1) surface recorded at a sample bias of 1.5 V. As this positive bias is applied to the sample, electrons are being injected into the conduction band (CB) of TiO_2 (tunneling current flowing from sample to tip). Under these conditions we are probing the CB that, as we said in chapter 3, it is mainly dominated by the in-plane Ti_{5f} atoms of the surface (figure 4.1.3 c)). For this reason we can attribute the observed bright rows running along the [001] direction to the Ti_{5f} rows, as it has been determined by different theoretical calculations for these tunneling conditions [72,73]. Complementary, the dark rows, also running along the [001] direction, correspond to the protruding O_{br} rows [37]. The periodicity along the [1-10] direction is approximately 6.5 Å, which is in good agreement with the expected value for the (1x1) surface. This is the accepted appearance for the STM image of the clean TiO_2 (110)-(1x1) surface and hereafter we will call it "*standard*" image. Apart from the bright rows, we can also see bright features in between the bright rows, and dark areas on the Ti rows. We can ascribe these features to surface defects. We will discuss them later, in the next section.

During STM measurements it is quite common that the tip experiences spontaneous changes. We present an example in figure 4.1.4 a). This image shows the clean (1x1) surface after being scanned from left to right and from bottom to top. We can distinguish up to five different regions which present different appearances at the STM. Each of these regions represents the way STM is "watching" the same surface with different tip terminations. If we focus in one of these tip changes, for example the area magnified in the zoom shown in figure 4.1.4 b), we can observe that the bright rows become wider and they shift by approximately half a unit cell along the [1-10] direction. This is not the first time these kinds of images are reported. Diebold *et al.* [39] and Guo *et al.* [122] already mentioned this effect and they explained it in base of a change in the tip state.

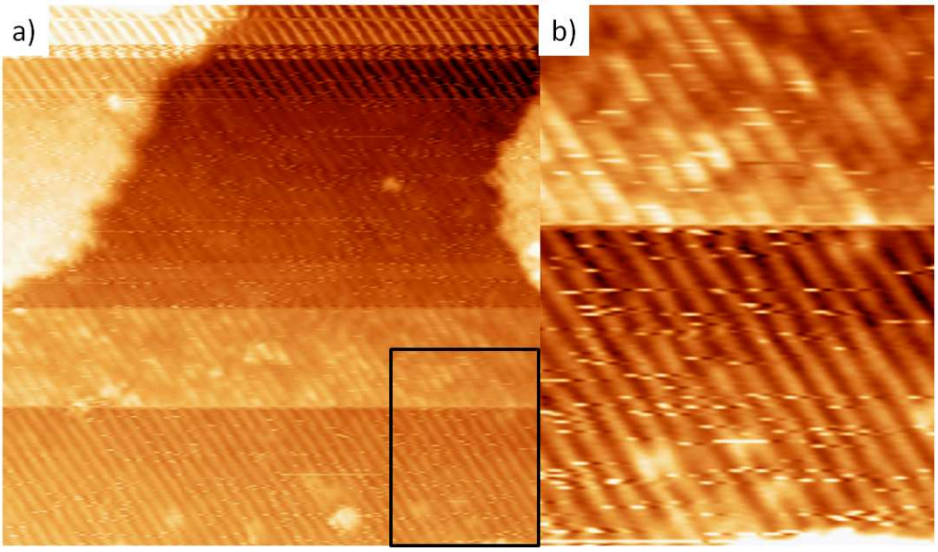

Figure 4.1.4.- *Tip changes during STM measurements*. a) STM image exhibiting multiple appearances of the clean TiO_2 (110)-(1x1) surface due to specific tip transitions. STM parameters: (300 Å x 300 Å), I = 0.35 nA, V = 1.5 V. b) Zoom area marked with a black rectangle in figure 4.1.4 a). On it we can observe a clear discontinuity at the center of the image due to a tip change. Size: (9.6 Å x 16.1 Å).

In order to have a reference for the comparison of the different effects and the influence of the tip states, it seems logical to start with the interpretation of the "standard" image. We have found experimentally two kinds of "standard" images, as shown in figure 4.1.5 a) and c). In both of these atomic-resolution images we distinguish the individual maxima which compose the bright rows. Each of these maxima corresponds to a Ti_{5f} atom and they are aligned along the [001] direction. The main differences between them are the resolution and corrugation along the bright rows (apart from the way defects are resolved, as we will see in the next section). Figure 4.1.5 c) presents higher resolution and corrugation although a careful consideration shows that similar information is present in figure 4.1.5 a), but with a larger noise to signal ratio. We can better appreciate this effect if we look at the corrugations along the rows ([001] surface direction), shown in figure 4.1.5 e) and f). In these panels we can see the experimental and theoretically calculated corrugations for both images. We have obtained the theoretical corrugations by tracing scan lines along the

bright rows of the simulated STM images shown in figure 4.1.5 b) and d). These calculated images are the result of the simulation of the clean surface using a clean W tip (**A** tip) and a W tip with an O atom replacing the W apex (**B** tip), respectively. If we compare the theoretical and experimental corrugations we observe that in both cases theory underestimates the experimental values but it is able to explain the features observed. We can affirm that the differences are due to a different tip termination. We have used the same bias (1.5 V) for the theoretical STM images and the experimental ones and the simpler CHM (we have used a sample-tip distance of 3 Å from the apex to the O_{br} atoms and 4.5 Å with respect to the Ti_{5f} atoms). Anyway, we have checked that the results obtained in the CCM are qualitatively and quantitatively indistinguishable. Therefore, we can conclude that the simplest models (**A** tip and **B** tip) can explain the experimental "standard" image. The only difference is the presence of an O atom at the apex of **B** tip which produces an enhancement of the resolution. The adsorption of an O atom at the tip is not an unlike process if we take into account that we are measuring on an oxygen-rich surface like TiO_2 [115]. The fact that both tips are able to reproduce the "standard" image is quite surprising as there are several examples of STM contrast inversion upon the adsorption of an O atom by the tip [118,119]. The reason why we do not observe this contrast inversion has to be sought in the DOS of the tip. If we look at the DOS represented in figure 4.1.2 b) (**B** tip) we can see that when we have an O atom replacing the W apex of the tip, the resulting DOS presents a p_z character as the contribution from this orbital is very strong below the Fermi level. This gives a maximum in the tunneling intensity on top of the Ti_{5f} atoms as it happens for the W tip. The major differences between **A** and **B** tips are: i) the intensity of the tunneling current is lower for the **B** tip (we cannot observe this effect experimentally as we are measuring in CCM), and ii) we obtain a better resolution with the **B** tip for the same sample-tip distance.

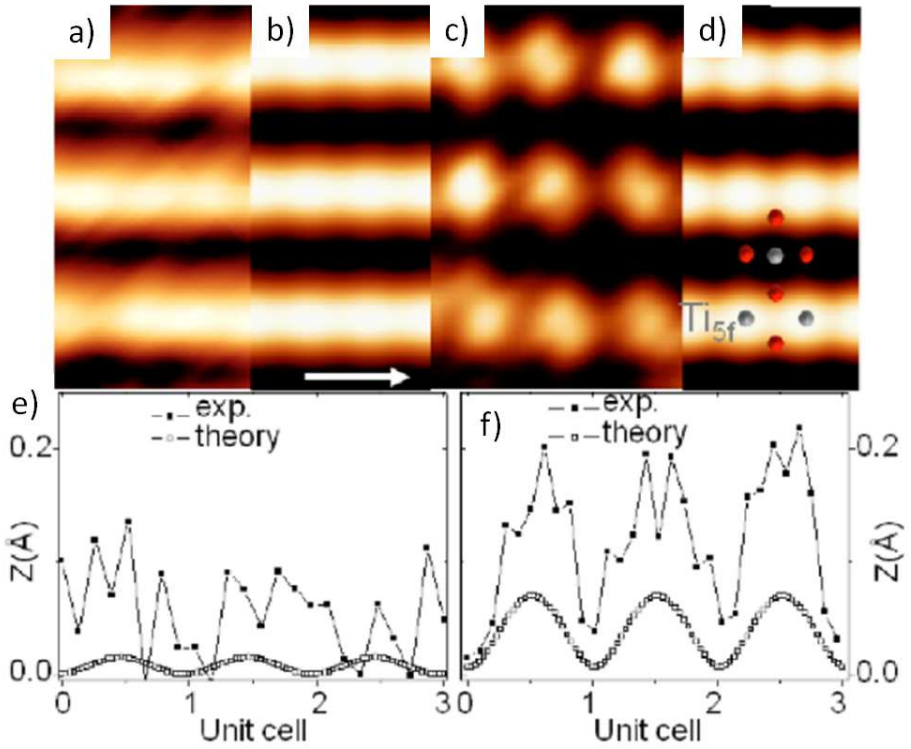

Figure 4.1.5.- *Experimental and theoretical STM images and profiles for the "standard" image.* a) and c) Experimental atomic-resolution STM images on the TiO_2 (110)-(1x1) surface. Each bright feature corresponds to a Ti_{5f} atom. STM parameters: (9 Å x 20 Å), a) I = 0.17 nA, V = 1.5 V; c) I = 0.22 nA, V = 1.5 V. b) and d) Calculated STM images obtained for **A** and **B** tips, respectively. The white arrow indicates the [001] direction. e) and f) Scan profiles along the [001] direction comparing experimental and theoretical corrugations. The tip-sample distance in the calculations is *Z* = 3 Å, with respect to the O_{br} rows.

However, these are not the unique kind of images found when scanning the surface. It is common to find bizarre atomic features during a STM session. One of the most usual (both, found by ourselves and reported in literature) corresponds to wide elliptical features located on the bright rows and elongated along the [1-10] direction [39,58,121,122]. Depending on the resolution, in some occasions we can even distinguish a double maximum inside the row. This effect is frequent during STM measurements but a complete study of this phenomenon is still missing. As an example we can

return to the upper part of figure 4.1.4 b). As we commented, after the tip change, bright rows become wider and they shift approximately half a unit cell along the [1-10] direction. Another example of this type of images, that we have called "elliptically shaped" images, is given in figure 4.1.6 a). There are several explanations for this effect in literature. In ref. [39] they assign it to a wide double tip and a lateral shift of the outermost atom at the tip apex. In another work [122] it is proposed that it is due to the tunneling into the Ti_{6f} atoms when scanning with a Si coated tip, or even into the in-plane oxygen atoms [112]. It is curious that this kind of effect is also visible when using AFM [112,116].

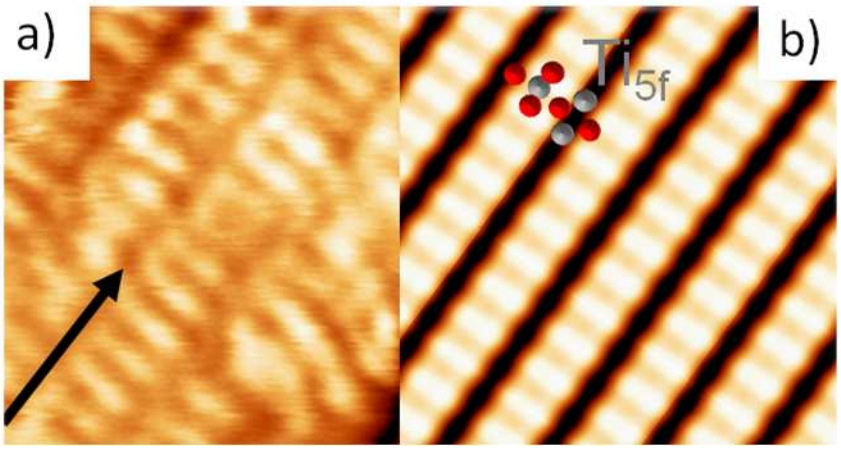

Figure 4.1.6.- *Experimental and theoretical STM images for the "elliptically shaped" image*. a) Experimental atomic-resolved STM image of the TiO_2 (110)-(1x1) surface. The black arrow indicates the [001] direction. b) Theoretical simulation of the clean (1x1) surface computed using the **C** tip. Experimental STM parameters: (27 Å x 35 Å), I = 0.3 nA, V = 1.3 V.

Among all the tips tested for the theoretical calculations, we obtained the best image reproducibility for the case of a W tip where the apex has been substituted by two O atoms (**C** tip). We show the result of the calculation in figure 4.1.6 b). This simulation is able to reproduce the most important and characteristic features of the "elliptically shaped" images: the shape and the shift. On the one hand, we have that the bright rows are imaged wider than in

the case of the "standard" images and are formed by elliptical maxima elongated along the [1-10] direction. On the other hand we observe a displacement of half a unit cell of the bright rows. The bright rows are on top of the O_{br} rows and not on the Ti_{5f} rows, as we can see in the schematic representation of the atomic positions. It is important to note that this shift is not due to the fact that electrons are tunneling into the O_{br} atoms as one could expect because of the position of the rows. As the tunneling conditions are kept constant (positive sample voltage) and we have not done any modification of the surface, the substrate DOS has not varied so we are still probing the CB of TiO_2, which is still dominated by the Ti_{5f} atoms. So if we are injecting electrons into the Ti_{5f} atoms, what we are seeing are those Ti_{5f} atoms. The real reason for this shift is the position of the O atoms at the tip apex. When the W apex is substituted by two oxygen atoms, a charge transfer from the W atoms to the O atoms occurs. This charge transfer will produce an electrostatic repulsion between both O atoms which will modify their equilibrium position. In this new configuration, these two O atoms are sideways-displaced 2 Å from the pure top W site (see figure 4.1.2 a)). Furthermore, the tunneling process is dominated by the p_z orbital of the O atoms in the tip, as the hopping matrices between p_x and p_y orbitals and the surface are much smaller than for the p_z one. In this way, when one of the O atoms is located on top of a Ti_{5f} atom, we have a maximum in the tunneling current, but this maximum will be shifted together with the relative position of the O atom in the tip. In the end, the STM image will be the combination of the two images seen by the two O atoms in the tip, displaced one from each other by approximately half a unit cell.

We present in figure 4.1.7 the experimental and theoretical profiles along the [1-10] direction for the "standard" and the "elliptically shaped" images. As we can see, the modulation of the profiles is different as we could expect: we just observe a single maximum on top of the rows for the "standard" image while for the "elliptically shaped" image we can distinguish two maxima per row. The qualitative agreement between theory and experiment is good as both present the same profile. On the other hand, experimental corrugations are larger than the ones obtained theoretically (0.6 Å vs 0.45 Å for the "standard" image and 0.35 Å vs 0.21 Å for the "elliptically shaped" image, respectively). This type of disagreement is not unusual when comparing theory and experiment for STM

but we stress that the trend is the same: larger corrugations for the “standard” images than for the “elliptically shaped” ones.

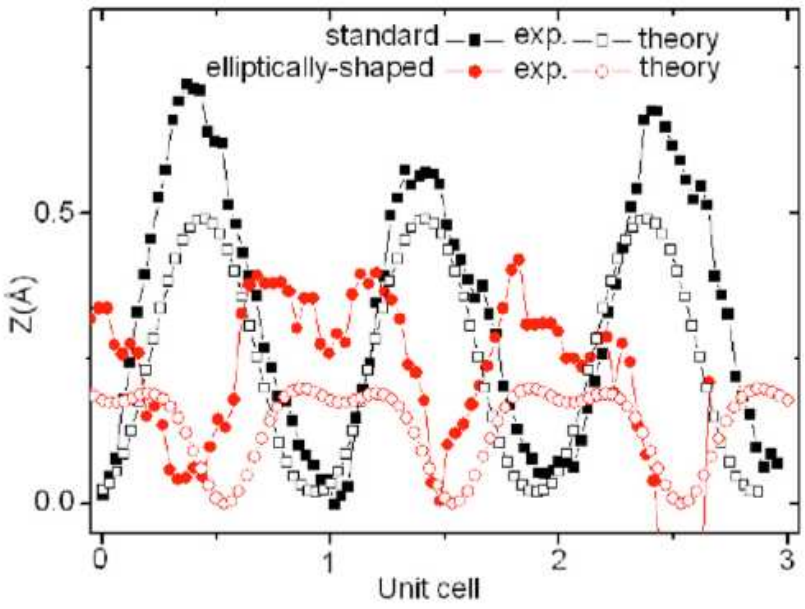

Figure 4.1.7.- *Experimental and theoretical corrugations along the [1-10] direction for the “standard” and “elliptically shaped” images.* As we can see, the “elliptically shaped” image presents a double maximum on the Ti rows while the “standard” image presents a single maximum. In both cases the theory underestimates the corrugation values.

The way these theoretical corrugations are obtained can be understood taking into account figure 4.1.8. In it we show two theoretical *I(z)* curves which correspond to the bright (red) and dark (black) rows of both STM images. The corrugation is obtained as the difference in the distance (*Z*) between tip and sample for the given experimental parameters (voltage and current). In other words, the corrugation is calculated by measuring the *Z* difference between both curves for a certain tunneling current.

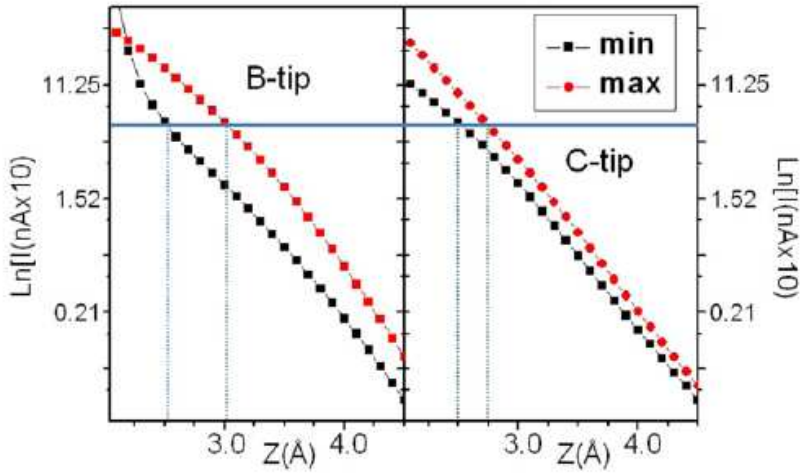

Figure 4.1.8.- *Theoretical tunneling current versus tip-sample distance (Å) for the **B** and **C** tips.* The corrugations are obtained as the difference between the red (bright rows) and black (dark rows) curves. The *Z* distance is referenced to the O_{br} rows.

As we mentioned before, the position of the adsorbed atom at the tip can completely change the appearance of the STM images as the tip DOS would be modified. We show an example in figure 4.1.9, where we present the theoretical STM simulations for a clean surface scanned with a tip where one O atom has been adsorbed below the W apex (**D** tip). The different position of this O atom at the tip modifies its DOS as it is shown in figure 4.1.2 b). Instead of having a p_z character as in the **B** tip, its major contributions come from the p_x and p_y orbitals. In this way, the region just below the O atom will have no DOS because it is moved out of the center and spread around it, giving rise to a ring-shaped DOS [118,119]. As a consequence when the tip is above the Ti_{5f} atoms the tunneling current maxima will appear surrounding them as it can be seen in figure 4.1.9. The resulting STM image will be very similar to the "elliptically shaped" one as it will be formed by elongated features along the [1-10] direction but, instead of having a half unit cell displacement of the rows along their perpendicular direction, this shift will appear along the rows direction. So if we want to distinguish between both tips (**B** and **D**) we have to check if there is a displacement of the rows of half a unit cell along the [1-10] direction.

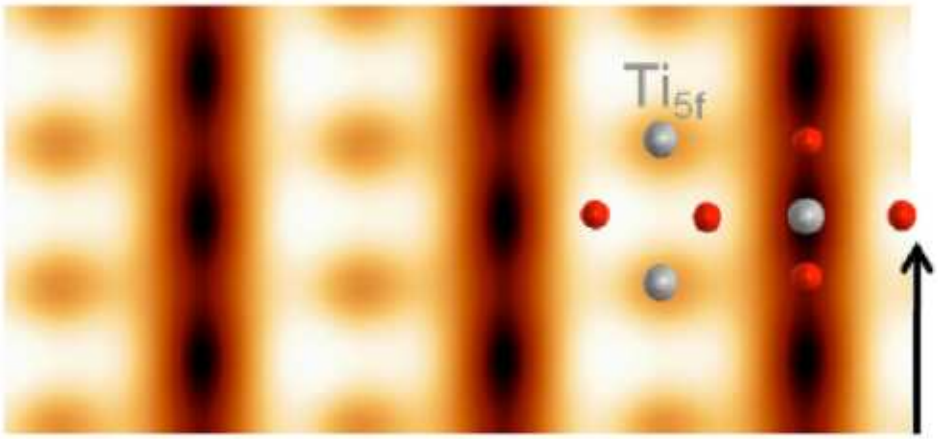

Figure 4.1.9.- *Theoretical STM simulation obtained with a D tip*. As we can see also in this case elliptical features are observed but no displacement of the rows along the [1-10] direction is observed. Instead, the shift is along the [001] direction (black arrow).

It is important to consider the effect of the relative orientation of the **C** tip with respect to the surface rows. In order to get the theoretical reproduction of the "elliptically shaped" image, it is necessary to have the virtual line crossing the oxygen atoms in the tip oriented perpendicularly to the rows while scanning the surface. The angle formed by the rows direction and the oxygen line at the tip will determine the elongation direction of the features inside the rows. If this orientation is different from 90°, the elongation will also change the angle. We have observed this effect when the angle is something in between. Figure 4.1.10 shows an experimental STM image for the clean surface. As we can see, we have broad bright rows running along the [001] direction and formed by elliptical features elongated along a different surface direction which forms approximately 30° with respect to the [1-10] direction. This image can be explained according to what we have commented above. If the angle between the O atoms in the tip and the Ti_{5f} rows is 30°, the features of the rows will appear rotated by this angle, as it is the experimental case. For example, if the O atoms are oriented parallel to the Ti_{5f} rows, we will not observe this elongation of the chains along the [1-10] direction, but it would be along the

[001] direction. We have never observed this effect experimentally, but this is not surprising as in order to be able to distinguish it we would need atomic resolution along the rows and the result would be a separation between maxima of approximately 1 Å. Anyway, the most observed case is the one in which the O atoms in the tip are almost perpendicularly oriented with respect to the surface rows.

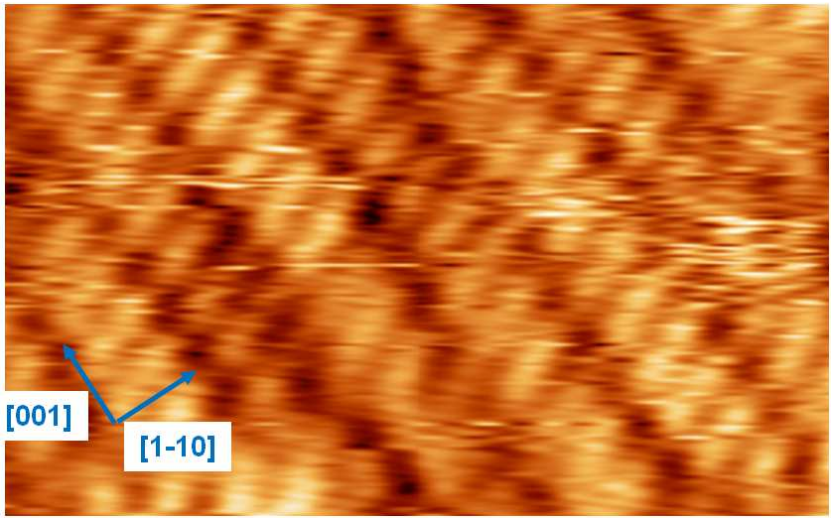

Figure 4.1.10.- *Experimental atomic-resolved STM image for a special case of "elliptically shaped" image for a different tip-rows angle*. In this case the relative angle between the O atoms in the tip and the Ti rows is different to 90°. For this reason the bright features are elongated along a different direction. STM parameters: (48 Å x 30 Å), I = 0.15 nA, V = 1.2 V.

We have also observed two other experimental effects whose interpretation is still not clear. In the first case, a recurrent STM image observed during measurements is the one we show in figure 4.1.11. As we can see the composition of the bright rows is very similar to the one in the "elliptically shaped" image as they are formed by elongated features along the [1-10] direction. The curious effect in these images is the modulation along the rows corrugation. We can distinguish two different modulation effects. One is relative to the intensity along the rows where we find a series of maxima and minima with no apparent order. The other effect is a modulation in the width

of the Ti rows. As we can see in figure 4.1.11, there is a relationship between both effects as the wider regions correspond to the brighter ones, and vice versa.

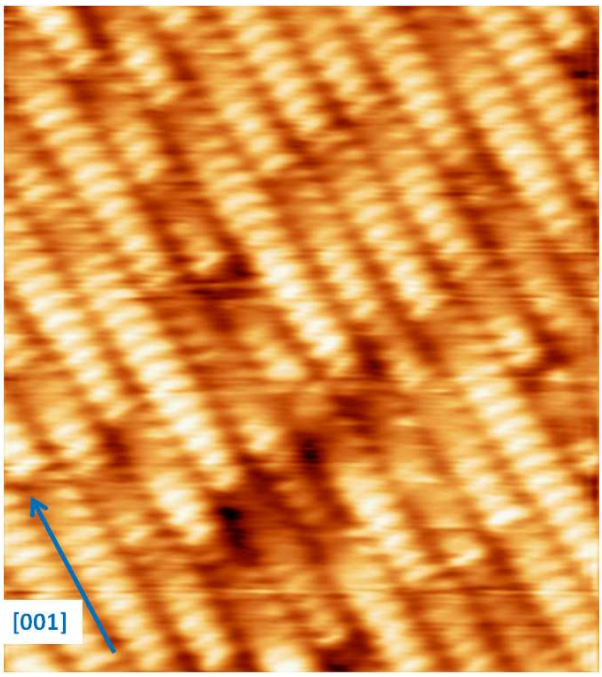

Figure 4.1.11.- *Experimental STM image of the "elliptically shaped" image*. In this image we can see the width and intensity modulation of the Ti rows. STM parameters: (75 Å x 84 Å), I = 0.2 nA, V = 1.5 V.

We have not been able to reproduce this effect with any of the tips so it seems it is not a tip-induced electronic effect. A possible explanation is that the tip apex is not stable and the atom at the apex is moving probably due to the interaction with the surface. This movement of the apex could account for both the variation in the rows width and in the rows intensity. However, since we have no further evidences, the interpretation of this effect remains unclear.

The second case of experimental STM images without a clear interpretation and repeatedly observed during our STM sessions is the one we show in figure 4.1.12 a) and in the upper part of figure 4.1.4 a). This image characterizes by rows running along the [001] direction with a periodicity of ~ 6.5 Å along the [1-10] direction, as in the case of the "standard" image. We do not observe any displacement of the rows along the [1-10] direction after this tip change, but we cannot say anything about the [001] direction due to the lack of resolution within the rows. The main differences with respect to the other kinds of images are the width and corrugation of the bright rows.

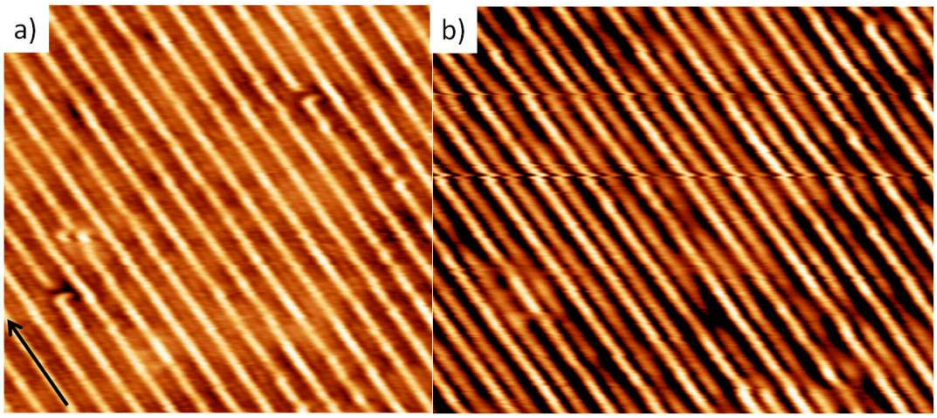

Figure 4.1.12.- *Experimental STM images for the "giant corrugation" case*. a) STM image of the "giant corrugation" image when scanning big areas (110 Å x 104 Å). The [001] direction is indicated by a black arrow. b) When we decrease the size of the image, a new stand appears within the Ti rows (86 Å x 70 Å). STM parameters for both images: I = 0.35 nA, V = 1.5 V.

They are slightly thinner than the other images, and, above all, the corrugation along the [1-10] direction is very large. This corrugation is about two times larger than the one observed for the "standard" image and even higher if we compare it with the "elliptically shaped" image, as we can see in figure 4.1.13. For this reason we have called them "*giant corrugation*" images. Large corrugations on STM images have been observed previously in the literature for metallic and non-metallic systems. They have been explained in terms of electronic effects as being the result of scanning with a tip with highly localized

metallic d_{z2} dangling bonds [129], or as an effect of elastic deformation of the substrate under strong interaction with the scanning tip [130-132]. None of the seventeen different tips that we have used for the simulations has been able to reproduce it so we discard a tip effect as the origin of this corrugation. In this sense we can find two possible explanations in terms of an elastic deformation of the tip apex or due to sample-tip interactions, which could induce a deformation of the surface. This is possible if we take into account that in order to achieve atomic resolution we need to reduce the substrate-tip distance (increasing the tunneling current) so interaction effects between oxygen atoms and the tip are no longer negligible.

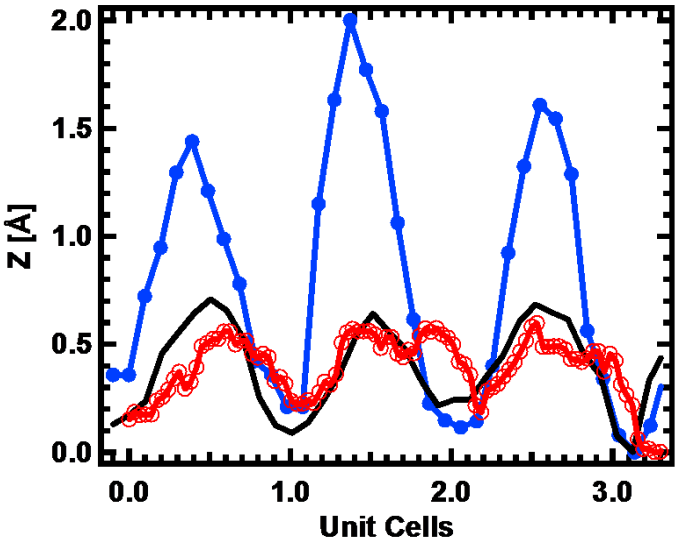

Figure 4.1.13.- *Experimental profiles along the [1-10] direction for the three different images*. As we can see, the corrugation of the "giant corrugation" image is double of the "standard" image. Color code: "standard" image (black line), "elliptically shaped" image (red open circles), and "giant corrugation" image (blue circles).

An additional curious effect of these "giant corrugation" images is the observation of a change in the appearance of the rows when we decrease the size of the STM image keeping the measurement parameters. We pass from

thin bright rows to wide double rows, being one less intense than the other one, as it can be seen in figure 4.1.12 b). The explanation of this effect is uncertain as the only change in the STM parameters is the size of the image and we do not observe any tip change. This means that, what initially seemed a narrow bright row was in reality a double bright row with one side more intense than the other.

4.1.3. Imaging point defects on the clean rutile TiO_2 (110)-(1x1) surface

Once we have seen the influence of the tip state in the appearance of the Ti_{5f} rows while scanning on the clean TiO_2 surface, we can go one step further and try to understand how point defects such as O_{vac}´s and OH groups are imaged. Furthermore, as we will see later, point defects will help us to better identify the state of the tip in the case of the "standard" image.

As we have seen in figure 4.1.3 b) the "standard" STM image presents different kinds of imperfections at the atomic scale: bright features in between Ti_{5f} rows and black depressions on Ti_{5f} rows. As the origin of these depressions is still uncertain [14,133,134] we will focus on the study of the bright features. We have performed STM theoretical calculations including different types of possible defects at the Ti_{5f} and O_{br} rows. We have used the tips already considered in the previous section.

To theoretically consider the presence of an O_{vac} we have relaxed the surface after creating a vacancy in an O_{br} site, as shown in figure 4.1.3 a), in a 7 x 3 periodicity. This vacancy influences the surrounding atoms inducing a small deformation in the height of the remaining O atoms in the row. Also the neighboring Ti atoms move downwards by a non-negligible value of ~ 0.25 Å. This deformation of the Ti atoms does not significantly affect the neighboring O atoms. Figures 4.1.14 a) and d) show the theoretical calculations of the O_{vac} when scanned with the **A** and **B** tips, respectively. As we can see they are simulated as bright regions located between the bright rows with a dark region of similar shape and size between the maxima. Only the fine details would allow us to distinguish the termination of the tip used to scan the surface.

We also have to consider the formation of a hydroxyl group on the O_{br} rows at the surface. This situation induces new deformations of the surface as the O_{br} bonded to an H atom shifts upwards by 0.15 Å while the other O atoms remain practically unaltered. We show the simulations of these OH groups using **A** and **B** tips in figures 4.1.14 b) and e), respectively. In this case the OH groups are imaged differently for both tips: for the **B** tip, they appear as a round bright protrusion between the surface rows (figure 4.1.14 e)), while for the **A** tip the brightest region is located directly on the rows (figure 4.1.14 b)). At this stage, we can consider the experimental images (figure 4.1.14 c) and f)), paying special attention to the regions where defects show up. Taking into account the theoretical calculations for the OH defects at the surface, we can ascribe the experimental image shown in figure 4.1.14 c) to the case of scanning with an **A** tip (clean W tip), while figure 4.1.14 f) is better matched with the image obtained with a **B** tip (O atom replacing the W apex).

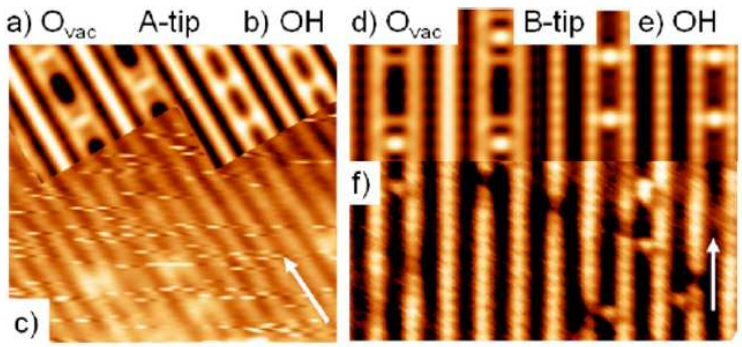

Figure 4.1.14.- *Experimental and theoretical atomic-resolved STM images for the defective TiO_2 (110)-(1x1) surface*. a) Theoretical STM image calculated with the **A** tip considering the presence of O_{vac}´s. b) Similar but with OH groups instead of O_{vac}´s. c) Experimental "standard" image for comparison (zoom from figure 4.1.4 b), lower part). d) Theoretical STM image calculated with the **B** tip considering the presence of O_{vac}´s. e) Similar but with OH groups instead of O_{vac}´s. f) Experimental "standard" image for comparison (zoom of figure 4.1.3 b)).

From a visual inspection of figure 4.1.14 it is clear that it is not straightforward to distinguish between O_{vac}´s and OH groups because of the experimental resolution. On the other hand, when we imaged defects as bright round

protrusions between Ti rows we can ascribe them to defects being imaged with a **B** tip (figure 4.1.14 f)). Again, the similarity in the STM simulation of both types of defects does not allow us to distinguish them. These results are in good agreement with similar kinds of STM images which have been reported previously for TiO_2, with the presence of both types of surface defects, oxygen vacancies [108] and hydroxyl groups [109].

Finally, we have studied the way defects are imaged with a **C** tip. The theoretical simulations that we obtain for both types of defects are very similar between them. They characterize by presenting a more intense elliptically shaped feature on top of the Ti rows (figure 4.1.15 c) and d) for O_{vac} and OH group, respectively). So, attending to our theoretical simulations we would not be able to distinguish between both types of defects when scanning with a **C** tip (W apex substituted by two O atoms). The theoretical results are in good agreement with the experimental images as we can observe bright elliptically-shaped features on top of the Ti rows (black circle in figure 4.1.15 a)). Although we cannot distinguish the type of defect that we are imaging at least we can ensure that they correspond to a point defect.

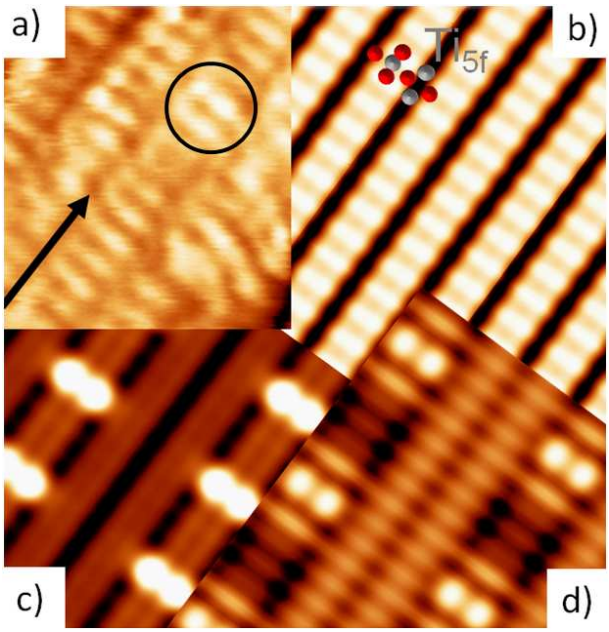

Figure 4.1.15.- *Experimental and theoretical STM images for the "elliptically shaped" image*. a) Experimental atomic-resolved STM image of the TiO_2 (110)-(1x1) surface. The black arrow indicates the [001] direction. The following theoretical images have been computed using the **C** tip: b) clean (1x1) surface, c) surface with O vacancies, and d) surface with OH groups. Experimental STM parameters: (27 Å x 35 Å), I = 0.3 nA, V = 1.3 V.

4.1.4. Conclusions

In this section we have carried out an exhaustive experimental and theoretical study of the nature of the atomic features observed in different STM images of the clean TiO_2 (110)-(1x1) surface. In order to be able to properly explain the experimental images that we have obtained we have considered different theoretical tip settings corresponding to the adsorption of different species on the tip apex.

We have been able to correctly simulate and understand the "standard" STM image as the one obtained when scanning the surface both with a clean W tip (**A** tip) and a W tip where the apex has been replaced by an O atom (**B** tip).

We also report the presence of two different kinds of STM images for the clean TiO_2 (110)-(1x1) surface. On the one hand we deal with the "elliptically shaped" image which characterizes by wide Ti rows composed of elongated features along the [1-10] direction and that it had been already reported on the literature. This image is the result of scanning the surface with a W tip where the apex has been substituted by two O atoms (**C** tip). The orientation of the O atoms line with respect to the Ti rows is crucial in the visualization of the STM images. In order to have an "elliptically shaped" image, the O atoms line must be perpendicular to the Ti rows. If the angle between both is different to 90°, we will obtain an elongation of the rows with a different angle. This type of image is always accompanied by a half unit cell displacement of the Ti rows, along the [1-10] direction. We have been able to simulate both effects: shape and shift of the rows. We have also observed extra effects in the form of width and intensity modulation. We do not have a clear explanation for his effect but we believe it can be due to movements in the tip apex.

Additionally, we report the existence of a new experimental STM image that we have called “giant corrugation” image. This kind of image characterizes by narrow bright Ti rows running along the [001] direction, which present an extremely high corrugation (double than in the “standard” image) along the [1-10] direction. We have not been able to find an explanation for this corrugation in terms of an electronic effect due to the tip termination. For this reason we think it can be due to an elastic deformation of the surface because of an interaction between tip and surface.

Finally, we have studied the way these tips image the typical surface defects, O_{vac}´s and OH groups. We have been able to correctly simulate defects for “standard” and “elliptically shaped” STM images. This has allowed us to discern between the two possible tips capable to reproduce the “standard” STM image.

4.2. Interaction of organic molecules with the (1x1) surface

Organic molecules are attracting a lot of expectation due to their outstanding properties and potential applications. From a fundamental point of view, it is interesting to study their behavior when interacting with all kind of materials, whether metallic, semiconducting or insulating. However, from a technological point of view, one of the most interesting aspects is to understand their interaction with wide gap semiconductors such as oxide surfaces because they present a low support-layer interaction.

Among all metal oxides, titanium dioxide is considered a prototypical one for surface science experiments as it can be easily prepared in-situ and it presents a good surface quality. Many different organic molecules have been deposited on the TiO_2 (110)-(1x1) surface, being a common behavior their low interaction with this substrate, as we will show during this work.

In this kind of systems, it is extremely interesting to study the morphology and electronic structure of the deposited organic layers. Additionally, when working with adsorbates on surfaces, and moreover with organic molecules, it is important to determine the thermal stability of the formed structures.

In this chapter we study the interaction of different organic molecules (C_{60}, pentacene, $C_{60}H_{30}$ and H_2PPIX) with the clean rutile TiO_2 (110)-(1x1) surface in order to advance in the comprehension of the properties of molecular – oxides systems.

4.2.1. C_{60}

Since its discovery in 1985 by Kroto et al. [135]*, C_{60} has been extensively studied as it has been shown that it presents many interesting properties in different fields* [136,137]*. One of the most promising applications of C_{60} is probably molecular electronics. C_{60} molecules have been successfully tested in the fabrication of field effect transistors* [138] *or solar cells* [139]*, whether by themselves or in combination with other organic molecules. They have also been used as lubricants thanks to their spherical shape and hardness* [140]*. They present medicinal applications as antioxidants as they present a very high reaction rate with free radicals* [141]*. Besides, they are being tested in many other applications as catalysis, superconductivity, water purification and bio-hazard protection, non-linear optics, etc* [142,143]*. In summary, C_{60} is a very interesting organic molecule with many potential applications in nanoscience and nanotechnology.*

As a consequence of the huge number of possible applications, it has been extensively studied by surface science. With this aim it has been deposited on metals, semiconductors and insulating materials [144,145]*. When deposited on metals, C_{60} molecules form well ordered close-packed structures where molecules are usually fixed on the surface with distances close to the van der Waals diameter* [146-149]*. This means a small interaction with the substrate which, however, is able to stabilize a particular adsorption geometry for the molecules. In the cases where this interaction is larger a modification of the molecular orbitals takes place, together with the alteration of the intrinsic C_{60} properties.*

In this section we study the interaction of C_{60} molecules with the TiO_2 (110)-(1x1) surface in order to elucidate the structural and electronic properties of the system. By means of STM, LEED, NEXAFS, XPD and DFT calculations we provide a full picture of the system.

4.2.1.1. Study of the C_{60} / TiO_2 (110)-(1x1) morphology

Figure 4.2.1.1 shows a schematic ball-and-stick representation of a C_{60} molecule. As we can see, it is formed by 60 carbon atoms arranged in a spherical shape formed by 20 hexagons and 12 pentagons. It presents a total of 90 C – C sp^2 bonds, 30 C = C bonds connecting carbon atoms in two hexagons, with a bond length of 1.36 Å, and 60 C – C bonds linking C atoms in one hexagon and one pentagon, with a bond length of 1.47 Å. C_{60} molecules usually present a van der Waals interaction between them with a van der Waals diameter of approximately 11 Å [150].

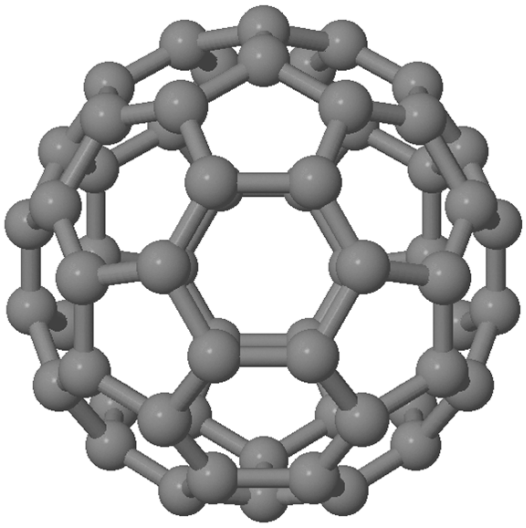

Figure 4.2.1.1.- *Ball-and-stick schematic representation of a C_{60} molecule*. Each grey ball corresponds to a carbon atom. It is composed by 60 C atoms arranged in 20 hexagons and 12 pentagons.

If we deposit less than 1 ML of C_{60} molecules on the clean TiO_2 (110)-(1x1) surface at RT, we observe the formation of single molecular islands which extend covering the surface (figure 4.2.1.2 a)). These islands start growing

from the step edges into the lower terraces of the surface as we can inferred from the material accumulation at the steps of figure 4.2.1.2 a). Both aspects are clear indications of molecular diffusion on the surface. To evidence this point, we trace a scan profile both on the TiO_2 surface and the C_{60} islands (green line). The result is shown in figure 4.2.1.2 b).

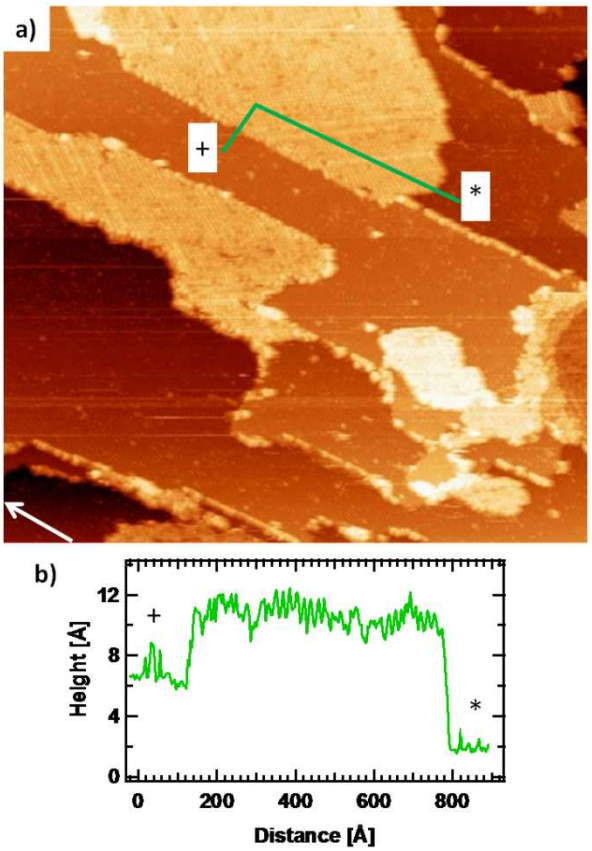

Figure 4.2.1.2.- *Evaporation of ~ 0.5 ML of C_{60} on the clean TiO_2 (110)-(1x1) surface at RT.* a) STM image of the surface after the evaporation. We observe the formation of C_{60} islands which start growing from the step edges into the lower terraces. The white arrow indicates the [001] surface direction. Size: (1500 Å x 1380 Å), I = 0.10 nA, V = 1.8 V. b) Scan profile on the substrate and C_{60} island. The apparent height of the molecular islands is approximately 8 Å.

If we move from * to +, we notice a first step-up of approximately 8 Å when passing from the TiO_2 terrace to the C_{60} island. Then we observe step-down of something more than 4 Å. These values are consistent with an apparent height of approximately 8 Å for the C_{60} islands which are growing on top of the lower terraces. The second step is the result of subtracting the TiO_2 step height (~ 3.2 Å) to the C_{60} apparent height.

For very low coverages, lower than approximately 0.2 ML, we are not able to observe C_{60} islands. Instead, we observe the accumulation of material in the step edges, which act as nucleation sites. The reason for this absence of molecular islands at low coverages is that they are stabilized by the van der Waals interaction between molecules as the interaction with the substrate is very low. We will discuss this issue later in this section.

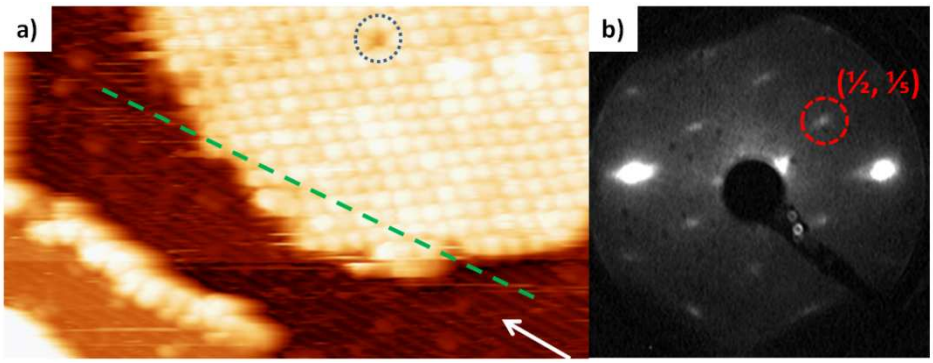

Figure 4.2.1.3.- *Periodicity and relative position of the molecular islands with the substrate*. a) High-resolution STM images where we can distinguish the substrate Ti_{5f} rows running along the [001] direction (white arrow) and the round bright features associated to C_{60} molecules. Molecular islands present a high degree of order although it is possible to find some defects as C_{60} vacancies (blue dotted circle). Green dashed line indicates the position of the Ti_{5f} substrate rows. As we can see, C_{60} molecules are sitting on top of the Ti_{5f} rows. Coverage: ~ 0.5 ML. Size: (300 Å x 180 Å), I = 0.07 nA, V = 1.8 V. b) LEED pattern associated to this surface. The two big bright spots correspond to the substrate (1,0) and (-1,0) beams while the bright small spots correspond to the super-periodicity associated to the molecules. We have marked in red one of the superstructure points. This new periodicity is compatible with a *p (5 x 2)* structure. E = 16 eV.

In order to extract more information about the nature of the C_{60} islands we zoom into one of these islands. The result is shown in the high-resolution STM image of figure 4.2.1.3 a). In this image we can distinguish bright round features forming islands. Each of these features corresponds to a C_{60} molecule. They form well-ordered close-packed bidimensional islands although it is possible to observe individual defects as the "hole" marked by a blue dotted circle in figure 4.2.1.3 a), corresponding to a missing C_{60} molecule.

The green dashed line indicates the position of the bright substrate rows which correspond to the Ti_{5f} rows, as discussed in the previous section. If we follow the line above the C_{60} island we observe that it passes on top the bright features associated to C_{60} molecules. This means that molecules are adsorbed on top of the Ti_{5f} rows of the surface. The borders of the island are not well defined and we can see some streaks. This is a clear evidence of diffusion of the C_{60} molecules at the borders of the island. It is very complicated to establish the periodicity of these C_{60} islands by STM as for this aim we would need simultaneous atomic resolution both inside the substrate rows and of the molecules. However, it is possible to get this information by LEED. Figure 4.2.1.3 b) shows the LEED pattern associated to this surface. As we can see, apart from the substrate spots (big bright spots), new extra spots appear after the deposition of C_{60} (small spots). These spots present a small elongation due to focalization problems associated to the very low energy of the electron beam (E = 16 eV). These new spots present a *p (5 x 2)* periodicity, compatible with the results obtained by STM if we consider a unit cell with two molecules, one divided into the four corners and one at the center. We present a schematic model in figure 4.2.1.4, where the big blue circles represent the C_{60} molecules and the black rectangle marks the superstructure unit cell. This model, as well as all the STM results already shown, is in good agreement with the AFM results obtained by Loske et al. [151]. The only difference is that in their work they propose, by visual inspection of the AFM images, a *c (5 x 2)* periodicity, although the model is essentially the same. We can easily solve this discrepancy if we notice that, in both models, C_{60} molecules are not at equivalent positions within the unit cell. In fact, in order to keep the van der Waals diameter, the central molecule in figure 4.2.1.4 has to be in a different adsorption site with respect to the surrounding molecules.

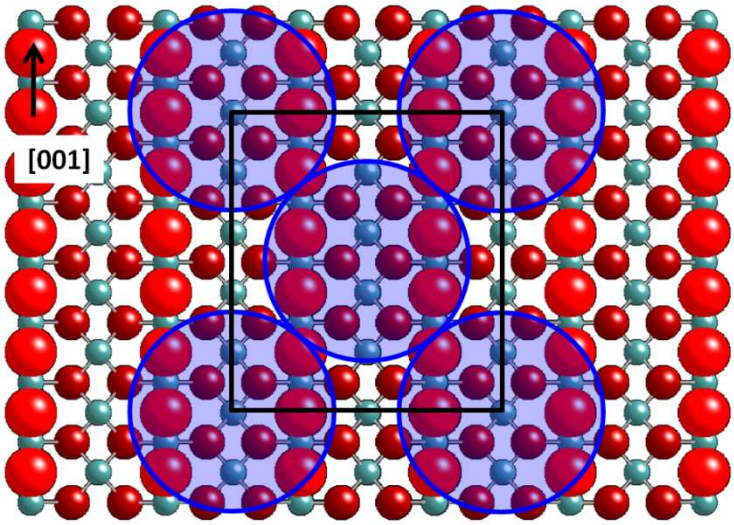

Figure 4.2.1.4.- *Schematic ball-and-stick representation of the model proposed for the molecular layer*. Red and light blue balls correspond to oxygen and titanium substrate atoms, where larger balls mean closer to the surface. Large blue circles correspond to C_{60} molecules represented by their van der Waals diameter. For the sake of clarity we have just represented the five molecules necessary to define the superstructure unit cell. As we can observe, it is composed by two C_{60} molecules, one divided into the four corners and one at the center. It is worthy to note that the position of the molecules at the corners (top Ti_{5f} position) is different to the position of the molecule at the center (bridge position).

Molecules at the corners are sitting on top of Ti_{5f} atoms while the molecule at the center falls in between two Ti_{5f} atoms. As we will show later, these different adsorption sites induce a different orientation of the molecule with respect to the substrate. The separation between molecules along the [2-25] surface direction, i.e. the close-packed superstructure direction, is approximately 9.85 Å. This value, which is slightly below the expected van der Waals diameter (11 Å), is compatible with a van der Waals interaction as we have to consider the effect of the surface topography in the arrangement of the molecules.

STM and LEED indicate a soft landing of the C_{60} molecules on the TiO_2 surface. However, we cannot say anything about the interaction between them. In principle, the values of the C_{60} diameter and height obtained by STM (11 Å and

8 Å, respectively) are compatible with a preservation of the spherical symmetry of the molecule after its deposition. The small difference in the aspect ratio can be understood as an electronic effect. Additionally, their diffusion on the surface indicates the absence of strong covalent bonds with it. However, the best way to corroborate this is by means of NEXAFS measurements. Figure 4.2.1.5 shows four different NEXAFS spectra measured for two different coverage values and for s and p-polarization conditions (see figure 3.11). Black curve represents the s and p-polarization spectra for 1.5 ML of C_{60} on TiO_2 measured at RT. As both curves are identical, we just show one of them for the sake of clarity. Blue and red curves correspond to 0.8 ML of C_{60} measured in s and p-polarization, respectively. For both values of the coverage we observe essentially the same spectra, with the same peaks and shape.

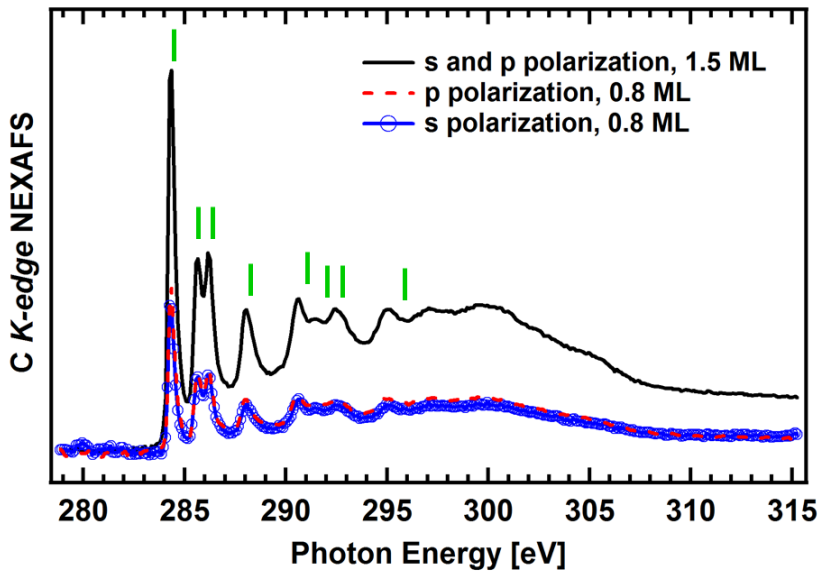

Figure 4.2.1.5.- *Carbon K-edge NEXAFS spectra for two different values of the coverage*. We represent three different NEXAFS curves which correspond to four different conditions. Black solid curve corresponds to the NEXAFS spectra measured for s and p-polarizations for 1.5 ML of C_{60}. Blue dotted and red dashed curves correspond to s and p-polarization spectra measured for 0.8 ML of C_{60} molecules, respectively. Green vertical lines mark the position of the main NEXAFS peaks measured for a C_{60} multilayer (obtained from [152]). As we can see there is a very good agreement between our results and the position of the peaks for a multilayer coverage.

The only difference is the intensity of the spectra. As a reference, we have marked with green vertical lines the energy position of the main peaks of the NEXAFS spectra for a multilayer coverage obtained from reference [152]. As we can see, the spectra for 1.5 ML and 0.8 ML are almost identical to the one obtained for a multilayer coverage. The shape and position of the peaks are surprisingly in good correspondence with the values from bibliography. We can extract two main conclusions from these spectra. First of all, as the spectra for s and p-polarization are identical we can ensure that the C_{60} molecules do not suffer any important variation of its aspect ratio when they are deposited on the TiO_2 surface at RT as they preserve the spherical symmetry. The second conclusion is that as the submonolayer NEXAFS spectra are almost identical to the ones obtained for a multilayer coverage, molecular orbitals are not being affected by the deposition of C_{60} on TiO_2. This indicates a very low molecule-substrate interaction.

In order to complete and corroborate our experimental results we have performed DFT calculations. We have obtained a model in which both C_{60} molecules in the unit cell present a different orientation but it has not been able to obtain their exact orientation. Unfortunately, the Fireball-LDA method used for our DFT calculations presents some limitations in this kind of weak-interacting systems. It is well known that LDA approximation doesn't work correctly in these interfaces and the van der Waals interactions should have been taken into account. Some work has been done in order to solve these deficiencies, but it makes no possible a confident energetic comparison between the different possible structures (formed by the combination of the C_{60} orientations). However, DFT will be used to optimize the models proposed by means of XPD, as we will show later.

Although in principle we can say nothing about the molecular orientation, we use DFT to obtain the theoretical DOS. Figure 4.2.1.6 shows the theoretical DOS for the clean TiO_2 and evaporated C_{60} surfaces. Both curves are very similar, as we could expect for low interacting systems. We observe the appearance of the HOMO state inside the band-gap region, in good agreement with photoemission measurements, as we will show in section 4.2.4.

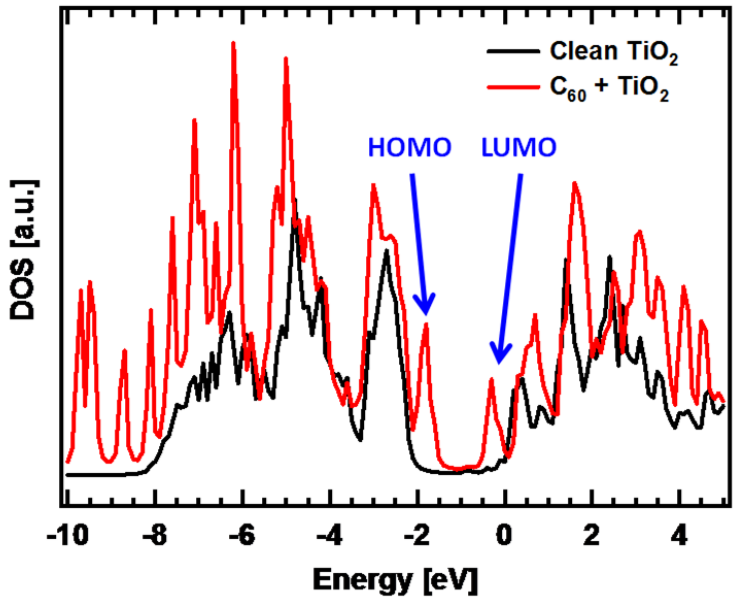

Figure 4.2.1.6.- *Theoretical DOS for the clean and C_{60} covered surfaces.* We find a very similar shape in the valence band before and after the deposition of the molecules, indicating a low interaction. We observe the appearance of a new state inside the gap associated to the HOMO.

4.2.1.2. Defects in the C_{60} / TiO_2 (110)-(1x1) system

Although the C_{60} islands present a very good order, it is possible to find some defects. Basically, we can distinguish three different types of defects. First of all, we can observe the presence of dark features inside the molecular islands as the ones marked with blue dotted circles in figure 4.2.1.7. These dark features present the dimensions of a single C_{60} molecule so we can assign them to missing molecules. As well explained in reference [151], these C_{60} vacancies cannot be associated to the presence of typical single defects on the substrate such as O_{vac} or OH groups as their density is much higher than the density of missing molecules. Thus, we can imagine two possible origins: they can be due to an unusual accumulation of defects in that area, for example

two O_{vac}´s or two OH groups; or they can be originated by a fault in the island formation.

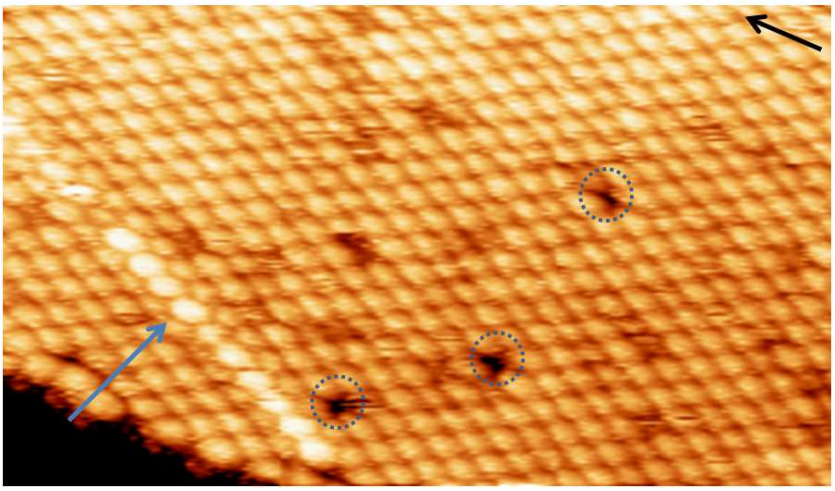

Figure 4.2.1.7.- *STM image of a C_{60} island. In this image we can see two of the main defects present in the molecular islands*. On the one hand we observe the C_{60} vacancies which correspond to missing C_{60} molecules (marked by blue dotted circles). On the other hand we detect the anti-phase boundaries due to a stacking fault during the coalescence of two C_{60} islands (marked by a blue arrow). The [001] direction is indicated by a black arrow. Coverage: ~ 0.6 ML. Size: (300 Å x 175 Å), I = 0.12 nA, V = 1.65 V.

The second kind of defect is what Loske et al. called *anti-phase boundaries* in ref [151]. This kind of defect consists of stacking faults occurring during the island growth. We can see some examples in figures 4.2.1.7 and 4.2.1.8 (marked with blue arrows). In the latter we can observe two boundaries running along two directions. When two different islands coalescence two molecules in the same substrate Ti_{5f} row can get into close contact. If this happens, a mismatch in the island order takes place and it is created a "boundary" between both islands where no C_{60} molecules can be accommodated. The only possibility is that extra C_{60} molecules sit on top of these boundaries, thus protruding from the island plane by approximately 0.7 – 0.8 Å, as measured by STM. These anti-phase boundaries can only have two

directions, the [2-25] and the [-225], as we can see in figure 4.2.1.8. Both boundaries join in the corner where the boundary is originated (a more extensive explanation can be found in ref [151]). In this case we cannot see the corner because it coincides with the border of the island. We can also observe that the boundary that is running towards the upper part of the image in figure 4.2.1.8 is not interrupted by the presence of a big defect as the cluster present on the surface. In fact, the boundary is just shifted parallel and it continues its way up until reaching the island border (not shown).

We also observe some intensity differences among C_{60} molecules. These differences are probably induced by the tip as we have observed many other images where all C_{60} molecules present the same intensity, except for those on the anti-phase boundaries (see for example figure 4.2.1.7).

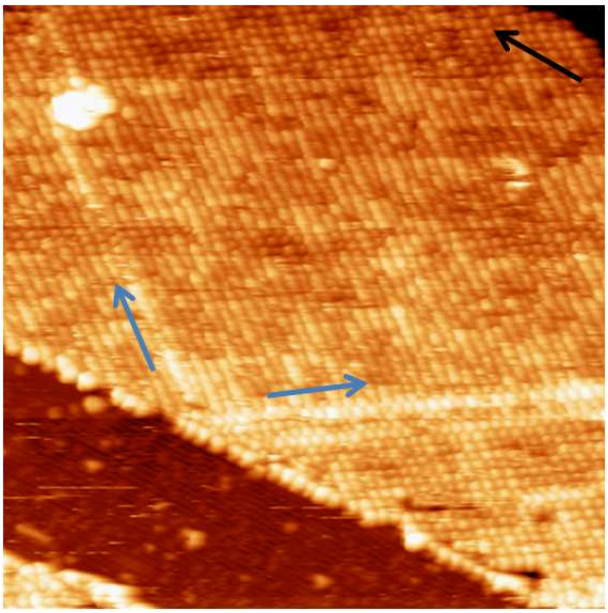

Figure 4.2.1.8.- *STM image of a defective island*. In this STM image we can see two anti-phase boundaries running along the two possible directions, [2-25] and [-225] (indicated by the blue arrows). The anti-phase boundary on the left continues beyond the contamination cluster but it suffers a parallel shift. Black arrow points along the [001] direction. Coverage: ~ 0.7 ML. Size: (520 Å x 520 Å), I = 0.05 nA, V = 1.8 V.

The anti-phase boundaries are always individual. However, we have found island areas where we observe an agglomeration of linear defects. We show an example in figure 4.2.1.9. In the right side of the STM image we can see that C_{60} molecules present a different structure. We have marked in blue the unit cells associated to both regions. The origin of this area with a different structure is unclear. The simplest model would be one in which, attending to the already observed anti-phase boundaries, an accumulation of these boundaries would take place. If it were so, we should see an alternation of brighter and darker C_{60} rows by STM. However, that it is not the case, as all molecules present the same brightness, thus indicating no topographical differences among them. In addition to this, if we measure distances between molecules in the experimental image and compare them with the values expected by the model of accumulation of *anti-phase boundaries*, we observe that there is not a good agreement between them. For this reason, an alternative model should be found.

The model we propose for the *"defective"* structure by means of STM is based in two factors. On one side, the measured STM distances, which must be handled carefully as they may present a certain error quantified in approximately a 5 – 10 % due to different factors such as drift or piezoelectric irregularities. The second factor considered for this model is the fact that DFT calculations predict a small energy difference (0.1 eV) between C_{60} molecules adsorbed on Ti_{5f} rows and those on O_{br} rows. We present in figure 4.2.1.10 the model we propose taking into account these two considerations. In this model, we have an alternation of C_{60} molecules sitting on top of Ti_{5f} and O_{br} rows. In this case, all molecules should present a very similar height as the adsorption height is larger than the protrusion of the O_{br} rows, as we will see by DFT calculations (see figure 4.2.1.16). This *defective* model shows a change in one of the close-packed directions passing from the [2-25] to the [3-32] direction. We also notice a variation in the superstructure unit cell. This new region presents an oblique lattice characterized by a periodicity given by the matrix:

$$\begin{pmatrix} 5 & -2 \\ 2 & 3 \end{pmatrix}$$

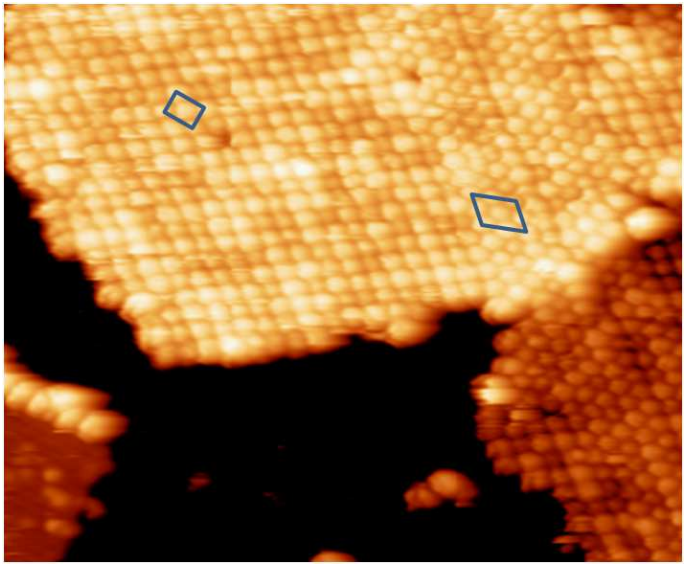

Figure 4.2.1.9.- *STM image of the third kind of defect, the agglomeration of linear defects.* In this STM image we can observe a region of the C_{60} island where molecules present a different structure. It is due to a new stacking of the molecules combining lines of C_{60} molecules on Ti_{5f} and O_{br} rows. This new structure presents a different unit cell, marked by a blue oblique parallelogram. Coverage: ~ 0.5 ML. Size: (350 Å x 290 Å), I = 0.05 nA, V = 1.8 V.

This oblique lattice presents a base formed by four C_{60} molecules, one divided into the four corners, two divided into the four sides and one at the center. Although it seems a rarely large unit cell, it is the smaller one as we have to take into account the registry with the substrate. Regarding the distances in the new region, we show in table 4.2.1.I the values obtained for both models and the experimental ones. Directions are given in figure 4.2.1.10.

	Anti-phase model	Defective model	Experiment
[001]	25.0 Å	28.1 Å	29.5 Å
Perpendicular	16.6 Å	18.6 Å	19.0 Å

Table 4.2.1.I.- *Experimental and modeled distances of the region showing an accumulation of defects.* Anti-phase model values taken from ref. [151]. Defective model, this work (figure 4.2.1.10).

If we consider a 10 % of error in the STM images, we observe that the best agreement is obtained for the defective model.

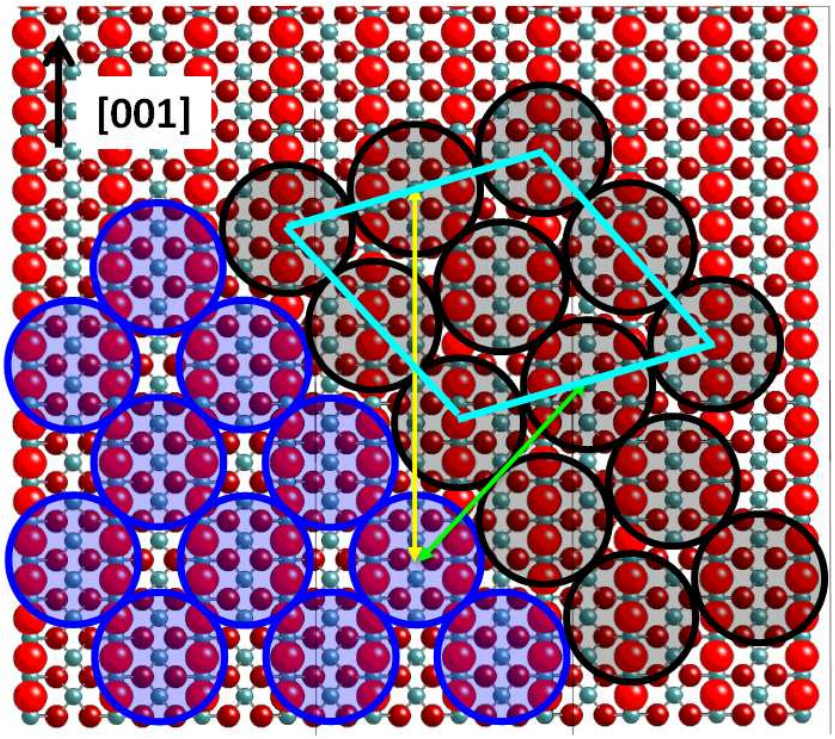

Figure 4.2.1.10.- *Schematic representation of the defective structure model we propose*. Red and light blue balls correspond to O and Ti substrate atoms, respectively. O_{br} atoms are larger and brighter than in-plane O atoms. Large blue and black circles correspond to C_{60} molecules in the *p (5 x 2)* and new "defective" structures, respectively. Yellow and green arrows indicate distances used for the model, measured along the [001] direction and perpendicularly to the boundary, respectively. We also show the new unit cell in light blue. As we can see, there is an alternation of C_{60} molecule rows sitting on top of O_{br} and Ti_{5f} rows as we move perpendicularly to the boundary.

4.2.1.3. Thermal stability

Figure 4.2.1.11 a) shows a STM image of the TiO_2 (110)-(1x1) surface with approximately 0.5 ML of C_{60} molecules after annealing the system at approximately 400 K (typically during 15 minutes). We observe the presence of C_{60} islands, very similar in size and shape to the ones obtained before the annealing. We do not observe a higher degree of order inside the islands as we still can find C_{60} vacancies. The apparent height of the molecular islands is also the same as before the annealing, ~ 8 Å, as we can see in the scan profile of figure 4.2.1.11 b). Summarizing, we do not observe any significative change after this soft annealing. The only observed difference is that we also find some isolated material on the terraces which presents different dimensions. Some of them can be associated to C_{60} molecules while the rest can be due to contamination. These molecules seem to be evaporated from the ordered islands.

If we increase the annealing temperature to ~ 500 K, we do observe significative changes in the surface topography (figures 4.2.1.12 a) and b)). First of all, as we can see in the STM image of figure 4.2.1.12 a), there is an increase in the amount of isolated material in the terraces, together with an increase in the number of molecular islands randomly distributed on the surface. These islands also present irregular shapes, as we can see in figure 4.2.1.12 b). It seems that, as a consequence of the higher thermal energy due to the annealing, molecules diffuse on the surface and interact more strongly with the substrate. The fragmentation of the molecular islands into many small ones produces the disappearance of the LEED pattern. Curiously, the same mechanism has been observed for the more interacting case of C_{60} on Pt (111) [153]. On the other hand, the increase in the interaction strength is evidenced by the decrease in the apparent height of the C_{60} islands measured by STM. The new value obtained after this annealing treatment is approximately 6.5 – 7 Å, i.e. a 10 – 20 % lower than before the annealing. This can be due to the establishment of new bonds between the C_{60} molecule and the O atoms underneath. Although the disorder in the C_{60} islands has increased, they still present the same rectangular structure and registry with respect to the substrate observed before the annealing.

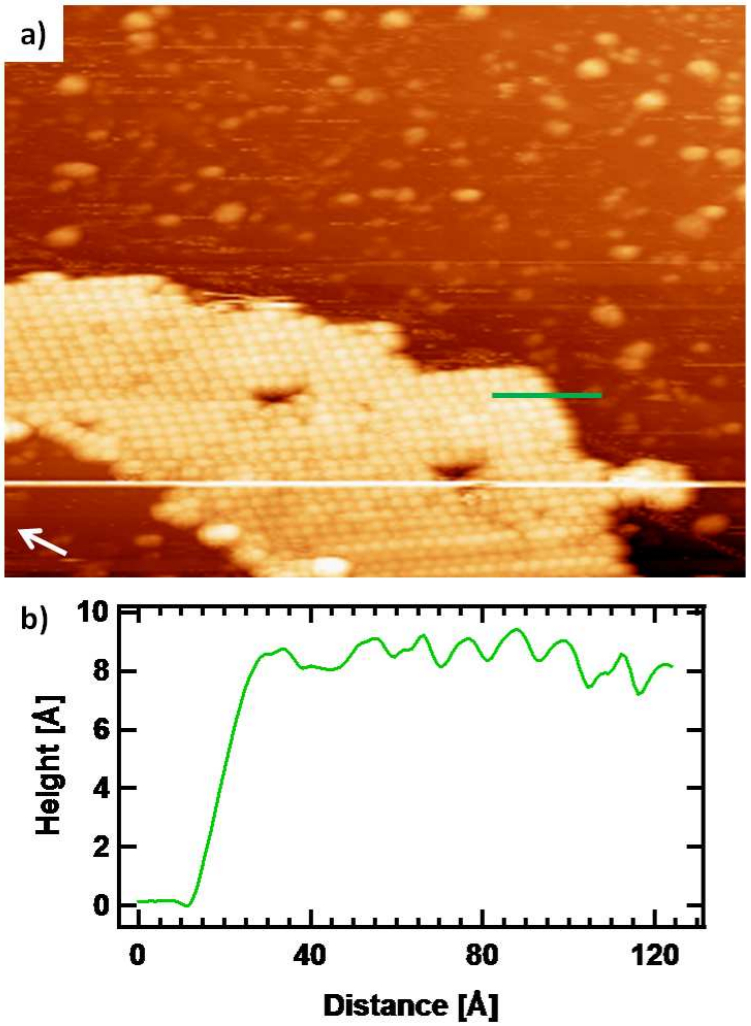

Figure 4.2.1.11.- *C_{60} layer after being annealed at 400 K*. a) STM image of a C_{60} island after the annealing. It presents the same structure and order as before the annealing. Initial coverage: ~ 0.6 ML. Size: (500 Å x 390 Å), I = 0.12 nA, V = 1.8 V. b) Scan profile on the C_{60} island and substrate surface. As we can see, islands keep the same apparent height after this soft annealing.

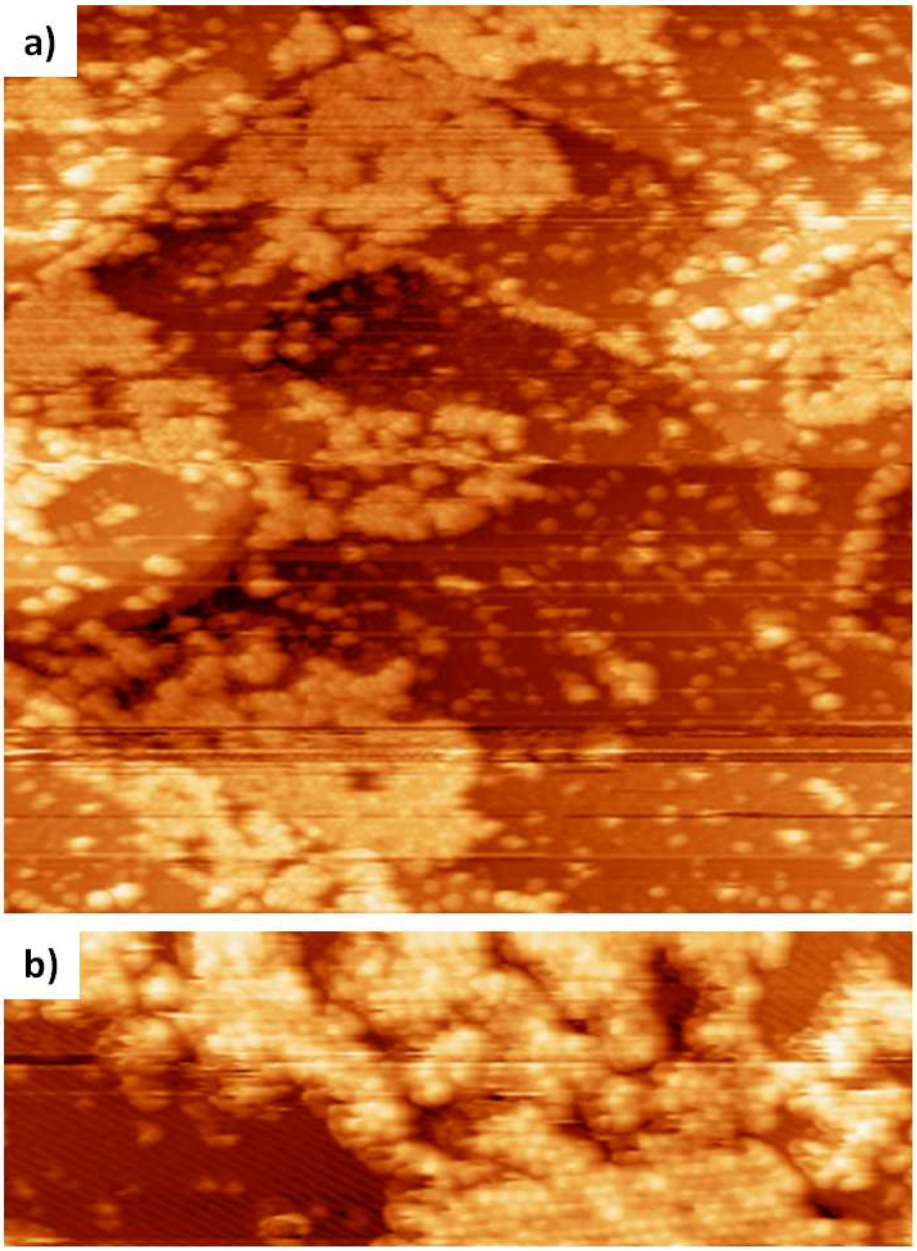

Figure 4.2.1.12.- *STM images of the surface after annealing at 500 K*. a) We observe the fragmentation of the C_{60} islands after the annealing together with a higher disorder and an increase in the amount of material in the terraces. Initial coverage ~ 0.6 ML. Size: (1000 Å x 1000 Å), I = 0.12 nA, V = 1.65 V. b) Closer inspection of the molecular layers. In this case we observe a decrease in the apparent height of approximately a 10 – 20 %. Size: (590 Å x 205 Å), I = 0.12 nA, V = 1.65 V.

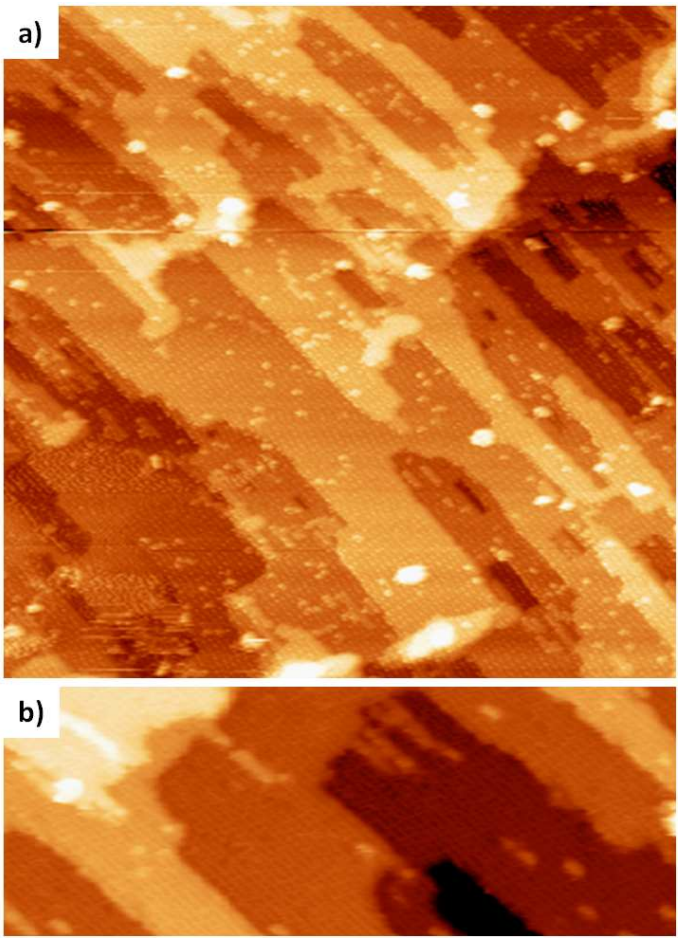

Figure 4.2.1.13.- *STM images of the surface after annealing at 700 K*. We observe a clear desorption of the C_{60} molecules. a) Size: (1500 Å x 1500 Å), I = 0.12 nA, V = 1.65 V. b) Size: (300 Å x 180 Å), I = 0.12 nA, V = 1.8 V. Initial coverage ~ 0.5 ML.

Finally, if we increase the annealing temperature to approximately 700 K, STM images show the desorption of C_{60} molecules (figure 4.2.1.13). We observe the presence of bright features randomly distributed on the surface which are probably related to C_{60} molecules although they present a higher diameter than the one expected for a molecule (bright features diameter: ~ 20 Å, height ~ 2.5 Å). This difference can also be due to the formation of higher order fullerenes or molecular domes (half-fullerenes). We do not observe any

evidence of graphene formation on this system as it has been reported after decomposition of this molecule on other systems such as Pt (111) [154].

4.2.1.4. Study of the C_{60} orientation with respect to the TiO_2 surface

In order to elucidate the relative orientation of the C_{60} molecules with respect to the TiO_2 surface, we have performed XPD measurements on the C1s core level. The idea behind this experiment is to discriminate between different adsorption sites by inspection of the XPD pattern. It is well known that XPD probes the spatial disposition of the atoms surrounding the emitter (in our case C atoms), producing important changes in the diffraction pattern according to the molecular orientation. Thus, comparing the experimental pattern with the ones obtained by simulating the most probable orientations, we should be able to determine the adsorption geometry of the C_{60} molecule (see section 3.6).

However, an important consideration must be taken into account before the data analysis. As derived from DFT calculations, the two C_{60} molecules composing the molecular unit cell present two different orientations as the adsorption site on the surface is different. This difference implies that the experimental XPD pattern will be the result of the sum of two different patterns, one associated to the central molecule of the unit cell, and the other to the molecules on the corners. It is very important to keep this in mind if we want to correctly interpret the experimental results.

Figure 4.2.1.14 shows the experimental XPD pattern. It covers a polar angular range going from 90° to 22° (θ = 90° means normal emission, only in the experimental pattern) and an azimuthal range extending from 0° to 130°, including both high-symmetry surface directions, [001] and [1-10]. Features in yellow correspond to more intense signal while those in black are associated to low intensity. The experimental XPD pattern is characterized by a very low anisotropy with just one bright belt which extends from θ = 52° to θ = 72° approximately. This result is very surprising as C_{60} molecules are supposed to produce a highly intense and anisotropic pattern [155].This belt is quite

homogeneous while moving along the azimuthal angle and the total anisotropy is very low (~ 0.1) for the coverage of approximately 1 ML. This result is not compatible either with fixed molecules on the surface or molecules randomly oriented with respect to it. In the first case, the pattern would present a very high anisotropy with well-defined diffraction peaks corresponding to the position of the emitter neighboring atoms. In the second case, the pattern would be a combination of all the individual patterns associated to all possible molecular orientations, giving rise to a homogeneous pattern. Thus, both possibilities can be rejected. We can also discard a third case in which molecules were rotating freely along all possible axis, as the result would be the same as in the second case. Then, only two possible molecular configurations are compatible with the data. One is that in which molecules present a particular orientation depending on the relative adsorption site on the surface but with a free azimuthal orientation in such a way that the final XPD pattern is a combination of infinite patterns with the same polar orientation but different azimuthal one. The other possibility is having all C_{60} molecules spinning along the surface normal. As the diffraction process presents a timescale in the order of picoseconds, we will not be able to distinguish between both possibilities as the molecular spinning would be frozen for this timescale [78]. In any case, it is reasonable to assume that C_{60} molecules are spinning as it is well known that they can rotate at room temperature, as it happens in C_{60} crystals and WO_2 [145,156].

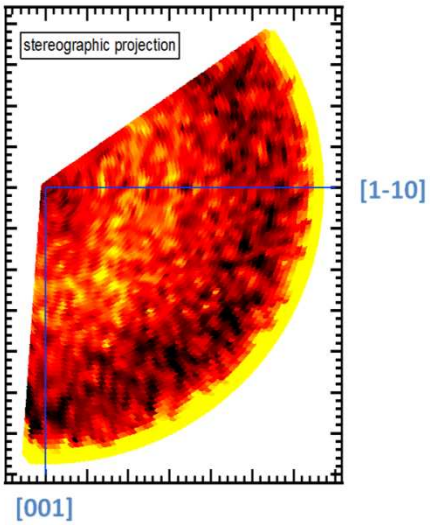

Figure 4.2.1.14.- *Experimental XPD pattern of the C1s core level.* We can distinguish a bright belt going from θ = 52° to θ = 72°. The center corresponds to normal emission (θ = 90°). The kinetic energy of the emitted photoelectrons is 850 eV.

Extra information can be extracted from the XPD patterns. Figure 4.2.1.15 shows the experimental and simulated patterns for the main molecular orientations of the C_{60} molecule adsorbed on the surface on a: hexagon, pentagon, hexagon-pentagon dimer (dimer-56), hexagon-hexagon dimer (dimer-66) and one atom. The names are given considering the part of the molecule that is facing the surface. In this case, the patterns are represented in their matrix format, which simplifies the comparison process. In this format, the diffraction anisotropy is represented versus the polar (vertical axis) and the azimuthal angles (horizontal axis). The upper part of the patterns corresponds to normal emission (θ = 90° for the experiment and θ = 0° for the simulations). For the sake of clarity, we have enclosed on a blue rectangle the angular position of the experimental bright belt. Among the five orientations checked in this experiment, we observe that two of them can be automatically rejected as they present maxima at polar angles where the experiment presents minima. Those two orientations are hexagon-hexagon dimer (dimer-66) and pentagon. Among the three remaining ones, we can also discard the atom orientation as, although the main maxima are located within the belt, it

presents another maximum at normal emission. On the other hand, both hexagon and pentagon-hexagon dimer (dimer56) present their maxima almost completely within the belt. Furthermore, their maxima appear at complementary polar angles in such a way that a combination of both orientations covers the entire belt. Although the agreement is good, this model fails in the region located around a polar angle of 40 - 50° (considering the experimental scale), where the dimer-56 orientation presents a maximum. This error can be understood if we take into account that only the five simplest orientations have been considered in the simulations. Probably, the real orientation of the molecules is more complex. It is quite probable that C_{60} molecules present orientations which are slightly rotated with respect to the ones considered here. For example, a better fit should be obtained for an orientation where one of the molecules is in between a pentagon and a dimer-56. This small rotation could probably accomplish with the error in the pattern comparison. Thus, we can conclude that we have two possible orientations for the C_{60} molecules, depending on their adsorption sites on the surface: molecules with a hexagon facing down and molecules with a pentagon-hexagon dimer facing the surface. Moreover, there should be the same number of molecules in each orientation as we have the same number of molecules on both adsorption sites in the p(5x2) structure.

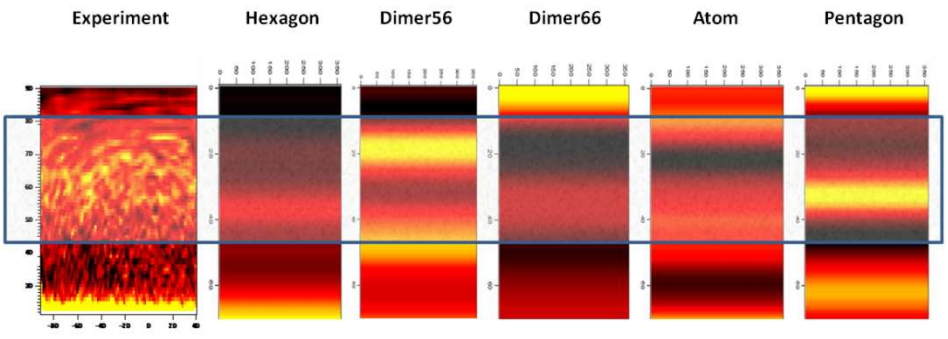

Figure 4.2.1.15.- *Experimental and simulated XPD patterns represented in their matrix format*. We have simulated the main five orientations for C_{60}. We have enclosed the bright belt in a transparent blue rectangle. The vertical axis corresponds to the polar angle while the horizontal one is the azimuthal angle. There are two orientations whose combination properly fit the experimental data: hexagon and pentagon-hexagon dimer (dimer-56).

A full DFT calculation of the adsorption site using the Fireball-LDA method would not be realistic because it fails describing low interacting systems as the one we are dealing with. Therefore, in order to have a quantitative value for these rotations, an exhaustive DFT study considering a wider spectrum of possible orientations around the positions compatible with XPD has been performed. The result of such an optimization starting from hexagon and pentagon-hexagon dimer orientations is given in figure 4.2.1.16. In the top view exhibited in figure 4.2.1.16 a), the molecule on top of a Ti_{5f} atom presents a quasi pentagon-hexagon dimer orientation, slightly rotated towards a pentagon orientation. On the other hand, the molecule in between two Ti_{5f} atoms presents a hexagon orientation with two Ti atoms in the center of hexagon borders. We can also notice that molecules are located in between the O_{br} channels, in good agreement with the STM observations.

Figure 4.2.1.16 b), shows a side view of the system, along the [1-10] surface direction. We observe that both molecules are separated from the surface plane determined by the Ti_{5f} atoms by approximately the same distance (~ 3.2 Å). This result is in good agreement with the STM observations where no difference in the apparent height is observed. Additionally, this distance is quite large, thus indicating a very low interaction between the molecules and the substrate, corroborating previous observations. From DFT calculations, we can also notice that molecules remain almost geometrically unaltered after their deposition on the TiO_2 surface. They preserve a spherical symmetry, with a very low deformation after their deposition (lower than 3 %). This result points in the same direction of a very low interacting system.

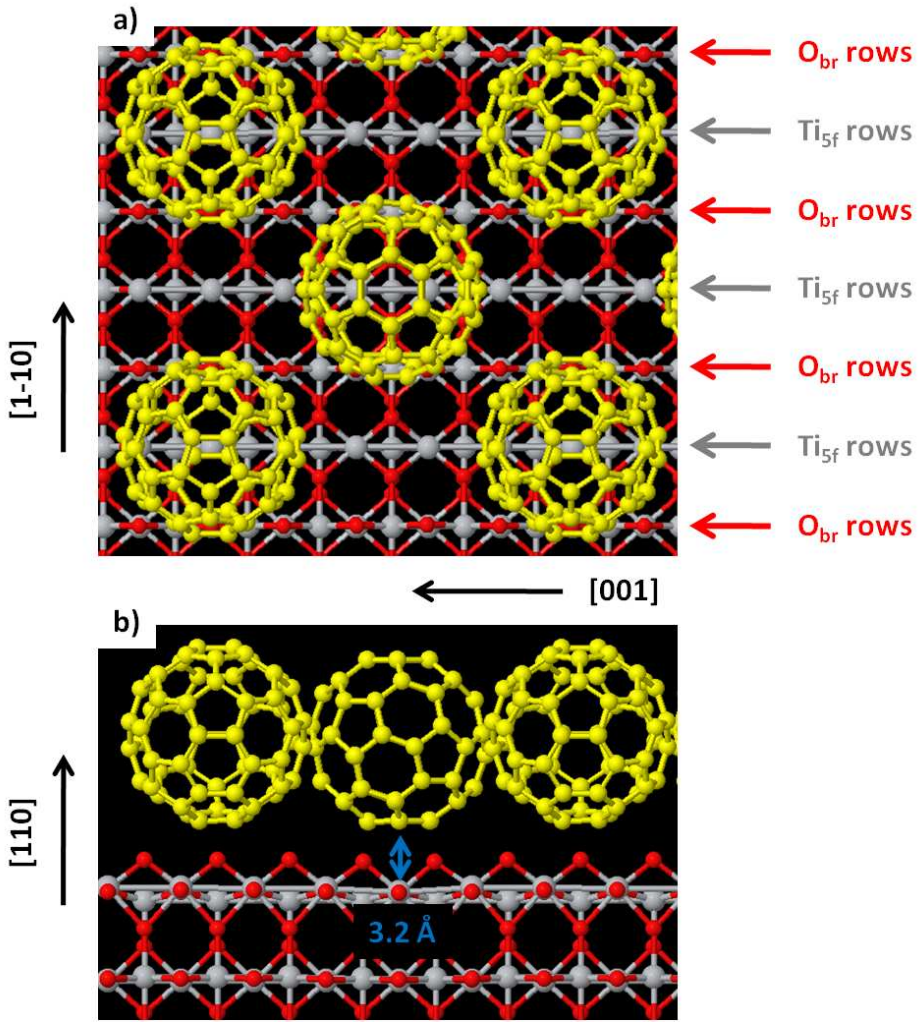

Figure 4.2.1.16.- *Schematic representation of the DFT optimized models for the C_{60} / TiO_2 model.* a) Top view. The superstructure unit cell is represented. We observe to different orientations depending on the adsorption site: hexagon (in between two Ti_{5f} atoms) and pentagon-hexagon dimer (on top of a Ti_{5f} atom). b) Side view along the [1-10] surface direction. Both molecules present a very similar adsorption height, approximately 3.2 Å, compatible with a low interacting system.

To rationalize a model where the molecules are spinning around an axis perpendicular to the surface we have performed molecular dynamics simulations for two C_{60} molecules arranged on a p(5x2) superstructure on the

rows of the TiO_2 (110)-(1x1) surface. These calculations are very expensive from a computational point of view; therefore, we abandon here the ab-initio approach and describe the interactions in the system by a classical force field optimized for simulations in a condensed matter environment (COMPASS [157,158]). Actual calculations have been performed with the program FORCITE as implemented in the Materials Studio Package [159].

Such a classical parameterization optimizes correctly the geometry for both the C_{60} molecule and the TiO_2 (110) surface, described by a slab formed by a (5x2) 2-dimensional unit cell and three tri-layers (the periodic unit cell is 14.8 x 13 x 40 Å, including a 20 Å vacuum gap to avoid interactions in the z-direction, and containing a basis of 300 atoms). This kind of parameterization is advantageous to describe long-range interactions, in particular the van der Waals interaction between pairs of C_{60} molecules. Van der Waals and other kind of non-chemical long range interactions are poorly described in DFT formalisms because of their limited ability to describe correlation and their dependence on the local value of the density; this precludes any typical power-law operating at large distances since densities decay exponentially (gradients corrections are not enough to properly describe the large distances required to account for interactions between two C_{60} molecules). Equilibrium parameters are: (1) d= 3.18 Å (bottom of the C_{60} molecule to the Ti_{5f} plane distance), (2) E_{ad} = 2.0 eV.

Starting from an optimized equilibrium geometry from DFT we run a molecular dynamics simulation in the microcanonical ensemble using 0.01 fs steps to integrate the dynamical equations during 1 ps. Velocities for all the atoms in the system are randomly assigned as to make an initial temperature of T=300 K, but the temperature is allowed to fluctuate accordingly with the chosen thermodynamic ensemble. After the first 1 ps the system is checked for equilibrium and dynamical variables are used to start a simulation for the next 4 ps in the canonical ensemble keeping now the temperature by an Andersen thermostat ($Standard\ deviation = T * \sqrt{\frac{2}{N}}$) [160]. These simulations show that at low temperatures (between 150 and 300 K) mainly breathing modes in the molecules are populated, while above room temperature molecules start rotating at typical angular frequencies of about 0.1 rad/ps. These rotations can be classified in two: (i) random rotations of the whole molecule showing that

barriers for rotations are in the same order of magnitude as kT, and (ii) correlated rotations where the total angular momentum of two neighboring molecules is conserved. We interpret that the later are associated to the off-axis interaction between two molecules located on different channels in the (5x2) reconstruction (see, for example, figure 4.2.1.16): it operates similarly as in two billiard balls making an off-axis collision and getting some rotational energy as a consequence. In a typical simulation (two snapshots are shown in figure 4.2.1.17) we can observe C_{60} molecules rotating around the surface normal, as we have predicted independently using our XPD measurements.

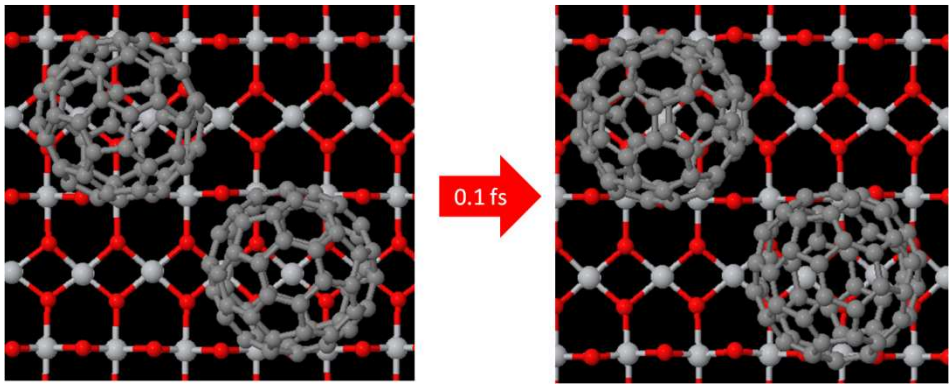

Figure 4.2.1.17.- *Ball-and-stick schematic representation of two snapshots obtained by molecular dynamics simulation.* In these two snapshots from a video (www.icmm.csic.es/esisna) we can observe how the azimuthal orientation of the C_{60} molecules is changing, thus indicating a rotation along the surface normal.

4.2.1.5. Conclusions

In this section we have studied the interaction, the morphology and the structure of C_{60} molecules adsorbed on the TiO_2 (110)-(1x1) surface at room temperature by means of STM, LEED, NEXAFS and XPD measurements and DFT calculations.

By STM we have observed the formation of well-ordered close-packed single molecule layers which grow from the step edges into the lower terraces. C_{60} molecules diffuse on the surface at RT, probably moving along the Ti_{5f} rows of the surface in good agreement with the results reported by Loske *et al.* [151]. This molecular superstructure presents a *p (5 x 2)* periodicity with a unit cell formed by two molecules: one divided into the four corners and one at the center.

Due to the absence of a NEXAFS dichroism as a function of the polarization we have seen that C_{60} molecules keep their spherical symmetry after their deposition. Additionally, there is no modification of the molecular orbitals of the deposited molecules with respect to the ones obtained for a multilayer. Both results are clear indications of a very low interacting system.

DFT calculations corroborate this low interaction between molecules and substrate as they indicate a very low deformation of the molecule (lower than 3 %) and a large adsorption distance. Theoretical calculations also predict a different molecular orientation for the two C_{60} molecules which compose the superstructure unit cell, as we could expect from the different adsorption site.

We report the existence of three different types of defects: C_{60} vacancies in the molecular islands, anti-phase boundaries due to stacking faults taking place during the island coalescence and regions with agglomeration of linear defects. We propose a structural model for this first time observed agglomeration consisting in an alternation of C_{60} molecules located on top of Ti_{5f} and O_{br} rows.

Additionally, we have carried out a study of the thermal stability of these molecular layers. We have observed that there are no significative changes when the system is annealed to 400 K. However, when the temperature is increased to approximately 500 K we discern the fragmentation of the C_{60} islands together with a decrease in their apparent height, indicating a stronger interaction with the substrate. For temperatures higher than 700 K, C_{60} molecules are fragmented and desorbed from the surface.

Finally, we have succeeded in the determination of the relative orientation of the C_{60} molecules which compose the superstructure unit cell, by means of XPD and DFT calculations. Molecules located on top of the Ti_{5f} atoms present

an almost pentagon-hexagon dimer orientation towards the surface, whereas molecules in between two Ti_{5f} atoms have a hexagon facing down. These results also suggest our model of spinning C_{60} molecules along the surface normal, as it is corroborated by molecular dynamics simulations.

4.2.2. Pentacene

Pentacene is an organic molecule which belongs to the family of Polycyclic Aromatic Hydrocarbons (PAH´s). Pentacene crystals and thin films behave as p-type organic semiconductors making them promising molecules for molecular electronics [161]*. They have been successfully tested in the assembly of high charge mobility organic thin film transistors (OTFT´s) and high efficiency organic photovoltaic cells (OPVC´s)* [161-165]*. The charge mobility properties highly depend on the film structure. Pentacene single-crystals grow in a triclinic lattice where molecules adopt a herring-bone packing with two molecules per unit cell* [166]*. The valley shape of this structure affects the charge mobility, so pentacene structures without valleys, such as lying-down pentacene molecules, would result in an improvement in the charge mobility properties of the system* [162].

Lying-down pentacene structures have been reported for the first layer when deposited on metal surfaces [167]*, although molecules tend to stand up from the second layer* [168,169]*. However, the molecule grows on semiconductors or insulating materials in a standing-up geometry since the initial stages of deposition as the assembling is driven by van der Waal´s intermolecular interaction* [167].

In this section we show how pentacene molecules grow forming lying-down structures with molecules aligned along the [001] direction on the TiO_2 (110)-(1x1) surface. Pentacene molecules interact repulsively along the [001] direction trying to maximize the separation distance, reaching a saturation value of ~ 17 Å. On the other hand, the intermolecular attraction along the [1-10] direction gives rise to the formation of stripes running along this direction, with a periodicity of 6.5 Å, the same as the substrate value. Molecules present a 25° tilt angle around their long axis ([001] direction) which corresponds with the structural arrangement of the molecular bulk crystal in the (010) plane, i.e. ***a-c*** *plane, allowing to keep a lying-down orientation in the next few layers.*

4.2.2.1. Monolayer phase

Pentacene is a PAH´s molecule composed by five fused benzene rings as we can see in figure 4.2.2.1. It is composed of 22 carbon atoms surrounded by 14 hydrogen atoms.

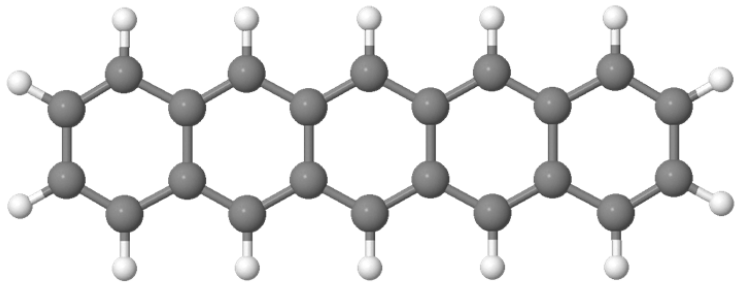

Figure 4.2.2.1.- *Ball-and-stick representation of a pentacene molecule*. As we can see, a pentacene molecule is composed of five benzene rings fused by one of their sides. It is made of 22 carbon atoms (big grey balls) and 14 hydrogen atoms (small white balls).

When we deposit pentacene at room temperature (RT) on the TiO_2 (110)-(1x1) surface, molecules diffuse on the surface as we have observed by STM measurements. We show in figure 4.2.2.2 an STM image for a pentacene coverage of approximately 0.4 ML. In it we can see the bright rows of the TiO_2 surface, running along the [001] direction but we have not been able to find any feature related with pentacene. In fact, we observe a fuzzy background. This is generally attributed to diffusing adsorbates on surfaces, in this case pentacene. This situation remains until we reach a coverage of approximately 0.5 ML, when we start detecting the formation of domains composed of irregular stripes running along the [1-10] direction and separated by approximately 20 Å along the [001] direction (figure 4.2.2.3 a)). For this coverage, although we observe the formation of domains, the diffusion is still high and the stripes present an irregular shape. So, basically, we have the competition between three interactions. On the one hand, we have the electrostatic repulsion between adjacent molecules along the [001] direction which tends to maximize the molecules distance. On the other hand, along the [1-10] direction, we have two kinds of attractive interactions: hydrogen bonds

between molecules mediated via the O_{br} atoms of the surface and electrostatic attraction between neighboring molecules, as it will be discussed later (see figure 4.2.2.3 d)). These attractive interactions are the reason of the stripes formation along this direction. However, as the coverage is still low, molecules move and the shape of these stripes is irregular.

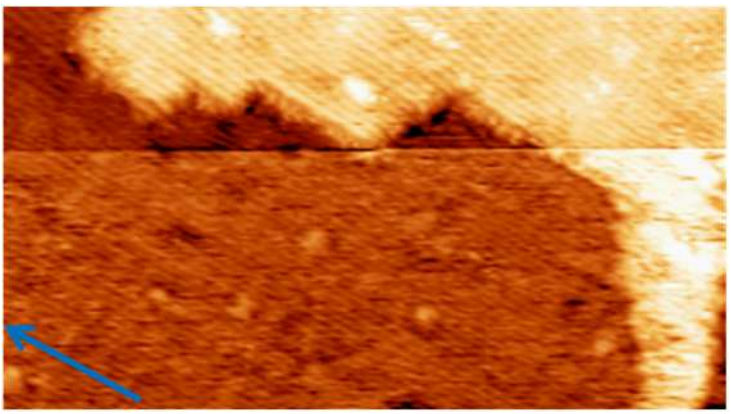

Figure 4.2.2.2.- *STM image of the pentacene / TiO_2 (110)-(1x1) system*. STM image for a coverage of 0.4 ML. We can see the Ti rows of the substrate running along the [001] direction (indicated by a blue arrow). The image is fuzzy, what it is a clear indication of diffusion on the surface. STM parameters: (560 Å x 310 Å), I = 0.15 nA, V = 1.8 V.

When we increase the coverage (0.8 ML) we observe the appearance of some changes in the molecular structures. The separation between molecules along the substrate rows decreases. This can be understood if we consider that as we increase the coverage, the density of molecules is increased, i.e. more molecules have to fit on the surface channels formed by consecutive O_{br} rows along the [001] direction (see figure 4.2.2.3 d)). This can only be achieved by reducing the intermolecular spacing along the [001] direction. Together with the reduction of the spacing along the substrate rows, we observe a certain degree of long range order along this direction associated to a straightening of the stripes, as we can see in figure 4.2.2.3 b). This is a confirmation of a stabilization of the molecular structures.

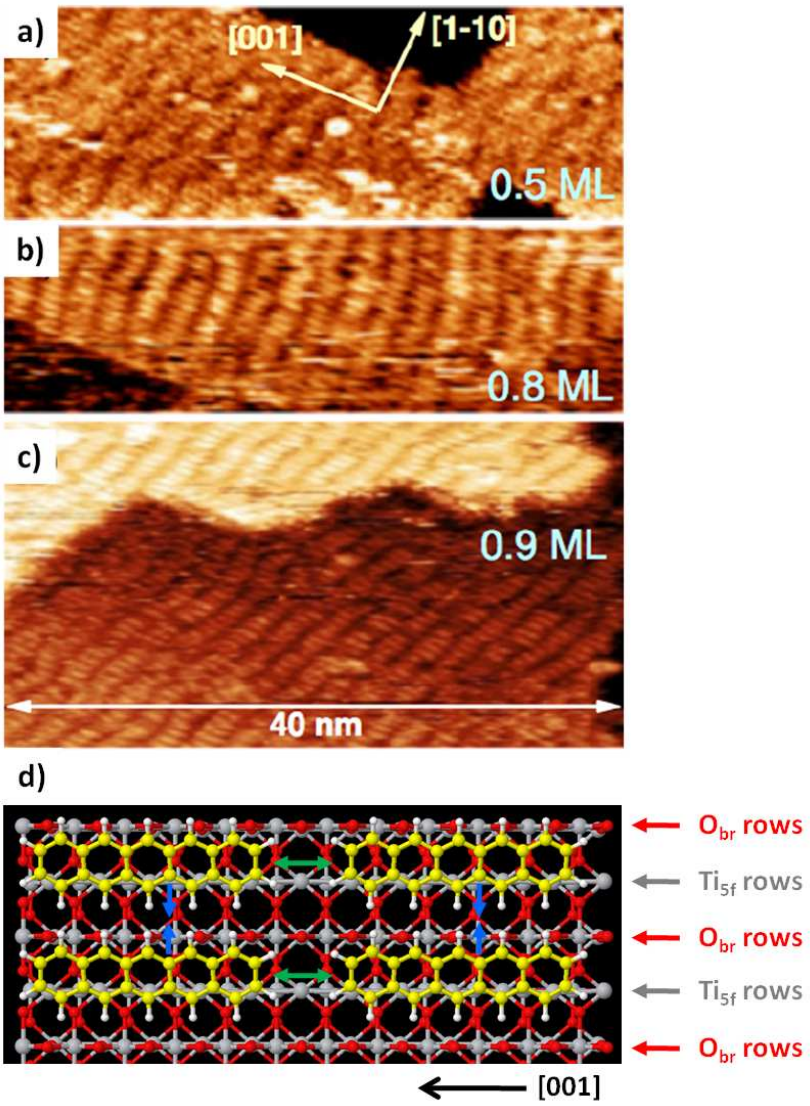

Figure 4.2.2.3.- *Set of STM images for three different values of the coverage: a) 0.5 ML, b) 0.8 ML and c) 0.9 ML*. We observe a straightening of the pentacene stripes oriented along the [1-10] direction with coverage, together with a decrease of the inter-stripes spacing. The size of the images is indicated in the figure. STM parameters: I = 0.1 nA (the same for the three STM images), a) V = 1.8 V, b) V = 1.65 V, c) V = 1.0 V. d) Schematic ball-and-stick representation of the pentacene / TiO_2 system. Molecules are located within the O_{br} channels and aligned along the [001] surface direction. The attractive and repulsive interactions between molecules along the [1-10] and [001] surface directions are indicated by blue and green arrows, respectively. Red, grey, yellow and white balls correspond to oxygen, titanium, carbon and hydrogen atoms, respectively.

Further increase of the pentacene coverage yields to additional reduction of the intermolecular spacing along the [001] direction, together with a more regular alignment along the [1-10] direction (figure 4.2.2.3 c)). However, the separation between molecules inside the stripes remains always the same (~ 6.5 Å) as this value is mediated by the surface topography (see figure 4.2.2.3 d)).

Figure 4.2.2.4 shows a high-resolution STM image of the pentacene molecules for a coverage of approximately 1 ML. Each stripe is formed by individual parallel segments aligned along the [001]. Each of these segments can be assigned to individual lying-down pentacene molecules as their length measured by STM (~ 16 Å) fits the expected value for pentacene molecules (~ 15.5 Å).

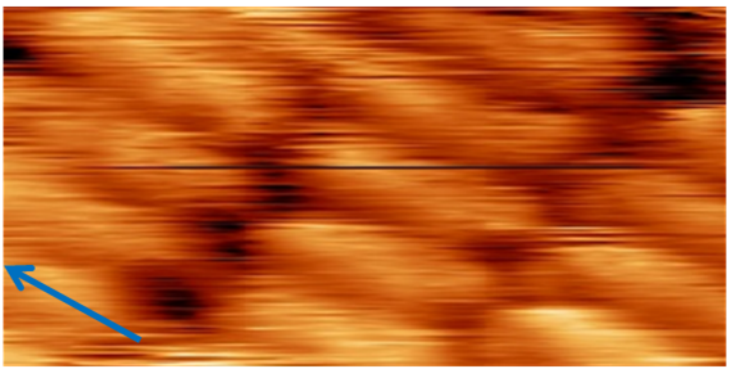

Figure 4.2.2.4.- *Molecular-resolution STM image for ~ 1 ML*. We can see in more detail the bright segments which compose the pentacene stripes. Each segment corresponds to one pentacene molecule. They are aligned along the [001] surface direction (blue arrow). STM parameters: (50 Å x 25 Å), I = 0.045 nA, V = 2.2 V.

This extra periodicity that appears along the [001] substrate direction it also observed by diffraction techniques such as LEED. We show in figure 4.2.2.5 the LEED pattern associated to approximately 1 ML of pentacene molecules. As we can see, it appears an extra spot which corresponds to a six-time periodicity along the substrate rows (~ 18 Å), approximately. This result is in good agreement with the value for the periodicity observed by STM (~ 17 Å) if we

take into account that both the STM and the LEED values have a small error. The error in the determination of the LEED periodicity is due to the fact that it is not easy to define exactly the value of the periodicity as we just observe one of the superstructure spots (marked with an arrow in figure 4.2.2.5).

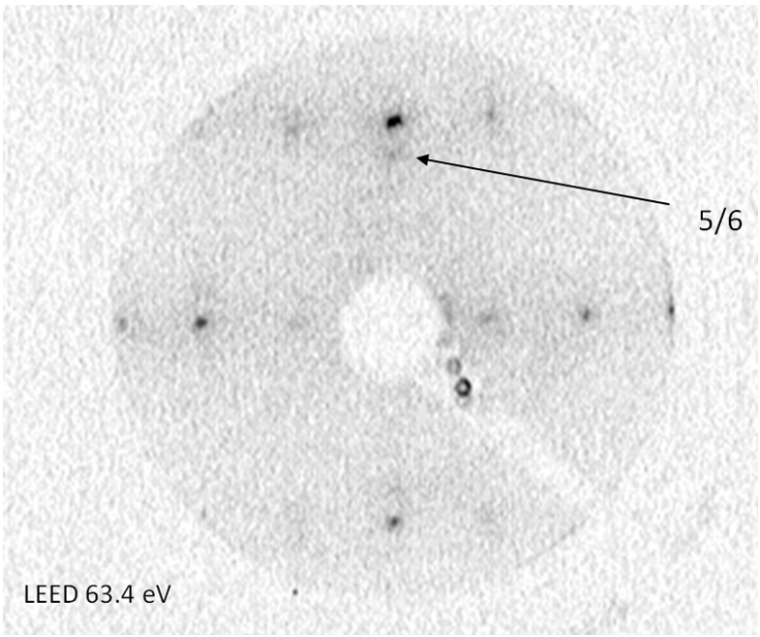

Figure 4.2.2.5.- *LEED pattern for 1 ML of pentacene on the TiO_2 (110)-(1x1) surface*. We can see the spots corresponding to the substrate periodicity and a small fuzzy spot which corresponds to the pentacene superstructure that appears along the [001] substrate direction (marked with a black arrow). This spot corresponds to a six-time periodicity along this direction. No extra spots along the [1-10] direction are observed. The energy of the incoming electrons is 63.4 eV.

In order to make a more quantitative study of the evolution of the periodicity along the [001] direction we have performed consecutive 1-dimensional HAS diffraction scans during pentacene deposition. These results corroborate the ones obtained by STM as no extra periodicities are observed along the [1-10] direction while a new diffraction peak along the [001] direction, associated to the pentacene superstructure, appears at a 0.5 ML coverage. We show in figure 4.2.2.6 a representative set of diffraction scans along the [001]

direction. These scans were taken at RT and they cover a coverage range from 0.5 to 1.5 ML. We can extract some information from these scans. We observe the appearance of a new diffraction peak at a coverage of approximately 0.5 ML. Its intensity increases with coverage up to 1 ML and at the same time it shifts away from the specular peak until it stabilizes at around 1 ML. If we continue depositing until reaching a coverage higher than 1 ML, the overall intensity of the diffraction pattern decreases. Additionally, analyzing the specularly reflected (0,0) peak we notice a strong decrease in its intensity without broadening (not shown in figure 4.2.2.6). This indicates that the surface gets covered layer by layer with uncorrelated molecules.

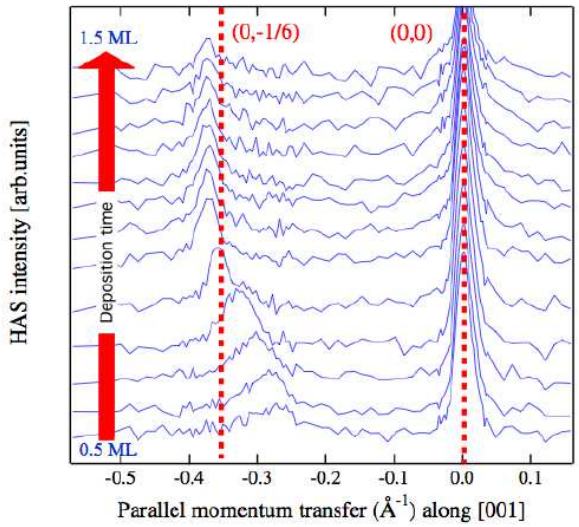

Figure 4.2.2.6.- *Set of consecutive diffraction patterns taken along the [001] direction during pentacene deposition with the substrate at RT*. The scans are shifted vertically according to the increased coverage. Each angular scan was recorded in approximately 1.5 minutes, corresponding to a deposition of approximately 0.08 ML. The vertical dotted red line a 0.0 Å^{-1} corresponds to the position of the (0,0) reflection. The one on the left indicates the nominal position of a fractional diffraction peak with a six-fold periodicity.

We show in figure 4.2.2.7 a quantitative analysis of the evolution of the intensity of the specular (0,0) peak, of the pentacene peak and of the

pentacene spacing along the [001] direction as a function of coverage. As we can see, the (0,0) reflectivity presents a single weak intensity oscillation with coverage. The presence of this maximum is associated with the formation of a new spatially ordered surface, i.e. a new ordered layer. Together with this oscillation of the specular reflectivity we observe the appearance of the new diffraction peak associated to the pentacene layer in correspondence with the intensity minimum of the specular peak. The pentacene peak also displays a maximum corresponding to the maximum of the (0,0) reflectivity. Regarding the mean spacing associated to the pentacene peak, we observe stabilization at a value of approximately 16.9 Å in correspondence with the maximum of the new peak. As a consequence, we can consider this coverage to define the value of a monolayer. The spacing between pentacene molecules along the [001] obtained by HAS fits well with the values found by STM, represented by blue dots.

As we have seen above, there is a continuous variation of the molecules spacing along the [001] direction from values of 24 to 16.9 Å, indicating that the straightening and alignment of the stripes is driven by head-to-head repulsion. The final spacing value is beyond the commensurated six-fold periodicity (17.7 Å), suggesting that there is not a significative contribution from the substrate atomic structure. Only when the stripe spacing is commensurated with the substrate we observe the appearance of a few very weak fractional peaks of higher order six-fold periodicity. When the coverage is different, the head-to-head repulsion is not enough to establish a long range order and the new diffraction peak is simply the preferred spacing between stripes, rather than a true periodicity. On the contrary, the substrate corrugation is dictating the pentacene azimuthal orientation while the side-by-side pentacene attraction drives the commensurated spacing along the [1-10] direction.

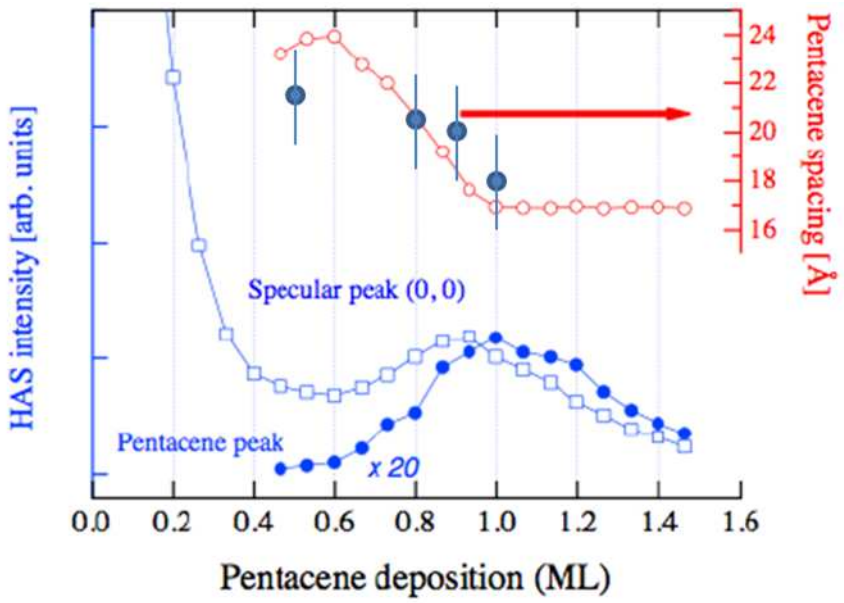

Figure 4.2.2.7.- *Evolution of the specular (0,0) and pentacene peaks intensities and of the inter-stripes spacing with coverage*. Blue curves correspond to the variation of the HAS intensity of both peaks mentioned above with the pentacene coverage. The specular peak presents one oscillation which corresponds to the formation of a complete monolayer. This maximum appears at a coverage which corresponds to the maximum of the pentacene peak. We also represent the variation of the pentacene spacing with the coverage measured by HAS and STM (red and blue dots, respectively). As we can see this spacing decreases with coverage until reaching stabilization for 1 ML.

If we take into account that there is no additional periodicity along the [1-10] direction and that the stripes spacing is only compatible with lying-down pentacene molecules we can conclude that all pentacene molecules are equivalent in the first wetting layer. The molecular density for the monolayer coverage is 0.91 molecule nm^{-2}, which is larger than the density obtained on Cu (110) (0.83 molecule nm^{-2}) where it is possible to grow a few additional lying-down layers [170]. Besides, the molecular spacing along the [1-10] direction perfectly matches the $d_{[100]}$ periodicity (**a** axis) of the pentacene crystal in the thin film phase, while the monolayer head-to-head spacing is ~ 8 % larger than the $d_{[001]}$ pentacene crystal periodicity (**a** = 6.49 Å, **b** = 7.41 Å, **c** = 14.75 Å) [166]. We remark that the molecules in the **a-c** bulk plane also

present a slight rotation around the long axis by ~ 25° off the **a-c** plane because of the herringbone packing.

Up to now, attending to STM and HAS results, we can establish that pentacene molecules form an ordered layer of lying-down molecules with a (6 x 1) periodicity. However, we can affirm nothing about a possible tilting of the pentacene molecules along its long axis. For this purpose we have performed NEXAFS measurements as this is the indicated technique for determining molecular orientations [82]. Pentacene is a planar molecule (*D2h* symmetry), whose transition dipole moment from the *s*-symmetry core levels to the π^*-symmetry unoccupied molecular orbitals, LUMO´s, is oriented perpendicular to the molecular plane. On the other hand, the transition dipole moments to σ^*-symmetry LUMO´s are lying down within the molecular plane. In this way, the intensity of the LUMO´s resonances depends on the relative orientation of the molecule with respect to the electric field of the incoming beam. If it exists a tilting of the molecules on the TiO_2 (110)-(1x1) surface we will be able to determine it by measuring the NEXAFS dichroism of the LUMO resonances at the C *K*-edge for different orientations of the surface with respect to the linear polarization of the x-ray beam.

Figure 4.2.2.8 shows the C *K*-edge NEXAFS spectra for a monolayer of pentacene molecules on the TiO_2 (110)-(1x1) surface. We can see three different curves which correspond to three different orientations of the incident beam with respect to the sample. We are using a grazing scattering geometry where the photon beam is kept at a constant incident angle of 6° with respect to the surface while the sample is rotated along the beam axis in order to change its polar angle (θ) with respect to the electric field. In this way we can change from *p*-polarization (θ = 90°) to *s*-polarization (θ = 0°). The black solid curve corresponds to a geometry where the incident electric field is perpendicular to the sample surface (*p*-polarization) and the photon beam is parallel to the [001] substrate direction. At this geometry we observe the presence of high intensity resonances in the π^* region (LUMO´s), going from 283 to 290 eV, associated with the presence of π orbitals oriented perpendicularly to the surface. When we change the incident geometry to *s*-polarization (blue dotted line), i.e. with the electric field parallel to the surface, we observe a strong decrease of the resonances intensity in the π^* region

although these peaks do not completely disappear [171]. This is consistent with π orbitals oriented almost perpendicularly to the surface, i.e. with pentacene molecules almost flat on the surface. We observe the inverse behavior for the σ^* region (290 - 305 eV) indicating the same adsorption geometry for the pentacene molecules predicted above. So from these spectra we can predict a tilt of the molecule around its long axis which it is oriented along the [001] substrate direction.

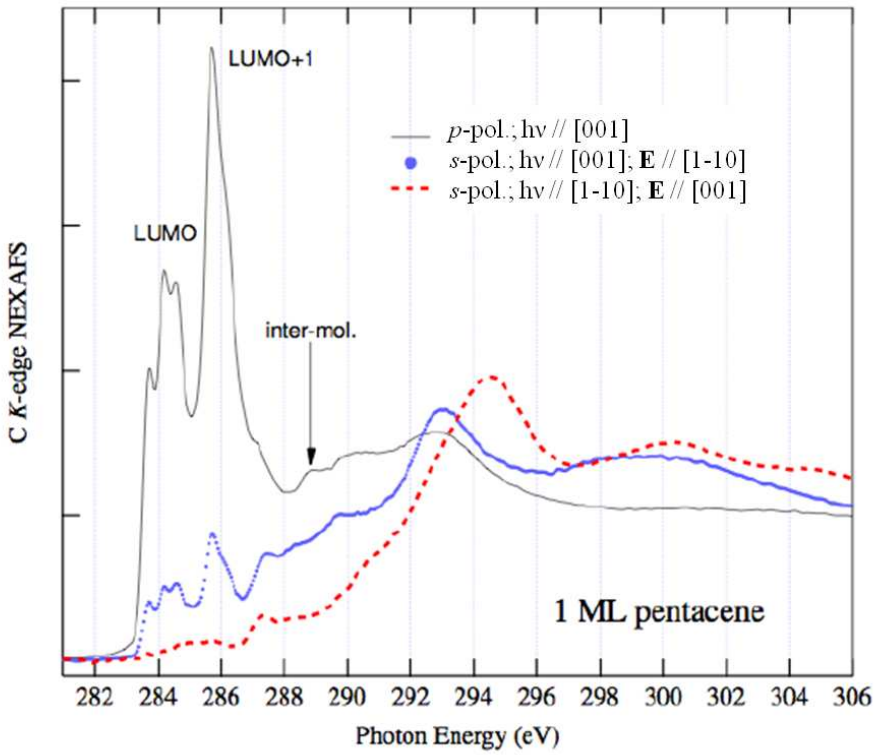

Figure 4.2.2.8.- *Carbon K-edge NEXAFS spectra for 1 ML of pentacene.* We can distinguish three different curves which correspond to three different geometries. Black solid line corresponds to p-polarization, i.e. the electric field is perpendicular to the surface, with the photon beam aligned along the [001] surface direction. Blue dotted line corresponds to s-polarization, i.e. electric field parallel to the surface, again with the photon beam aligned along the [001] direction. Red dashed line is relative to a geometry in which the photon beam is aligned along the [1-10] direction and the electric field is parallel to the surface. With these three geometries we can unequivocally define the adsorption geometry of the pentacene molecules.

We can evaluate this tilting angle (γ), i.e. the angle formed by the molecular plane and the surface, by making a quantitative analysis of the LUMO intensity variation with the polar angle (θ) in the NEXAFS spectra [82]. As we explained in section 3.5, it is known that the ratio between the two opposite polarizations, $I_{s\text{-}pol} \ / \ I_{p\text{-}pol}$, for a π-plane transition symmetry and two-fold surface symmetry is proportional to $tan^2\ \gamma$. Thus, we directly obtain a tilt angle γ = 25° ± 2°. This tilting angle around the molecular long axis oriented along the [001] direction is consistent with the NEXAFS results obtained when we azimuthally rotate the sample 90°. When we do this, the incoming beam is now aligned along the [1-10] surface direction, i.e. the electric field is parallel to the [001] direction (see figure 4.2.2.9). The NEXAFS spectrum for *s*-polarization in this geometry (red dashed line) presents no π-symmetry LUMO´s. This result is consistent with an adsorption geometry where the molecular plane is perfectly parallel to the electric field when the latter is oriented along the [001] direction.

This kind of strong azimuthal dichroism has been observed previously for the pentacene nanorails grown on Au (110) [169]. In this case, 1/3 of the pentacene molecules lie on their long edge rotated 90° with respect to the surface. If we compare both systems, we expect a strong rotational vibration of the tilted molecules around the main pentacene axis. This is consistent with the strong Debye-Waller intensity attenuation that we observe by HAS. A similar tilt angle of 30° and 28° has been reported for benzene and anthracene molecules deposited on TiO_2 [172,173], respectively. In the latter case molecules form a disordered phase, as we can inferred from the absence of azimuthal changes in the NEXAFS spectra, thus suggesting a mixture of lying-down and standing-up molecules. However, in our case we can unequivocally state that the pentacene long axis is parallel to the surface.

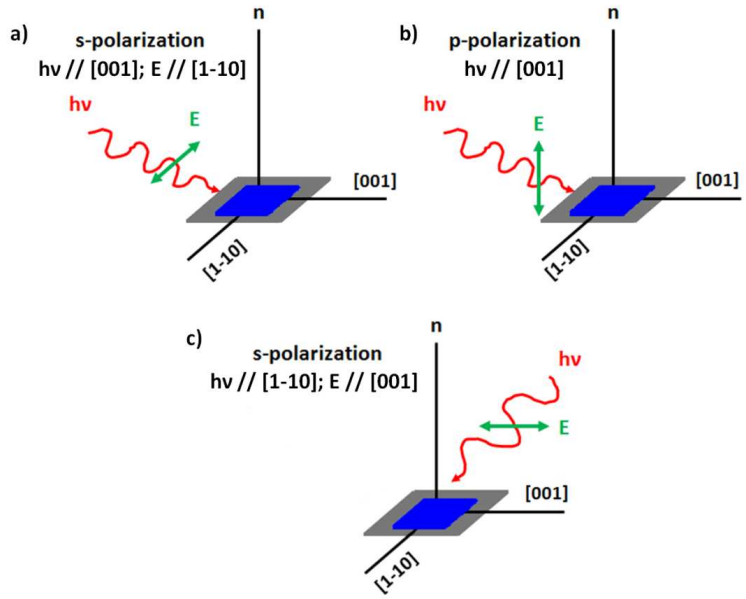

Figure 4.2.2.9.- *Schematic representation of the different orientations of the incoming electric field used in the NEXAFS measurements.*

In order to verify the structural model depicted by NEXAFS, we have performed DFT-LDA calculations with the Fireball code. We have simulated the adsorption of a pentacene molecule on the clean TiO_2 (110)-(1x1) surface on a (6x1) superstructure. The result is depicted in figure 4.2.2.10. We appreciate that the molecule is almost flat on the surface, with the extremes a little bit lifted with respect to the center of the molecule (figure 4.2.2.10 a)). This result is in good agreement with the observations by Gross *et al*. [174], where they notice an increase in the tunneling intensity in the borders of the pentacene molecules. We observe a tilting of the pentacene molecule around its long axis. This tilt angle is around 22°, in very good agreement with the value obtained from NEXAFS measurements, 25° (figure 4.2.2.10 b)). The distance between the molecule and the Ti_{5f} atoms of the surface is between 3.1 (lower part of the molecule) and 4.2 Å (upper part). Both values are too large to be associated to strong interactions, so it is another indication of the weak interaction of the system. Attending to figure 4.2.2.10, it seems that the molecule tries to maximize the number of C atoms facing O_{br} atoms, probably

because in this way it can maximize the number of H-bonds with them. In fact, the distances between the H and C atoms in the lower part of the molecule and the O_{br} atoms ($O_{br} \cdots H \sim 2.2 – 2.4$ Å; $O_{br} \cdots C \sim 3.3 – 3.4$ Å) are in the range of the weak H-bond interactions, as it can be inferred by comparison with the values given in ref. [175]. Thus, we can imagine a scenario where we have three types of interactions in the system, as we depict in figure 4.2.2.10. First, we have the repulsive interaction between molecules along the [001] surface direction which tries to maximize their distance along the Ti_{5f} rows. Secondly, we have an attractive interaction along the [1-10] surface direction which is the result of the establishment of hydrogen bonds between C-H atoms at the lower part of the molecules and the O_{br} surface atoms. Finally, we have another attractive interaction along the [1-10] surface direction which is due to an electrostatic interaction between the atoms in the lower part of one molecule and those in the higher part of the next molecule along the [1-10] direction. This last interaction is the result of charge redistribution inside the molecule, as it is suggested by DFT calculations. We will return to this point in section 4.2.4. Thus, theoretical calculations suggest a weak interacting system with pentacene molecules tilted by 22°, in good agreement with the experimental results.

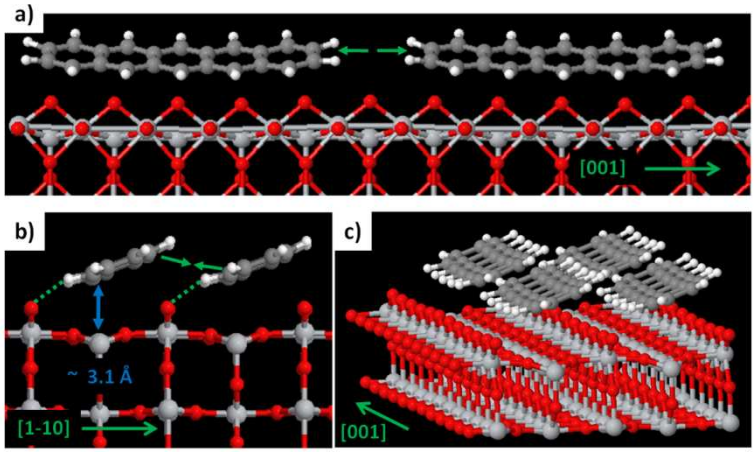

Figure 4.2.2.10.- *Ball-and-stick schematic representation of the pentacene / TiO_2 structure obtained from DFT.* a) Side view along the [1-10] surface direction. The molecule tries to maximize the number of C atoms facing O_{br} atoms to maximize the H-bonds. b) Side view along the [001] surface direction. The molecule is tilted by approximately 22°, in good agreement with NEXAFS measurements. The two attractive interactions taking place along the [1-10] surface

direction are depicted (H-bond: green dotted lines; Electrostatic attraction: green arrows) c) Perspective view. Light grey, dark, grey, white and red balls correspond to Ti, C, H and O atoms, respectively.

We have also calculated the DOS associated to this system. The result is shown in figure 4.2.2.11. The theoretical VB of the pentacene / TiO_2 system is very similar to the one of the clean TiO_2 surface, as we could expect for a low interacting system. Additionally, we observe the appearance of two new electronic states in the band-gap region, associated to the HOMO and HOMO-1 states of the molecule. As we will show in section 4.2.4.2, these results are in very good agreement with the experimental photoemission data. Furthermore, the theoretical HOMO – HOMO-1 energy separation is very similar to the one obtained experimentally.

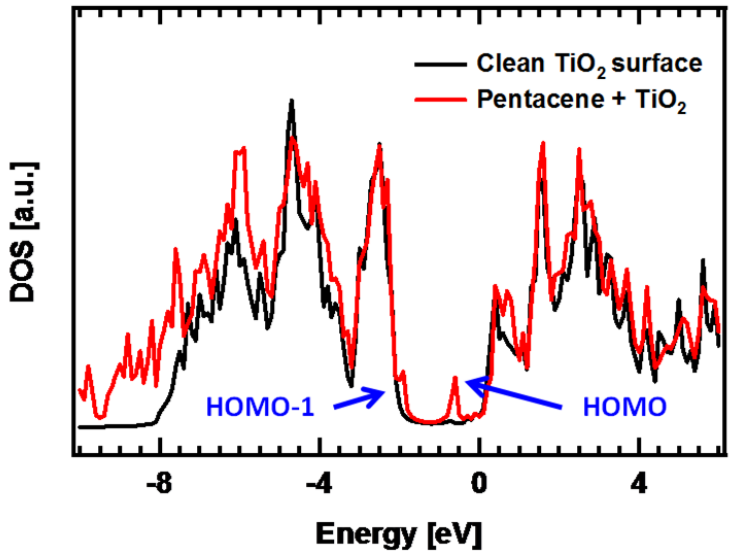

Figure 4.2.2.11.- *Theoretical DOS of the clean and pentacene evaporated TiO_2 surface.* Both the clean and the evaporated VB are very similar, thus indicating a very weak interaction. We observe the appearance of two new states in the band-gap region associated to the HOMO and HOMO-1 molecular orbitals.

We can extract more information from the NEXAFS spectra. The spectrum taken in *p*-polarization in figure 4.2.2.8 shows characteristic additional features of thick pentacene films present at 288.8 and 290 eV. The identification of these peaks has been controversial in the past since they are typically absent or largely shifted in the single layer phases [170]. In any case, they are expected to have a negligible contribution in the NEXAFS spectra when the electric field is parallel to the pentacene long axis as we have observed for s-polarization. Nowadays, from comparison with data and calculations for the case of benzene, there is a general consensus in assigning the peak at 288.8 eV to the σ^* state of the C-H bond while the state at 290 eV probably has a π^* character with relevant contributions from Rydberg states [176]. The energy position of the $\sigma^*_{C\text{-}H}$ state will be affected by the variation of the C-H bond length, apart from substrate induced rehybridization effects. In addition, the pentacene gas phase NEXAFS spectra present no features in the 289 – 290 eV range [171]. Thus, we can consider these NEXAFS resonances as being due to the intermolecular interaction in the pentacene herringbone packing, i.e. to the interaction of the pentacene rim atoms and bonds with the electronic cloud of adjacent molecules. In principle, these electronic states should be only detectable for a monolayer coverage if all molecules were standing-up [177,178] but it has never been reported for a lying-down phase, where the molecule-substrate interaction usually dominates over the intermolecular interaction. In our case, molecules present a weak interaction with the substrate together with a strong side-by-side attraction and molecular tilting. These circumstances allow molecules to develop a bulk-like electronic structure along the stripes, even in a lying-down monolayer phase.

4.2.2.2. Multilayer phase

As we have seen, pentacene forms ordered monolayers of lying-down molecules when deposited on the TiO_2 (110)-(1x1) surface. These molecules have their long axis parallel to the surface and aligned along the [001] direction and present a tilt of 25° around it. These conditions are very promising for the accommodation of additional lying-down molecular layers. In figure 4.2.2.12, we show a set of STM images for different coverages, always above 1 ML. As

we can see in figure 4.2.2.12 a), the STM images corresponding to a nominal coverage of 1.7 ML show a second layer of pentacene molecules whose structures resemble the ones obtained for 1 ML. They preserve the striped morphology and intermolecular spacing along the [1-10] surface direction. The main difference is the appearance of molecular vacancy islands, which are always of one single molecule width and extend along the molecular stripes. We will return to this aspect later. All these results suggest a relatively strong intermolecular attraction both side-by-side and with the molecules underneath which is able to overcome the repulsive head-to-head interaction that drives the stripe spacing.

If we increase the coverage up to a third layer, we observe that molecules start losing the striped morphology growing in squared irregular patches, even if molecules preserve a certain degree of vertical coherence with the monolayer phase (figure 4.2.2.12 b) and c)). This overlayer fragmentation has also been observed for a more "flexible" system as α-sexithienyl on Au (110) [179] where molecules recover the natural herringbone structure (planar orientation in the (120) 6T crystal plane) at 4 ML due to a strain release (mainly rotational) among adjacent bulk lattice cells. This happens even if the second layer is perfectly commensurate with the substrate. In our case, the same mechanism is probably operative both along the pentacene stripes and the molecular axis. In fact, we have to take into account that in order to have a bulk-like structure, not only the lateral coupling of the molecules has to be coherent with the herringbone structure along the [1-10] direction but also molecules stacked along the **c** axis must be tilted with respect the **a**-**b** plane [166]. So some reorientation of the pentacene molecules is needed when the herringbone packing starts to develop as the 8% spacing mismatch observed and the perfect head-to-head azimuthal orientation along the [001] direction are not compatible with the pentacene bulk packing along the **c** axis.

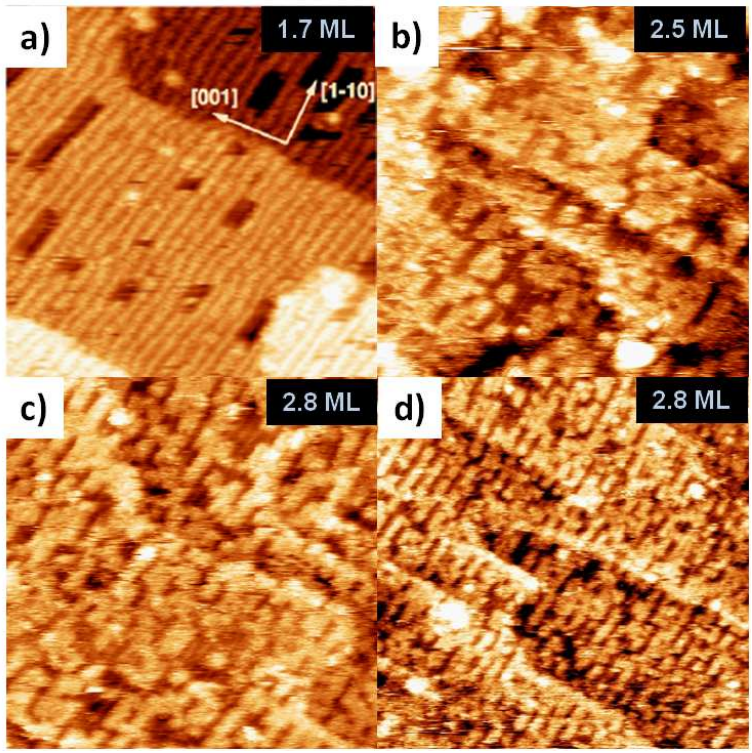

Figure 4.2.2.12.- *Set of STM images for coverages higher than 1 ML*. a) STM image for 1.7 ML of pentacene on the (1x1) surface. We can see the appearance of 1-dimensional vacancy islands running along the [1-10] surface direction. Size: (500 Å x 500 Å), I = 0.14 nA, V = 0.94 V. b) STM image corresponding to 2.5 ML of pentacene molecules. We observe a variation in the growth mode passing from straight stripes to squared irregular patches. We can no longer see 1-dimensional vacancy islands. Size: (500 Å x 500 Å), I = 0.09 nA, V = 1.8 V. c) STM image for a pentacene coverage of 2.8 ML measured just after evaporation. We observe the same growth mode as in b). The surface seems fuzzy probably due to molecular diffusion. Size: (700 Å x 700 Å), I = 0.09 nA, V = 1.8 V. d) STM image obtained for the same surface as in c) but measured 24 hours later. It seems there is a stabilization of the pentacene molecules. Size: (1000 Å x 1000 Å), I = 0.15 nA, V = 1.8 V.

We have also observed by STM a certain molecular stabilization with time, as we can see in figure 4.2.2.12 d). This STM image corresponds to the same surface shown in figure 4.2.2.12 c) but it was taken approximately 24 hours after the deposition. We can see that the STM image of the just evaporated surface presents a fuzzy aspect due to the diffusion of pentacene molecules on

it, while the STM image after 24 hours is much clearer. Besides, it seems that after this time the coverage has increased although it has not been deposited additional material. This is not surprising if we consider that this extra material was already on the surface but it was not visible to the STM due to its diffusion. This change in the STM images suggests a temporal stabilization of the pentacene molecules probably driven by the side-by-side interaction between adjacent molecules and with the molecules underneath. We have not deeply studied this effect as it is out of the objectives of this work. For this reason it remains as an open question worthy to be studied in the future.

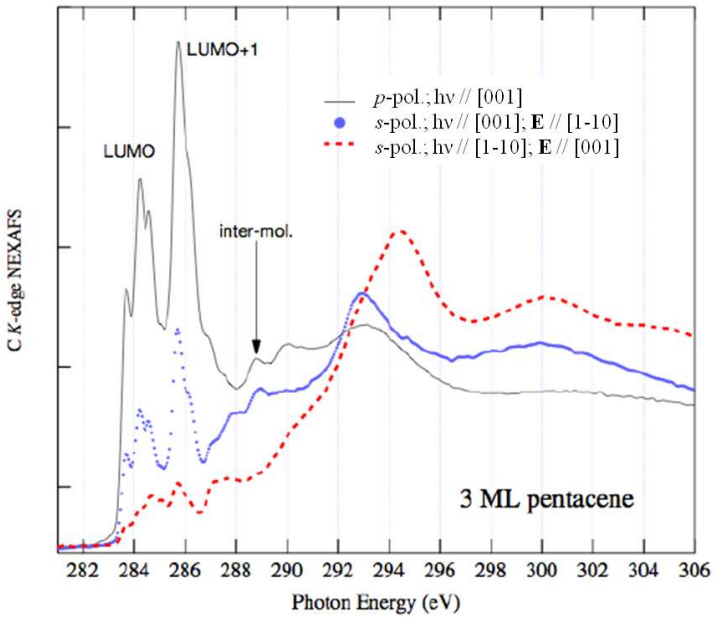

Figure 4.2.2.13.- *Carbon K-edge NEXAFS spectra for 3 ML coverage of pentacene*. As in figure 4.2.2.8, we show three different spectra for three different geometries. Black solid line corresponds to p-polarization, i.e. the electric field is perpendicular to the surface, with the photon beam aligned along the [001] surface direction. Blue dotted line corresponds to s-polarization, i.e. electric field parallel to the surface, again with the photon beam aligned along the [001] direction. Red dashed line is relative to a geometry in which the photon beam is aligned along the [1-10] direction and the electric field is parallel to the surface. With these three geometries we can unequivocally define the adsorption geometry of the pentacene molecules.

This lying-down geometry which remains for a few layers is confirmed by the polarization dichroism observed in the NEXAFS spectra corresponding to 3 ML (figure 4.2.2.13). These NEXAFS spectra present the same dichroic behavior of the monolayer phase, although we observe an increase of the tilt angle to 30°, which is still compatible with the herringbone bulk packing. We also obtain a strong dichroism for *s*-polarization when we change the azimuthal angle but the π^* LUMO intensity does not completely disappear and some residual signal stays when the electric field is oriented along the [001] direction.

From comparison with STM images, we attribute this residual intensity to lying-down molecules which have slightly changed their azimuthal orientation, rather than to uncorrelated clusters of standing-up molecules.

We have not been able to follow with enough resolution the vertical stacking of the pentacene molecules because of their high mobility. In particular, we cannot exclude a close co-facial stacking of the second layer molecules from the overall small tilt angle. This packing structure has been recently claimed to enhance the pentacene photosensitivity to the solar spectrum [180]. In any case, pentacene stripes may favor the charge mobility parallel to the surface even if they present a lying-down structure, thanks to the strong molecular coupling along the stripes in the [1-10] direction, as evidenced by the full development of the bulk-like electronic states from the first layer in NEXAFS spectra. This result is somehow surprising as pentacene [161,181] and the majority of oligomers [182,183] show an enhancement of the intralayer lateral transport when they present a standing-up geometry with respect to the dielectric substrate.

From a technological point of view, this geometry implies a favoring of the charge transfer at electrodes in top-contact architecture. Besides, this geometry overcomes the bad contact resistance of most usual bottom-contact geometry, which requires the chemical modification of the electrode surface by a self-assembled monolayer in order to limit the formation of topological defects at the metal / organic interface [181]. In addition, the organic semiconducting film maintains a good structural coherence thanks to the crystalline nature of the substrate without the need of chemical modification of the gate dielectric surface [184].

4.2.2.3. Molecular vacancy islands

As we have seen in the previous section, the second layer of pentacene molecules grows with the same geometric structure of lying-down molecules arranged in stripes oriented along the [1-10] surface direction thanks to the side-by-side molecular attraction. However, there is an important difference with molecules in the first layer as now pentacene molecules do not "see" O_{br} surface atoms. This gives rise to the disappearance of the H-bonds between molecules and substrate. However, we can expect a higher van der Waals interaction between molecules from both layers. The molecular separation inside stripes is the same as in the first layer and it is given by the substrate periodicity (~ 6.5 Å). We observe the appearance of new structures when the coverage is close to complete the second layer. This new features are "holes" in the molecular layer which are associated to molecular vacancy islands. We can see some of these vacancies in the images of figure 4.2.2.14. These vacancy islands present a minimum width of a single molecule and extend along the [1-10] surface direction. They are due to missing pentacene molecules and they are always grouped forming islands.

The size and position of these vacancy islands are variable and they are influenced by the scanning tip, as we can see in the two consecutive STM images shown in figures 4.2.2.14 a) and b). Both STM images correspond to the same surface area and position (except for a small drift) and they have been acquired consecutively. After scanning with the STM tip, we observe an important increase of the number of vacancy islands (their number is more than double after the scanning) and even of their length. This effect suggests a high molecular diffusion (also evidenced by the fuzzy aspect of the STM images) and a weak interlayer interaction. Probably, the fact that vacancy islands present a single molecular width is due to a certain influence of the neighboring molecules inside the stripes and the absence of a stabilizing H-bond interaction. When one pentacene molecule is removed from the layer creating a vacancy, the neighboring molecules of the same stripe are less coordinated losing one half of the side-by-side interaction and making easier their subsequent removal.

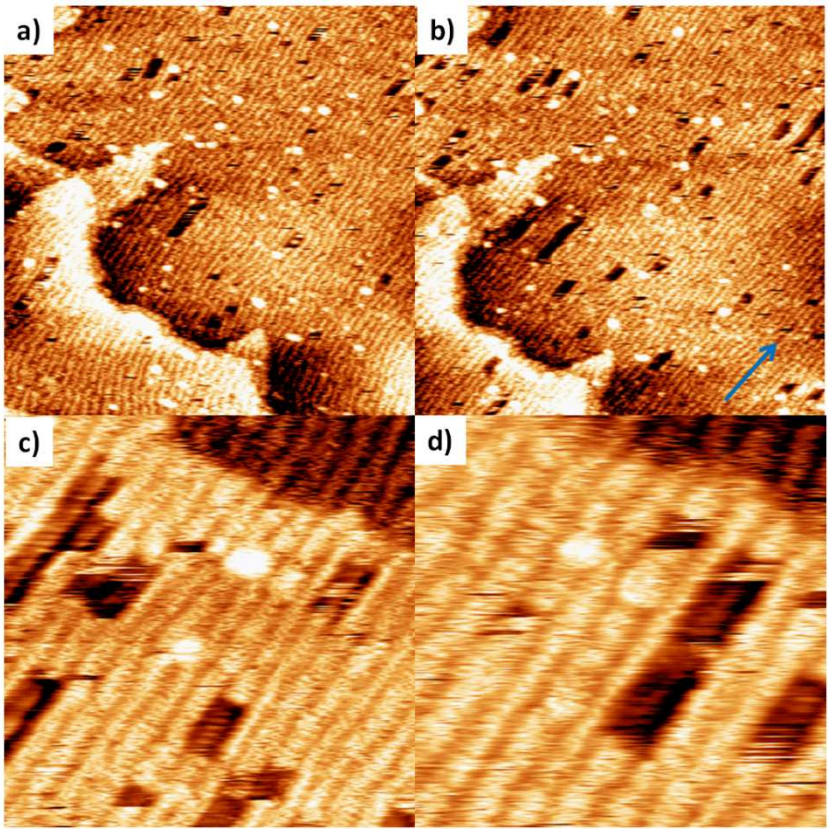

Figure 4.2.2.14.- *STM images of the molecular vacancy islands in the second pentacene layer*. a) and b) Consecutive STM images of the same area of the pentacene / TiO_2 (110)-(1x1) surface. We can see the formation of new vacancies islands after scanning with the STM tip. The [1-10] surface direction is indicated by a blue arrow. Coverage: ~ 1.9 ML. Size: (1000 Å x 1000 Å), I = 0.16 nA, V = 0.9 V. c) and d) Zoom in the previous STM images. We can see streaks inside the islands probably due to pentacene molecules diffusing from the borders. Size: (300 Å x 300 Å), I = 0.14 nA, V = 1.0 V and (200 Å x 200 Å), I = 0.14 nA, V = 0.9 V, respectively.

Also the neighboring pentacene molecules present in the same substrate Ti row (along the [001] direction) are less coordinated. As the interaction between stripes is a head-to-head repulsion, pentacene molecules at the border of a vacancy can move easily as they are no longer constraint because of the presence of the neighboring molecule. In this way, these molecules can diffuse in and out of the stripe into the vacancy as we can see in figures 4.2.2.14 c) and d). If we try to look inside the vacancy islands, we observe that

there are some streaks due to molecular diffusion inside the vacancy. In fact, the stripes which form the borders of the vacancy islands seem to be thinner than the other stripes or even than the same stripes when they are not close to a vacancy. This effect can be explained by this diffusion inside the vacancies as we have a mobile border or stripe and the effect can be a "virtual" decrease of the stripes width. This observation somehow strengths our model based on H-bonds interaction mediated by the O_{br} atoms proposed in the previous section.

If we increase the coverage to a third layer, this kind of vacancy islands disappear as the grown mode changes from stripes morphology to squared irregular patches, as we have seen in the previous section (figure 4.2.2.12 b) and c)). So we can conclude that these structures are characteristic of the second pentacene layer grown on the TiO_2 (110)-(1x1) surface.

4.2.2.4. Thermal stability of the molecular layers

As in the C_{60} case, it is necessary to study the effect of temperature on the molecular layer. For that purpose, we have carried out STM and HAS experiments to evaluate the influence of temperature.

First of all we have monitored by HAS reflectivity the effect of temperature in the growth of pentacene layers. Figure 4.2.2.15 shows a set of HAS curves where we represent the variation of the HAS specular reflectivity (0,0) intensity with coverage in the range of 0.4 – 2 ML, for three different values of the substrate temperature. The black curve represents the (0,0) reflectivity at room temperature, which is taken as reference. As we can see, the (0,0) reflectivity undergoes a fast decrease of intensity followed by an intensity maximum associated to the formation of an ordered monolayer. Beyond this point, the intensity of the (0,0) reflectivity rapidly decreases until vanishing for a coverage of approximately 1.6 ML. This behavior after completing the first monolayer indicates a proliferation of uncorrelated defects, either static or dynamical, like enhanced molecular vibration. If we repeat the measurement with the substrate at 350 K during pentacene deposition (blue curve), we find an improvement of the structural quality of the monolayer as it can be derived

from the peak intensity and width, measured after cooling the sample to RT. If we increase the coverage above 1 ML we observe a gradual decrease of the intensity without the appearance of any additional periodicity. The behavior of the reflectivity intensity at 410 K is shown in the red curve. After the formation of the monolayer, the intensity suffers a small decrease but rapidly reaches a stable value. If we stop the deposition at a constant substrate temperature, we observe that the (0,0) intensity quickly recovers the intensity of the monolayer maximum. As a consequence, no second layer molecules can be accommodated at 410 K on the lying-down pentacene phase, in full agreement with previous findings for the pentacene flat phases on the Au (110) surface [185]. This means that the monolayer phase corresponds to the saturation coverage for a substrate temperature of 410 K.

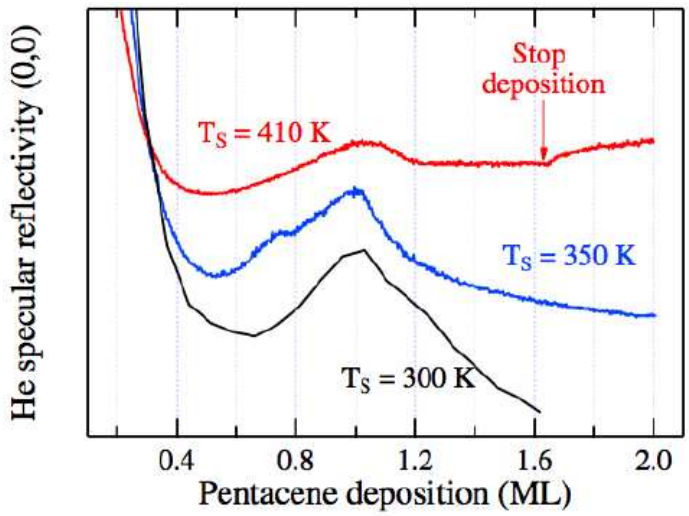

Figure 4.2.2.15.- *Evolution of the He specular reflectivity (0,0) with coverage, for three different substrate temperatures during the deposition*. The black line corresponds to deposition with the substrate at room temperature. Blue and red lines correspond to deposition with the sample at 350 K and 410 K, respectively. We observe a different behavior for the red line, where we find a saturation value related to the formation of 1 ML.

We have also observed the effect of temperature by STM. Figure 4.2.2.16 shows the surface of TiO_2 before and after annealing it at ~ 500 K (coverage

before annealing ~ 2.5 ML). As we can see in figure 4.2.2.16 a), before the annealing molecules form squared irregular patches in the third layer on top of two complete layers of lying-down molecules. If we anneal this surface to ~ 500 K, we observe that the surface morphology has completely changed. Now we observe clusters randomly distributed on the surface, with no internal structure. These clusters present different sizes and heights with values in between 10 – 20 Å of diameter and 1.5 – 4 Å of height. These values are not consistent with complete pentacene molecules, whether flat on the surface or in a standing-up geometry.

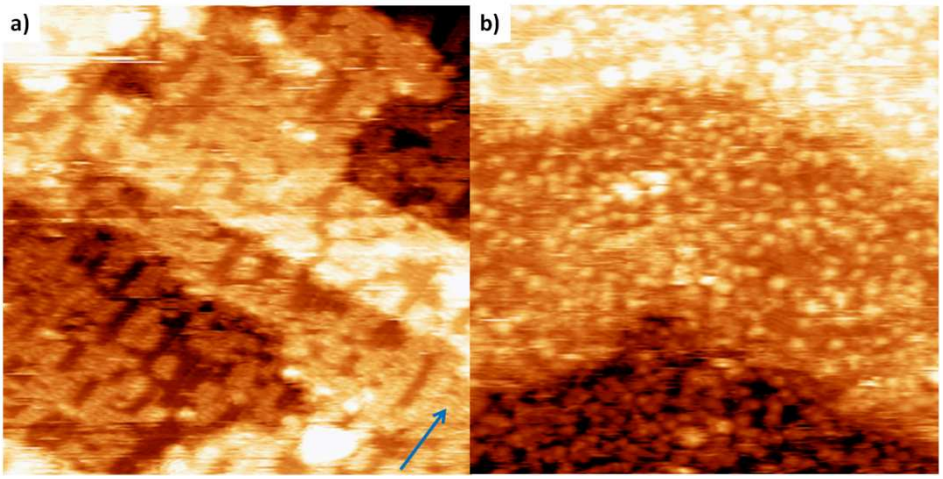

Figure 4.2.2.16.- *STM images before and after high temperature treatment*. a) STM image of a surface covered by 2.5 ML of pentacene acquired before annealing the sample. The blue arrow indicates the [1-10] surface direction. Size: (500 Å x 500 Å), I = 0.09 nA, V = 1.8 V. b) The same sample after annealing it at ~ 500 K. We observe the formation of clusters randomly distributed on the surface. Size: (500 Å x 500 Å), I = 0.095 nA, V = 2.0 V.

Probably they are formed by carbon atoms coming from the decomposition of pentacene molecules, although the annealing temperature is slightly lower than the decomposition one (~ 600 K for the free molecule [186]). We have to take into account that the surface can play a role in the variation of the decomposition temperature. The surface does no longer present a layer by layer growth and the substrate surface is visible under the clusters. We do not

observe evidences of graphene formation after the annealing process as it has been reported for other systems [187]. This is not surprising as pentacene molecules weakly interact with the TiO_2 substrate so any annealing of the surface will lead to desorption of the molecules or to their partial decomposition, without the dehydrogenation of the hydrogen atoms located at the edge of the molecule.

4.2.2.5. Conclusions

In this section we have studied the deposition of pentacene molecules on the rutile TiO_2 (110)-(1x1) surface by means of STM, LEED, HAS and NEXAFS. We have complemented the experimental results with theoretical calculations. We have seen that it is possible to grow a few planar pentacene layers. The adsorption geometry is dictated by the 6.5 Å periodicity of the substrate that perfectly matches the intermolecular spacing along the **a** axis of the pentacene crystals in the thin film phase. The long axis of pentacene molecules is oriented along the [001] surface direction due to the molecule-to-substrate interaction, while the side-by-side attraction (both electrostatic and H-bond) gives rise to the appearance of continuous stripes along the [1-10] direction. Molecules within stripes are tilted by 25° around their long axis. This value is corroborated by DFT calculations which predict a 22° angle. We have also observed that the inter-stripe spacing decreases with coverage due to the head-to-head intermolecular repulsion until reaching a steady value of ~ 17 Å for a complete monolayer. We have proved by NEXAFS resonances that the monolayer phase presents the full development of the pentacene bulk-like electronic states. It is possible to form lying-down molecules structures up to the third layer thanks to the fact that the tilting angle and the monolayer spacing mimics the structure of the pentacene **a-c** crystal planes. We have shown the presence of characteristic 1-dimensional molecular vacancy islands in the formation of the second layer. These islands are very mobile due to the high pentacene diffusion on this surface. Finally, thermal annealing of pentacene layers gives rise to the formation of carbon clusters randomly distributed on the surface and probably due to the partial decomposition of pentacene molecules.

4.2.3. $C_{60}H_{30}$

As we have seen in section 4.2.1, fullerenes, and particularly C_{60}, are among the most promising organic molecules for applications in nanoscience and nanotechnology. Up to now, there are several strategies which can be used for the formation of fullerenes. In this way, they can be created by laser vaporization of graphite [135]*, by electric discharge vaporization of graphite, sooting flames* [188,189]*, by graphite vaporization with resistive heating* [150] *and by cyclodehydrogenation of* Polycyclic Aromatic Hydrocarbons *(PAH´s)* [190-192]*. With all of them it is possible to create different kinds of fullerenes with different size and shape. It is mainly obtained C_{60} but other related fullerenes such as C_{70}, C_{76}, C_{78}, C_{84}, etc. appear in a much lower amount. Nowadays, the most used methodology is graphite vaporization with resistive heating as it allows us to obtain macroscopic amounts of C_{60}. However, the most promising strategy at this moment is the use of PAH´s as precursors as it is possible to obtain fullerenes with the desired size and shape by removing the hydrogen atoms located at their perimeter. This method was successfully tested by Scott et al. for the formation of C_{60} using $C_{60}H_{30}$ as a precursor* [191]*. For this purpose they applied a high power laser to $C_{60}H_{30}$ molecules in gas phase. However, the efficiency of this method is very low as approximately only 1% of the precursors are transformed into C_{60}. Recently, a new strategy has been proposed by our group consisting in using the catalytic properties of certain materials to perform an efficient cyclodehydrogenation of PAH´s* [193]*. In this work we use a platinum substrate, which is known to present catalytic properties at the surface, to efficiently cyclodehydrogenate the precursor $C_{60}H_{30}$ to obtain C_{60}. The biggest advantages of this method are its extremely high efficiency, which is close to 100%, and selectivity. Besides, by changing the precursor molecule to $C_{57}N_3H_{33}$, it is possible to create different fullerenes like triazafullerenes ($C_{57}N_3$). Recently, this methodology has been used by other group to produce larger fullerenes as C_{70} and C_{84}* [152]*.*

In this section, we study the interaction of $C_{60}H_{30}$ with the rutile TiO_2 (110)-(1x1) surface by means of STM, LEED, UPS / XPS and NEXAFS. Additionally, we are complementing the experimental results with theoretical calculations (in progress). In this way we are able to completely characterize the system keeping a double objective in mind. First, we want to explore whether it is possible to fold this molecule to form C_{60}, as in [193]*, or to form graphene on the TiO_2 surface by decomposition of the molecule. As an additional aim this*

molecule could be another example of a large organic molecule with possible applications in Molecular Electronics.

4.2.3.1. Deposition at room temperature

Figure 4.2.3.1 shows a ball-and-stick schematic representation of the flat precursor we have used for this study, $C_{60}H_{30}$. The sixty C atoms are arranged in hexagons and pentagons which compose the three arms of this three-leaved clover shaped molecule. The H atoms are located at the perimeter of the molecule, saturating the dangling bonds of the molecule.

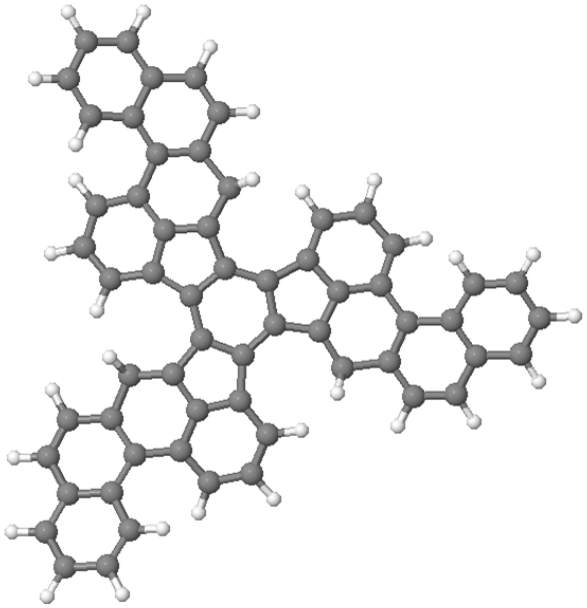

Figure 4.2.3.1.- *Ball-and-stick schematic representation of the $C_{60}H_{30}$ molecule*. Large gray and small white balls correspond to carbon and hydrogen atoms, respectively. As we can see, the molecule presents a three-leaved clover shape.

Figure 4.2.3.2 a) shows a typical STM image for approximately 0.8 ML of $C_{60}H_{30}$ deposited on the TiO_2 (110)-(1x1) surface. The evaporation has been carried out with the sample at room temperature and a rate of about 0.05ML/min.

Under these conditions, even though the coverage is high, we are just able to find some molecules located at the step edges as they act as nucleation sites. These molecules are visualized as bright triangles in good agreement with their known triangular shape when deposited on metal surfaces [154]. This is a clear indication of a flat or almost flat adsorption on the surface. This is also true for the very small amount of molecules fixed on terraces (see fig. 4.2.3.2 b)). We can also observe the presence of many streaks aligned along the fast scanning direction which are usually associated to adsorbates diffusing on the surface. This is a very common behavior when depositing organic molecules on the TiO_2 (110)-(1x1) surface at room temperature, as we are seeing along this thesis. The scan profile of figure 4.2.3.2 c) shows triangular molecules which present borders of approximately 18 Å long. This value is slightly lower than the one observed when these molecules are deposited on Pt (111) (approximately 22 Å) [193]. This difference is not surprising as the interaction with the substrate is very different. Additionally, as molecules are diffusing in our system, the accuracy of these measurements is not very high. We must take into account that even the low amount of fixed molecules presents a fuzzy appearance, making more difficult to measure distances on them. Regarding their height, it is in the range of 1.7 – 2.5 Å depending on its own corrugation and the interaction with the surface. This value is significantly higher than the one observed in ref [193]. This can be understood taking into account two effects. First, we have a structural effect as the interaction between $C_{60}H_{30}$ and TiO_2 is smaller than in the case of Pt. This smaller interaction place the molecule at a higher distance from the surface. Secondly, we have an electronic effect, as the molecular orbitals are decoupled from the surface and protrude out of it.

As we can find a very low amount of fixed molecules and the resolution is not very good due to the diffusion, it is not easy to find out the relative position of the molecule with respect to the main crystallographic directions of the surface. The molecule shown in figure 4.2.3.2 b) seems to be fixed on the surface with one of its corners pointing along the direction of the surface rows, that is, along the [001] surface direction. The exact position of the corners with respect to the O_{br} rows and Ti rows is not clear from STM images as molecules present a fuzzy appearance. In any case, this nucleation position would be influenced by the presence of surface point defects such as O_{vac} as they are probably responsible for the stabilization of $C_{60}H_{30}$ at RT. In order to be able to

know the exact relative position of molecules with respect to the surface high-resolution STM images are required. Thus, we have observed clear evidences of a low interacting system, with molecules probably in a physisorption state.

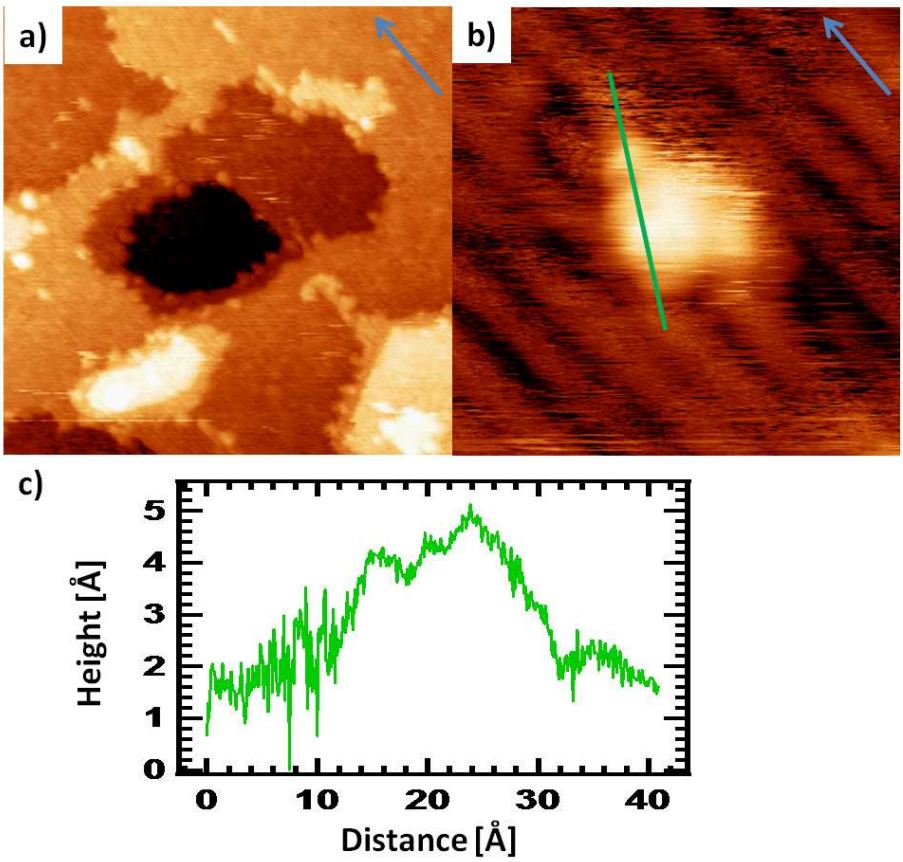

Figure 4.2.3.2.- *Deposition of $C_{60}H_{30}$ at room temperature*. a) STM image of the TiO_2 (110)-(1x1) surface after evaporation of approximately 0.8 ML of $C_{60}H_{30}$ at RT. We observe some molecules fixed at the step edges and a fuzzy background, indicating molecular diffusion. Size: (500 Å x 500 Å), I = 0.07 nA, V = 1.8 V. b) STM image of a $C_{60}H_{30}$ molecule fixed on a terrace. It presents the expected triangular shape although the borders appear fuzzy because of the possible movement of the molecule as a consequence of the interaction with the scanning tip. Size: (50 Å x 50 Å), I = 0.13 nA, V = 1.45 V. c) Scan profile of one of the sides of the molecule. We can see that it presents a side of approximately 17 Å and a height of around 2.5 Å, as it corresponds to the free molecule.

4.2.3.2. Temperature induced molecular transformation

An important molecular transformation takes place when the sample temperature is increased above 375 K. Beyond this temperature, molecules have enough thermal energy to interact with the substrate, changing from a physisorption to a chemisorption state, getting fixed to the surface and making possible their "visualization" with the STM. This is evident from the STM images shown in figure 4.2.3.3. For 20% lower nominal coverage than in the case of figure 4.2.3.2, we observe a much higher amount of molecules randomly fixed on the surface terraces after the annealing treatment. This means that those molecules were already there when the evaporation was done at RT but it was not possible to "see" them because of their diffusion. This is in good agreement with the fact that we observed spikes in the STM images taken RT. A similar fixing effect upon annealing has also been observed for $C_{60}H_{30}$ deposited on Au (111) [154].

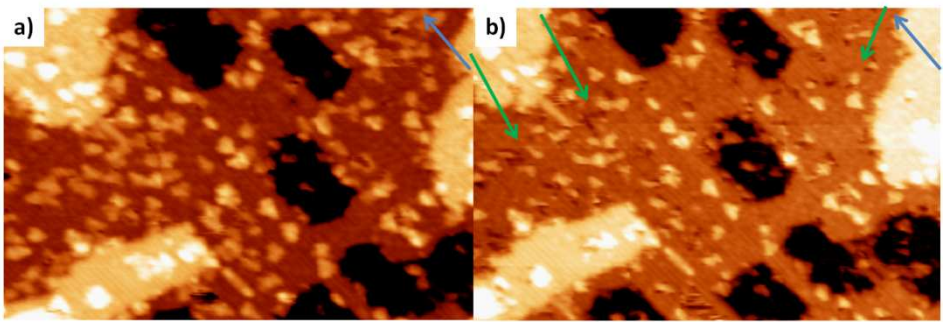

Figure 4.2.3.3.- *STM images after annealing the system at a temperature in the range of 400 – 450 K.* a) STM image where we can see an increase in the "visible" material after the annealing even though the coverage is lower than in figure 4.2.3.2 (now the coverage is approximately 0.6 ML). Molecules are randomly fixed on the surface probably because of a change in the bonding state from physisorption to chemisorption. Size: (500 Å x 330 Å), I = 0.20 nA, V = 1.6 V. b) Consecutive STM image of the same area of the surface. As we can see, the tip has removed some of the molecules (some of them are marked with green arrows), indicating that although they are chemisorbed on the surface, the interaction is low. Size: (500 Å x 330 Å), I = 0.15 nA, V = 1.45 V.

A plausible explanation for this molecular stabilization is that they have undergone a partial dehydrogenation. If this is so, the molecule should present free bonds ready to interact with the surface. We do not see any long range order of the molecules either by STM or LEED. In the last technique we just observe an increase of the pattern background associated to lack of order. Although the interaction between the molecules and the substrate has changed from a physisorption to a chemisorption state, it is still weak. This can be deduced from figures 4.2.3.3 a) and b) where it is shown two consecutive STM images measured on the same region. We can appreciate a decrease in the number of molecules on the surface, which have been removed during the tip scanning above the surface. Some of them are marked by green arrows.

As molecules are now fixed on the surface, we can study their relative orientation with respect to the substrate. Figure 4.2.3.4 shows two high-resolution STM images of $C_{60}H_{30}$ molecules after the annealing treatment. As we can see in figure 4.2.3.4 a), there is a preferential two-fold molecular orientation where molecules present one of the corners of the triangle oriented along the [001] surface direction. However, in some occasions it is possible to see molecules oriented with one of their corners pointing along the [1-10] surface direction, as we can see in figure 4.2.3.4 b). This is probably due to an accumulation of surface defects which affect the molecular orientation. In both cases, the borders of the molecules are sitting on top of the black rows of the surface (marked with dotted green lines), i.e. the O_{br} rows. On the other hand, we can say nothing about the relative position of the molecules along the [001] surface direction as we do not have atomic-resolution STM images. However, in some cases, defects, such as the substrate topography, force the molecule to present a different register with respect to the surface, as we can see in the molecule marked with a yellow arrow in figure 4.2.3.4 a). In this case, the molecule is in between two steps and it is forced to shift half a unit cell along the [1-10] direction, but it still keeps the azimuthal orientation with respect to the other molecules. This is another indication of low molecule-substrate interaction as the surface topography is more important in the final molecular position than the registry with the substrate.

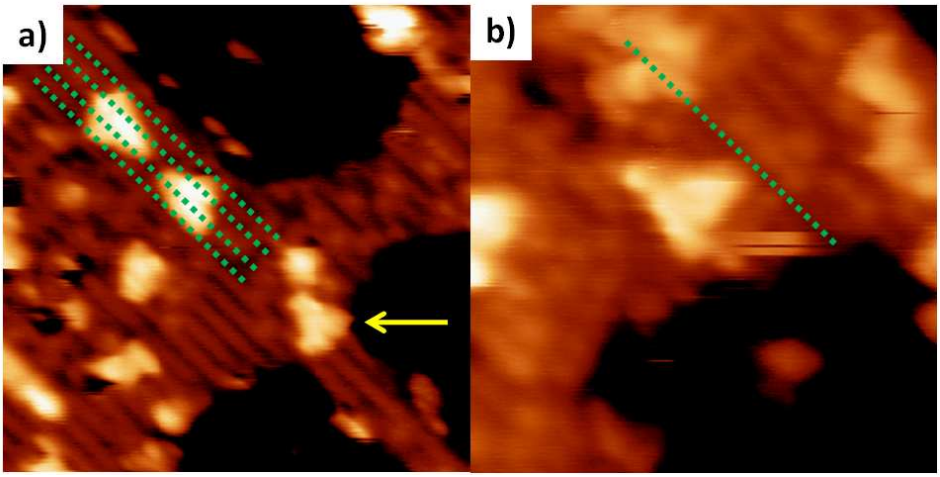

Figure 4.2.3.4.- *Orientation of the $C_{60}H_{30}$ molecules with respect to the surface*. a) High-resolution STM image of the $C_{60}H_{30}$ system after annealing at 400 K for a coverage of approximately 0.6 ML. Green dotted lines indicate the position of the O_{br} rows of the surface. As we can see the corners of the molecules are sitting on top of them unless the orography forces a different register with the substrate, as in the molecule indicated by a yellow arrow. We observe a preferential orientation of the molecules, with one of their corners pointing along the [001] surface direction. Size: (150 Å x 150 Å), I = 0.15 nA, V = 1.76 V. b) STM image of a different area. We observe a different orientation of the molecule, with one of the corners pointing along the [1-10] surface direction. This orientation is much less common and it can be due to surface defects. Size: (100 Å x 100 Å), I = 0.20 nA, V = 1.45 V.

We can see a model for both molecular orientations in figure 4.2.3.5. The model is the result of superimposing the molecule on the surface without taking into account any interaction between both. On the left we present the model of the preferential molecular orientation where one of the corners of the molecule is pointing along the [001] surface direction. As we can see, the two other corners of the molecule are "touching" the O_{br} rows while the first corner is sitting on top of the Ti_{5f} rows. On the right, we present the model for the less common case in which the molecule is oriented with one of its corners pointing along the [1-10] surface direction. In this case, one of the sides of the molecule, which is parallel to the [001] direction, is sitting on top of the O_{br} rows as well as the opposite corner. In both cases we can say nothing about the registry with the surface along the [001] direction. However, it seems the molecule tries to maximize the number of benzene rings centered on top of Ti_{5f}

atoms, as we can see in the left panel of figure 4.2.3.5. On the other configuration (right panel), we suggest a maximization of the number of O_{br} atoms interacting with the benzene rings.

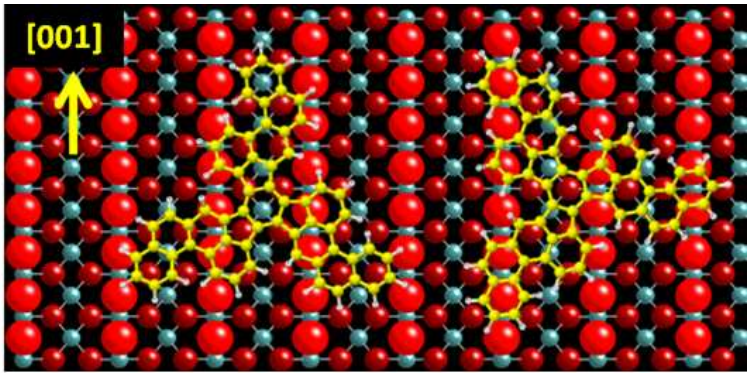

Figure 4.2.3.5.- *Ball-and-stick model of the adsorption orientations of the molecules with respect to the surface found after the analysis of the STM images*. Yellow and white atoms in the molecule correspond to C and H atoms, respectively, while surface red and blue atoms correspond to O and Ti atoms, respectively. The election of the color of C atoms has been done attending to visualization criteria. The larger the surface atoms the closer to the surface. In these simple models, the molecules are just superimposed on the surface without taking into account relaxations. Both molecule and substrate are scaled. On the left we represent the most common orientation where one of the corners is pointing along the [001] surface direction. As we can see, the two other corners "touch" the O_{br} rows (bright large red balls). On the other hand, we have the less common orientation where one of the corners is pointing along the [1-10] surface direction. This model is shown on the right. As we can see, all the external benzene rings of the molecule fall on top of O_{br} rows.

The size and shape of the molecules after this soft annealing is basically the same as in the previous case, as we can see from the scan profile shown in figure 4.2.3.6. The length of the sides of the triangles is approximately 22 Å while the height is around 2.5 Å. Both values are in good agreement with the ones obtained before the annealing, taking into account that the dimension of the molecule depends on the tunneling bias. We do not observe any evidence of shape transformation after the annealing as the molecule keeps its triangular shape, corroborating that probably is sitting flat on the surface.

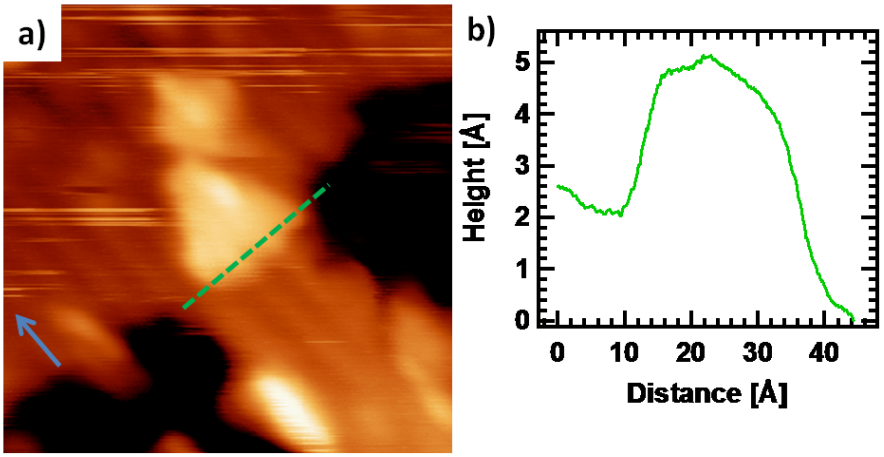

Figure 4.2.3.6.- *Molecular dimensions after the annealing at 400 K*. a) High-resolution STM image of a $C_{60}H_{30}$ molecule. The dimension are very similar to the ones obtained before the annealing taking into account that they depend on the tunneling bias, as we will see later. Blue arrow indicates the [001] direction. Size: (80 Å x 80 Å), I = 0.15 nA, V = 2.1 V. b) Scan profile of the molecule, as indicated by the green dashed line.

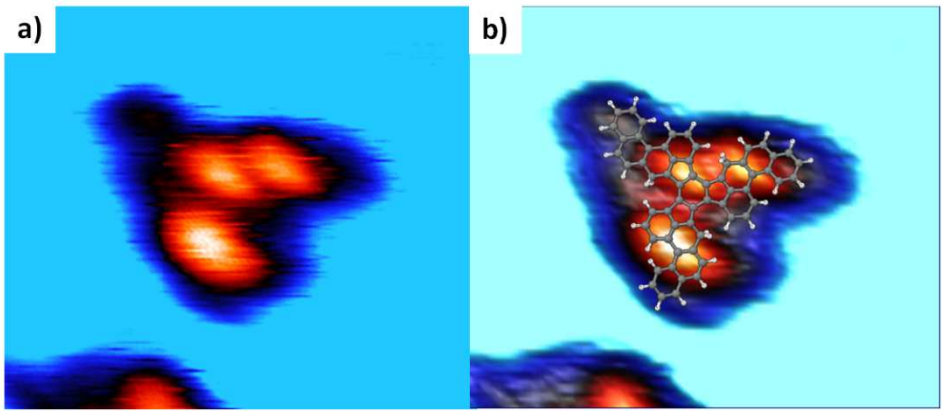

Figure 4.2.3.7.- *High-resolution STM images of the $C_{60}H_{30}$ molecule*. a) 2-dimensional representation of the molecule. We can distinguish three bright bumps inside the molecule. b) 3-dimensional representation of the same molecule. We do not observe any correspondence between the bright features and the atomic positions. For these reason we attribute them to the molecular orbitals. Size: (43 Å x 37 Å), I = 0.13 nA, V = 1.3 V.

Under high-resolution conditions of the STM tip we can distinguish some features inside the molecules. As we can see in figure 4.2.3.7, it is possible to distinguish three bright bumps inside the molecule. These features are probably associated to molecular orbitals. If we superimposed the scaled model of the molecule, we cannot establish any correspondence between these features and the molecular geometry. The presence of three bright bumps inside the molecule is in good agreement with the previous observations by Otero *et al*. where these features were assigned to the short-arms of the molecule [154]. On the other hand it seems that the visualized molecules present a certain helicoidal aspect when imaged with the STM. This is in good accordance with the own helicoidal shape of the free molecule due to the shape of its arms. Looking at the orientation of the helicoidal shape it should be possible to know the face of the molecule which is in contact with the surface. Due to a lack of high-resolution STM images on this system, we have not been able to perform a complete analysis on this effect as the one carried out in [154], but in principle there should be the same amount of molecules adsorbed on both faces and no differences in the adsorption orientation should be found because of the two-fold symmetry of the surface.

Another curious effect of these molecules when deposited on the TiO_2 (110)-(1x1) surface is the dependence of the appearance of some molecules with the bias applied during the STM acquisition. Figure 4.2.3.8 shows an STM sequence of consecutive STM images taken under the same experimental conditions. The only difference among images is the tunneling bias. It is possible to observe a certain range of voltages were the molecule disappears. Starting with a bias of 2.1 V, we observe the typical triangular shape expected for this molecule. As we decrease the bias, we observe a decrease in the size of the molecule until it completely disappears for voltages lower than 1.2V, meaning that we are tunneling through its energy gap into the sample. Since this process is completely reversible we can discard any interaction effect between molecule and tip. This could be an indication of the absence of chemical bonds or new induced electronic states in the semiconductor gap. However, this effect, although quite general, does not affect to all $C_{60}H_{30}$ molecules. We have been able to find some molecules which do not undergo these shape changes upon variation of the applied bias. An example is shown in figure 4.2.3.9. When we vary the bias in the same range of the previous case, the molecule

does not disappear. Taking into account that this difference is observed for molecules measured in the same experiment, we can discard any preparation or tip effect. Probably this difference is due to a local change in the DOS of the molecule driven by the presence of defects.

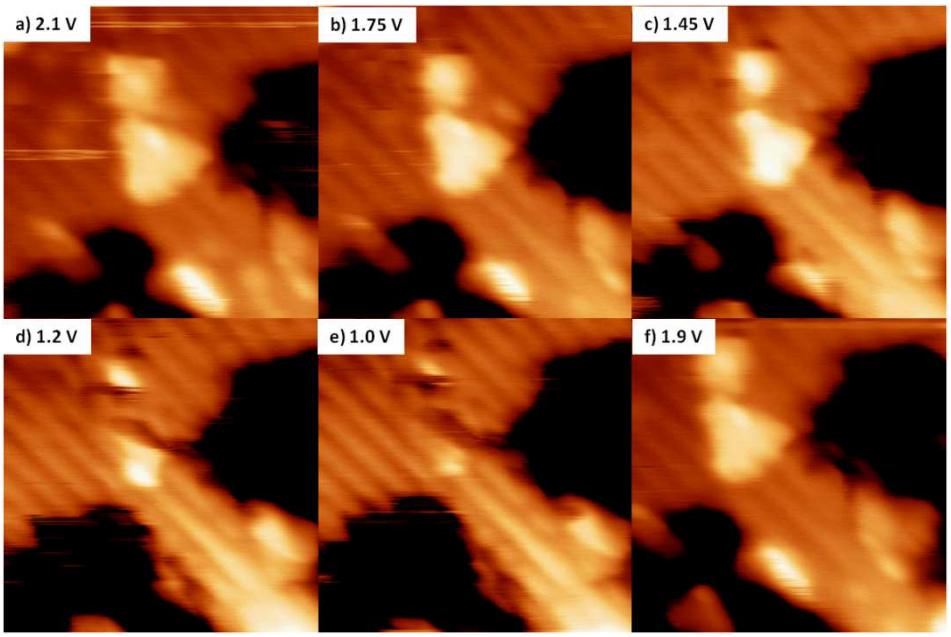

Figure 4.2.3.8.- *Dependence of the molecule shape with the tunneling bias*. In this set of STM images we can see how the size of the molecule decrease as we reduce the tunneling bias until its disappearance for voltages lower than 1.0 V. This effect is completely reversible and we have observed it in several molecules. We can interpret it as being tunneling through the gap of the molecule directly into the substrate states. Size: (80 Å x 80 Å), I = 0.15 nA. The tunneling bias is indicated in each image.

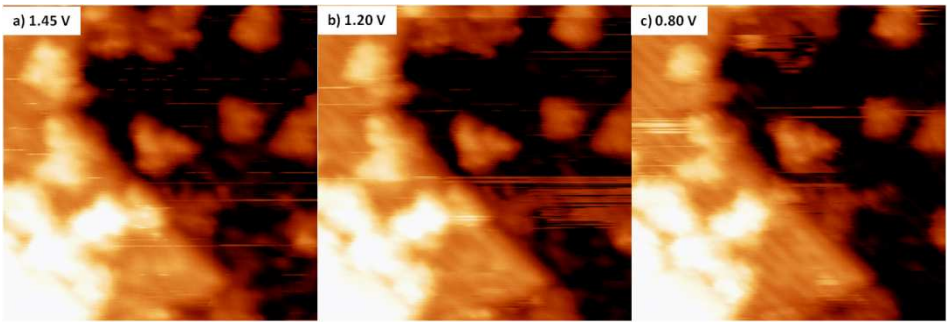

Figure 4.2.3.9.- *Set of STM images of another molecule varying the bias*. As we can see we can find some cases where molecules do not present any variation with the bias. This can be due to a higher interaction with the substrate driven by surface defects. Figures 4.2.3.8 and 4.2.3.9 where measured in the same STM session. Size: (150 Å x 150 Å), I = 0.15 nA. Voltages indicated in each image.

As we have seen by STM, molecules seem to be adsorbed flat and parallel to the surface. However, STM is not the most indicated technique to study the relative orientation of the molecules with respect to the surface. For this purpose we have carried out NEXAFS measurements on the C K-edge for two polarizations: p and s-polarization. We show the results in figure 4.2.3.10. When the electric field is perpendicular to the surface (p-polarization, black curve) we observe a very pronounced peak in the π* region, together with a smaller one (peaks **A** and **B** in figure 4.2.3.10, respectively). The asymmetry of peak **A** suggests a double contribution probably from the LUMO and LUMO+1 states, while peak **B** could be associated to the LUMO+2 state. However, there are no peaks in the σ* region. On the other hand, when the electric field is parallel to the surface (s-polarization, red curve) the peak in the π* region nearly disappears while new states in the σ* region appear (peak **D**). This behavior is consistent with a flat adsorption of the molecule on the surface. Curiously, a new small peak appears at approximately 288.1 eV for s-polarization (peak **C**). The nature of this peak is uncertain as this molecule has been deposited on surfaces for the first time by our group [193]. For this reason there is no scientific background to be used for the interpretation of this data. However we can compare our experimental data with results obtained for similar systems such as C_{60} or aromatic molecules. If we contrast them with the NEXAFS spectra obtained for C_{60} on this surface (see section

4.2.1), we observe that C_{60} presents a peak at approximately 288.1 eV, which has been associated to the LUMO+3. However this peak is present for both polarizations while for $C_{60}H_{30}$ it only appears for s-polarization. Therefore, we have to think about another possibility. If we compare them with the aromatic molecules data, we observe a peak at 288.8 eV which is associated to the σ* state of the C-H bonds [195-197]. This result is compatible with our measurements as it would imply that when the electric field is parallel to the surface we are able to detect the σ* state of the C-H bonds of the molecule, which would then be also parallel to the surface. The small variation in the peak position can be understood if we take into account that our molecule is more complex as it is formed by benzene rings but also by pentagons. This interpretation of the peak is also compatible with the fact that this peak is not observed for C_{60}, as C_{60} does not have H atoms.

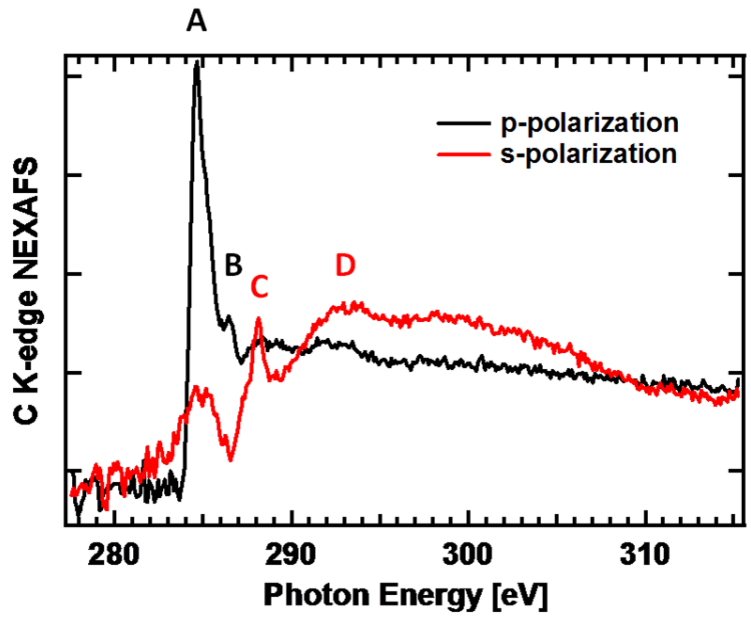

Figure 4.2.3.10.- *C K-edge NEXAFS spectra for the $C_{60}H_{30}$ molecule before annealing*. Black and red curves correspond to p and s polarizations, respectively. The clear variation with the polarization is an indication of flat molecules on the surface. The peak at approximately 288 eV observed for s-polarization could be assigned to C-H bonds in the plane of the molecule.

4.2.3.3. Study of the thermal stability

As we have mentioned in the introduction, $C_{60}H_{30}$ may undergo a transition to C_{60} upon dehydrogenation when annealed at high temperatures. As an example, when this molecule is deposited on Pt (111) and the substrate is annealed at approximately 725 K, the C-H bonds are cleaved and new C-C bonds are created, forcing the molecule to fold forming a new C_{60} molecule. For this process to take place, there are two crucial points that must be considered. First of all, and probably the most important point, is the substrate where these molecules are deposited. As the molecule is undergoing a dehydrogenation process, i.e. the removal of the C-H bonds, it is of major importance to use a substrate with catalytic properties, like Pt. In this way we will be able to considerably reduce the annealing temperature needed to overcome the energy barrier of the dehydrogenation process. Secondly, we need a strong substrate-molecule interaction in order to avoid desorption of the molecules during the annealing. As an example, Otero *et al.* showed that this dehydrogenation process does not work on less reactive materials such as Au (111) and only partially works on Cu (111) [154]. The question is, will it work on the TiO_2 (110)-(1x1) surface? In principle, this surface accomplishes with one of the two conditions mentioned above, as it is well known that O_{vac}´s present a catalytic behavior as they are able to dissociate H_2O into OH^- + H^+ [102-104,107,198-200]. However, it is also true that, as we have seen for other molecules deposited on this surface, the substrate-molecule interaction is usually weak.

For this aim we have carried out a study of the thermal stability of these molecules by annealing the deposited substrate to five different temperatures in the range 650 – 950 K. For the sake of clarity we will show four of these cases. Figure 4.2.3.11 shows two STM images taken after annealing the substrate to approximately 650 – 750 K (coverage ~ 0.7 ML). After this annealing, we still find material homogeneously distributed on the surface. The shape of these features has changed to more irregular ones, although we can find some rounded features as the ones marked with lines in figure 4.2.3.11 b). These bright rounded features present mainly three sizes (see histogram in figure 4.2.3.12). Some have diameter values below 20 Å and an apparent height of approximately 2.5 Å as we can see in the scan profile of figure

4.2.3.11 c). Others present a diameter of approximately 24 Å and an apparent height of 5 Å, as it is shown in figure 4.2.3.11 d). Finally, we can observe bigger features with a mean diameter of approximately 32 Å and a mean height oscillating between 3 and 6 Å. The first of these features resemble the ones observed after annealing at 700 K the C_{60} / TiO_2 system (see section 4.2.1.3). They present very similar values for the diameter and the height so they could be related to C_{60} molecules formed upon the partial / total dehydrogenation of $C_{60}H_{30}$ molecules. In fact, the values are in good agreement with the ones obtained by Otero et al. after annealing the $C_{60}H_{30}$ precursor above 700 K [154,193]. However, the number of these features is small, thus indicating a low efficiency in the dehydrogenation process, as it happens on Au (111) [154]. This low efficiency could be associated to the low O_{vac} density present in the surface. The larger bright features can be also associated to carbon-like clusters or even partially formed fullerenes, maybe of higher order than C_{60} (C_{70}, C_{84} …). It can happen that two close $C_{60}H_{30}$ molecules react together forming a carbon-like amorphous cluster or a higher order fullerene.

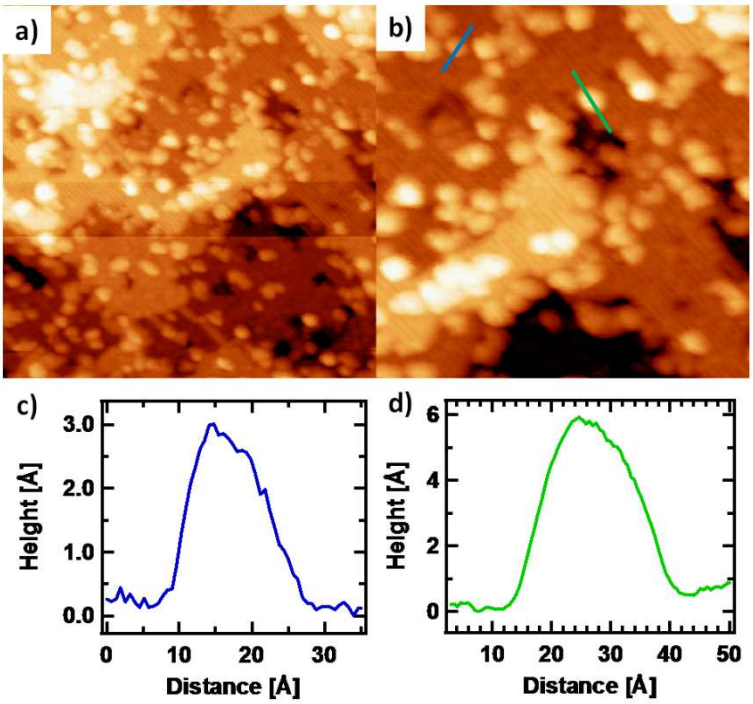

Figure 4.2.3.11.- *$C_{60}H_{30}$ / TiO_2 system after annealing at 650 – 750 K.* a) STM image of the surface. We observe the presence of bright features randomly distributed on the surface. They present different irregular shapes although some rounded features are observed. Size: (500 Å x 500 Å), I = 0.11 nA, V = 1.9 V. b) In this STM image we can observe some of these bright rounded features. Size: (300 Å x 300 Å), I = 0.11 nA, V = 1.9 V. c) and d) Blue and green lines correspond to scan profiles on two of them. The dimensions of the features do not match with the expected values for C_{60}.

Figure 4.2.3.13 shows two of these bright features which present a more irregular shape. The one marked with a blue arrow presents an irregular triangular shape, similar to the one observed for open $C_{60}H_{30}$ molecules although they are slightly larger (side ≈ 27 Å, height ≈ 3 Å). The irregular shape could be due to a partial dehydrogenation of the molecule inducing a shape transformation. The difference in the length on the molecule can be attributed to a tip effect or to a partial dehydrogenation of one side of the molecule. On the other hand, we have the irregular feature marked by the green arrow. This shape is compatible with a partial folding of the molecule where two of the arms are folded and the third one is still flat (the small protuberance on the left side of the molecule). This kind of partial molecular folding has been also observed by Otero *et al*. and it has been explained as an intermediate state previous to the complete folding of the molecule [154].

Thus, at this annealing temperature we find some evidences of partial folding of the $C_{60}H_{30}$ precursors giving rise in some cases to bright features very similar to those found after annealing C_{60} at equivalent temperatures. However, we cannot discard the formation of carbon-like clusters with an internal structure which should not be very different from the one of the precursors as the annealing temperature is not high enough to completely decompose the molecule.

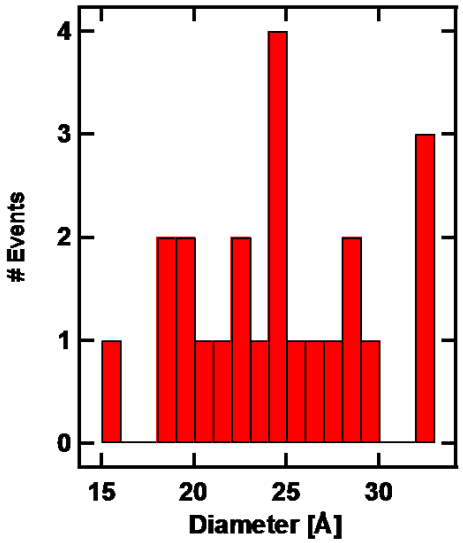

Figure 4.2.3.12.- *Histogram of the diameter of the bright features observed by STM*. There are three main diameters. We have features with a lateral size below 20 Å, others with a diameter of approximately 24 Å and some with diameters larger than 30 Å. Taken from figure 4.2.3.11 b).

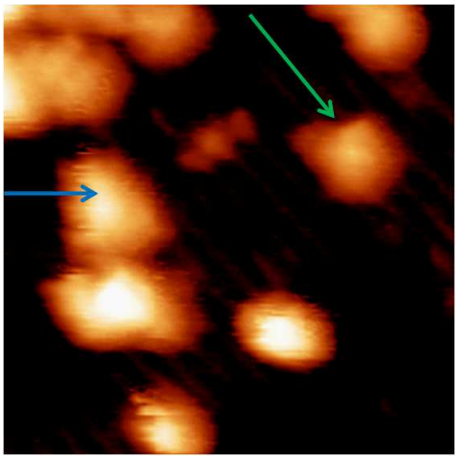

Figure 4.2.3.13.- *STM image showing features with different shapes after annealing at around 700 K*. Apart from the round shape features, we observe some with an irregular triangular shape (blue arrow) and others with almost round shape but presenting a protuberance in one of the sides (green arrow). The latter may be associated to partially folded molecules, with one of their arms still flat. STM parameters: (110 Å x 110 Å), I = 0.11 nA, V = 1.9 V.

If we increase the annealing temperature to 750 – 800 K, we observe again bright features randomly distributed on the surface (figure 4.2.3.14 a)). These features present irregular shapes and sizes, as in the previous case. In fact, as we can see in figure 4.2.3.14 b), we can find some features which still present the characteristic triangular shape of $C_{60}H_{30}$ even after the annealing. When we trace a profile on it (figure 4.2.3.14 c)), we observe that the values obtained for their side and apparent height are identical to the ones obtained for $C_{60}H_{30}$ when annealed to 400 – 450 K. This means that some molecules seem to remain unaltered up to 800 K.

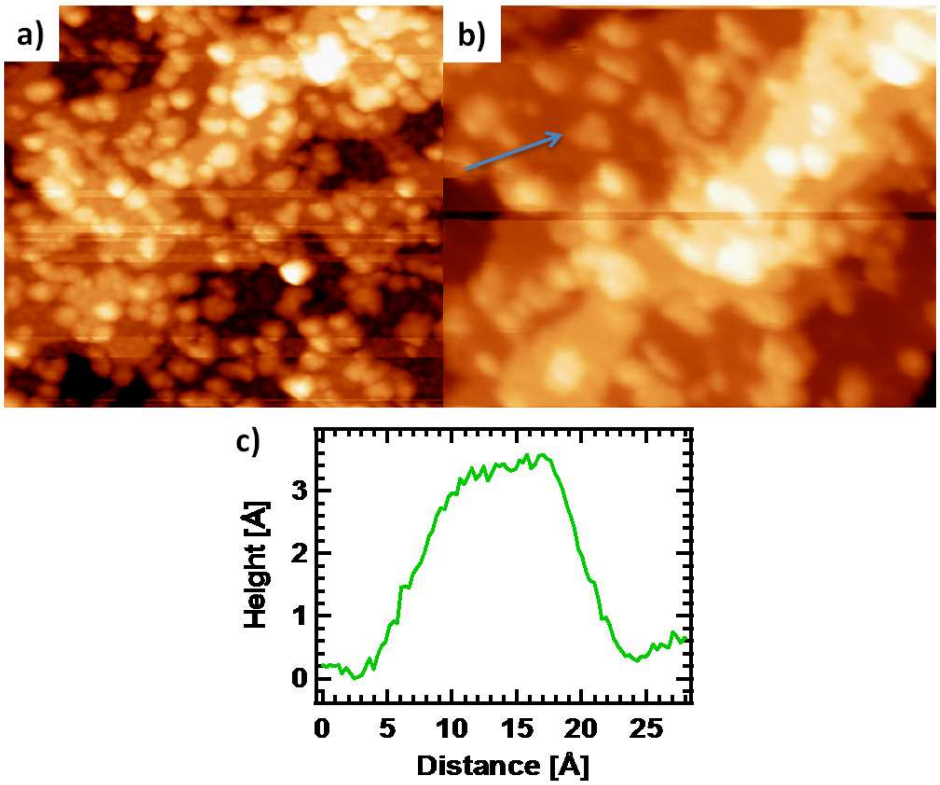

Figure 4.2.3.14.- *$C_{60}H_{30}$ / TiO_2 system after annealing at 750 – 800 K.* a) STM image of the surface. We observe the presence of bright irregular carbon clusters randomly distributed on the surface. Size: (500 Å x 455 Å), I = 0.12 nA, V = 1.6 V. b) In this STM image we can observe a triangular bright feature which resembles a $C_{60}H_{30}$ molecule. Size: (150 Å x 120 Å), I = 0.12 nA, V = 1.6 V. c) Green line corresponds to a scan profile on it. The dimensions correspond to the ones obtained before the high temperature annealing.

Figure 4.2.3.15 shows the NEXAFS spectra for less than 1 ML of $C_{60}H_{30}$ on the TiO_2 (110)-(1x1) surface after annealing at 750 – 800 K. We represent four curves which correspond to four different angles between the electric field of the incoming photon beam and the surface. We observe some resonances in the π* region for p-polarization which stem for s-polarization. This dichroism indicates whether a non-planar geometry of the C-C bonds on the surface, i.e. molecules in a partial folded configuration, or different orientations of the C-C bond associated to 3-dimensional clusters. According to the STM images, both possibilities seem plausible. We also notice that the C-H state at 288 eV previously observed for s-polarization has completely disappeared for all the geometries tested after this annealing. This is a clear indication of dehydrogenation of the $C_{60}H_{30}$ molecules but as the NEXAFS spectra present a dichroic behavior, is not compatible with the fully-formation of C_{60} molecules as they present a rotational symmetry. Therefore, we can assign these bright features observed by STM to carbon-like clusters coming from the reaction of $C_{60}H_{30}$ molecules or to partially formed fullerenes, as in the previous temperature. A new feature emerges at approximately 290.5 eV, just at the beginning of the σ* region. This peak appears for all geometries and its intensity is more or less stable. Its origin can be associated to carbonyl species formed on the surface as a consequence of the interaction of dehydrogenated molecular C atoms with O atoms from the surface, probably O_{br} atoms [201].

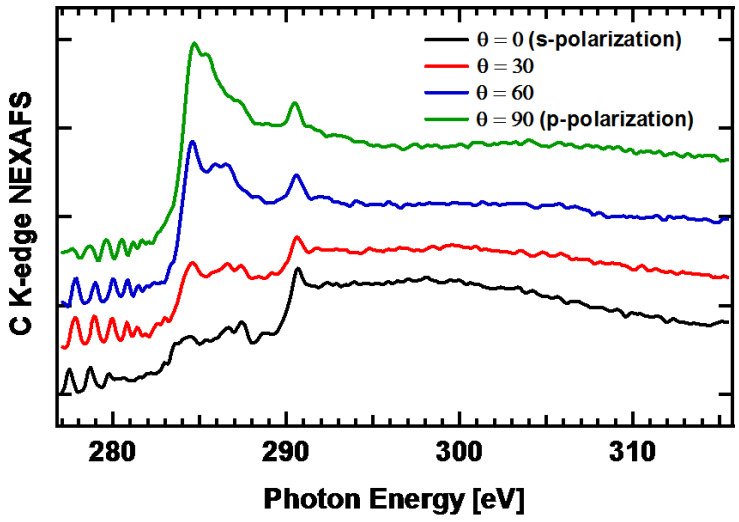

Figure 4.2.3.15.- *C K-edge NEXAFS spectra for the molecule after annealing at 750 – 800 K*. We observe four curves which correspond to four different angles between the electric field of the incoming beam and the surface, where θ = 90° means normal to it (p-polarization). After the annealing we still observe dichroism with the angle meaning that we do not have spherical symmetries in our system (we have not formed fullerenes). However, the C-H bond peak has disappeared indicating the dehydrogenation of the molecule. Probably the molecule has decomposed to form the carbon-like clusters that we observe by STM. A new peak at 290.5 eV appears for all geometries. This peak is related to carbonyl species.

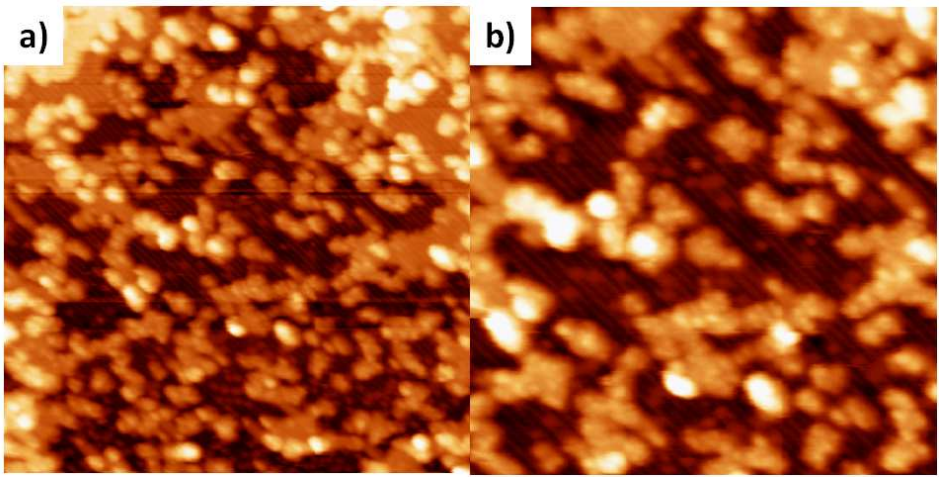

Figure 4.2.3.16.- *STM images after annealing the system at approximately 850 K*. We observe the formation of C-like islands probably coming from the coalescence of different clusters. These islands present inner structure but it is not related to C_{60}. Θ < 1 ML. Size: a) (500 Å x500 Å), I = 0.13 nA, V = 1.6 V. b) (300 Å x 300 Å), I = 0.13 nA, V = 1.6 V.

Figure 4.2.3.16 shows two STM images of the surface of TiO_2 after deposition of less than 1 ML and annealing at approximately 850 K. In both images we can observe the bright Ti_{5f} rows of the TiO_2 surface and some bright irregular islands on it. These islands seem to be composed by the union of many small clusters, as if they had diffused on the surface until coalescence. In fact we can distinguish some internal structure which probably has a topographical character. We think so because the appearance of these features does not change when we vary the tunneling bias between 2.1 and 1.1 eV (range in which we observed significative shape changes on the open molecule) as we can see in the set of consecutive STM images shown in figure 4.2.3.17. However, it is also true that this voltage range is small. The dimensions of

these bright islands are diameter ~ 10 Å and apparent height ~ 4 Å, while the bright round features on top of them present a much lower apparent height (~ 1 Å). These values could be associated to C_{60} molecules, with the bright round features on top of the islands being fullerenes on a second layer. This would explain the lower apparent height they exhibit. In fact, we can find isolated round bright features which present a very similar diameter (~ 18 Å) and height (~ 2.5 Å) to the ones observed for C_{60} molecules after annealing at the same temperature. Additionally, they exhibit an inner structure that resembles the one observed for fullerenes (figure 4.2.3.18) [202]. This result could suggest the formation of some fullerenes upon the dehydrogenation of $C_{60}H_{30}$.

As we have seen, there are some indications of fullerenes formation upon dehydrogenation of $C_{60}H_{30}$ but if we want to assert it, further complementary experiments are mandatory. Until these other experiments are carried out, we cannot discard a carbon-like nature for these islands. These results are very similar to those obtained after annealing the same precursor on low reactive metal surfaces as Au and Cu, thus indicating that TiO_2 presents a very similar behavior with respect to the decomposition of these molecules [154].

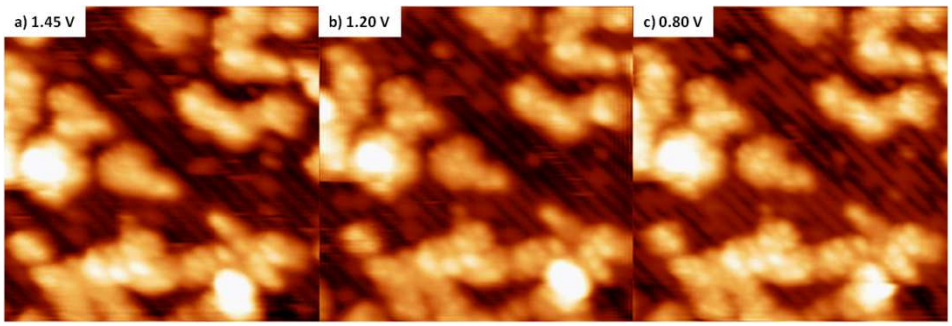

Figure 4.2.3.17.- *Set of STM images varying the tunneling bias.* We do not observe any change either in the internal features or the height of the islands when we modify the bias, indicating that these islands probably present an amorphous structure as they no longer present molecular orbitals. Size: (150 Å x 150 Å), I = 0.13 nA. Voltages indicated in the images.

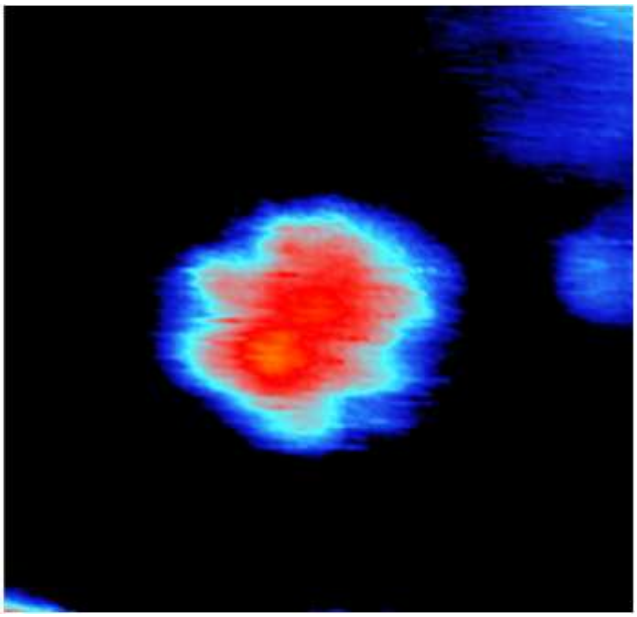

Figure 4.2.3.18.- *High-resolution STM image of one of the round bright features appearing after annealing at 850 K.* In it we can distinguish some structure inside the molecule which resembles the one observed for C_{60} molecules. STM parameters: (40 Å x 41 Å), I = 0.13 nA, V = 1.8 V.

Finally, further annealing of the system yields to material desorption as we can appreciate in figure 4.2.3.19. When annealing to approximately 900 K we observe a dramatic decrease of material on the surface. The remaining material forms carbon-like clusters with an amorphous structure. At this point, we can assure that there are no evidences of graphene formation upon high-temperature treatments of the precursors, as suggested for other systems like Pt [154].

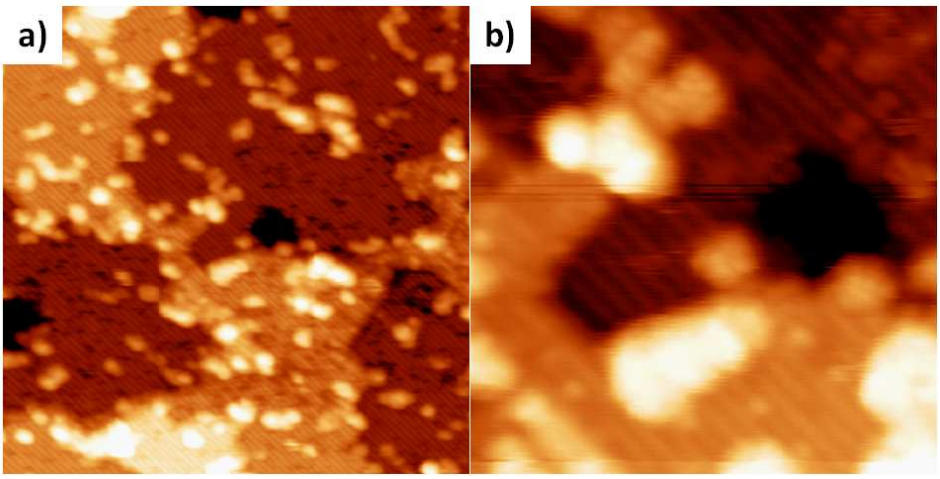

Figure 4.2.3.19.- *Evaporated TiO_2 surface after annealing at 900 K*. We observe an important decrease of material on the surface indicating it has been desorbed. They remaining material forms small clusters randomly distributed on the surface. Size: a) (500 Å x500 Å), I = 0.15 nA, V = 1.3 V. b) (150 Å x 150 Å), I = 0.15 nA, V = 1.3 V.

4.2.3.4. Conclusions

We have studied the adsorption geometry and the interaction of $C_{60}H_{30}$ molecules with the TiO_2 (110)-(1x1) surface. We have observed clear evidences of high diffusion rates when we deposit these molecules at RT. Under these conditions they present a flat lying-down geometry on the surface probably on a physisorption state. However, this low interaction is modified when the system is annealed over 375 K. In this case, molecules overcome the chemisorption barrier and start interacting more strongly with the substrate. This is evidenced by the stabilization of diffusing molecules on the surface. A preferential orientation is observed, where one of the corners of the triangular molecules is pointing along the [001] surface direction but in some cases we can observe molecules with one of the corners aligned along the [1-10] direction. This change in the orientation is probably due to the presence of surface defects. High-resolution STM images show some structure inside the molecules which is probably associated to the molecular orbitals of $C_{60}H_{30}$ as it is not related with the molecular topography. We have also shown that it is

possible to tunnel through the molecule making them disappear in the STM images for values of the tunneling bias lower than 1.2 V. This is an indication of low interaction between the molecule and the substrate as there is no hybridization of the molecular orbital with the TiO_2 states in the band-gap region. NEXAFS measurements corroborate the STM results as they suggest a flat adsorption of the molecule on the surface, with the H atoms in the same plane of the carbon rings.

The annealing of the system yields the apparent formation of structures which resemble C_{60} molecules and other higher order fullerenes. This assumption is based on the apparent dimensions of the features observed after the annealing treatments and in the absence of the C-H bond peak in the NEXAFS spectra. This result is very similar to the one obtained for other low reactive metal systems as Au and Cu. This surprising result for an oxide surface can be understood in terms of the role played by surface defects such as O_{vac} in the cleavage of the C-H bond present in the precursor. However, extra experiments should be carried out in order to completely discard a carbon-like amorphous nature of the clusters obtained by STM. No evidences of graphene formation have been observed upon annealing the system up to 900 K, temperature at which we notice a clear material desorption.

4.2.4. Comparative study

As we already mentioned before, future technology is thought to be based on molecular electronics [203-205]*. Several are the examples of organic molecules tested in prototypical devices, obtaining in the majority of the cases very promising results. For this reason it is of crucial importance to understand from a fundamental point of view the atomic processes operating in the molecule-support interface. With this aim, in the last decades, a wide variety of organic molecules has been deposited on all kind of metallic, semiconducting and insulating surfaces and subsequently studied by means of many different techniques* [14,206-208].

Depending on the balance of the molecule-molecule and molecule-substrate interaction, the growing mode and ordering of the molecules can vary completely and with it, their application possibilities. These interactions can be of very diverse nature such as covalent bonding, electrostatic interaction, hydrogen bonding, van der Waals interaction, ionic bonding, charge transfer, etc. Nowadays, we are able to self-fabricate organic molecules with different functional groups. This capability of tuning the molecular functional groups open a wide spectrum of possibilities as it allows us to create molecules "à la carte". This means that we can tailor the interaction properties of those molecules in advance and in function of our necessities. But the reactivity of a certain molecule is not only defined by its functional groups. The shape and electronic saturation of the molecule also play an important role in their interaction properties. As we have seen in the previous sections, molecules with a very similar composition as C_{60} and $C_{60}H_{30}$, present very different behaviors when deposited on the same surface. While the first forms self-assembled layers, the second does not give rise to ordered structures. In the case of $C_{60}H_{30}$ this is probably due to the absence of intermolecular van der Waals interactions due to their planar shape. Thus, the shape and electronic saturation can dramatically influence the growing mode of these molecules.

In previous sections we have studied the growth morphology of different organic molecules on TiO_2. In this section we investigate the electronic properties of these systems both individually and collectively. In order to extend the spectrum of studied molecules, we include a more reactive molecule as protoporphyrin IX, which presents donor character. With this aim we first analyze, by means of spectroscopic techniques, the interaction of each

individual molecule with the TiO_2 surface comparing it with the clean substrate surface. Then, we perform a comparative study of the different molecules in order to obtain general conclusions about the molecule-substrate interactions.

4.2.4.1. Interaction of commercial C_{60} with the rutile TiO_2 (110)-(1x1) surface

The XPS measurements on the C_{60} / TiO_2 system were carried out at LT (between 150 and 200 K). Figure 4.2.4.1 shows one example of the C1s emission for a C_{60} coverage of approximately 0.8 ML. As we can see, the main emission of this peak presents a slightly asymmetric shape towards higher binding energies (BE), together with two less intense peaks at even higher BE. If we decompose this main peak we observe the presence of a very intense peak at 284.6 eV, which corresponds to the C-C bonds present in the C_{60} molecules. This value is in good agreement with other values reported in the literature [209-213]. In fact, this value is very close to the one obtained by other authors for multilayer coverage, confirming a very low interaction between the molecular layer and the substrate, as already mentioned in section 4.2.1. Regarding the second peak inside the main C emission peak, appearing at 285.0 eV, we attribute it to small charge redistributions inside the C_{60} molecule induced by the effect of the substrate which slightly interacts with the carbon atoms of the molecule facing it. Although the molecule-substrate interaction is very low, there is a certain influence of the substrate on the molecules as it is the one who drives the molecular orientation. The ratio between the areas of both peaks is approximately 0.1, i.e. this second peak presents an area which is a 10% of the area of the main peak. This means a charge redistribution affecting 6 carbon atoms. This result is very reasonable as we have seen by DFT calculations and XPD measurements that the molecules are oriented with a hexagon and a pentagon-hexagon dimer facing the surface.

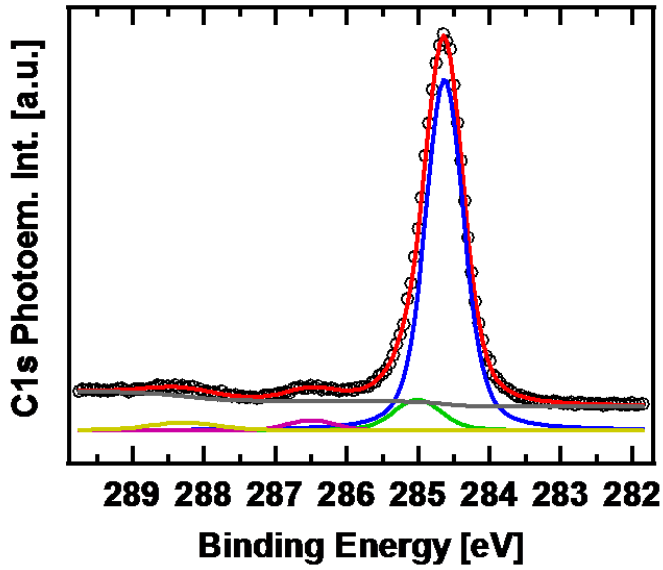

Figure 4.2.4.1.- *C_{60} C1s photoemission spectrum decomposition*. We observe the presence of four different components, two of them giving rise to the main peak and the other two being due to molecular shake-ups. The green curve can be due to small charge redistributions inside the molecules as a consequence of the very low interaction with the substrate. E_{ph} = 400 eV.

However, there are two other peaks in the C1s photoemission spectrum. They appear at BE of 286.5 and 288.3 eV and they present a much lower intensity. We assign them to π type shake-up satellites. They are separated from the main peak by approximately 1.9 and 3.7 eV, values which agree with the HOMO-LUMO and HOMO-LUMO+2 monopole like electron transitions of bulk C_{60} [214]. These peaks have two important implications in the understanding of the interaction of C_{60} with TiO_2. The first one is that their presence for coverages lower than 1 ML is somehow surprising as they are usually associated to multilayer coverages. Thus, it is clear indication of a low interacting system as the submonolayer coverage presents a very similar behavior to the multilayer one. The second implication is that these shake-up peaks appear at the same energy difference as in the case of multilayer coverage. This means that the C_{60} molecular orbitals are not affected by their deposition on TiO_2, not even at the first layer. This result is in full agreement with the NEXAFS results shown in section 4.2.1 where the same conclusion is

obtained by comparing the NEXAFS spectra for submonolayer coverage with the ones obtained for a multilayer. Again, we have another clear evidence of a low interacting system.

On the other hand, we do not observe any significative change either in the O1s or in the Ti2p XPS spectra with respect to the corresponding for the clean surface (see figure 4.2.4.2 a) and b), respectively). This is another evidence of a very low interacting system as the C_{60} deposition does not affect the substrate either.

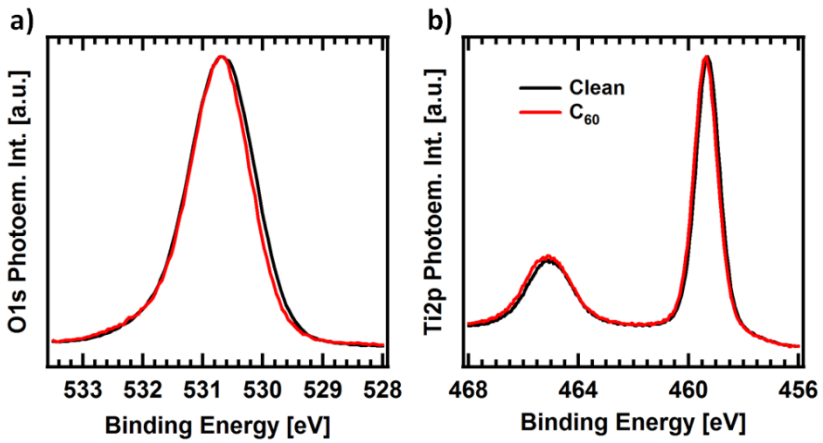

Figure 4.2.4.2.- *Clean TiO_2 surface and C_{60} / TiO_2 system O1s and Ti2p photoemission spectra*. a) O1s spectra. We observe a small decrease of the C_{60} O1s peak width due to the lower temperature at which it was measured (T_{clean} = RT, T_{C60} = 190 K). b) Ti2p spectra. As we can see, both of them are almost identical, as expected because of their low interaction. E_{ph} = 650 eV.

As we are dealing with adsorbates, it is always interesting to look at the valence band spectrum as it is the valence band of a material the one which suffers more significative changes upon adsorption of other materials. This is so because the electrons close to the Fermi level are the ones that will take part in the interaction whether it is physisorption or chemisorption. Figure 4.2.4.3 exhibits the valence band spectrum for 0.8 ML of C_{60} on TiO_2. If we carry out a qualitative analysis, we notice that the C_{60} / TiO_2 VB spectrum is almost identical to the clean TiO_2 one. The shape of the VB is basically the

same in both cases, except for a small variation in the region around 6 eV, where we observe a narrowing of the peak. As we mentioned in chapter 2 (substrate), the origin of this region is complex so we cannot make a clear assignment of this modification of the VB. However, there are two possibilities for this change. One is that, as the VB has mainly an O2p character, this modification is due to a weak interaction between C_{60} and the O_{br} atoms of the surface. The second possibility is that this modification is due to the presence of C_{60} molecular orbitals. It is known that a multilayer of C_{60} presents some wide features around 5.5 – 6 eV of BE which correspond to a mixture of π and σ orbitals. If this were the case, another variation of the VB spectrum should appear in the region between 7 and 8 eV [212]. However, we cannot appreciate changes in this region so we can neglect this second possibility in favor of an interaction explanation. Continuing with the analysis of the VB spectrum, we observe the appearance of a new state in the energy band gap region (figure 4.2.4.3 b)). This new state at 2.1 eV corresponds to the HOMO state of C_{60}. Its energy is in very good agreement with the one obtained for a multilayer coverage [212], indicating again a very low interaction between C_{60} and TiO_2.

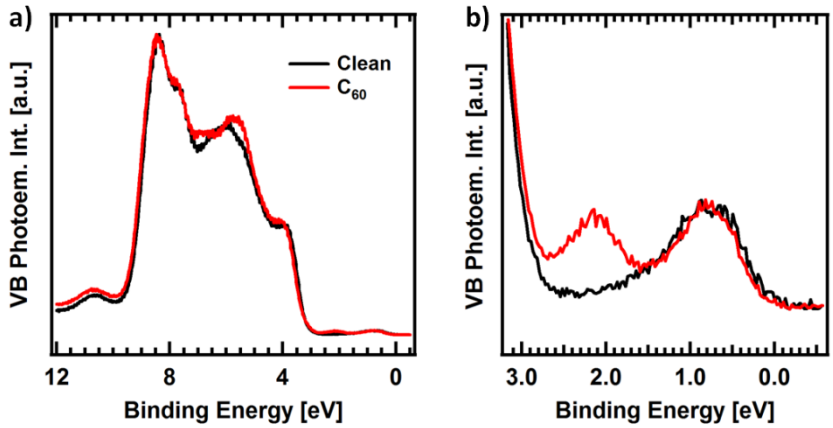

Figure 4.2.4.3.- *Valence band spectra for the clean TiO_2 surface and the C_{60} / TiO_2 system.* a) Valence band region. Both spectra are very similar, with some differences in the features at 5 eV. b) Zoom in the band gap region. We observe the appearance of a new state associated to the C_{60} HOMO. E_{ph} = 130 eV.

4.2.4.2. Interaction of pentacene with the rutile TiO_2 (110)-(1x1) surface

We have studied the electronic structure of the pentacene / TiO_2 system for a pentacene coverage of approximately 1 ML. For this purpose we have performed XPS measurements on the C1s, O1s, Ti2p and valence band regions. These measurements have been carried out at RT. The high-resolution C1s core level spectra present a resolution of approximately 80 meV.

Before doing the C1s spectrum fitting, it is important to keep in mind the different chemical environments present inside the pentacene molecule. For this purpose we have followed a similar strategy to the one reported for pentacene molecules deposited on different substrates [215,216]. In these cases, they make use of an assignment of the different atomic environments supported by DFT calculations. Following this strategy, we have considered the charge redistributions obtained in our DFT calculations to differentiate three types of C atoms inside the molecule, classified as it is shown in figure 4.2.4.4. It must be taken into account that probably this is not the unique possible assignment but it is the most reasonable one as our DFT calculations have been able to correctly reproduce both the molecular and electronic structures. On one side, we have the four inner carbon atoms located at the top part of the molecule (blue circles, C_1). These four atoms present the highest charge value, very close to neutral C atoms, so we can assume that they are only slightly affected by the surface or other molecules. Consequently, these four C atoms will present the lowest BE. Secondly, we can group the nine C atoms sited at the lower part of the molecule (green circles, C_2). They are less charged than C1 atoms, thus presenting a higher BE. This charge difference comes from their interaction with the surface O_{br} atoms and with the top part of the neighboring molecules. Finally, we have the nine C atoms located at the border of the pentacene molecule (violet circles, C_3). They present the lower charge value, probably because they are affected by different interactions, as the electrostatic repulsion along the [001] surface direction and the electrostatic attraction between consecutive molecules along the [1-10] surface direction. They give rise to the higher BE peak of the spectrum. The difference in the core level peaks associated to the different net charge of the atoms should be very small.

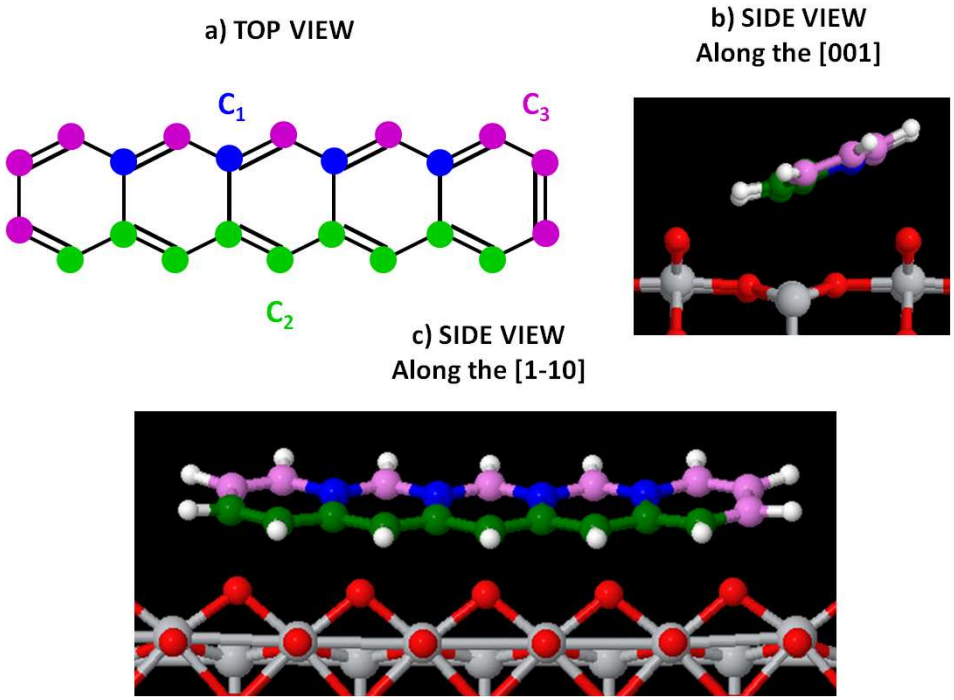

Figure 4.2.4.4.- *Schematic representation of the different charges at the C atoms inside the pentacene molecule after DFT calculations.* We have marked the three different types of carbon atoms inside the molecule. C_1 atoms refer to the four inner C atoms located at the top part of the molecule (blue circles). C_2 atoms correspond to the nine C atoms at the lower part of the molecule (green circles). Finally, C_3 atoms are those which are surrounding the molecule, except in the lower part (violet circles). We show three different views: a) Top view, b) Side view along the [001] surface direction, c) Side view along the [1-10] surface direction.

We have seen in a previous chapter that pentacene layers present a double lateral attractive interaction. One between the lower part of the molecule and the surface, which is probably a H-bond mediated by the substrate O_{br} atoms, and another one between molecules, which probably has an electrostatic origin due to a charge redistribution inside the molecule. This charge redistribution will reflect in the shape of the C1s core level.

Thus, we can order the C atoms attending to their charge as follows:

$$Q(C_3) < Q(C_2) < Q(C_1)$$

Or, expressed in terms of the binding energy:

$$BE(C_3) > BE(C_2) > BE(C_1)$$

Attending exclusively to these initial state considerations, we have carried out the C1s photoemission peak fitting using four components, three associated to these different chemical environments and a fourth peak which can be related to the pentacene molecular shake-up or to defects due to molecules on a different configuration (figure 4.2.4.5). During the fitting, we have forced the system to preserve the correct area ratios attending to the number of C atoms of the same type existing inside the molecule (1 vs 2.25 vs 2.25 for C_1, C_2 and C_3, respectively). Under these constrictions, we have obtained the following peak parameters:

	BE [eV]	FWHM [eV]	$FWHM_G$ [eV]	Area [a.u.]
C_1	284.30	0.17	0.73	295
C_2	284.66	0.15	0.78	664
C_3	284.95	0.14	0.77	664
Shake-up/ Defects	285.72	0.14	0.41	28

Table 4.2.4.I.- *Peak parameters values used for the fitting.*

where FWHM is the Lorentzian width and FWHMG is the Gaussian width of the Voigt curves used for the fitting.

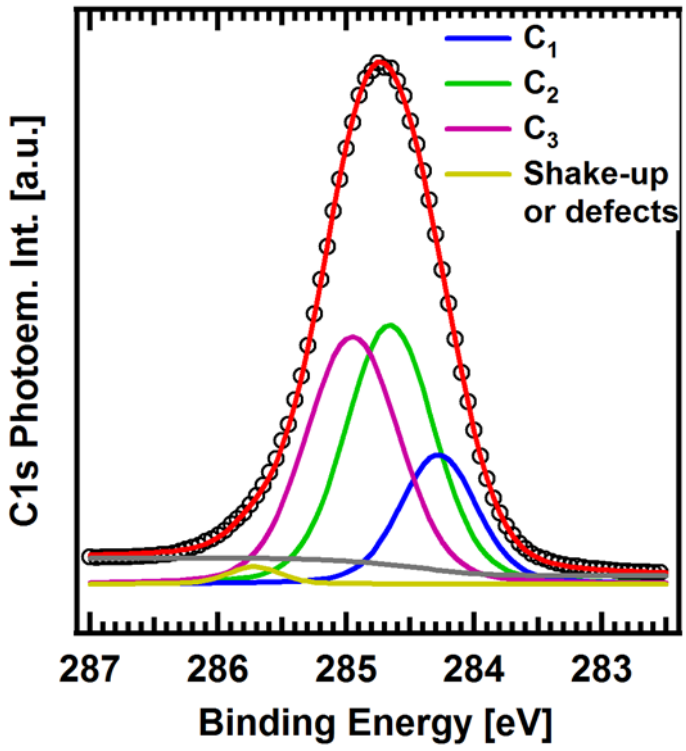

Figure 4.2.4.5.- *Pentacene C1s spectrum decomposition*. During the fitting procedure we have forced the system to keep the intensity ratios expected from the different number of atoms composing each type of C atoms inside the molecule. A fourth peak corresponding to a molecular shake-up has been included for the completeness of the fitting. E_{ph} = 400 eV.

Regarding the O1s and Ti2p photoemission peaks, we do not observe significative changes on them except for a very small increase in the $Ti2p_{1/2}$ peak. This intensity variation may be due to small charge redistributions taking place also in the surface atoms because of the low interaction with the molecules (Figure 4.2.4.6).

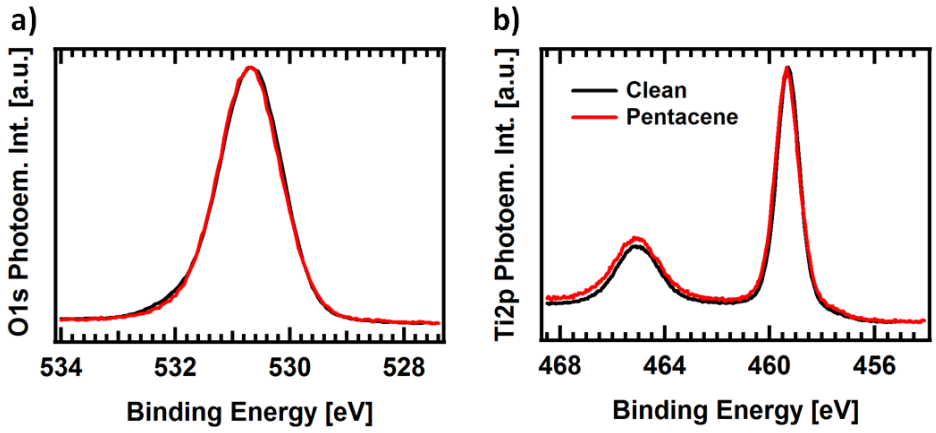

Figure 4.2.4.6.- *Clean TiO_2 surface and pentacene / TiO_2 system O1s and Ti2p photoemission spectra*. a) O1s spectra. No significative changes are observed. b) Ti2p spectra. We observe a small increase in the $Ti2p_{1/2}$ peak. E_{ph} = 650 eV.

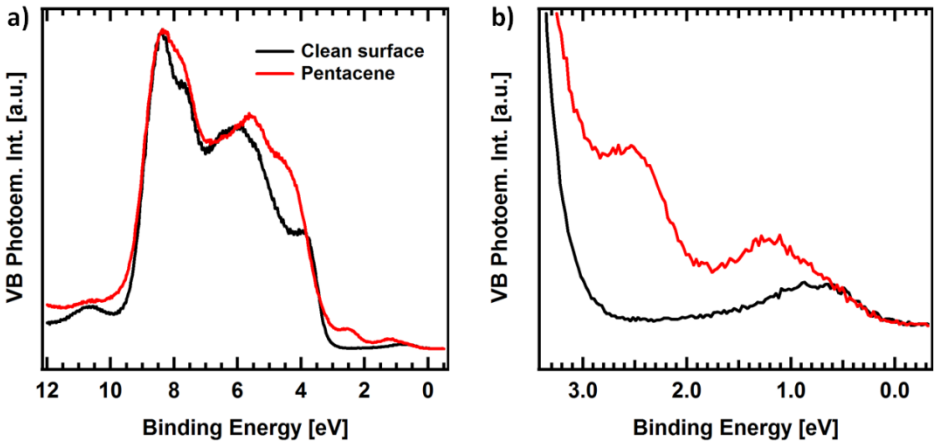

Figure 4.2.4.7.- *Valence band spectra for the clean TiO_2 surface and the pentacene / TiO_2 system.* a) Valence band region. Pentacene spectrum presents some differences in the main features probably due to the O_{br} mediated interaction between pentacene molecules along the [1-10] surface direction. b) Zoom in the band gap region. We observe the appearance of two new states associated to the pentacene HOMO and HOMO+1. E_{ph} = 130 eV.

Finally, we have the spectrum associated to the valence band of the system (figure 4.2.4.7). We can observe some significative changes as the valence band is the more affected region when interactions are taking place. We observe a broadening of the main VB features located at 4, 6 and 8 eV. As the valence band has a predominant O2p character, these variations indicate an interaction between pentacene molecules and the O atoms at the surface. As we saw in section 4.2.2, pentacene structures are stabilized by lateral intermolecular interaction mediated by the substrate O_{br} rows. As a consequence, these O_{br} atoms are altered and so is the VB. In any case, these changes are small and consistent with a low interacting system.

However, the most interesting result is obtained in the band gap region. As we can observe in figure 4.2.4.7 b), two new states appear in the TiO_2 gap region. They are located at approximately 1.2 – 1.3 eV and at 2.5 – 2.6 eV. We assign them to the HOMO and HOMO-1 molecular states, in very good agreement with previous observations in other systems like graphite, SiO_2 and Au [217-219]. Particularly, in the case of the wide peak located at 1.2 eV, we have a double contribution to this peak coming from the superposition of the molecular HOMO and the substrate defects peak. In fact, it is possible to observe a very subtle inflection at approximately 1 eV, indicating the point where the HOMO peak starts. By comparing the initial and final energy for the HOMO state with the ones obtained in [217] we get a very good agreement with the values corresponding to low coverage. Furthermore, they decompose the HOMO peak into three different components all of them related to a HOMO – hole / vibration coupling due to the existence of domains of well-ordered flat-lying pentacene molecules. This result is in accordance with our STM and NEXAFS observations of lying-down pentacene layers. Additionally, the energy difference we find between HOMO and HOMO-1 states (~ 1.3 eV) agrees with the values obtained for the gas phase pentacene (~ 1.23 eV) and with the theoretical DOS of the system (see section 4.2.2), thus indicating a very low interaction between pentacene and the TiO_2 surface as molecular orbitals remain unaltered.

4.2.4.3. Interaction of $C_{60}H_{30}$ with the rutile TiO_2 (110)-(1x1) surface

For the case of $C_{60}H_{30}$, we have performed XPS measurements at three different temperatures: 175 K, 375 K and 750 K, approximately. Due to our impossibility to carry out STM measurements at low temperature (LT), we cannot compare the XPS results at 175 K with any STM image. However, it seems reasonable to think that the situation at this LT should not be very different to the one observed at RT. In the best case, molecules would be "frozen" but that would not affect the interaction itself and, consequently, the electronic structure.

Figure 4.2.4.8 shows the C1s XPS core level peaks taken at 175K, 375 and 750 K, after the evaporation of less than 1 ML of C_{60} H_{30}. In the low temperature case, we can distinguish up to five different components located at 284.9, 285.7, 286.9, 287.9 and 289.0 eV. As we are dealing with a very low interacting system, it is surprising the wide variety of C components present in the spectrum. It is complicated to make a straightforward assignation of the peaks as it is very possible that there are contributions from physisorbed contaminants due to the LT. For this reason we have annealed the system to approximately 375 K in order to get rid of some of these contaminants. The XPS spectrum after this annealing is shown in the middle panel of figure 4.2.4.8. The spectrum can now be fitted with four components: 284.4, 285.3, 286.4 and 289.0 eV. The new spectrum (except for the peak at 289.0 eV) has moved towards lower BE by approximately 0.5 eV, thus indicating a stronger interaction between the molecules and the substrate. Attending to the STM images obtained at approximately this annealing temperature, we can attribute this shift to the molecular transformation taking place when the system is annealed above 375 K, i.e. to the partial dehydrogenation of the molecules that allows a higher interaction between them and the substrate.

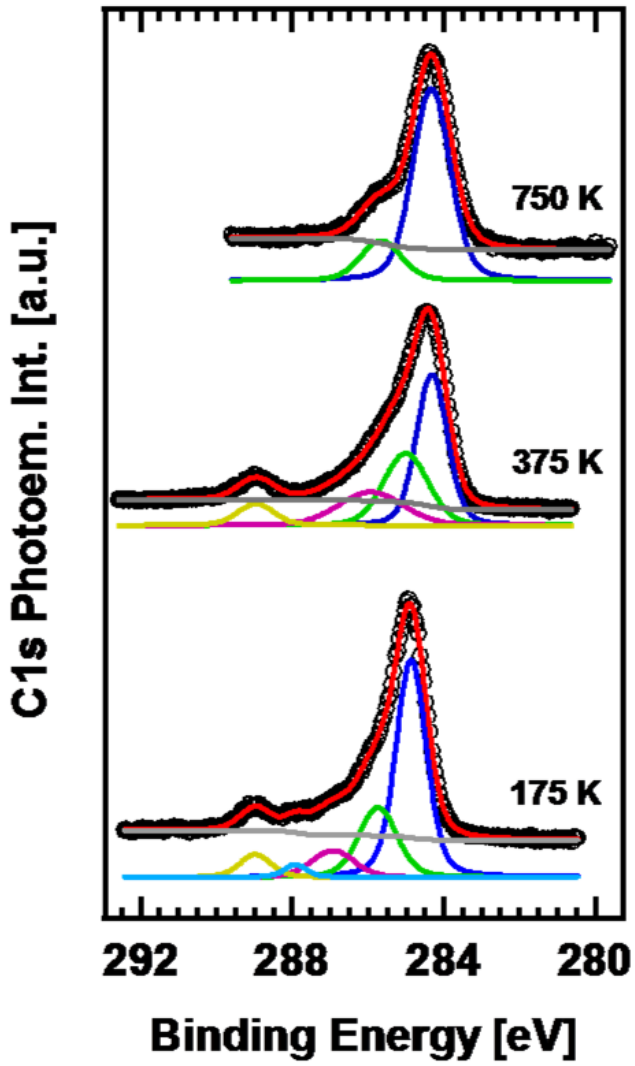

Figure 4.2.4.8.- *$C_{60}H_{30}$ C1s photoemission spectra decomposition in curve components for the three different annealing temperatures*. **Lower panel:** Low temperature core level. We observe the necessity of five Voigt components in order to be able to properly fit (red solid curve) the experimental data (open black circles). Measured at approximately 175 K. **Middle panel:** Soft annealing. One of the components disappears after annealing at 375 K. This component was probably due to physisorbed CO or CO_2 molecules as a consequence of the LT. The main peak shifts approximately 0.5 eV towards lower BE, thus indicating a change in the interaction. **Upper panel:** High temperature annealing. After this annealing just two components remain. They are probably associated to C – C bonds and COx species present on the surface in the form of clusters. Spectrum measured at 750 K. E_{ph} = 400 eV.

Comparing the spectra taken at 175 and 375 K, the main difference is that the component at 287.9 eV has disappeared. We can attribute this component to CO and CO_2 contaminants physisorbed on the surface because of the LT. In fact, it is well known that both species, when adsorbed on the defective TiO_2 (110)-(1x1) surface, desorb at approximately 350 and 175 K, respectively [220,221]. Thus, it is compatible with the disappearance of the peak at 287.9 eV after annealing the system at 375 K. The fact that all the peaks except for the one at 289.0 eV shift towards lower BE indicates that this latter peak is probably due to contaminant species independent of the $C_{60}H_{30}$ molecules. The other three components should then be associated to the molecules. The peak at 284.4 eV probably corresponds to the C – C bonds between atoms of the molecule. The other two peaks can be related to different C environments inside the molecule.

In order to try to find out the origin of the different C peaks appearing in the C1s photoemission spectrum, we have measured it after the annealing at 750 K. As we have seen in section 4.2.3, after this annealing cycle STM images reveal the formation of partial / total fullerenes and amorphous carbon-like clusters coming from the decomposition of the $C_{60}H_{30}$ molecules, as it is indicated by the disappearance of the NEXAFS feature associated to the C – H bonds. The upper panel of Figure 4.2.4.8 shows the corresponding C1s photoemission spectrum. As we can see, two more components have disappeared after the high temperature annealing, the ones at 286.4 and 289.0 eV. The two remaining peaks appear at similar BE, 284.3 and 285.7 eV. Considering that after annealing fullerenes and carbon-like clusters are formed, these two peaks must be associated to C – C bonds for the lower energy component and C = C or C – O_{br} for the higher energy one. In fact, the C – C peak presents a BE which is in very good agreement with the value expected for C in a graphite structure [78,222]. On the other hand, the existence of CO_x species is corroborated by the appearance of the peak at 290.5 eV in the NEXAFS spectra, as we have seen in section 4.2.3.

As in the previous cases, we do not observe significative changes either in the O1s or in the Ti2p photoemission spectra with respect to the clean TiO_2 surface after the annealing at 375 K (figure 4.2.4.9). The same behavior is found for the O1s and the Ti2p spectra after the high temperature (HT) annealing (figure

4.2.4.9). These results indicate a low interaction with the substrate even after the HT treatment.

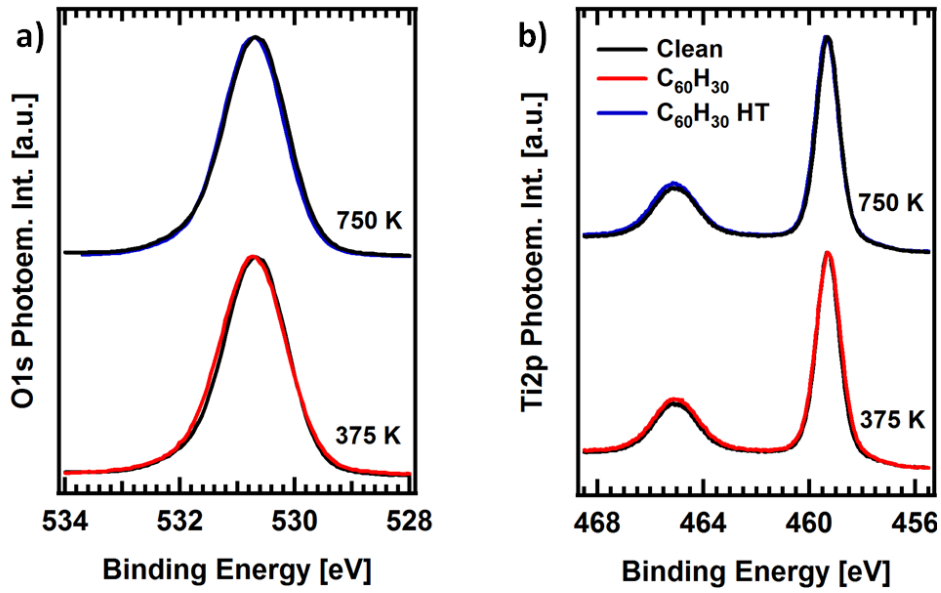

Figure 4.2.4.9.- *Comparison of the $C_{60}H_{30}$ after the 375 K and the 750 K annealing with the clean surface O1s and Ti2p spectra.* a) $C_{60}H_{30}$ and clean TiO_2 surface O1s spectra. No significative changes are observed. b) $C_{60}H_{30}$ and clean TiO_2 surface Ti2p spectra. As in the case of O1s, no important changes occur. These results indicate a low interaction between the molecules and the substrate. E_{ph} = 650 eV.

Figure 4.2.4.10 shows the valence band photoemission spectra of the clean and evaporated surface after annealing at 375 K and at 750 K. For the case of the low temperature annealing we find small changes in the shape of the valence band which basically confirm the suggestion of a low interacting system. In fact, no new states appear in the band gap region and the TiO_2 defects peak remains unaltered upon the $C_{60}H_{30}$ evaporation, thus indicating a low interaction with the O_{br} atoms as the Ti^{3+} states remain unaltered. We just notice a small increase in the intensity between the defects peak and the valence band which can be associated to new states related to the soft interaction between the molecules and the surface. The $C_{60}H_{30}$ valence band

spectrum after the HT annealing is even more similar to the clean one. All the valence band features are identical to the ones in the clean surface, including the defects state. As this spectrum corresponds to the TiO_2 surface covered with carbon-like clusters, we can suggest the formation of amorphous carbon clusters randomly distributed on the surface without an appreciable contribution to the valence band electronic structure.

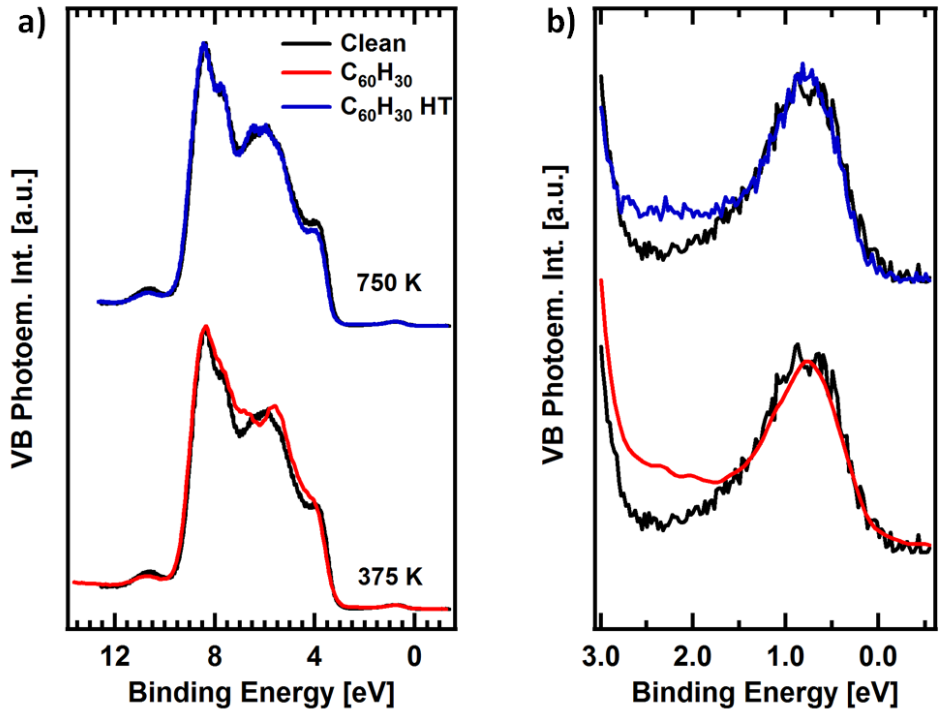

Figure 4.2.4.10.- *Comparison of the valence band region of the clean TiO_2 surface and the $C_{60}H_{30}$ / TiO_2 system after annealing at 375 K and at 750 K.* a) Valence Band region. In the case of the low temperature annealing, some small differences in the shape of the main features are observed, indicating a non-negligible interaction although still very low. However, after the high temperature annealing both spectra are almost identical. This result suggests the formation of amorphous carbon-like structures with no effect on the VB electronic structure. b) Zoom at the band gap region. We do not observe important changes in the defects peak intensity in any of both cases, indicating that the possible interaction is not mediated by the defects. E_{ph} = 130 eV.

4.2.4.4. Interaction of H_2PPIX with the rutile TiO_2 (110)-(1x1) surface

Figure 4.2.4.11 exhibits a schematic representation of the free H_2PPIX molecule. As we can see, it is composed by 34 carbon, 34 hydrogen, 4 oxygen and 4 nitrogen atoms. The O atoms form two carboxylic groups located at the "legs" of the molecule, while we have 2 different types of nitrogen atoms, iminic (not bonded to a H atom) and pyrrolic (bonded to a H atom) ones. Finally, we have the C atoms which are divided into three different groups: those directly bonded to the N atoms, the other C atoms which take part of the iminic and pyrrolic pentagons and the rest, which are aliphatic.

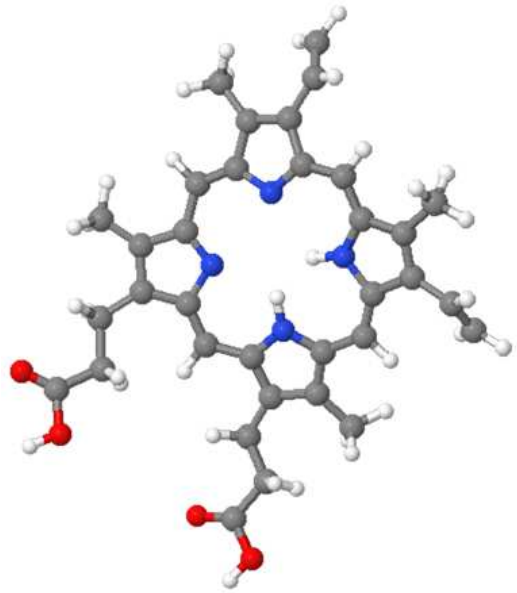

Figure 4.2.4.11.- *Ball-and-stick schematic representation of the H_2PPIX molecule*. The molecule is composed by 34 C atoms (grey balls), 34 H atoms (white balls), 4 N atoms (blue balls) and 4 O atoms (red balls). The two C atoms bonded to O atoms form carboxylic groups. The two N atoms bonded to H atoms form pyrrolic rings while the ones without H atoms form iminic rings.

It exits a wide variety of molecules within the porphyrin family. The one we have studied, H_2PPIX, is the one appearing in biological systems. We can find

metallated protoporphyrins, which present a central metal atom bonded to the N atoms present at the central molecular ring; or “empty” ones where two of the central N atoms are hydrogenated (protoporphyrin IX). Examples of metallated protoporphyrins are hemoglobin, where the metal is an iron atom; chlorophyll, where the N atoms are bonded to a magnesium atom, etc. Very recently it has been reported the metallation of protoporphyrin IX molecules with substrate metal atoms after deposition at RT [223].

For the special case of H_2PPIX, it is worthy to start the analysis with the N1s photoemission peak as this signal is going to give us one of the most important clues related to this molecule, if it is metallated or not. Figure 4.2.4.12 shows the N1s photoemission intensity corresponding to approximately 0.7 ML of H_2PPIX on TiO_2 measured at low temperature (~ 175 K). The peak can be reproduced by a single Voigt component located at 400.4 eV and with Lorentzian and Gaussian widths of 0.35 and 1.02 eV, respectively.

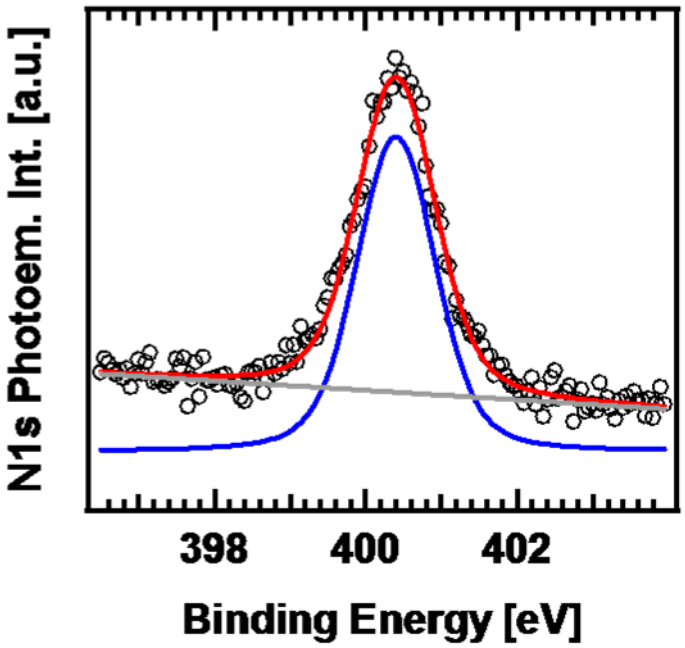

Figure 4.2.4.12.- *H_2PPIX N1s spectrum decomposition*. As we can see, just one peak is needed to properly fit the experimental data, indicating that all the N atoms are equivalent. E_{ph} = 650 eV.

The molecule, in its free configuration, presents two different kinds of N atoms, as seen above. It is well known that both nitrogen atoms give rise to two equally intense photoemission peaks, located at approximately 398 and 400 eV (iminic and pyrrolic, respectively). In our case, the N1s peak presents a single component, as we can see in figure 4.2.4.12. This is a common behavior for metallated porphyrin molecules as, after receiving the metal atom, all the N atoms become equivalent. However, if this is the case, the disappearance of one of the N peaks entails a shift of the remaining N peak towards lower binding energies, as the N atoms are bonded to a metal atom. On the contrary, the N1s spectrum shown in figure 4.2.4.12 presents a single component located at approximately 400.4 eV. This value is very similar to the pyrrolic one observed in literature, although it presents a small shift towards higher binding energies. This shift is not compatible with the metallation of the molecule with a Ti atom, as the corresponding TiN peak should appear at much lower BE [224]. This situation is compatible with having all the N atoms deprotonated (iminic state) and bonded to the bridging oxygen atoms of the surface. In fact, the position of the N1s peak is compatible with a more oxidized state of the N atoms as a consequence of being bonded to an O atom.

Figure 4.2.4.13 shows the corresponding C1s photoemission peak. The fitting parameters are shown in table 4.2.4.II.

	BE [eV]	FWHM [eV]	$FWHM_G$ [eV]	Area [a.u.]
Aromatic C	284.9	0.19	1.00	65
Aliphatic C	285.6	0.21	0.81	130
C - N	286.3	0.20	1.13	65
Carboxylic C	289.4	0.19	0.59	2.3

Table 4.2.4.II.- *Peak parameters values used for the fitting.*

In this case we observe the presence of four different C atoms associated to four distinct chemical environments. First of all, we have the peak at 284.9 eV which we assign to the aromatic C atoms present in the iminic and pyrrolic rings and that are not bonded to the N atoms (8 C atoms in total). Secondly, we have the peak at 285.6 eV that we associate to the aliphatic C atoms present in the molecule. It presents an area which is two times the area of the aromatic C atoms as there are double aliphatic atoms than aromatic ones. There is a third peak at 286.3 eV related to the C atoms bonded to the N atoms. In this case the peak presents the same area as the aromatic C atoms peak as there is the same number of C atoms in both cases. It is important to note that after the deposition of the molecule on the TiO_2 surface, pyrrolic N atoms lose their H atoms and probably bond to the surface O_{br} atoms. Thus, all the N atoms are equivalent and so are the C atoms bonded to them. Finally, there is a small peak at 289.4 eV which is due to the carboxylic groups. The position of the peaks is very similar to the ones obtained by Rienzo *et al.* in ref [225] when they deposit zinc protoporphyrin on the same surface. The only difference is the area ratios, which can be understood in terms of the different number of peaks used in the analysis. They fit their results with three peaks while we need four in order to be able to properly fit our experimental data. In fact, we are able to distinguish the C atoms bonded to the N atoms which should present a different BE to that of the rest of the C atoms present in the ring.

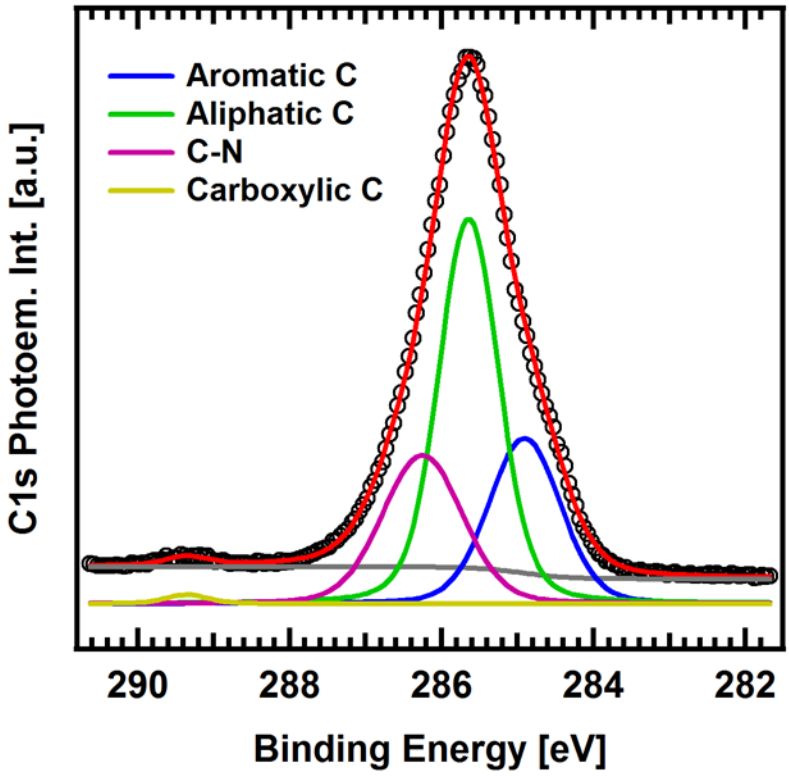

Figure 4.2.4.13.- *H_2PPIX C1s spectrum decomposition*. We have used four peaks in the fitting procedure corresponding to the four different types of C atoms inside the molecule: carboxylic C atoms, C – N bonds, aromatic C atoms and aliphatic C atoms. We have maintained the intensity ratios between components considering the number of atoms of each type. E_{ph} = 500 eV.

In Figure 4.2.4.14 we present the O1s photoemission peak associated to this coverage. Apart from the two well-known substrate peaks, two new ones appear at higher BE. They are located at 532.4 and 534.0 eV and we assign them to the C=O and C-OH oxygen atoms of the carboxylic group, respectively [225]. The fact that we have both types of O atoms after deposition indicates that the carboxylic groups are not deprotonated when they get in contact with the surface. This result is in good agreement with previous observation on similar systems when prophyrins are deposited at LT [226].

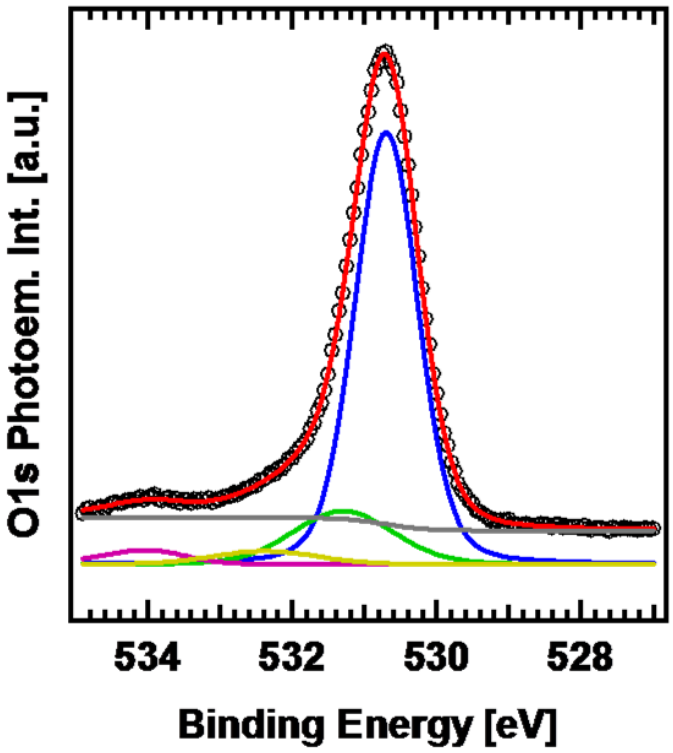

Figure 4.2.4.14.- *H_2PPIX O1s spectrum decomposition*. We observe the appearance of two new peaks (yellow and pink curves) apart from those associated to the clean TiO_2 surface (blue and green curves). These new curves correspond to =O and OH oxygen atoms composing the carboxylic groups. As we find both of them after the deposition, it indicates that no deprotonation is taking place. E_{ph} = 650 eV.

The reason why we do not observe any particular peak associated to the possible NO bond can be explained taking into account the low amount of oxygen atoms bonded to the N ones (maximum one O atom per N atom). If we consider that the N1s signal is very low (12 times lower than the C signal, considering the corresponding cross-sections) and that the oxidation state of the O atoms should be very similar to the O-C species mentioned above, we can conclude that this component of the peak is so small that it must be included in some of the other peaks.

To conclude with the core-level peak analysis, we have the Ti2p spectrum, which is represented in figure 4.2.4.15.

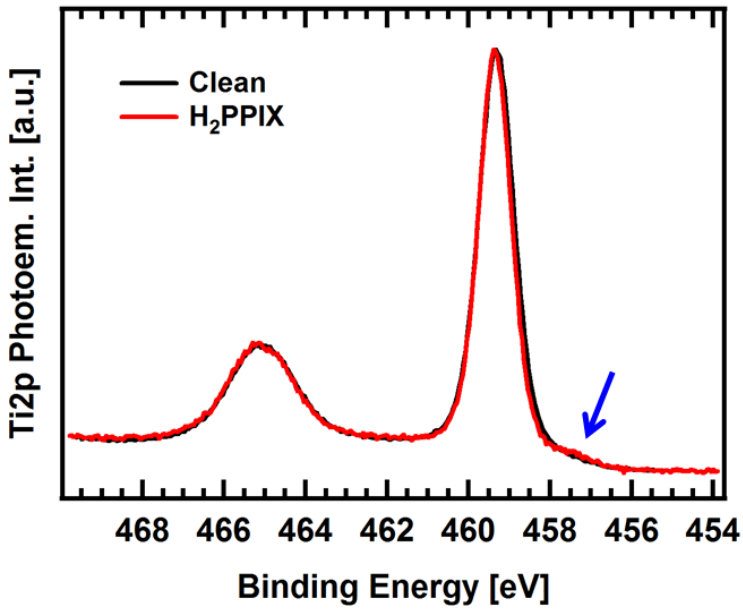

Figure 4.2.4.15.- *Comparison of the Ti2p spectra associated to the clean and H_2PPIX surfaces.* As we can see both of them are almost identical except for a small increase in the pre-edge region corresponding to the Ti^{3+} states (marked with a blue arrow). This increase indicates a charge transfer from the molecules to the Ti atoms. E_{ph} = 650 eV.

We must mention that we have included a 0.1 eV shift towards lower BE to the H_2PPIX Ti2p spectrum. The reason is that we observed an equivalent shift towards higher BE, taking as a reference the clean Ti2p spectrum. It is extremely improbable that this shift is due to the presence of a single molecular layer on the TiO_2 surface. We believe it is an experimental artifact probably due to a small instability in the photon energy. When we correct this small error, we observe an increase in the pre-edge region of the Ti2p peak, as indicated by the arrow. This region is associated to the Ti^{3+} states (as already shown in chapter 2) so this increase in the intensity suggest an increase of the Ti^{3+} states as a consequence of the interaction of the N atoms with the O_{br} ones.

If we analyze the valence band region, which is more sensitive to interaction changes, we observe an important variation in the VB shape (figure 4.2.4.16).

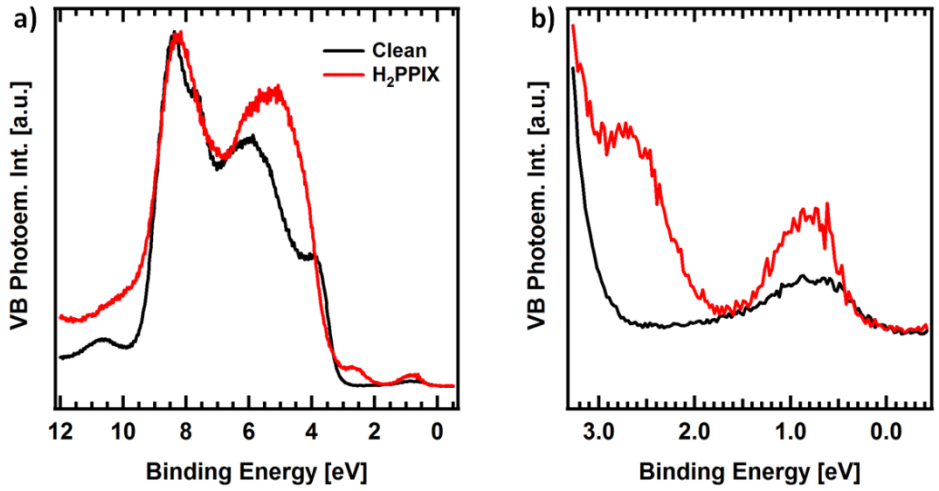

Figure 4.2.4.16.- *Valence band spectra for the clean TiO_2 surface and the H_2PPIX / TiO_2 system.* a) Valence band region. We observe important changes in the valence band shape thus indicating a strong interaction between molecules and surface. b) Zoom in the band gap region. We observe the appearance of a new state associated to the H_2PPIX HOMO together with an increase of the defects peak intensity associated to a charge transfer from the molecule to the surface. E_{ph} = 130 eV.

Basically, we appreciate a broadening and an increase of the VB features appearing at 5 and 8 eV which mainly present an O2p character. This result suggests (and support our previous claim) an interaction between the nitrogen atoms of the molecule and the bridging oxygen atoms at the surface. If we focus on the band gap region (figure 4.2.4.16 b)), we observe the presence of a new state located at approximately 2.7 eV, which we assign to the HOMO state of the H_2PPIX molecules. We also see an increase in the defects state peak after the deposition. This result points in the same direction as previous ones, indicating a charger transfer from the molecule to the substrate thanks to the bond between the N in the molecule and the O_{br} surface atoms. As we already

suggested when analyzing the Ti2p photoemission peak, this extra charge is being injected into the Ti3d states which give rise to the defects state.

Summarizing, the mechanism which is probably operating can be understood as follows: first, the N atoms react with the O_{br} surface atoms, thus the H_2PPIX molecules give charge to the O_{br} atoms through them. As we know by the analysis of the VB of the clean TiO_2 substrate, it exists a hybridization between the O2p and the Ti3d states. Thus, the charge transferred from the molecules to the O_{br} atoms travels to the Ti3d states, increasing the number of Ti atoms in a Ti^{3+} state.

4.2.4.5. Comparative study of the C1s, O1s and Ti2p core-levels photoemission peaks and the valence band region.

Figure 4.2.4.17 shows the C1s photoemission spectra of the four organic molecules used in this thesis. In order to be able to carry out a comparative analysis, a reference is mandatory. In this sense, there are two possibilities. On the one hand we can consider the C_{60} and Pentacene C1s peaks as a relative reference as we have seen they present a weak interaction with the surface. On the other hand, we can use the C1s signal of C contamination (285.0 eV, marked by a dashed black line) as an absolute reference, as it is supposed to be in its neutral state. In principle both references are valid but we have chosen the contamination peak as we believe this reference is more appropriate. Attending at the energy position of contamination C1s signal, we observe shifts in the C1s peaks corresponding to the different molecules. We find shifts of 0.4, 0.5, 0.7 and 0.3 eV towards lower BE for C_{60}, $C_{60}H_{30}$ after annealing at 375 K, $C_{60}H_{30}$ after the high temperature annealing and pentacene, respectively. For the case of C_{60} and pentacene, we observe that the shifts suggest an increase in the charge of the molecules. For the case of C_{60} this movement is in good agreement with the expected acceptor character of this molecule. However, pentacene presents a shift which indicates a modification of the expected character for this molecule. For $C_{60}H_{30}$, we

appreciate a larger shift associated to a more interacting system, thus probably indicating a more efficient charge transfer from the substrate to the molecule.

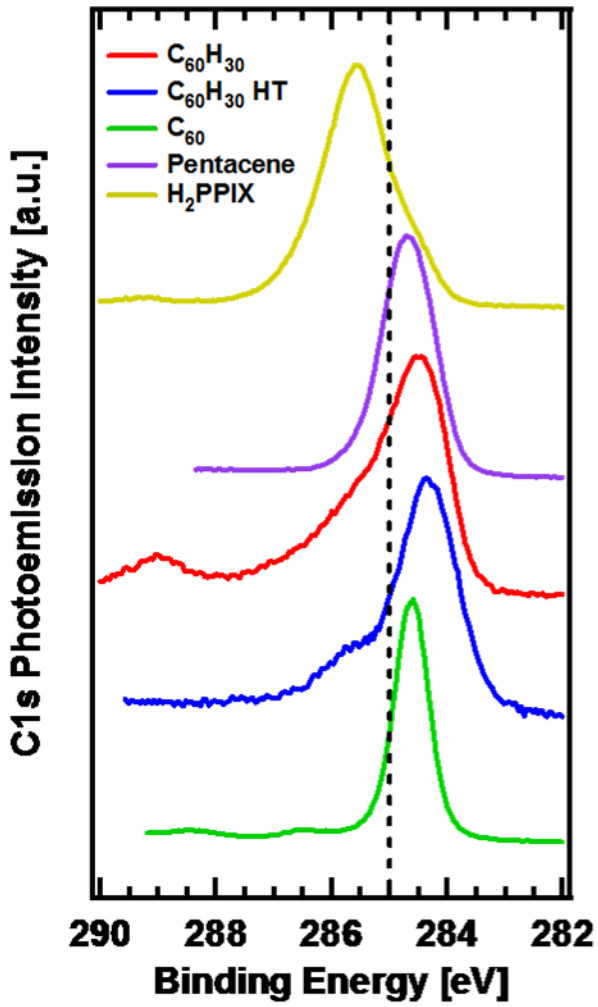

Figure 4.2.4.17.- *Comparison of the C1s photoemission peaks associated to the different molecules used in this thesis*. As a reference, we have marked with a vertical black dashed line the energy position of the C signal for contamination. As contamination is supposed to be in a neutral state, we can see the different shifts occurring. The higher the shift, the stronger is the interaction. E_{ph} = 400 eV, except for H_2PPIX (E_{ph} = 500 eV).

This result is reasonable if we take into account that this is the only system of the ones mentioned above in which we were able to "see" individual molecules with the STM. Assuming an acceptor character for this molecule, as observed when it is deposited on Pt (111) [154], we conclude that the shift is in good agreement with previous observations. However, in less interacting systems such as C_{60} and pentacene, where it is not possible to observe individual molecules and it is necessary to have intermolecular interactions in order to stabilize molecular structures, we find smaller shifts which could be affected by final state effects [78].

Again, H_2PPIX molecules present a different behavior as shown in figure 4.2.4.17. In this case we have a 0.6 eV shift of the C1s peak towards higher BE. This shift is not surprising as we have seen that this molecule interacts strongly with the substrate. The shift direction indicates a charge transfer from the molecule to the substrate probably operated through the N-O bond established between the substrate O_{br} atoms and the molecule. This behavior is in good agreement with the donor character of porphyrin molecules.

Regarding the O1s and Ti2p photoemission spectra, we observe a very similar behavior for all the molecules except for H_2PPIX (see figure 4.2.4.18). Pentacene, C_{60} and $C_{60}H_{30}$ (before and after the high temperature annealing) O1s and Ti2p curves are almost identical to the ones corresponding to the clean TiO_2 surface. This result is reasonable as we have seen that these systems present a very low interaction with the substrate. Additionally, just the surface atoms interact with the molecules while with XPS we get information about several layers, typically 4 – 5 atomic layers. For this reason, any change in the surface atoms would have a very small effect in the O1s and Ti2p bulk peaks. However, things are different for the case of H_2PPIX. In this case, we observe significative differences both in the O1s and Ti2p spectra. For the case of O1s (figure 4.2.4.18 a)), we observe the appearance of two new peaks at high BE, as already observed in section 4.2.4.4. As we showed before, they are associated to protonated and deprotonated carboxylic groups. This result indicates that the carboxylic groups remain unaltered after the deposition. On the other hand, the H_2PPIX Ti2p spectrum shows a small increase of the Ti^{3+} states located in the Ti2p pre-edge region. This result indicates an increase of the number of Ti atoms in a 3+ oxidation state and,

therefore, that the O_{br} atoms are involved in the reaction with the N atoms of the molecule. So, on the one hand we have that the H_2PPIX molecule gives energy to the substrate, as already seen on the C1s peak, and on the other hand, we have an increase of the Ti^{3+} states.

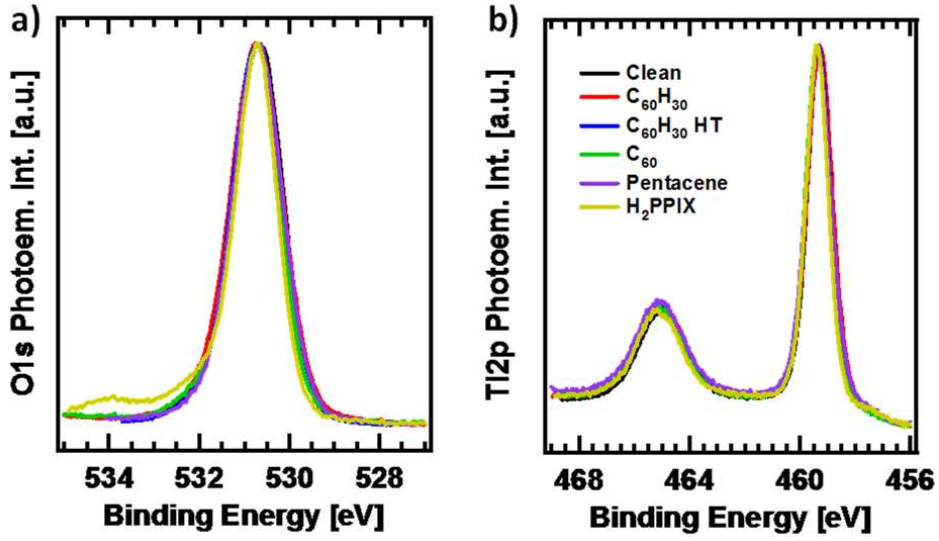

Figure 4.2.4.18.- *Comparison of the O1s and Ti2p photoemission spectra for the whole set of molecules used in this thesis, including the clean TiO_2 surface*. a) O1s spectra. The only spectrum changing significantly from the clean one is the H_2PPIX curve, as we can expect for a strong interacting system. b) Again, the only spectrum showing some difference is the H_2PPIX. The same legend is valid for both graphs. E_{ph} = 650 eV.

Thus, we can infer from both results that the charge leaving the molecules is transferred to the Ti atoms via O_{br} atoms, increasing the occupancy of Ti^{3+} states. This behavior is very similar to the one obtained when Na is deposited on the stoichiometric TiO_2 surface [227]. In that case we observe the appearance of a Ti^{3+} state in the band gap region, equivalent to the one observed for reduced TiO_2 substrates. This effect can be explained considering that the Na atoms give their 1s electron to the substrate. The resulting effect is an increase of the total charge of the substrate with this extra charge going to the Ti^{3+} states.

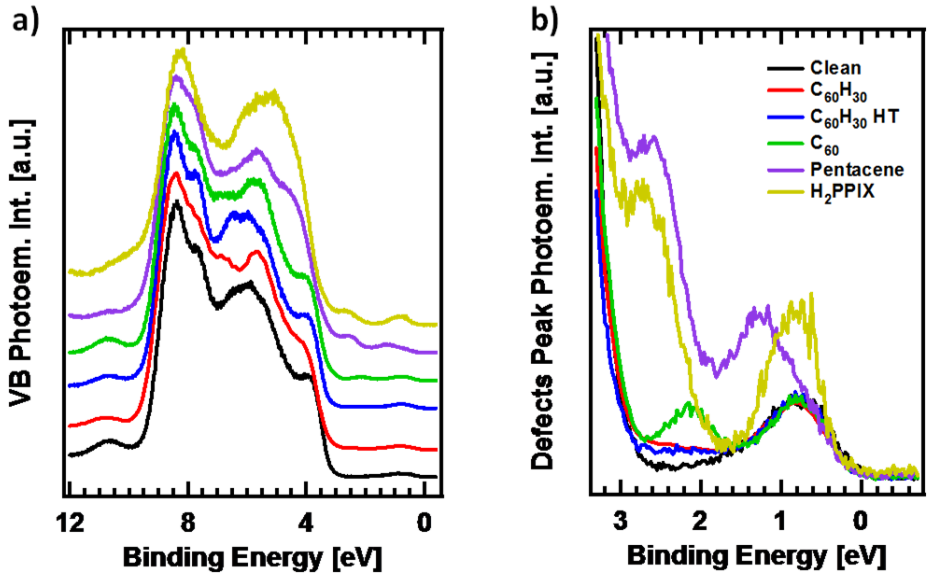

Figure 4.2.4.19.- *Comparison of the valence bands of the different systems.* a) Valence band region. The major changes appear for the H_2PPIX valence band and, to a lesser extent, in the pentacene one. b) Band gap region. We observe the appearance of new states associated to the molecular HOMO´s. In the particular case of H_2PPIX, we also see an increase in the defects peak intensity associated to a charge transfer. The same legend is valid for both graphs. E_{ph} = 130 eV.

Finally, we compare the valence band region in figure 4.2.4.19. As we can see, the most significant changes occur for the most interacting system, H_2PPIX, while the VB presents a very similar aspect for the rest of the cases, including the clean surface. However, more differences appear in the gap region (figure 4.2.4.19 b)). For the case of low interacting systems as $C_{60}H_{30}$ (before and after the high temperature annealing), pentacene and C_{60}, we observe that the characteristic substrate defects state remains unaltered. We also see the appearance of the HOMO states at the same energies as they appear for multilayer coverages or in gas phase, thus indicating again a very low interaction. However, once more the H_2PPIX case is different. We observe a very important increase of the defects state intensity. There are two possible explanations for this increase. It can be due to a superposition of the HOMO state, giving rise to a fictitious increase of this peak. Or it can be due to a

charge transfer from the molecule into the Ti atoms, giving rise to Ti^{3+} states. Although we do not know the position of the HOMO state for the case of H_2PPIX on TiO_2, we can discard the first possibility as we have observed clear evidences of charge transfer from the molecule to the substrate Ti atoms, thus favoring the second possibility.

4.2.4.6. Conclusions

We have seen that as the TiO_2 reactivity is very low, except at the O_{br} sites, its interaction with organic adsorbates is mainly driven by the molecule-molecule interaction. In this sense, molecules capable of interact between them, whether by van der Waals forces (as in the case of C_{60}) or by electrostatic (as for pentacene), form ordered structures, while other molecules such as $C_{60}H_{30}$, which do not present any kind of intermolecular interaction, do not give rise to any type of order on the TiO_2 surface. On the other extreme, H_2PPIX interacts strongly with this surface as it presents four N atoms which are able to bond it to the TiO_2 surface. However, in all cases the reactivity is mainly given by the molecule itself and not by the substrate, which presents a very low reactivity.

5. The rutile TiO_2 (110)-(1x2) reconstructed surface

In this chapter we study some unclear aspects of the (1x2) reconstructed surface. Particularly, we focus our efforts in the understanding of the morphology of the (1x1) → (1x2) phase transition. We analyze the way temperature and annealing time affect the surface quality. Secondly, we characterize the valence band electronic structure of this reconstructed surface. Special attention is paid to the study of the defects peak. Finally, we investigate the initial stages of the platinum growth on the TiO_2 (110)-(1x2) surface. We compare these results with the ones obtained for the deposition of platinum on the unreconstructed (1x1) surface.

5.1. Study of the influence of temperature and annealing duration on the surface 1x1 → 1x2 phase transition

In chapter 2, we showed that the rutile TiO_2 (110)-(1x2) surface structure has been under debate during several years, with four different proposed structural models [45-48]*. Nowadays it is commonly accepted the Ti_2O_3 added row model for this surface structure* [49,50]*. In this model, the new Ti_2O_3 rows are formed on top of the underlying (1x1) rows. The formation mechanism is based on the diffusion of interstitial Ti ions and O atoms from the bulk into the surface, where they react forming the new rows* [228]*. These new rows use the step edges as preferential nucleation sites, growing from them into the TiO_2 terraces* [46,229,230]*.*

Additionally, different (1x2) surface structures have been reported depending on the reduction level of the substrate. There are two main trends. On the one side, Bennet et al. suggest a Ti_2O_3 / Ti_3O_5 structure for low / heavily reduced substrates, respectively [48]*. On the other hand, Asari et al. suggest a Ti_2O / Ti_2O_3 structure, respectively* [228]*.*

Particularly, Asari et al. carried out a temperature and temporal annealing study of the different structures occurring on TiO_2 [228,231]*. As a result of these works, they suggest that the most stable structure below 1000 K is the (1x1) surface, while above this temperature, the (1x2) structure is the most stable one.*

However, a complete study of the influence of the temperature and time of the annealing cycles is still missing. Particularly, it is essential to understand the initial stages of the (1x2) structure formation, together with the best procedure to obtain a good quality (1x2) surface, understanding as good quality surfaces those which are completely reconstructed, with a low density of defects and extended on large terraces (larger than 1000 Å).

In this section we study the influence of temperature and duration of the annealing cycles on the quality of the (1x2) surface.

5.1.1. Influence of the annealing temperature and duration in formation the (1x2) surface reconstruction

In this section we study the effect of the annealing temperature and duration on the formation of the (1x2) surface reconstruction after performing a 30 minutes, 1.0 keV Ar^+ sputtering on an already formed (1x2) surface. We have carried out seven different experiments consisting in annealing at three different temperatures (1000, 1050 and 1100 K) during three different periods of time (10, 30 and 60 minutes) and checking the surface quality by means of the STM. The results we have obtained are shown below.

5.1.1.1. Annealing at 1000 K

At this temperature we have performed three experiments corresponding to the three different annealing durations. Figure 5.1.1 shows two STM images of the TiO_2 surface after annealing at 1000 K during 10 minutes. Figure 5.1.1 a) shows a surface area with an evident accumulation of bright irregular features. These features are TiO_x clusters formed at surface regions where atoms could not reach their crystallographic atomic positions. However, in the upper part of figure 5.1.1 a) it is possible to observe small areas where the (1x2) surface reconstruction is present. The assignment of the bright rows with the (1x2) surface can be done because of two factors. First of all, the separation between rows is approximately 13 Å, as it is expected for the (1x2) surface. Secondly, we observe the presence of bright linking features in between the (1x2) rows. These linking features are *single-links* (SL) and *cross-links* (CL) (see chapter 2) which are known to be characteristic of the (1x2) surface. We can affirm from figure 5.1.1 a) that some surface areas are not only not reconstructed (with a (1x2) structure) but even not formed (with a (1x1) structure) as they present the same appearance of a recently sputtered surface with no evidences of (1x1) surface formation.

Figure 5.1.1 b) shows another region of the annealed surface. In this case, there are no rests of TiO_x clusters as in figure 5.1.1 a). Instead, we clearly observe the coexistence of (1x1) bulk-like surface areas and regions with the already reconstructed (1x2) surface. We can distinguish narrow bright rows, running along the [001] surface direction and wider bright rows running along the same direction. First ones correspond to surface areas with a (1x1)

surface structure while the seconds correspond to (1x2) surface reconstruction regions. The (1x2) bright rows grow on top of the (1x1) rows, in good agreement with the expected position considering the Ti_2O_3 added-row model [49,50]. These bright rows do not necessarily start growing from the step edges. We can observe some of them growing directly in the middle of a terrace. The growth mode seems to be a 1-dimensional growth along the [001] and [00-1] directions from a certain nucleation site. Its position is unclear although it can be related to the presence of defects. Additionally, these bright (1x2) rows present brighter extremes, which can be attributed to an increase in the local density of states (LDOS) due to a lower coordination of the final Ti atoms [232]. Another curious aspect is that SL and CL appear since the very beginning of the (1x2) surface reconstruction formation. As we can see in the bottom left corner of figure 5.1.1 b), there are already SL´s in the growing (1x2) bright rows. It is also worthy to mention that the (1x2) surface formation seems to start in the lower terraces, spreading to higher ones once they are formed, as can be observed in figure 5.1.1 b), where the lower terrace is completely formed while the higher one is still in its formation process.

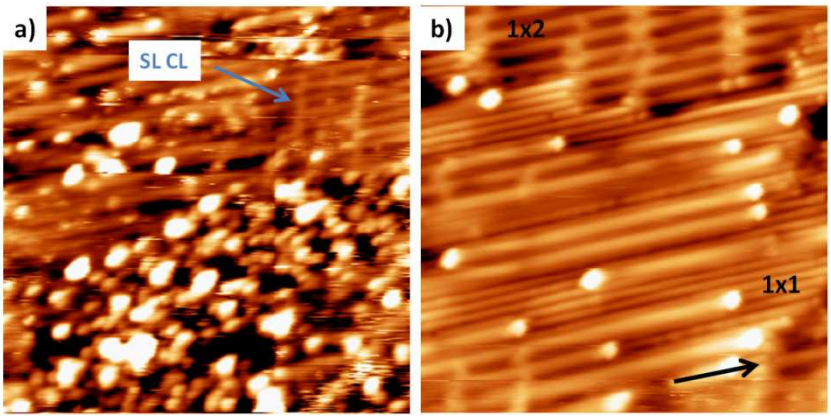

Figure 5.1.1.- *TiO_2 surface after annealing 10 minutes at 1000 K*. Both STM images correspond to two different surface regions of the same sample. a) In this part of the sample we observe areas where the surface still presents a high corrugation (lower part of the image) together with some areas where the (1x2) structure is formed (upper-right corner). Size: (750 Å x 750 Å), I = 0.10 nA, V = 1.2 V. b) Another surface region. In this case it is possible to see both structures, (1x1) and (1x2), coexisting. Black arrow indicates the [001] surface direction, that it is the same for both images. Size: (500 Å x 500 Å), I = 0.10 nA, V = 1.2 V.

Figure 5.1.2 shows a STM image of the TiO_2 surface after annealing the previous surface at the same temperature for twenty more minutes (total annealing time: 30 minutes). Despite the STM tip has no good resolution, we can see the presence of wide bright rows running along the [001] surface direction, together with the presence of CL´s. Due to the bad tip quality we just can say that there is an increase in the surface area covered with the (1x2) structure. This result could be expected as an increase in the duration of the annealing implies that surface atoms have more time to find their minimum energy structure.

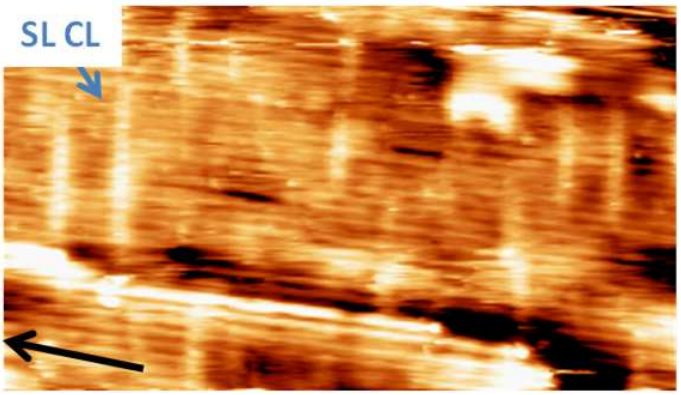

Figure 5.1.2.- *TiO_2 surface after annealing the previous surface 20 more minutes at 1000 K (total annealing time: 30 munites)*. Despite the low tip resolution, we can observe bright rows running along the [001] surface direction (indicated by a black arrow), separated between them by approximately 13 Å. Thus we can associate them with the (1x2) rows. They almost cover the entire surface, indicating a high reconstruction degree. Vertical bright lines correspond to SL and CL. Size: (1000 Å x 570 Å), I = 0.10 nA, V = 1.2 V.

If we finally increase the annealing time another thirty minutes, getting a total annealing time of 60 minutes, we obtain the STM image shown in figure 5.1.3. After this long lasting annealing, we can see that the surface is completely covered with the (1x2) structure. This result is corroborated by the LEED pattern taken after this treatment, which presents round and sharp spots (see inset figure 5.1.3). We also observe the presence of SL and CL, as expected for this surface. Additionally, we can see some bright spots on top on the (1x2)

rows which can be associated to the positions where the bright (1x2) extremes of different rows have made contact (blue dotted circles). It is also possible to distinguish surface areas where there are domain frontiers due to anti-phase rows touching in a certain point (green dotted ellipse).

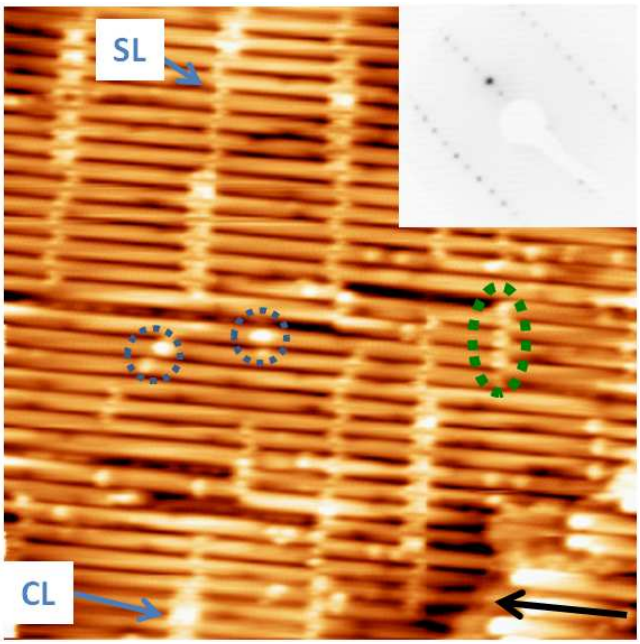

Figure 5.1.3.- *TiO_2 surface after annealing 10 + 20 + 30 minutes at 1000 K*. This STM image shows that the surface is completely reconstructed after annealing at 1000 K during 60 minutes. We observe the presence of some defects like bright features on top of the (1x2) bright rows, which are probably associated to the bright extremes of two growing rows when closed to touch one each other (blues dotted circles). It is also possible to see domain frontiers due to the meeting of (1x2) rows separated between them by just one (1x1) unit cell along the [1-10] (the [001] direction is indicated by a black arrow). Finally we can also distinguish the presence of SL and CL. Inset: LEED pattern taken at 133 eV. Spots are round and well-defined, thus indicating a good surface quality. Size: (500 Å x 500 Å), I = 0.10 nA, V = 1.2 V.

Summarizing, after annealing the surface at 1000 K during 10 minutes a coexistence of three types of surfaces is observed. We have areas where the surface have not even been formed with the initial (1x1) structure, areas

exhibiting a well formed (1x1) structure and areas where the (1x2) reconstruction is starting to be formed. In fact, we can propose a growing model in which the sequence would be, starting from the sputtered surface, first the formation of the bulk-like (1x1) structure and once it is formed, the subsequent formation of the (1x2) reconstruction. These new rows start growing on top of (1x1) ones. We also observe the appearance of SL and CL since the very beginning of the (1x2) formation. As we increase the duration of the annealing cycle, it increases the surface area covered by the (1x2) structure until we have its complete formation for an annealing of 60 minutes. At this point we also find domain frontiers due to the coalescence of two different rows separated only by one (1x1) unit cell along the [1-10] direction.

5.1.1.2. Annealing at 1050 K

When the sputtered surface is annealed at 1050 K during 10 minutes, it exhibits the same aspect at the STM as the one shown in figure 5.1.4. Although the STM tip quality is poor, it is enough to see a higher degree of (1x2) structure formation than in the case of the same annealing duration at 1000 K (figure 5.1.1). It seems there are still some surface areas not properly formed, like the one in the upper-right corner of figure 5.1.4, but we observe that the lower terraces are almost reconstructed. We can also find (1x2) structure free areas, like the one marked with a blue dotted ellipse in figure 5.1.4. It is not easy to know what the structure in that region is, but probably it is not formed.

If we increase the annealing duration to 30 minutes, we appreciate an important improvement in the surface quality although we still have a rough tip. We can see an example of the surface appearance in figure 5.1.5. After this second annealing, we observe that almost all the surface is covered with the (1x2) reconstructed structure, except for some dark regions where the (1x1) surface is probably still present. We also notice an improvement in the size of the terraces, becoming larger (at least 1000 Å). However, we still have detected unreconstructed areas after this annealing so a longer one is mandatory to obtain a good quality surface.

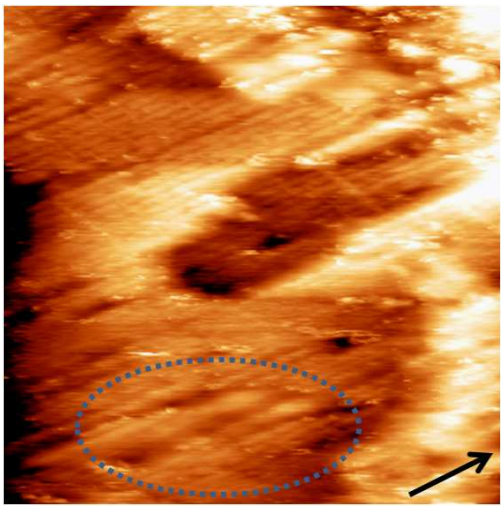

Figure 5.1.4.- *TiO_2 surface after annealing 10 minutes at 1050 K.* After this short annealing we observe an increase in the (1x2) coverage with respect to the value obtained for the same annealing time but at lower temperature, even though the tip resolution is poor. But we still can find regions with a high corrugation (upper-right corner) and areas with undefined structures, like the one marked by the blue dotted ellipse. Size: (1000 Å x 1000 Å), I = 0.10 nA, V = 1.2 V.

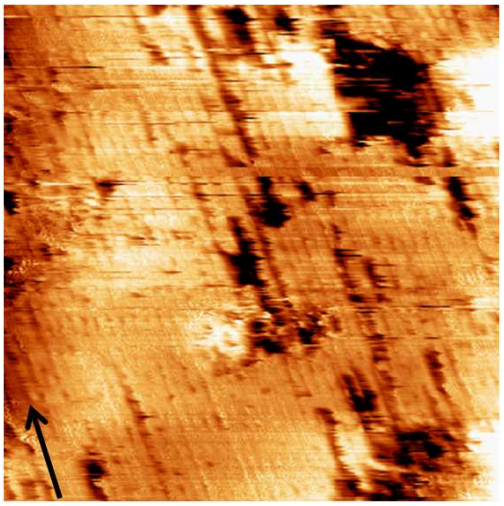

Figure 5.1.5.- *TiO_2 surface after annealing 10 + 20 minutes at 1050 K*. Despite the low tip resolution, it is possible to observe that the surface is almost completely reconstructed. However, there are still some dark areas where the surface probably presents a (1x1) structure. Size: (1000 Å x 1000 Å), I = 0.10 nA, V = 1.2 V.

Figure 5.1.6 shows two STM images of the surface after annealing at 1050 K during 60 minutes. As we can see in figure 5.1.6 a), the surface presents a quite good quality. We have large flat terraces extending for more than 2000 Å, composed by well reconstructed (1x2) rows running along the [001] surface direction. We can still distinguish some dark small areas in the terraces related to regions where the surface still presents a (1x1) structure. However, some of the dark lines visible in the STM image are due to domain frontiers. Approximately at the center of the image it is possible to see a variation in the rows directions (blue arrow). This zigzag is not a real effect but induced by an irregular behavior of the piezoelectric system during the scanning or a movement of the tip apex. If we look in detail the (1x2) rows we obtain images like the one exhibited in figure 5.1.6 b). In this high-resolution STM image we can see the (1x2) rows inner structure. They are composed of two maxima rows running parallel along the [001] direction, in good agreement with the position of the Ti atoms inside the Ti_2O_3 model for these rows [49,50]. However, we can see that the (1x2) rows are not completely straight but they present a slight modulation along the [001] direction, i.e. their width is not constant. This is probably due to some Ti or O atoms missing in the structure, associated to a lack of temperature during the annealing cycle.

Curiously, we do not observe SL or CL in the TiO_2 surface after these preparation cycles. The reasons remains unclear and it would be interesting to study this effect in detail.

From these experiments we can conclude that there is an improvement in the surface quality and in the terraces dimension when increasing the annealing temperature. However, the surface it is still not perfectly formed as there are small unreconstructed regions and evidences of Ti or O atoms missing in the (1x2) rows.

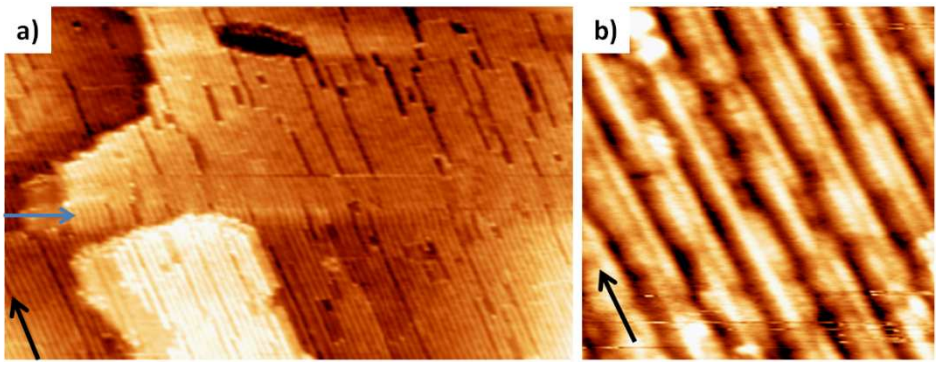

Figure 5.1.6.- *TiO_2 surface after annealing 10 + 20 + 30 minutes at 1050 K*. a) In this large STM image we can see that the surface is almost completely reconstructed. There are just some small dark regions where the surface still presents the (1x1) structure. However, some of the dark lines are not unreconstructed regions but a consequence of domain frontiers. Blue arrow indicates the position where a piezoelectric instability occurs. Size: (2000 Å x 1250 Å), I = 0.10 nA, V = 1.2 V. b) Closer inspection of the (1x2) rows. As we can see they do not present a constant width probably due to Ti or O atoms missing in the rows because of a lack of temperature. Size: (150 Å x 150 Å), I = 0.17 nA, V = 1.1 V.

5.1.1.3. Annealing at 1100 K

For this temperature we have just carried out one experiment, annealing the surface during 60 minutes. The surface obtained is shown in the images in figure 5.1.7. In both STM images of the surface we can observe an important improvement of the surface quality. In this case, the entire surface is completely covered with the (1x2) rows except for some dark lines which are usually associated to domain frontiers. Terraces are flat and very large, extending along more than 2000 Å. Again, there are no evidences of SL or CL in the surface. We can consider this surface as a good quality one to be used in studies related to the (1x2) surface.

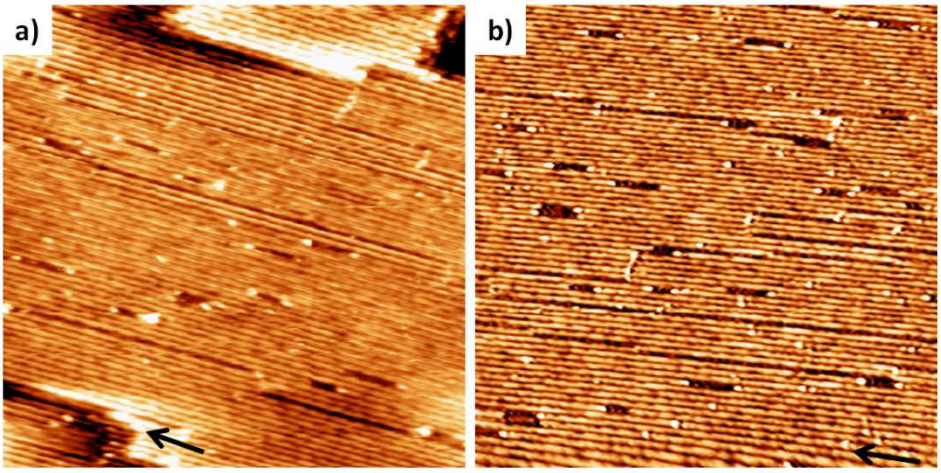

Figure 5.1.7.- *TiO_2 surface after annealing 60 minutes at 1100 K*. In both STM images we can see that the surface is completely reconstructed with almost no defects, except for the domain frontiers. We also observe an important improvement of the surface quality reflected in an increase in the terraces dimensions. a) Size: (1000 Å x 1000 Å), I = 0.16 nA, V = 1.2 V. b) Size: (1200 Å x 1200 Å), I = 0.23 nA, V = 1.6 V.

5.1.2. Conclusions

In this section we have shown that not only the temperature but also the duration of the annealing cycles are important in order to obtain a good quality surface, understanding by that a surface with large well ordered terraces. We have demonstrated that in order to have well formed (1x2) rows it is necessary to anneal at least at 1100 K during 60 minutes. Lower temperature annealing cycles result in not totally formed (1x2) rows, while shorter ones do not allow the complete formation of the surface. We have also noticed that the sequence followed by the surface for the (1x2) structure formation starting from the sputtered surface is, firstly, the formation of the (1x1) structure and, afterwards, the creation of the (1x2) one. These reconstruction rows start growing at any point of the surface, step edges or terraces, and grow on top of the (1x1) rows. This is the reason why they need the previous formation of the (1x1) rows. The growing (1x2) rows present bright features in the extremes due to an electronic effect related to the lower coordination of the Ti atoms in these positions. We have also shown that the

characteristic SL and CL appear since the very beginning of the (1x2) surface formation. However, under certain conditions, these SL and CL disappear. The reasons remain unclear and this effect deserves a detailed study.

5.2. Characterization of the valence band electronic structure of the rutile TiO_2 (110)-(1x2) surface

In order to completely characterize the behavior of a widely used material such as TiO_2 it is important to understand its electronic properties. A huge amount of studies have been carried out on the rutile TiO_2 (110)-(1x1) surface (see [14] *and references therein) but much less it is known about the electronic structure of the (1x2) surface reconstruction. From the theoretical point of view, the lack of information about the exact atomic positions of the surface atoms made impossible to perform an accurate model of the electronic structure. This problem is already solved since the determination of the surface atomic positions, four years ago* [49,50]*. In the first work, it is also reported the possibility of a 1-dimensional metallicity along the surface reconstruction rows extending along the [001] surface direction. Such a behavior, recently observed in another oxide system as STO* [233] *would have very important fundamental and technological implications as this metallic character means having a high catalytic activity on an insulating material.*

One important issue in the study of TiO_2 is the presence of defects of different nature and their influence in the material as they will confer it unusual properties. As they exhibit a local character, scanning probe microscopies are crucial for their study although its assignation is not straightforward [109,110,112-115,234]*. These defects have to be characterized both, from a topological and electronic point of view to be fully understood. Although they have a local character, the important amount of defects present in the substrate allows us to study them with spectroscopic techniques.*

Ideally, the electronic configuration of stoichiometric TiO_2 corresponds to Ti^{4+}-$3d^0$. The presence of a defect will induce a local redistribution of the charge density which will affect the Ti atoms located in the surroundings of this defect (O_{vac}, interstitial Ti atoms or any other adsorbate transferring charge to the substrate [227]*)* [44,235,236]*. These new electrons will populate the Ti 3d orbitals changing the Ti oxidation state from 4+ to 3+. This change in the oxidation state produces basically two modifications in the electronic structure of TiO_2, which are detected in photoemission: the appearance of the shoulder in the low binding energy region of the Ti 2p state and the new electronic state in the band gap region, at about 0.8 eV below the Fermi level. This defects state has been extensively studied, mainly in the TiO_2 (110)-(1x1) surface* [14,63,237]*. As the (1x2) surface reconstruction is formed by further reduction of the (1x1)*

surface, a large amount of defects are created in this process giving as a result the enhancement of the Ti^{3+} state [238]*. But this enhancement, as we will show later, it is not only due to an increase in the amount of defects. The formation of the (1x2) surface reconstruction formed by Ti_2O_3 rows will also increase the emission from the defects state, as Ti atoms present a 3+ character.*

In this section we study the valence band electronic structure of the TiO_2 (110)-(1x2) surface reconstruction both experimentally and theoretically by UPS / ARUPS and DFT calculations, respectively. We pay special attention to the study of the origin of the defects state that appears at a BE of approximately 0.8 eV. We show that for the (1x2) surface this state presents a double contribution, one associated to the Ti^{3+} present in the (1x2) reconstruction rows, and the other one related to the Ti^{3+} atoms present throughout the crystal bulk. We also report the presence of a dispersive band along the [001] direction and centered at a BE of 7 eV and a $k_{\parallel}$ = 0.35 $Å^{-1}$. We show that this band is associated to the bulk structure. Finally, we report a nice agreement between the experimental and theoretical total density of states (DOS) of the system.

5.2.1. Band dispersion of the TiO_2 (110)-(1x2) surface

We have studied the valence band dispersion along the two main high-symmetry crystallographic directions. In this way we completely characterize the electronic structure of this surface. Figure 5.2.1 shows a schematic representation of the *Surface Brillouin Zone* (SBZ) corresponding to the (1x1) and (1x2) surfaces. Two rectangles can be observed, one black and one red, which are associated to the reciprocal space surface unit cells of the (1x1) and (1x2) structures, respectively. The dimensions of these unit cells along both high-symmetry directions are given in the figure.

We have measured the valence band dispersion of the TiO_2 (110)-(1x1) surface along the two high-symmetry directions. The result is represented in figures 5.2.2 a) and b). We indicate in both graphics the high-symmetry points of the SBZ as well as the Fermi level (E_F). In these bidimensional representations, the

darkest features correspond to more intense photoemission peaks while the brightest ones represent the less intense emissions.

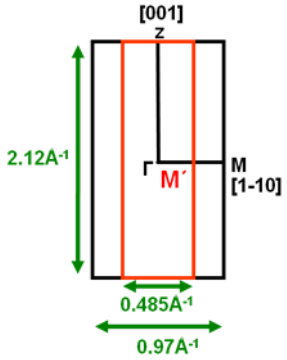

Figure 5.2.1.- *Schematic representation of the Surface Brillouin Zone (SBZ).* The red rectangle corresponds to the reciprocal space unit cell of the (1x2) surface while the black one is the reciprocal space unit cell of the (1x1) surface. We have marked the high-symmetry direction and the periodicity along them.

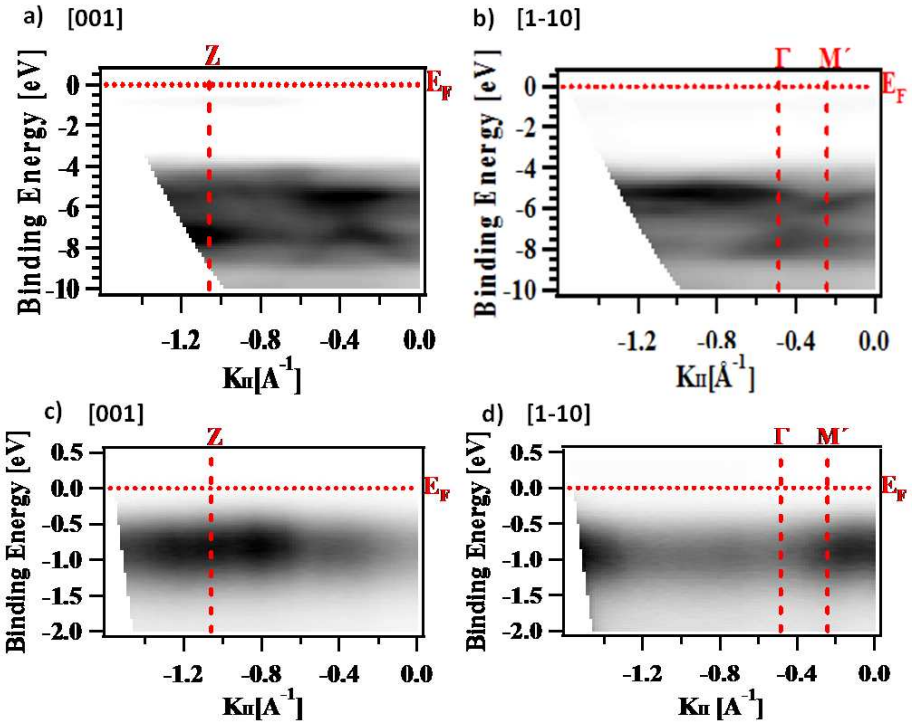

Figure 5.2.2.- *Bidimensional representations of the ARUPS spectra for the TiO_2 (110)-(1x2) surface*. a) and b) ARUPS spectra for the valence band region along the [001] and [1-10] directions. c) and d) The same for the defects state region. Darker features correspond to more intense emission. We have marked the reciprocal space high-symmetry points together with the Fermi edge.

We can observe a dispersive band along the [001] direction at a BE of 7 eV and centered at 0.35 $Å^{-1}$. On the other hand we do not observe any dispersion state along the [1-10] direction, i.e. perpendicularly to the reconstruction rows.

In figures 5.2.2 c) and d), we present a bidimensional representation of the experimental defects state dispersion along the [001] and [1-10] directions, respectively. We cannot observe any dispersion of this state along any of the directions. This result contrasts with the DFT theoretical prediction of a metallicity along the [001] direction [49]. This disagreement can be explained by two different facts. It could be due to a lack of experimental resolution close to the Fermi level, which would not allow us to appreciate the presence of a small upwards dispersing component. In this case, high-resolution images, as the ones shown in ref. [233], have to be taken using Synchrotron Radiation. The second plausible explanation is that the theoretical calculations carried out in ref [49] were not accurate enough in this point. We have to remind that DFT calculations usually fail when trying to reproduce the conduction band. In any case, inverse photoemission or Synchrotron Radiation valence band photoemission dispersion could be indicated techniques for clarifying this point.

Figures 5.2.2 c) and d) present intensity maxima at 0.8 $Å^{-1}$ (along the [001] direction) and at 0.15 $Å^{-1}$ (along the [1-10] direction), approximately. This intensity modulation can be explained by final-state scattering effects, i.e. as an ultraviolet photoelectron diffraction effect (UPD) [239].

Let´s focus now on the understanding of the origin of the dispersive band observed along the [001] direction. Figure 5.2.3 shows a zoom of the 0 - 0.5 $Å^{-1}$ region in figure 5.2.2 a). We have superimposed to it, in red, a theoretical dispersive band obtained from DFT calculations, which is located at 7 eV of BE and around 0.35 $Å^{-1}$. The agreement between theory and experiment is very good, thus indicating the bulk origin of this band.

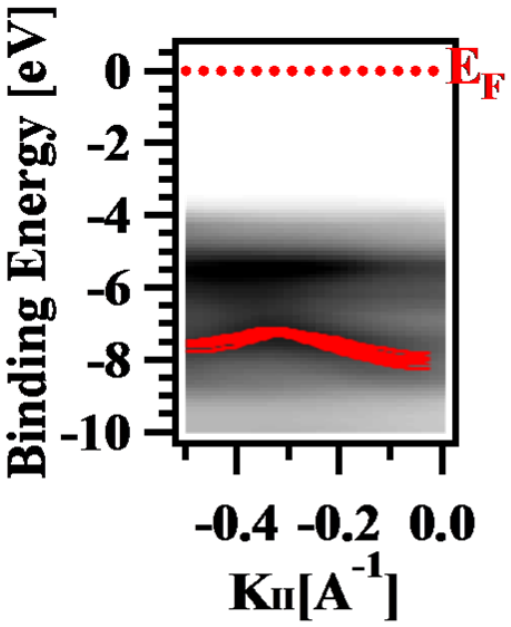

Figure 5.2.3.- *Zoom of the bidimensional representation of the valence band dispersion along the [001] direction*. We can observe a dispersive band at BE = 7 eV and centered at 0.35 $Å^{-1}$. We have superimposed the theoretical DFT calculation for the dispersive band.

An easy and approximate way to have an experimental estimation of the total DOS of the rutile TiO_2 (110)-(1x2) surface is to integrate all the measured valence band spectra along both high-symmetry directions, as obtained in figures 5.2.2 a) and b). We show the resulting DOS in figure 5.2.4. We also present in the same figure the theoretical DOS obtained from DFT calculations. It is important to mention that the symmetric slab constitutes an improvement on the model used in [49], which contains a spurious contribution from the bulk-terminated (1x1) surface. This caused a splitting in the deeper energy levels that vanishes in the present calculation. Since regular DFT-GGA calculations fail in the gap value determination, the theoretical DOS shown in figure 5.2.4 just exhibits the valence band region. For its representation, we have introduced an offset in the BE in order to make it fit with the experimental DOS. If we compare them we can observe that we obtain a nice

agreement between theory and experiment, both in the shape and width of the DOS.

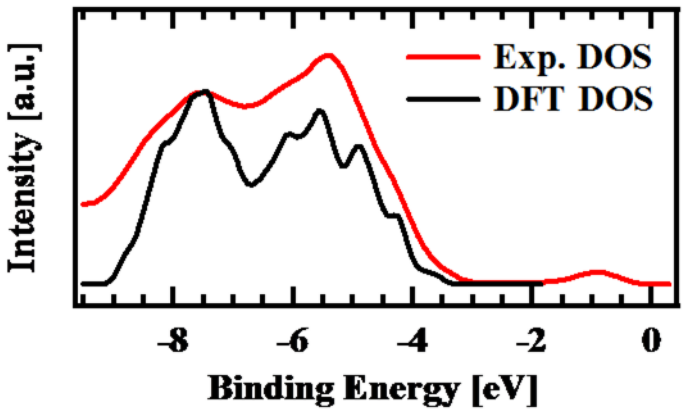

Figure 5.2.4.- *Comparison between the experimental and theoretical total density of states*. The experimental DOS has been estimated integrating the ARUPS spectra obtained for both high-symmetry directions. The theoretical one has been obtained from DFT calculations.

5.2.2. Characterization of the band-gap state

As mentioned in the introduction we have carried out an exhaustive study of the defects state located in the TiO_2 (110) band-gap. We have studied the origin of this state depending on the reduction level of the substrate and, consequently, of the corresponding surface. In this sense we have performed UPS measurements for three different reduction levels of the substrate. As we mentioned before, the origin of this defects peak is the existence of Ti^{3+} states due to the reduction of the substrate. However, there also exist Ti^{3+} states associated to the Ti atoms in the (1x2) reconstruction. As both chemical environments are different, they should give rise to two different photoemission signals separated by a certain binding energy, making possible their distinction by means of UPS. We show in figure 5.2.5 UPS spectra of the band-gap states region for both a poorly reduced and a highly reduced substrate with a (1x1) surface symmetry and for a heavily reduced (1x2)

symmetry at the surface. In all spectra, the red solid line through the black data circles represents the result of the least-squares fit, with the blue dashed-dotted component giving the signal corresponding to the low binding energy (BE) peak and the green solid curve showing the high BE emission. The yellow dashed line represents the linear background. Just one peak is necessary to properly fit the experimental data associated to the poorly reduced TiO_2 (110)-(1x1) surface, as we can see in figure 5.2.5 a). This Gaussian peak presents a BE of 0.78 eV and a full-width half-maximum (FWHM) value of 0.62 eV. By further reduction of the substrate maintaining a (1x1) surface, we observe an enhancement of the defects state photoemission intensity, as it is evident from figure 5.2.5 b). Again, we just need one peak to fit the experimental data, being this peak almost identical to the one used for the previous case except for an increase in the intensity. The parameters of this Gaussian peak are BE = 0.77 eV and FWHM = 0.63 eV. If we keep on reducing the substrate, at a certain point the surface undergoes a phase transition from a (1x1) to a (1x2) surface symmetry. As we know, this new surface characterizes by a Ti_2O_3 stoichiometry at the surface and the associated defects state becomes wider and more intense. This makes impossible to fit it just with one peak and a second Gaussian subspectrum has to be added. This second peak appears at a slightly higher BE as we can see in figure 5.2.5 c), while the first peak remains at the same position as in the previous cases. The parameters of the two subspectra used for the fitting are summarized in table 5.2.I. As one could expect from the existence of two different chemical environments associated with the Ti^{3+} states, the UPS experiment clearly indicates the presence of two different contributions to the band-gap state: one related to the bulk defects characteristic of the (1x1) surface and another one due to the Ti atoms present at the (1x2) surface reconstruction.

	Binding Energy [eV]	FWHM [eV]
Peak 1	0.75	0.67
Peak 2	1.18	0.51

Table 5.2.I.- *Peak parameters of the two components obtained in the defects peak fitting*. Peak 1 corresponds to the peak already obtained in the two previous cases while peak 2 is a new peak that we have to introduce in order to be able to fit the experimental results.

The possibility of being able to distinguish the two components for the defects state can have several important consequences. For example, it can be used to determine the existence and quality of the (1x2) surface reconstruction on the surface by just fitting the defects state. It can also be used to determine the nature of the interaction of adsorbates with the (1x2) reconstruction by analyzing the evolution of the relative intensity of the different components of the band-gap state upon deposition.

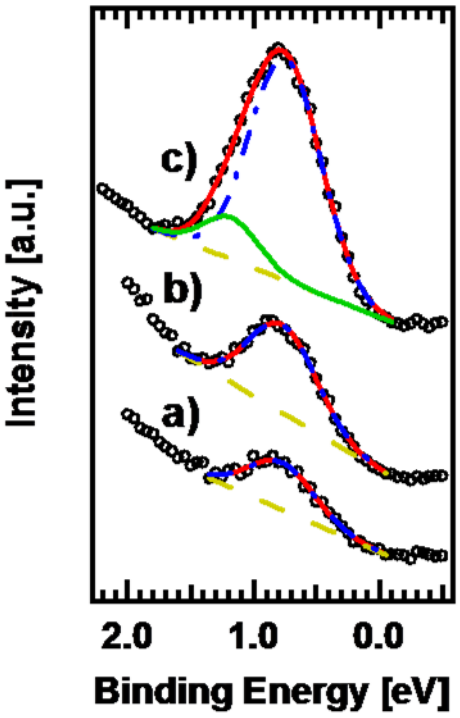

Figure 5.2.5.- *Evolution of the defects state with the reduction level*. a) Defects peak signal for a poorly reduced TiO_2 (110)-(1x1) surface. B) Defects peak signal for a highly reduced TiO_2 (110)-(1x1) surface. c) Defects peak signal for a heavily reduced TiO_2 (110)-(1x2) surface. When the (1x2) surface is created, a new peak in the defects state appears. This peak is associated to the Ti3+ states present in the reconstruction rows. Color code: Black circles (raw data), red solid line (least-squares fit), blue dashed-dotted curve ((1x1) contribution), green solid line ((1x2) contribution) and dashed yellow line (linear background). Excitation source: HeI lamp (hv = 21.22 eV).

5.2.3. Conclusions

In this section we have characterized the electronic structure of the rutile TiO_2 (110)-(1x2) surface, paying special attention to the Ti^{3+} band-gap state. By means of ARUPS we report the presence of a downwards dispersive band along the [001] direction. By comparison with the theoretical DFT DOS we show that this dispersive band located at 7 eV below the Fermi edge and centered at 0.35 $Å^{-1}$ has a bulk origin. We also estimate the experimental total density of states for this surface by integrating the ARUPS spectra obtained along both high-symmetry directions. The agreement with the theoretical total density of states is very good. On the other hand, we do not observe any dispersion of the defects state.

Regarding the defects state emission, we show that this peak presents a double contribution. One component is associated to the Ti^{3+} cations related to the bulk defects. The other one, which is only observed for the TiO_2 (110)-(1x2) surface, is due to the Ti^{3+} atoms present in the Ti_2O_3 surface reconstruction.

5.3. Morphological study of the platinum / rutile TiO_2 (110)-(1x2) system

TiO_2 is one of the most widely used catalytic supports [14]. *Its catalytic properties dramatically depend on its electronic structure. Variations in the electronic structure can result in changes in the catalytic properties of the system. As we have shown in the previous section, the presence of defects modifies the electronic structure of TiO_2. As an example, we have seen that the defects peak that appears in the energy band-gap changes depending on the surface stoichiometry and structure. When the surface undergoes a phase transition from the (1x1) to the (1x2) surface, a new contribution appears in the defects peak, which is associated to the Ti^{3+}atoms located at the Ti_2O_3 reconstruction rows. Other characteristic features of the (1x2) surface such as "single-links" and "cross-links" can also influence the catalytic properties of TiO_2* [48,55-60]. *These surface peculiarities are associated TiO_2 and Ti_2O_3 units, respectively, which diffuse on the surface until they are trapped by two neighboring Ti_2O_3 rows. As a consequence, a rearrangement of the surrounding atoms takes place giving rise to the formation of rows running along the [1-10] surface direction, interrupting the characteristic rows of the reconstruction.*

The combination of TiO_2 with noble metals such as Pt, Pd, Ir, etc., is much utilized for technological applications. However, most of the noble metals adsorption studies have been performed on the stoichiometric (1x1) surface [14]. *Platinum is one of the most studied catalysts as it is the most commonly used one. Its deposition on the TiO_2 (110)-(1x1) surface has been extensively investigated. It has been determined that Pt films present a Volmer-Weber growth with randomly distributed clusters on this surface* [17,22]. *For Pt coverages of 25 ML and upon annealing at high temperature, the majority of the clusters present a quasi-hexagonal shape, although some square cluster are also present* [19]. *These Pt clusters undergo encapsulation by titanium oxides after the high temperature annealing process* [19,21,22,240].

Some of these noble metals such as Rh [241,242], *Ir* [243,244] *and Pt* [245,246] *have also been deposited on the TiO_2 (110)-(1x2) surface. In ref. [245], the study deals with the effect of the Pt cluster size on the adsorption chemistry of CO. For the analysis, they considered a surface structure model based on added-rows with Ti_3O_5 stoichiometry. However, it has been recently established experimentally and theoretically a Ti_2O_3 added-row model for the TiO_2 (110)-*

(1x2) surface [49,50]*, so it is advisable to revisit the Pt growth process taking into account these considerations.*

In this section, we study the initial stages of the Pt growth on the TiO_2 (110)-(1x2) surface by means of a combination of STM experiments and DFT calculations. We propose a Volmer-Weber (VW) growth where Pt atoms are sitting on top of the Ti_2O_3 rows at hollow positions. Additionally, after annealing at ~ 825 K, we observe diffusion of the Pt clusters to the cross-links nucleation sites together with an increase in their size and height. Contrary to the (1x1) surface, we show that for small particle sizes there are not evidences of Pt encapsulation.

5.3.1. Study of the platinum deposition at room temperature

We have used the TiO_2 (110)-(1x2) surface as a template for the deposition of very small amounts of platinum (coverage << 1 ML). As we can see in the schematic representation of the TiO_2 (110)-(1x2) surface shown in figure 5.3.1 a) this surface is composed by Ti_2O_3 rows which extend along the [001] direction. The appearance of this surface to the STM is shown in figures 5.3.1 b) and c) (the [001] surface direction is indicated by a black arrow). Each of the bright rows which run along the [001] direction correspond to a Ti_2O_3 row of the reconstruction [14]. All the STM images have been measured with positive voltages applied on the sample. This means that electrons are traveling from the tip into the unoccupied states of TiO_2, which present a predominant Ti 3d character. For this reason the bright features inside the bright rows can be assigned to the Ti atoms which form the Ti_2O_3 rows. In these STM images we can also distinguish bright features running along the [1-10] surface direction and linking some of the bright rows of the reconstruction. They are associated to the “single-links” (SL) and “cross-links” (CL) that we have already mentioned (marked by arrows in figure 5.3.1 b)) [55]. We present in figure 5.3.1 c) a closer view of some CL´s perpendicular to the Ti_2O_3 rows of the TiO_2 (110)-(1x2) surface reconstruction. We can distinguish some bright features arranged in a cross-shaped configuration inside the atomic resolution STM image of the CL´s shown in figure 5.3.1 c). These features are in agreement with the previous proposed model for these linking structures. On the other hand, SL´s are

considered as one half of a fully CL [48] and they are ascribed to TiO_2 or TiO units trapped between Ti_2O_3 rows [55]. Their formation is still an open question as it has been reported that they appear after re-annealing an oxygen-treated TiO_2 (110) surface in UHV [48,55-59] but we have shown in the previous chapter that they are also formed after annealing in UHV at high temperatures (~ 1200 K) [60].

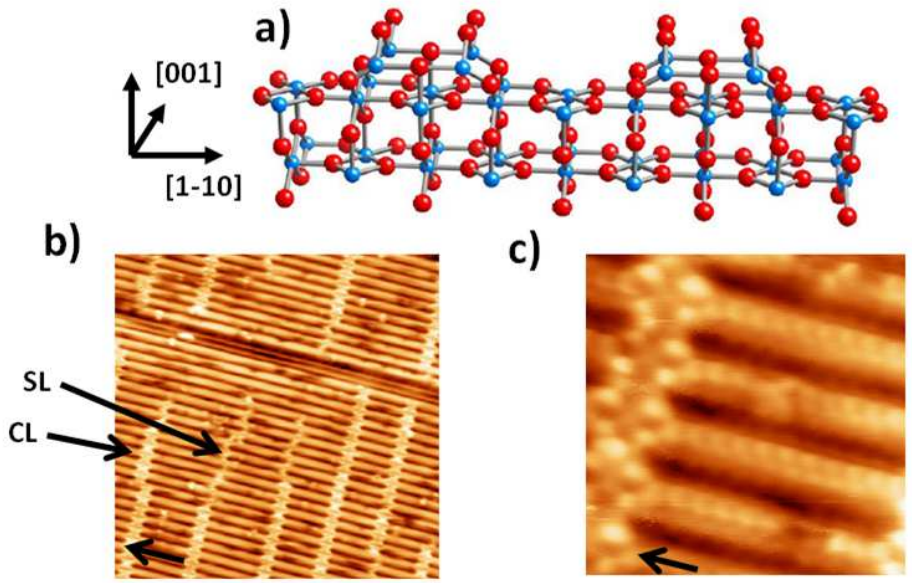

Figure 5.3.1.- *The TiO_2 (110)-(1x2) surface*. a) Schematic ball-and-stick model of the surface reconstruction. Big red and small blue balls correspond to oxygen and titanium atoms, respectively. We can see that the surface presents a Ti_2O_3 stoichiometry at the surface with rows running along the [001] surface direction. b) STM image of the (1x2) surface reconstruction. Bright rows running along the [001] direction (indicated by a black arrow) correspond to the Ti_2O_3 rows of the reconstruction. We can also observe bright features which extend along the [1-10] direction. Some of them present a zigzag shape and others a cross shape. They correspond to single-links and cross-links, respectively (marked by arrows). Size: (500 Å x 500 Å), I = 0.10 nA, V = 1.2 V. c) Zoom of the previous STM image. In this atomic resolution image we can see in detail the cross-shaped feature corresponding to a CL. Size: (80 Å x 80 Å), I = 0.10 nA, V = 1.2 V.

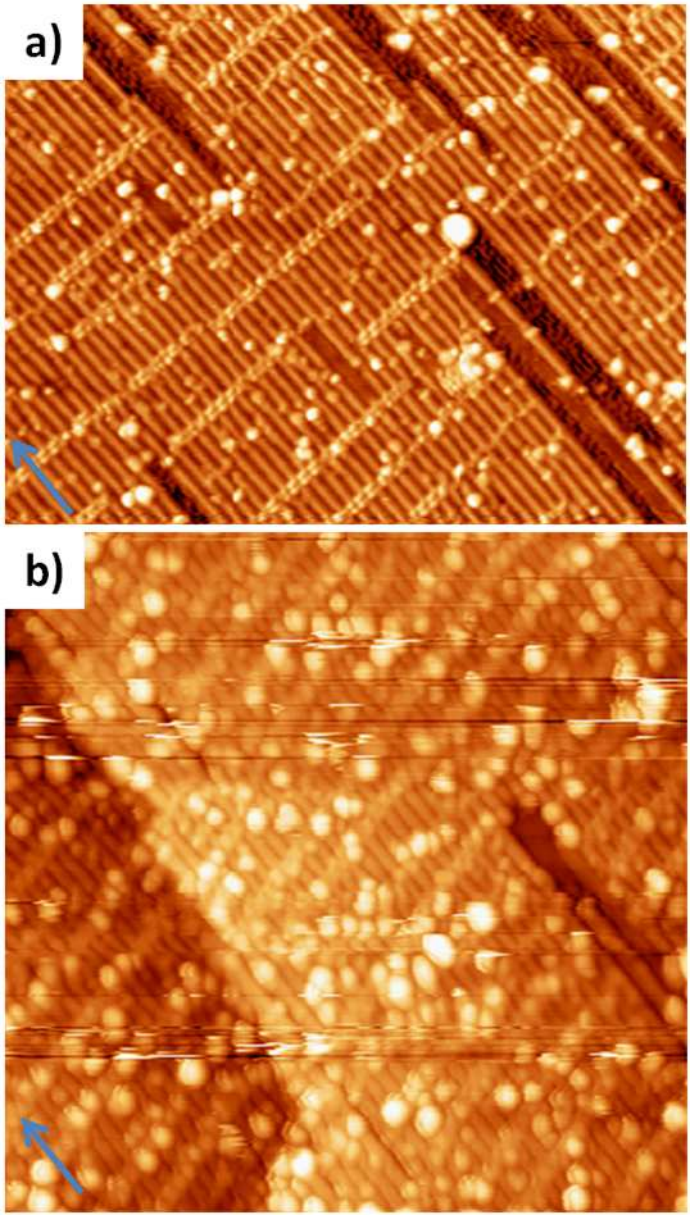

Figure 5.3.2.- *STM images of the (1x2) surface of TiO_2 after deposition of platinum*. a) STM after deposition of 0.1 ML. We can see the formation of Pt clusters randomly distributed on the surface. In both images, the [001] direction is indicated by a blue arrow. Size: (500 Å x 380 Å), I = 0.13 nA, V = 1.5 V. b) STM after deposition of 0.4 ML. We observe an increase in the number of clusters which are again randomly distributed on the surface. Size: (500 Å x 500 Å), I = 0.11 nA, V = 1.5 V.

We have used this surface for the deposition of Pt atoms at room temperature for two different values of the coverage, 0.1 ML (figure 5.3.2 a)) and 0.4 ML (figure 5.3.2 b)). Analyzing these images, it is evident that the deposited material is homogeneously distributed on the TiO_2 surface with the Pt clusters mainly located on top of the bright rows of the (1x2) reconstruction. This result is more visible for figure 5.3.2 a) where the Pt coverage is lower. In both cases we cannot observe any preference for the formation of Pt clusters at step edges thus indicating that there is a very low diffusion rate of platinum at RT. The size and height distributions for low coverage will be discussed later in detail. We do not observe a big difference in the size and height values obtained for 0.1 ML and those for 0.4 ML, just an increase of the coverage. This is an indication of very low diffusion of platinum atoms on this surface. We have not detected any long range ordering of the Pt clusters for any of the coverages studied in this work either by STM or LEED, as it was also reported for the deposition of Pt on the TiO_2 (110)-(1x1) surface [247].

In order to determine the preferred adsorption site for Pt atoms, we have carried out DFT calculations on this system. We have checked the adsorption energy for four different sites (two at the reconstruction rows and two at the troughs). We have marked these positions in figure 5.3.3 a). DFT calculations predict the row hollow site as the most energetically favorable adsorption site with an adsorption energy of approximately -2.5 eV. The other three sites present higher adsorption energies going from the -1.92 eV of the trough hollow site to the -1.44 eV of the row bridge position or the -1.63 eV of the trough bridge site. This prediction is corroborated by the STM results as we observe that Pt clusters are mainly located on top of the reconstruction bright rows (see figure 5.3.3 b)). From our STM images we cannot distinguish the exact position of the Pt atoms within the rows as atomic resolution STM images are missing. However, taking into account that theoretical calculations predict an energy difference of approximately 1.1 eV between both row sites (hollow and bridge), we can unequivocally assign the row hollow positions as the preferential nucleation sites for Pt atoms.

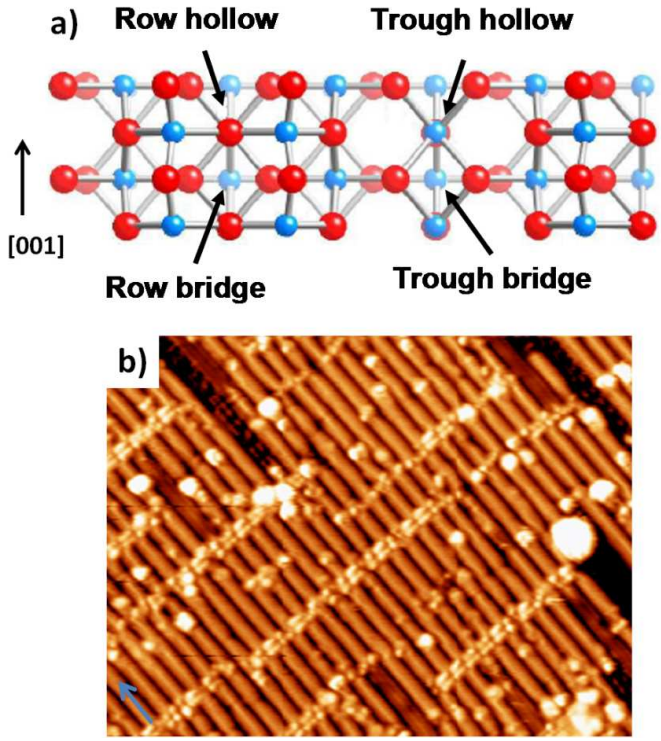

Figure 5.3.3.- *Study of the nucleation sites for Pt atoms*. a) Top view of the schematic ball-and-stick model of the (1x2) surface. We have indicated the four high-symmetry sites considered in the DFT calculations of the adsorption energy. These calculations predict a preferential adsorption at row hollow positions. b) STM of the (1x2) surface after deposition of 0.1 ML of Pt. We can see that Pt clusters nucleate on top of the Ti_2O_3 bright rows of the reconstruction, in correspondence with the DFT results. Size: (300 Å x 230 Å), I = 0.13 nA, V = 1.5 V.

5.3.2. Thermal stability of Pt clusters

As we already did in the studies of the deposition of organic molecules on the TiO_2 (110)-(1x1) surface, we have investigated the thermal stability of Pt clusters. We show in figure 5.3.4 a STM image of the (1x2) surface with 0.1 ML of platinum after an annealing cycle at approximately 825 K. After this process we observe a noticeable increase of material at the surface CL´s. Additionally, the size and height of the new clusters has increased in detriment of the number of dispersed ones. Both effects indicate a migration of platinum atoms from their initial nucleation sites on top of the bright rows of the

reconstruction towards the intersections between them and the CL´s. As there is a lower amount of Pt clusters we can try to analyze the initial stages of platinum growth. Figures 5.3.4 c) and d) show the formation of a platinum dimer and trimer on top of the Ti_2O_3 rows. This position of the Pt atoms with respect to the surface is in good agreement with the theoretical predictions [246]. This is a clear evidence of the tendency of Pt atoms to agglomerate after the annealing treatment.

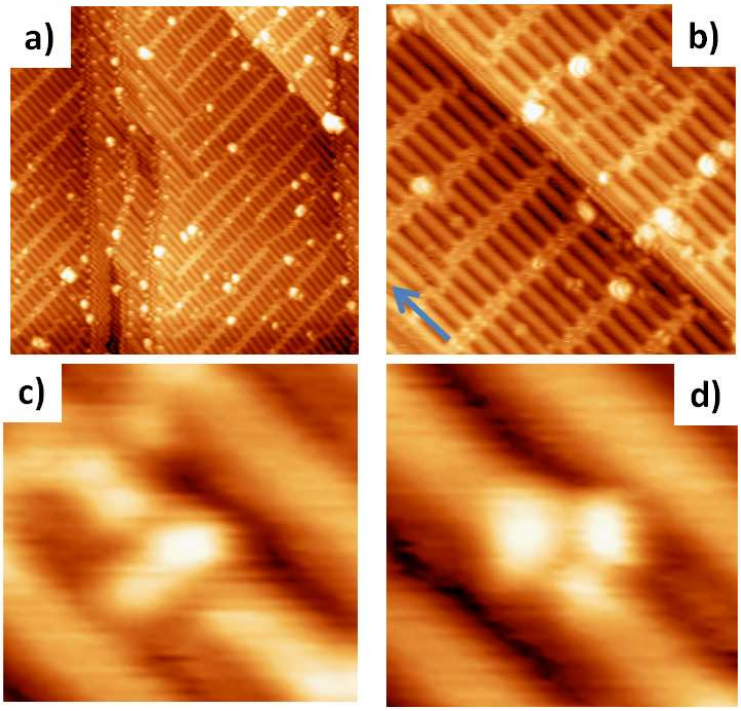

Figure 5.3.4.- *Set of STM images of the TiO_2 (110)-(1x2) surface with 0.1 ML of platinum after annealing at ~ 825 K.* a) and b) STM images of the surface after evaporation and annealing. We observe a change of the nucleation site with respect to the STM images before the annealing. Now clusters nucleate on the surface CL´s. We also observe a reduction in the number of clusters. Size: (500 Å x 500 Å) and (200 Å x 200 Å), respectively. c) High-resolution STM image where we can observe the formation of a Pt dimer on top of a Ti_2O_3 row and close to a SL. Size: (25 Å x 27 Å). d) High-resolution STM image where we can observe the formation of a Pt trimer on top of a Ti_2O_3 row in the middle of a terrace. Size: (24 Å x 23 Å). In all cases the tunneling parameters are I = 0.15 nA, V = 2.0 V.

We have carried out a quantitative and comparative study on the size and height of the Pt clusters before and after the thermal treatment. We present in figure 5.3.5 two histograms that represent the area and height distribution of the clusters before and after the annealing (figures 5.3.5 a) and b), respectively). In both cases we have included the values of the bright features already present at the clean surface. These features are associated to small adsorbates coming from the residual gas, like H_2O, OH groups, etc. They present a mean area of 100 $Å^2$ and a mean height of 1 Å.

In the area distribution graph we can see that the Pt clusters present a very homogeneous area before the annealing, with a mean value of approximately 50 $Å^2$, with an abrupt decrease in the area beyond 75 $Å^2$. However, it is possible to find clusters with a maximum area of 175 $Å^2$. From figure 5.3.4 c), we can assign an experimental area of ~ 25 $Å^2$ to a single Pt atom. Taking into account this assignment, we can see that there is a prevalence of clusters formed by one, two or three Pt atoms at the base (green bars). However, after the annealing treatment, we observe a higher variety in the size of the Pt clusters, being possible to find clusters formed by even nine Pt atoms at the base. We observe a prevalence of 25 $Å^2$ features, together with a monotonous decrease of the number of clusters upon increasing area. Regarding the height of these clusters (figure 5.3.5 b)), we find a mean height of approximately 3 Å before the annealing, which should correspond to two Pt atoms as the minimum height we obtain is half of it. On the other hand, after the annealing we can find higher clusters with a mean height value of approximately 4.5 Å, which should correspond to three Pt atoms. These results indicate that before the annealing, we have small clusters randomly distributed on the surface due to the very low diffusion rate at RT. However, when we supply thermal energy through an annealing at ~ 825 K, Pt atoms start diffusing on the surface and tend to nucleate on the CL´s forming larger clusters.

Finally, we should mention that from our STM images we have not detected evidences of encapsulation of the Pt clusters after annealing in the low coverage regime. This result contrasts with previous observations on the TiO_2 (110)-(1x1) surface [48,55-60]. There are two possible reasons for this phenomenon. From one side, the coverage regimes that we have used in the

present study for the investigation of the initial stages of the Pt growth mode are lower than those used in the case of Pt encapsulation on the (1x1) surface. From the other side, the different structure of (1x1) and (1x2) surfaces can induce a variation of the catalytic properties, having an influence in the metal-support interaction.

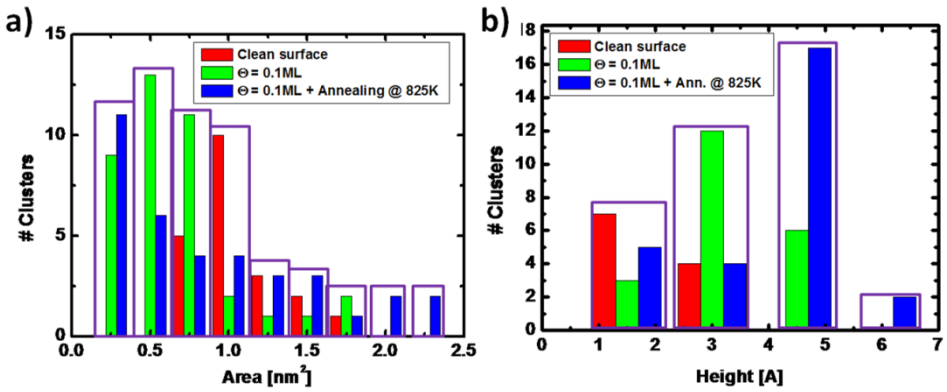

Figure 5.3.5.- *Study of the changes in size and height of Pt clusters after the thermal treatment*. a) Bar graph where we represent the number of clusters as a function of their area. We observe the formation of bigger clusters after the annealing. b) In this bar graph we show the clusters height. We also observe an increase in the height after the annealing.

5.3.3. Conclusions

In this section we have studied the initial stages of the Pt growth on the rutile TiO_2 (110)-(1x2) surface. For submonolayer coverage, the growth mode at room temperature is three-dimensional islanding, i.e. VW-like. When we evaporate at RT, the arriving Pt atoms nucleate on top of the Ti_2O_3 rows of the reconstruction forming small particles of one, two or three atoms at the base, with an area smaller than 100 $Å^2$. The mean height of these clusters is approximately 3 Å. These nanoparticles are homogeneously distributed on the surface. We have proved by STM measurements and DFT calculations that the preferential nucleation sites are the row hollow positions of the Ti_2O_3 rows. On the other hand, after the annealing at ~ 825 K, we observe an increase of the mean area and height of the Pt clusters on the surface, in detriment of their

number. Thermally activated, these clusters diffuse on the surface and nucleate at the cross-links of the (1x2) surface reconstruction. We have not observed any evidences of cluster encapsulation after annealing at 825 K, for the Pt coverage studied in this experiment.

6. Conclusions

In this thesis, we have studied the interaction between different kinds of adsorbates (organic and inorganic) with the two main surfaces of rutile TiO_2 (110) face: the bulk-like (1x1) structure and the reconstructed (1x2) surface. We also shed light on some other aspects which remained unclear as the interpretation of atomic resolved features appearing in STM images of the (1x1) clean surface and the characterization of the (1x2) surface electronic structure. For this aim we have combined a wide variety of experimental techniques with theoretical calculations and simulations. In this way, we have contributed to a better understanding of the rutile TiO_2 (110) surfaces and their interaction with different adsorbates.

The main results of this thesis can be summarized as follows:

- ***Influence of the tip state in the interpretation of atomic-resolved STM images on the rutile TiO_2 (110)-(1x1) surface.*** We have been able to correctly interpret and simulate three of the four recurrent atomic resolution STM images appearing during STM measurements. We have seen that there are two types of "standard" images which are the result of scanning the TiO_2 surface with two different tips: a clean W tip and a W tip whose apex has been substituted by an O atom. Regarding the third type of atomic resolved STM images, that we have called "elliptically shaped" images, we have shown that they are due to a STM tip contaminated by two O atoms substituting the apex. We have also reported the existence of a fourth kind of atomic resolved STM images ("giant corrugation" images) which present a huge corrugation along the [1-10] surface direction. Their origin is still unclear although we think it can be due to elastic deformations of the TiO_2 surface as a consequence of surface-tip interactions. Additionally, we have been able to correctly identify by theoretical calculations the two main defects present in this surface: O_{vac}´s and OH groups.

- ***The interaction of C_{60} molecules with the rutile TiO_2 (110)-(1x1) surface.*** We have studied the interaction between C_{60} and the (1x1) surface of TiO_2 (110), both from an experimental and a theoretical point of view. We have investigated the morphological structure and

electronic properties of the molecular layers formed when molecules are deposited at RT on the surface. We have seen that C_{60} molecules form well-ordered close-packed molecular islands with a p (5x2) superstructure. C_{60} molecules are sitting on top of the Ti_{5f} substrate rows, with half of them located on top of Ti_{5f} atoms and the other half in between two Ti_{5f} atoms. The two different adsorption sites induce diverse orientations of the molecules with respect to the substrate. We have also shown that the molecular layer presents a very low interaction with the substrate and that they are probably spinning along the surface normal, as it happens in C_{60} crystals. Finally, we have proved that the organic structures disappear when the system is annealed over 700 K.

- ***The interaction of Pentacene with the rutile TiO_2 (110)-(1x1) surface.*** We have shown the existence of a flat pentacene structure on a wide gap semiconductor as TiO_2, which extends up to the third layer. In this structure, for coverages up to 1 ML, pentacene molecules are lying-down with their long axis oriented completely parallel to the surface and along the [001] surface direction. Pentacene molecules are rotated along their long molecular axis by approximately 25°. These structures are stabilized by a side-by-side attractive interaction taking place between molecules located on different Ti rows, while within the same Ti row, molecules present a repulsive interaction. When the coverage is increased to a second layer, the growth mode remains the same although 1-dimensional vacancy islands start appearing. These islands present a high mobility and can be influenced by the STM tip. The structure at the third layer changes to irregular squared patches which may be probably related to molecules growing in a herring-bone structure as it occurs in pentacene crystals. Finally, annealing the system at ~ 500 K gives rise to the decomposition of the organic layers and the formation of carbon clusters

- ***The interaction of $C_{60}H_{30}$ with the rutile TiO_2 (110)-(1x1) surface.*** We have seen that $C_{60}H_{30}$ molecules diffuse on the TiO_2 surface when they are deposited at RT. However, when the system is annealed above 375 K, molecules undergo a transformation changing from a physisorption

to a chemisorption state and, consequently, getting fixed to the surface in a flat orientation. In this way we have seen that $C_{60}H_{30}$ molecules present two main orientations with one of the corners pointing along the [001] or the [1-10] surface direction, respectively. However, the first is the most common one. We have also noticed a very important variation of the molecular shape with the tunneling bias making possible to tunnel through the molecules for low voltages, and indicating a low interaction of the molecules with the substrate. When the system is annealed over 750 K, we observe the formation fullerene-like structures coming from the partial / total dehydrogenation of the $C_{60}H_{30}$ precursors. This process is probably possible thanks to the catalytic properties of surface defects, mainly O_{vac}´s. There are no evidences of graphene formation on TiO_2.

- ***Comparative study of the electronic interaction of different organic molecules with the TiO_2 (110)-(1x1) surface.*** We have analyzed the electronic structure of the different molecular systems, both individually and by comparing them with the other ones. We have shown that H_2PPIX is the most interacting molecule of all of those investigated on this surface in this work. For this reason it presents the major differences with respect to the clean TiO_2 surface both in the core-levels and in the valence band. The photoemission results for the rest of the molecules corroborate the previous conclusions and point towards a low interaction between molecules and surface. Additionally, in the case of H_2PPIX, we observe a charge transfer from the molecule to the surface, increasing in this way the amount of Ti^{3+} atoms of the substrate, whereas for the others, the charge transfer goes in the opposite direction.

- ***The (1x1) → (1x2) phase transition.*** We have studied the way (1x2) reconstructed surface is formed. Specifically, we have investigated the influence of temperature and annealing duration on the formation of the (1x2) surface from the (1x1) structure. We have determined that in order to obtain good quality (1x2) surfaces from the atomistic point of view, it is necessary to anneal at 1100 K for at least 60 minutes. Shorter annealing cycles (30 minutes) yield to defective surfaces with

regions that still present the underlying (1x1) structure. When the annealing cycles are even shorter (10 minutes) we have shown that the surface presents the coexistence of both the (1x1) and the (1x2) structures. We have also demonstrated that both single-links and cross-links, characteristic of the (1x2) surface, appear since the very beginning of the (1x2) formation. The reasons for their appearance are still unclear.

- **Valence Band electronic characterization of the rutile TiO_2 (110)-(1x2) surface.** We have completely characterized the electronic structure of the (1x2) surface reconstruction. We have investigated the valence band dispersion along the two high symmetry surface directions, the [001] and the [1-10] directions, observing the existence of a dispersive bulk band along the [001] direction. However, within our experimental resolution, no dispersion of the defects peak located in the band gap could be detected in contradiction with theoretical predictions. We have obtained the total density of states of the TiO_2 (110)-(1x2) surface which presents a very good agreement with the theoretical one. We have also demonstrated the presence of a double contribution in the defects state peak located in the band gap. This double contribution arises from the Ti^{3+} atoms located in the bulk and associated to defects, and from the Ti^{3+} atoms present in the Ti_2O_3 rows of the surface reconstruction. Both components are displaced one from each other by 0.45 eV, approximately, as it corresponds to two different chemical environments.

- ***Study of the submonolayer deposition of Pt on the rutile TiO_2 (110)-(1x2) surface*.** We have studied the initial stages of the Pt deposition at RT on the (1x2) surface of rutile TiO_2 (110). We report a 3-dimensional growth with the formation of Pt clusters randomly distributed on the surface. These clusters nucleate on top of the Ti_2O_3 rows of the reconstruction and present a mean area of approximately 50 $Å^2$ and a mean height of 3 Å. When the system is annealed to 825 K, we have observed the agglomeration of Pt forming bigger clusters with a mean area of 100 $Å^2$ and a mean height of 5 Å. These new clusters diffuse on

the surface during the annealing and end up nucleating at the surface single-links and cross-links.

7. Conclusiones

En esta tesis hemos estudiado la interacción entre distintos tipos de adsorbatos y las dos principales superficies de la cara (110) del rutilo TiO_2: la superficie (1x1) y la reconstrucción superficial (1x2). También hemos profundizado sobre algunos aspectos oscuros relacionados con este substrato, como la interpretación de las imágenes de resolución atómica de la superficie limpia (1x1) y la caracterización electrónica de la reconstrucción (1x2). Para ello hemos combinado una gran variedad de técnicas experimentales con cálculos y simulaciones teóricas. De esta manera hemos contribuido a un mejor entendimiento de las superficies del TiO_2 y de su interacción con diversos adsorbatos.

Los principales resultados de esta tesis se resumen a continuación:

- **Influencia del estado de la punta en la interpretación de imágenes de resolución atómica de la superficie limpia (1x1) del TiO_2.** Hemos sido capaces de interpretar y simular correctamente tres de las cuatro imágenes de resolución atómica que aparecen recurrentemente durante las medidas de STM. Hemos visto que hay dos tipos de imágenes "standard" que son el resultado de barrer la superficie con dos puntas diferentes: una punta limpia de W y otra en la que el vértice ha sido reemplazado por un átomo de O. En lo que respecta al tercer tipo de imágenes, las que hemos dado en llamar imágenes "elliptically shaped", hemos demostrado que se deben a que han sido obtenidas con puntas de STM contaminadas con dos átomos de O sustituyendo al vértice. Adicionalmente, mostramos la existencia de un cuarto tipo de imagen de resolución atómica (imágenes "giant corrugation") que presentan una corrugación enorme a lo largo de la dirección [1-10]. Su origen es incierto aunque pensamos que se pueden deber a deformaciones elásticas de la superficie del TiO_2 como consecuencia de la interacción punta-muestra. Finalmente, mediante cálculos teóricos, hemos sido capaces de identificar correctamente los dos principales defectos de esta superficie: O_{vac}´s y grupos OH.

- **Interacción del C_{60} con la superficie (1x1) del TiO_2.** Hemos estudiado la interacción entre moléculas de C_{60} y la superficie (1x1), desde un punto de vista experimental y teórico. Hemos analizado la estructura

morfológica y las propiedades electrónicas de las capas moleculares que se forman tras la deposición de las moléculas a RT. Hemos visto que forman islas compactas, bien ordenadas y de altura mono-molecular con una periodicidad (5x2). La moléculas están situadas sobre las filas de átomos Ti_{5f}, con la mitad de las mismas ocupando una posición entre átomos Ti_{5f} y la otra mitad encima de los mismos. Esta diferencia en las posiciones de adsorción induce una orientación diferente para cada tipo de molécula con respecto al substrato. También mostramos que la capa molecular presenta una interacción muy débil con la superficie por lo que las moléculas, probablemente, se encuentran rotando alrededor de un eje perpendicular a la misma. Finalmente, hemos demostrado que las moléculas desaparecen tras calentar a más de 700 K.

- **Interacción del pentaceno con la superficie (1x1) del TiO_2.** Hemos probado la existencia de una estructura plana de moléculas de pentaceno en un semiconductor de gap ancho como el TiO_2, que se extiende hasta la tercera capa. En esta estructura, para recubrimientos menores de 1 ML, las moléculas están tumbadas con su eje largo orientado paralelo a la superficie y a lo largo de la dirección [001]. Éstas presentan una rotación de aproximadamente 25° a lo largo del eje largo. Estas estructuras están estabilizadas mediante interacciones laterales atractivas a lo largo de la dirección [1-10], mientras que a lo largo de la dirección [001] la interacción es repulsiva. Cuando aumentamos el recubrimiento a una segunda capa, se mantiene el modo de crecimiento aunque aparecen islas de vacantes de una molécula de anchura. Estas islas presentan una gran movilidad y se pueden ver influenciadas por la punta del STM. Sin embargo, en la tercera capa, la estructura cambia a parches cuadrados e irregulares que probablemente se deba al crecimiento en estructura *herring-bone*, tal y como ocurre en los cristales de pentaceno. Finalmente, calentar el sistema a temperaturas del orden de 500 K da lugar a la descomposición de las moléculas y la formación de clusters de carbono.

- **Interacción del $C_{60}H_{30}$ con la superficie (1x1) del TiO_2.** Hemos visto que las moléculas de $C_{60}H_{30}$ difunden sobre la superficie a RT. Sin embargo, cuando el sistema se calienta por encima de los 375 K, las moléculas experimentan una transformación pasando de la fisisorción a la quemisorción, quedando fijas y planas sobre la superficie. Una vez fijas, vemos dos orientaciones principales de la molécula, donde uno de los lados de la misma está orientado a lo largo de la dirección [001] ó [1-10] de la superficie, respectivamente. La primera de las orientaciones anteriormente citada es la predominante. También hemos observado una variación importante de la forma de las moléculas con el voltaje túnel, pudiendo hacer túnel a través de las mismas para voltajes inferiores a 1.2 V. Cuando el sistema se calienta por encima de los 750 K, se observa la formación de estructuras tipo fulereno provenientes de la deshidrogenación parcial / total de las moléculas. Es probable que este proceso sea posible gracias a las propiedades catalíticas de los defectos superficiales. No hemos observado evidencias de formación de grafeno sobre esta superficie.

- **Estudio comparativo.** Hemos analizado la estructura electrónica de los diferentes sistemas moleculares, tanto individualmente como en comparación con los demás. Hemos demostrado que, dentro de las moléculas que hemos estudiado, la protoporfirina H_2PPIX es la más interaccionante con la superficie del TiO_2. Por ello, es la que presenta mayores diferencias con respecto a la superficie limpia en los niveles profundos y la banda de valencia. Los resultados de fotoemisión de las demás moléculas corroboran las conclusiones previas y apuntan hacia una débil interacción con la superficie. Adicionalmente, para el caso de la H_2PPIX, observamos una transferencia de carga de la molécula al substrato, mientras que en los otros casos, la transferencia es en la dirección inversa.

- **La transición 1x1 → 1x2.** Hemos estudiado la manera en que se forma la superficie (1x2). Concretamente, nos hemos centrado en investigar la influencia de la temperatura y el tiempo de calentamiento en la calidad de la superficie reconstruida. Hemos visto que la mejor receta para obtener una superficie de buena calidad es calentar a 1100 K

durante 60 minutos. Así, calentamientos más cortos (30 minutos) dan lugar a superficies con defectos, incluyendo regiones donde todavía se puede observar la superficie (1x1) de debajo. Si los ciclos son aún más cortos (10 minutos), se observa la coexistencia de las dos estructuras. También hemos demostrado la aparición de los single y cross-links desde los primeros estadios de la formación de la (1x2). Las razones de su aparición no están todavía claras.

- **Caracterización electrónica de la banda de valencia de la superficie (1x2).** Hemos caracterizado completamente la estructura electrónica de la reconstrucción superficial (1x2). Hemos medido la dispersión tanto de la banda de valencia como del pico de defectos a lo largo de las dos direcciones de alta simetría del substrato, obteniendo una banda dispersiva que se extiende a lo largo de la dirección [001]. Sin embargo, dentro de la resolución experimental, no hemos sido capaces de encontrar ninguna dispersión del pico de defectos situado en el gap, en contraste con predicciones teóricas. Hemos obtenido experimentalmente la densidad de estados total del sistema, la cual presenta un buen acuerdo con la teórica. Finalmente, hemos demostrado la existencia de una doble contribución al pico de defectos. Esta doble contribución viene de los Ti^{3+} presentes en el volumen y de los Ti^{3+} que forman parte de las cadenas Ti_2O_3 de la reconstrucción.

- **Pt / TiO_2 (110)-(1x2).** En esta última sección hemos estudiado los primeros estadios del crecimiento de Pt sobre la superficie (1x2) a RT. Proponemos un crecimiento 3D con la formación de clusters de Pt aleatoriamente distribuidos por la superficie. Estos clusters nuclean sobre las filas Ti_2O_3 de la reconstrucción, presentando un área media de 50 $Å^2$ y una altura aparente media de 3 Å. Cuando se calienta el sistema por encima de los 825 K, observamos una aglomeración de Pt con la consiguiente formación de clusters mayores, con un área media de 100 $Å^2$ y una altura aparente media de 5 Å. Después del calentamiento, se observa una nucleación preferencial en los single y cross-links de la superficie.

Bibliography

[1] "http://www.nano-world.org/frictionmodule/content/0200makroreibung/0400historisch/?=lang=en."

[2] F.P. Bowden and D. Tabor, *The Friction and Lubrication of Solids*, Oxford: Oxford University Press, 1950.

[3] Http://depts.washington.edu/nanolab/ChemE554/Summaries%20ChemE%20554/Introduction%20Tribology.htm, "Amontons law."

[4] "http://www.tribology-abc.com/abc/history.htm."

[5] G. Amontons, "No Title," *Histoire de l'Académie Royale des Sciences avec les Mémoires de Mathématique et de Physique*, 1699, p. 206.

[6] S. Burbano de Ercilla, E. Burbano Garcia, and C. Gracia Muñoz, *Fisica General*, Zaragoza: 1993.

[7] J.W. Gibbs, "On the equilibrium of heterogeneous substances," *Transactions of the Connecticut Academy of Arts and Sciences*, vol. III, 1876, pp. 108-248.

[8] J.W. Gibbs, "On the equilibrium of heterogeneous substances," *Transactions of the Connecticut Academy of Arts and Sciences*, vol. III, 1878, pp. 343-524.

[9] "http://nobelprize.org/nobel_prizes/chemistry/laureates/1932/langmuir-bio.html."

[10] C. Davisson and L.H. Germer, "The Scattering of Electrons by a Single Crystal of Nickel," *Nature*, vol. 119, 1927, pp. 558-560.

[11] W. Shockley, "On the surface states associated with a periodic potential," *Physical review*, vol. 56, 1939, p. 317–323.

[12] I. Tamm, “Uber eine mögliche art der elektronenbindung an kristalloberflächen,” *Phys. Z. Sowjetunion*, vol. 1, 1932, pp. 733-746.

[13] “http://nobelprize.org/nobel_prizes/physics/laureates/1956/.”

[14] U. Diebold, “The surface science of titanium dioxide,” *Surface Science Reports*, vol. 48, Jan. 2003, pp. 53-229.

[15] S.J. Tauster, S.C. Fung, and R.L. Garten, “Strong metal-support interactions. Group 8 noble metals supported on titanium dioxide,” *Journal of the American Chemical Society*, vol. 100, Jan. 1978, pp. 170-175.

[16] S.J. Tauster, “Strong metal-support interactions,” *Accounts of Chemical Research*, vol. 20, Nov. 1987, pp. 389-394.

[17] K.D. Schierbaum, S. Fischer, M.C. Torquemada, J.L. De Segovia, E. Román, and J.A. Martín-Gago, “The interaction of Pt with TIO2(110) surfaces: a comparative XPS, UPS, ISS, and ESD study,” *Surface Science*, vol. 345, 1996, pp. 261-273.

[18] A. Berkó, a Kiss, and J. Szoko, “Formation of vacancy islands tailored by Pt nanocrystallites and Ar sputtering on TiO(110) surface,” *Applied Surface Science*, vol. 246, Jun. 2005, pp. 174-182.

[19] O. Dulub, W. Hebenstreit, and U. Diebold, “Imaging cluster surfaces with atomic resolution: the strong metal-support interaction state of Pt supported on TiO2(110),” *Physical review letters*, vol. 84, Apr. 2000, pp. 3646-9.

[20] S. Fischer, K.D. Schierbaum, and W. Göpel, “Submonolayer-Pt on TiO2 (110) surfaces: electronic and geometric effects,” *Sensors and Actuators B: Chemical*, vol. 31, Feb. 1996, pp. 13-18.

[21] Y.M. Sun, D.N. Belton, and J.M. White, “Characteristics of Pt Thin Films on TiO2(110),” *Journal of Phys. Chem*, vol. 90, 1986, pp. 5178-5182.

[22] F. Pesty, H.-P. Steinrück, and T.E. Madey, “Thermal stability of Pt films on TiO2(110): evidence for encapsulation,” *Surface Science*, vol. 339, Sep. 1995, pp. 83-95.

[23] O. Ozturk, J.B. Park, S. Ma, J.S. Ratliff, J. Zhou, D. Mullins, and D. a Chen, “Probing the interactions of Pt, Rh and bimetallic Pt–Rh clusters with the TiO2(110) support,” *Surface Science*, vol. 601, Jul. 2007, pp. 3099-3113.

[24] A. Berkó, “Effect of CO on the morphology of Pt nanoparticles supported on TiO2(110)-(1xn),” *Surface Science*, vol. 566-568, Sep. 2004, pp. 337-342.

[25] S. Fischer, “Surface defects and platinum overlayers on TiO2(110) surfaces: STM and photoemission studies,” *Vacuum*, vol. 48, Sep. 1997, pp. 601-605.

[26] B. O´Regan and M. Grätzel, “A low-cost, high-efficiency solar cell based on dye-sensitized colloidal TiO2 films,” *Nature*, vol. 353, 1991, pp. 737-740.

[27] M.K. Nazeeruddin, A. Kay, I. Rodicio, R. Humphry-Baker, E. Müller, P. Liska, N. Vlachopoulos, and M. Grätzel, “Conversion of light to electricity by cis-X2bis (2, 2’-bipyridyl-4, 4'-dicarboxylate) ruthenium (II) charge-transfer sensitizers (X= Cl-, Br-, I-, CN-, and SCN-) on nanocrystalline titanium dioxide electrodes,” *Journal of the American Chemical Society*, vol. 115, 1993, p. 6382–6390.

[28] M. Gratzel, “Dye-sensitized solar cells,” *Journal of Photochemistry and Photobiology C: Photochemistry Reviews*, vol. 4, Oct. 2003, pp. 145-153.

[29] M. Lahav, A.B. Kharitonov, and I. Willner, “Imprinting of chiral molecular recognition sites in thin TiO2 films associated with field-effect transistors: novel functionalized devices for chiroselective and chirospecific analyses.,” *Chemistry - A European Journal*, vol. 7, Sep. 2001, pp. 3992-7.

[30] C. Kleverlaan, M. Alebbi, R. Argazzi, C. a Bignozzi, G.M. Hasselmann, and G.J. Meyer, “Molecular rectification by a bimetallic Ru-Os compound anchored to nanocrystalline TiO2.,” *Inorganic chemistry*, vol. 39, Apr. 2000, pp. 1342-3.

[31] N. Greenwood and A. Earnshaw, *Chemistry of the Elements*, Oxford: Pergamon, 1984.

[32] R. Hengerer, B. Bolliger, M. Erbudak, and M. Grätzel, “Structure and stability of the anatase TiO2 (101) and (001) surfaces,” *Surface Science*, vol. 460, Jul. 2000, pp. 162-169.

[33] W. Hebenstreit, N. Ruzycki, G. Herman, Y. Gao, and U. Diebold, “Scanning tunneling microscopy investigation of the TiO2 anatase (101) surface,” *Physical Review B*, vol. 62, Dec. 2000, p. R16334-R16336.

[34] F. Grant, “Properties of rutile (titanium dioxide),” *Reviews of Modern Physics*, vol. 31, 1959, pp. 646-674.

[35] M. Ramamoorthy, D. Vanderbilt, and R. King-Smith, “First-principles calculations of the energetics of stoichiometric TiO2 surfaces,” *Physical Review B*, vol. 49, 1994, p. 16721–16727.

[36] G. Cabailh, X. Torrelles, R. Lindsay, O. Bikondoa, I. Joumard, J. Zegenhagen, and G. Thornton, “Geometric structure of TiO2(110)(1×1): Achieving experimental consensus,” *Physical Review B*, vol. 75, Jun. 2007, p. 241403.

[37] W. Busayaporn, X. Torrelles, A. Wander, S. Tomić, A. Ernst, B. Montanari, N.M. Harrison, O. Bikondoa, I. Joumard, J. Zegenhagen, G. Cabailh, G. Thornton, and R. Lindsay, “Geometric structure of TiO2(110)(1×1) : Confirming experimental conclusions,” *Physical Review B*, vol. 81, Apr. 2010, p. 153404.

[38] R. Lindsay, A. Wander, A. Ernst, B. Montanari, G. Thornton, and N. Harrison, “Revisiting the Surface Structure of TiO2(110): A Quantitative low-Energy Electron Diffraction Study,” *Physical Review Letters*, vol. 94, Jun. 2005, p. 246102.

[39] U. Diebold, “Intrinsic defects on a TiO2(110)(1×1) surface and their reaction with oxygen: a scanning tunneling microscopy study,” *Surface Science*, vol. 411, Aug. 1998, pp. 137-153.

[40] V.E. Henrich and R.L. Kurtz, “Surface electronic structure of TiO2: Atomic geometry, ligand coordination, and the effect of adsorbed hydrogen,” *Physical Review B*, vol. 23, 1981, p. 6280.

[41] V.E. Henrich, G. Dresselhaus, and H. Zeiger, “Observation of Two-Dimensional Phases Associated with Defect States on the Surface of TiO2,” *Physical Review Letters*, vol. 36, 1976, p. 1335–1339.

[42] S. Pétigny, H. Mostéfa-Sba, B. Domenichini, E. Lesniewska, A. Steinbrunn, and S. Bourgeois, "Superficial defects induced by argon and oxygen bombardments on (110) TiO2 surfaces," *Surface Science*, vol. 410, Aug. 1998, pp. 250-257.

[43] I.F. Ziegler, J.P. Biersack, and U. Littmark, *The Stopping and Range of Ions in Solids*, New York: Pergamon Press, 1985.

[44] P. Krüger, S. Bourgeois, B. Domenichini, H. Magnan, D. Chandesris, P. Le Fèvre, A. Flank, J. Jupille, L. Floreano, A. Cossaro, A. Verdini, and A. Morgante, "Defect States at the TiO2(110) Surface Probed by Resonant Photoelectron Diffraction," *Physical Review Letters*, vol. 100, Feb. 2008, p. 055501.

[45] P.J. Møller and M.C. Wu, "Surface geometrical structure and incommensurate growth: Ultrathin Cu films on TiO2 (110)," *Surface Science*, vol. 224, 1989, p. 265–276.

[46] H. Onishi and Y. Iwasawa, "Reconstruction of TiO2(110) surface: STM study with atomic-scale resolution," *Surface Science*, vol. 313, 1994, p. L783-L789.

[47] C.L. Pang, S.A. Haycock, H. Raza, P.W. Murray, G. Thornton, R. James, D.W. Bullett, and O. Gülseren, "Added row model of TiO2 (110)-(1x2)," *Physical Review B*, vol. 58, 1998, pp. 1586-1589.

[48] R.A. Bennett, P. Stone, N. Price, and M. Bowker, "Two (1×2) Reconstructions of TiO2(110): Surface Rearrangement and Reactivity Studied Using Elevated Temperature Scanning Tunneling Microscopy," *Physical Review Letters*, vol. 82, May. 1999, pp. 3831-3834.

[49] M. Blanco-Rey, J. Abad, C. Rogero, J. Mendez, M.F. López, J.A. Martín-Gago, and P. de Andrés, "Structure of Rutile TiO2(110)-(1x2): Formation of Ti2O3 Quasi-1D Metallic Chains," *Physical Review Letters*, vol. 96, Feb. 2006, p. 55502.

[50] M. Blanco-Rey, J. Abad, C. Rogero, J. Méndez, M.F. López, E. Román, J.A. Martín-Gago, and P. de Andrés, "LEED-IV study of the rutile TiO2(110)-(1×2) surface with a Ti-interstitial added-row reconstruction," *Physical Review B*, vol. 75, Feb. 2007, p. 081402.

[51] S.D. Elliott and S.P. Bates, “Energetically accessible reconstructions along interstitial rows on the rutile (110) surface,” *Physical Chemistry Chemical Physics*, vol. 3, 2001, pp. 1954-1957.

[52] K. Park, M. Pan, V. Meunier, and E. Plummer, “Surface Reconstructions of TiO2(110) Driven by Suboxides,” *Physical Review Letters*, vol. 96, Jun. 2006, p. 226105.

[53] N. Shibata, A. Goto, S.-Y. Choi, T. Mizoguchi, S.D. Findlay, T. Yamamoto, and Y. Ikuhara, “Direct imaging of reconstructed atoms on TiO2 (110) surfaces.,” *Science*, vol. 322, Oct. 2008, pp. 570-3.

[54] A. Kokalj, “XCrySDen - a new program for displaying crystalline structures and electron densities,” *Journal of Molecular Graphics and Modelling*, vol. 17, 1999, pp. 176-179.

[55] S. Takakusagi, K.-ichi Fukui, F. Nariyuki, and Y. Iwasawa, “STM study on structures of two kinds of wide strands formed on TiO2 (110),” *Surface Science*, vol. 523, 2003, pp. 0-5.

[56] M. Li, W. Hebenstreit, and U. Diebold, “Morphology change of oxygen-restructured TiO2(110) surfaces by UHV annealing: Formation of a low-temperature (1×2) structure,” *Physical Review B*, vol. 61, Feb. 2000, pp. 4926-4933.

[57] R. Smith, R.A. Bennett, and M. Bowker, “Measurement of the surface-growth kinetics of reduced TiO2(110) during reoxidation using time-resolved scanning tunneling microscopy,” *Physical Review B*, vol. 66, Jul. 2002, p. 035409.

[58] A. Szabo and T. Engel, “Structural studies of TiO2(110) using scanning tunneling microscopy,” *Surface Science*, vol. 329, May. 1995, pp. 241-254.

[59] M. Sander, “Atomic level structure of TiO2(110) as a function of surface oxygen coverage,” *Surface Science*, vol. 302, Jan. 1994, p. L263-L268.

[60] P.W. Murray, N. Condon, and G. Thornton, “Effect of stoichiometry on the structure of TiO2(110),” *Physical Review B*, vol. 51, 1995, p. 10989–10997.

[61] V.E. Henrich and P.A. Cox, *The surface science of metal oxides*, Cambridge: Cambridge University Press, 1994.

[62] V.E. Henrich, "The surfaces of metal oxides," *Reports on Progress in Physics*, vol. 48, 1985, pp. 1481-1541.

[63] Z. Zhang, S.P. Jeng, and V.E. Henrich, "Cation-ligand hybridization for stoichiometric and reduced TiO2(110) surfaces determined by resonant photoemission," *Physical Review B*, vol. 43, 1991, p. 12004–12011.

[64] J. Abad, "Estudio de la estructura cristalina y electronica del sistema SiOx-TiO2 (110) y su reactividad con NO," 2005.

[65] R. Wiesendanger, *Scanning Probe Microscopy and Spectroscopy: methods and applications*, Cambridge: Cambridge University Press, 1994.

[66] R.J. Behm, N. García, and H. Röhrer, *Scanning Tunneling Microscopy and Related Methods*, The Netherlands: Kuwler Academic Publishers, 1990.

[67] G. Binnig and H. Röhrer, "Scanning Tunneling Microscopy," *Helvetica Physica Acta*, vol. 55, 1982, pp. 726-735.

[68] G. Binnig, H. Rohrer, C. Gerber, and E. Weibel, "Surface studies by scanning tunneling microscopy," *Physical Review Letters*, vol. 49, 1982, p. 57–61.

[69] R. Eisberg and R. Resnick, *Física cuántica de átomos, moléculas, sólidos, núcleos y partículas.*, México, D. F. Editorial Limusa, S. A., 2002.

[70] J. Bardeen, "Tunneling from a many-particle point of view," *Physical Review Letters*, vol. 6, 1961, pp. 57-59.

[71] I. Horcas, R. Fernández, J.M. Gómez-Rodríguez, J. Colchero, J. Gómez-Herrero, and A.M. Baro, "WSXM: a software for scanning probe microscopy and a tool for nanotechnology.," *The Review of scientific instruments*, vol. 78, Jan. 2007, p. 013705.

[72] U. Diebold, J. Anderson, K. Ng, and D. Vanderbilt, “Evidence for the Tunneling Site on Transition-Metal Oxides: TiO2(110).,” *Physical review letters*, vol. 77, Aug. 1996, pp. 1322-1325.

[73] K.-O. Ng and D. Vanderbilt, “Structure and apparent topography of TiO2(110) surfaces,” *Physical Review B*, vol. 56, Oct. 1997, pp. 10544-10548.

[74] M.P. Seah and W. a Dench, “Quantitative electron spectroscopy of surfaces: A standard data base for electron inelastic mean free paths in solids,” *Surface and Interface Analysis*, vol. 1, Feb. 1979, pp. 2-11.

[75] J.B. Pendry, *Low-Energy Electron Diffraction*, London: Academic Press, 1974.

[76] M.A. Van Hove, V.H. Weinberg, and C.-M. Chan, *Low-Energy Electron Diffraction*, Berlin: Springer-Verlag, 1986.

[77] H. Lüth, *Surfaces and Interfaces of Solid Materials*, Berlin: Springer, 1995.

[78] D. Briggs and M.P. Seah, *Practical Surface Analysis Vol.1*, New York: Ed. Wiley, 1990.

[79] C.R. Brundle and A.D. Baker, *Electron Spectroscopy, Theory, Techniques and Applications*, Pergamon Press, 1978.

[80] G. Margaritondo, *Introduction to Synchrotron Radiation*, Oxford: Oxford University Press, 1988.

[81] G. Ertl and J. Küppers, *Low Energy Electrons and Surface Chemistry*, Weinheim: VCH, 1985.

[82] J. Stöhr, *NEXAFS spectroscopy*, Springer, 1992.

[83] M. Sagurton, E.L. Bullock, and C.S. Fadley, “The analysis of photoelectron diffraction data obtained with fixed geometry and scanned photon energy,” *Surface science*, vol. 182, 1987, pp. 287-361.

[84] D.P. Woodruff, “Adsorbate structure determination using photoelectron diffraction: Methods and applications,” *Surface Science Reports*, vol. 62, Jan. 2007, pp. 1-38.

[85] Y. Che and M.A. Van Hove, "MSCD package user guide: Simulation of photoelectron diffraction using Rehr-Albers separable representation," 1997.

[86] D.P. Woodruff, "Surface structural information from photoelectron diffraction," *Journal of Electron Spectroscopy and Related Phenomena*, vol. 178-179, May. 2010, pp. 186-194.

[87] G. Granozzi and M. Sambi, "Angle-Scanned Photoelectron Diffraction: Probing crystalline ultrathin films," *Advanced Materials*, vol. 8, Apr. 1996, pp. 315-326.

[88] F. García de Abajo, M. Van Hove, and C. Fadley, "Multiple scattering of electrons in solids and molecules: A cluster-model approach," *Physical Review B*, vol. 63, Jan. 2001, p. 075404.

[89] D. Farías and K.-H. Rieder, "Atomic beam diffraction from solid surfaces," *Reports on Progress in Physics*, vol. 61, Mar. 1998, pp. 1575-1664.

[90] B. Poelsema and G. Comsa, *Scattering of Thermal Energy Atoms from Disordered Surfaces*, France: Springer Tracts in Modern Physics, 1989.

[91] "ESISNA Group," *www.icmm.csic.es/esisna*.

[92] "ALOISA beamline," *www.elettra.trieste.it/experiments/beamlines/aloisa/*.

[93] R. Martin, *Electronic Structure: Basic Theory and Practical Methods*, Cambridge: Cambridge University Press, 2004.

[94] M. Payne, M. Teter, D. Allan, T. Arias, and J. Joannopoulos, "Iterative minimization techniques for ab initio total-energy calculations: molecular dynamics and conjugate gradients," *Reviews of Modern Physics*, vol. 64, 1992, p. 1045–1097.

[95] S.J. Clark, M.D. Segall, C.J. Pickard, P.J. Hasnip, M.J. Probert, K. Refson, and M.C. Payne, "First principles methods using CASTEP," *ZEITSCHRIFT FUR KRISTALLOGRAPHIE*, vol. 220, 2005, pp. 567-570.

[96] A.A. Demkov, J. Ortega, O.F. Sankey, and M.P. Grumbach, “Electronic structure approach for complex silicas,” *Physical Review B*, vol. 52, 1995, p. 1618–1630.

[97] J. Lewis, K. Glaesemann, G. Voth, J. Fritsch, A. Demkov, J. Ortega, and O.F. Sankey, “Further developments in the local-orbital density-functional-theory tight-binding method,” *Physical Review B*, vol. 64, Oct. 2001, p. 195103.

[98] P. Jelínek, H. Wang, J. Lewis, O.F. Sankey, and J. Ortega, “Multicenter approach to the exchange-correlation interactions in ab initio tight-binding methods,” *Physical Review B*, vol. 71, Jun. 2005, p. 235101.

[99] O.F. Sankey and D.J. Niklewski, “Ab initio multicenter tight-binding model for molecular-dynamics simulations and other applications in covalent systems,” *Physical Review B*, vol. 40, 1989, p. 3979–3995.

[100] L.V. Keldysh, “Diagram technique for nonequilibrium processes,” *Soviet Physics JETP-USSR*, vol. 20, 1965, p. 1018.

[101] J.M. Blanco, “Estudio teórico del Microscopio de Efecto Túnel con métodos de primeros principios,” 2004.

[102] Z. Zhang, O. Bondarchuk, B.D. Kay, J.M. White, and Z. Dohnálek, “Imaging water dissociation on TiO2(110): Evidence for inequivalent geminate OH groups.,” *The journal of physical chemistry. B*, vol. 110, Nov. 2006, pp. 21840-5.

[103] I. Brookes, C.A. Muryn, and G. Thornton, “Imaging Water Dissociation on TiO2(110),” *Physical Review Letters*, vol. 87, Dec. 2001, p. 266103.

[104] G. Teobaldi, W. Hofer, O. Bikondoa, C.L. Pang, G. Cabailh, and G. Thornton, “Modelling STM images of TiO2(110) from first-principles: Defects, water adsorption and dissociation products,” *Chemical Physics Letters*, vol. 437, Mar. 2007, pp. 73-78.

[105] D. Matthey, J.G. Wang, S. Wendt, J. Matthiesen, R. Schaub, E. Laegsgaard, H. Hardtdegen, and F. Besenbacher, “Enhanced bonding of gold nanoparticles on oxidized TiO2(110).,” *Science*, vol. 315, Mar. 2007, pp. 1692-1696.

[106] S. Wendt, P.T. Sprunger, E. Lira, G.K.H. Madsen, Z. Li, J.Ø. Hansen, J. Matthiesen, A. Blekinge-Rasmussen, E. Laegsgaard, B. Hammer, and F. Besenbacher, "The role of interstitial sites in the Ti3d defect state in the band gap of titania.," *Science*, vol. 320, Jun. 2008, pp. 1755-1759.

[107] O. Bikondoa, C.L. Pang, R. Ithnin, C. a Muryn, H. Onishi, and G. Thornton, "Direct visualization of defect-mediated dissociation of water on TiO2(110)," *Nature Materials*, vol. 5, Feb. 2006, pp. 189-192.

[108] X. Cui, B. Wang, Z. Wang, T. Huang, Y. Zhao, J. Yang, and J.G. Hou, "Formation and diffusion of oxygen-vacancy pairs on TiO2(110)-(1x1).," *The Journal of chemical physics*, vol. 129, Jul. 2008, p. 044703.

[109] X. Cui, Z. Wang, S. Tan, B. Wang, J. Yang, and J.G. Hou, "Identifying Hydroxyls on the TiO2 (110)−(1 × 1) Surface with Scanning Tunneling Microscopy," *The Journal of Physical Chemistry C*, vol. 113, Jul. 2009, pp. 13204-13208.

[110] C.L. Pang, O. Bikondoa, D.S. Humphrey, A.C. Papageorgiou, G. Cabailh, R. Ithnin, Q. Chen, C.A. Muryn, H. Onishi, and G. Thornton, "Tailored TiO2 (110) surfaces and their reactivity," *Nanotechnology*, vol. 17, Nov. 2006, pp. 5397-5405.

[111] A.C. Papageorgiou, N.S. Beglitis, C.L. Pang, G. Teobaldi, G. Cabailh, Q. Chen, A.J. Fisher, W. Hofer, and G. Thornton, "Electron traps and their effect on the surface chemistry of TiO2(110).," *Proceedings of the National Academy of Sciences of the United States of America*, vol. 107, Feb. 2010, pp. 2391-6.

[112] A. Yurtsever, Y. Sugimoto, M. Abe, and S. Morita, "NC-AFM imaging of the TiO2(110)-(1 x 1) surface at low temperature.," *Nanotechnology*, vol. 21, Apr. 2010, p. 165702.

[113] J.V. Lauritsen, A.S. Foster, G.H. Olesen, M.C. Christensen, A. Kühnle, S. Helveg, J.R. Rostrup-Nielsen, B.S. Clausen, M. Reichling, and F. Besenbacher, "Chemical identification of point defects and adsorbates on a metal oxide surface by atomic force microscopy.," *Nanotechnology*, vol. 17, Jul. 2006, pp. 3436-41.

[114] H.P. Pinto, G.H. Enevoldsen, F. Besenbacher, J.V. Lauritsen, and A.S. Foster, "The role of tip size and orientation, tip-surface relaxations and surface impurities in simultaneous AFM and STM studies on the TiO2(110) surface.," *Nanotechnology*, vol. 20, Jul. 2009, p. 264020.

[115] R. Bechstein, C. González, J. Schütte, P. Jelínek, R. Pérez, and A. Kühnle, "'All-inclusive' imaging of the rutile TiO(2)(110) surface using NC-AFM.," *Nanotechnology*, vol. 20, Dec. 2009, p. 505703.

[116] G.H. Enevoldsen, H.P. Pinto, A.S. Foster, M. Jensen, A. Kühnle, M. Reichling, W. Hofer, J.V. Lauritsen, and F. Besenbacher, "Detailed scanning probe microscopy tip models determined from simultaneous atom-resolved AFM and STM studies of the TiO2(110) surface," *Physical Review B*, vol. 78, Jul. 2008, p. 045416.

[117] G.H. Enevoldsen, A.S. Foster, M.C. Christensen, J.V. Lauritsen, and F. Besenbacher, "Noncontact atomic force microscopy studies of vacancies and hydroxyls of TiO2(110): Experiments and atomistic simulations," *Physical Review B*, vol. 76, Nov. 2007, p. 205415.

[118] J.M. Blanco, C. González, P. Jelínek, J. Ortega, F. Flores, R. Pérez, M. Rose, M. Salmeron, J. Méndez, J. Wintterlin, and G. Ertl, "Origin of contrast in STM images of oxygen on Pd(111) and its dependence on tip structure and tunneling parameters," *Physical Review B*, vol. 71, Mar. 2005, p. 113402.

[119] C. Corriol, F. Calleja, a Arnau, J. Hinarejos, a Vazquezdeparga, W. Hofer, and R. Miranda, "Role of surface geometry and electronic structure in STM images of O/Ru(0001)," *Chemical Physics Letters*, vol. 405, Mar. 2005, pp. 131-135.

[120] C. Rogero, J. Martín-Gago, and J. Cerdá, "Subsurface structure of epitaxial rare-earth silicides imaged by STM," *Physical Review B*, vol. 74, Sep. 2006, p. 121404.

[121] O. Bondarchuk and I. Lyubinetsky, "Preparation of TiO2(110)-(1x1) surface via UHV cleavage: an scanning tunneling microscopy study.," *The Review of scientific instruments*, vol. 78, Nov. 2007, p. 113907.

[122] Q. Guo, I. Cocks, and E.M. Williams, "Dual tunnelling sites on metal-oxide surfaces : a scanning tunnelling microscopy study of TiO2 (110)," *Journal of Physics. D: Appl. Phys*, vol. 31, 1998, pp. 2231-2235.

[123] M. Basanta, Y. Dappe, P. Jelinek, and J. Ortega, "Optimized atomic-like orbitals for first-principles tight-binding molecular dynamics," *Computational Materials Science*, vol. 39, Jun. 2007, pp. 759-766.

[124] J. Abad, C. González, P. de Andrés, and E. Román, “Characterization of thin silicon overlayers on rutile TiO2(110)-(1x1),” *Physical Review B*, vol. 82, 2010, p. 165420.

[125] C. González, J. Guo, J. Ortega, F. Flores, and H. Weitering, “Mechanism of the Band Gap Opening across the Order-Disorder Transition of Si(111)(4×1)-In,” *Physical Review Letters*, vol. 102, Mar. 2009, p. 115501.

[126] N. Mingo, L. Jurczyszyn, F.J. Garcia Vidal, R. Saiz Pardo, P. de Andrés, F. Flores, S.Y. Wu, and W. More, “Theory of the scanning tunneling microscope: Xe on Ni and Al,” *Physical Review B*, vol. 54, 1996, p. 2225.

[127] P. de Andrés, F.J. Garcia Vidal, K. Reuter, and F. Flores, “Theory of ballistic electron emission microscopy,” *Progress in Surface Science*, vol. 66, Jan. 2001, pp. 3-51.

[128] J.M. Blanco, F. Flores, and R. Perez, “STM-theory: Image potential, chemistry and surface relaxation,” *Progress in Surface Science*, vol. 81, 2006, pp. 403-443.

[129] C.J. Chen, “Origin of atomic resolution on metal surfaces in scanning tunneling microscopy,” *Physical review letters*, vol. 65, 1990, p. 448–451.

[130] J.M. Soler, A.M. Baro, N. Garcia, and H. Röhrer, “Interatomic forces in scanning tunneling microscopy: Giant corrugations of the graphite surface,” *Physical review letters*, vol. 57, 1986, p. 444.

[131] W. Hofer, a Garcia-Lekue, and H. Brune, “The role of surface elasticity in giant corrugations observed by scanning tunneling microscopes,” *Chemical Physics Letters*, vol. 397, Oct. 2004, pp. 354-359.

[132] J. Blanco, C. González, P. Jelínek, J. Ortega, F. Flores, and R. Pérez, “First-principles simulations of STM images: From tunneling to the contact regime,” *Physical Review B*, vol. 70, Aug. 2004, p. 085405.

[133] S. Fischer, A.W. Munz, K.D. Schierbaum, and W. Göpel, “The geometric structure of intrinsic defects at TiO2(110) surfaces: an STM study,” *Surface Science*, vol. 337, Aug. 1995, pp. 17-30.

[134] C. Lun Pang, R. Lindsay, and G. Thornton, “Chemical reactions on rutile TiO2(110).,” *Chemical Society reviews*, vol. 37, Oct. 2008, pp. 2328-53.

[135] H. Kroto, J. Heath, S. O´Brien, R. Curl, and R. Smalley, “C60: Buckminsterfullerene,” *Nature*, vol. 318, 1985, pp. 162-163.

[136] P.W. Stephens, L. Mihaly, P.L. Lee, R.L. Whetten, S.-M. Huang, R. Kaner, F. Deiderich, and K. Holczer, “Structure of single-phase superconducting K3C60,” *Nature*, vol. 351, 1991, pp. 632-634.

[137] K. Tanigaki, I. Hirosawa, J. Mizuki, and T.W. Ebbesen, “Lattice parameters of alkali-metal-doped C60 fullerides,” *Chemical Physics Letters*, vol. 213, Oct. 1993, pp. 395-400.

[138] T. Kanbara, K. Shibata, S. Fujiki, Y. Kubozono, S. Kashino, T. Urisi, M. Sakai, A. Fujiwara, R. Kumashiro, and K. Tanigaki, “N-channel field effect transistors with fullerene thin films and their application to a logic gate circuit,” *Chemical Physics Letters*, vol. 379, Sep. 2003, pp. 223-229.

[139] D. Chirvase, Z. Chiguvare, M. Knipper, J. Parisi, V. Dyakonov, and J.C. Hummelen, “Temperature dependent characteristics of poly(3 hexylthiophene)-fullerene based heterojunction organic solar cells,” *Journal of Applied Physics*, vol. 93, 2003, p. 3376.

[140] B. Feng, “Relationship between the structure of C60 and its lubricity: A review,” *Lubrication Science*, vol. 9, 1997, pp. 181-193.

[141] P.J. KRUSIC, E. WASSERMAN, P.N. KEIZER, J.R. MORTON, and F.K. PRESTON, “Radical Reactions of C60,” *Science*, vol. 254, 1991, p. 1183.

[142] T. Da Ros, G. Spalluto, and M. Prato, “Biological Applications of Fullerenes Derivates: A Brief Overview,” *Croatia Chemica Acta*, vol. 74, 2001, pp. 743-755.

[143] A. Mateo-Alonso, C. Ehli, G.M.A. Rahman, D.M. Guldi, G. Fioravanti, M. Marcaccio, F. Paolucci, and M. Prato, “Tuning electron transfer through translational motion in molecular shuttles.,” *Angewandte Chemie International Ed.*, vol. 46, Jan. 2007, pp. 3521-5.

[144] N. Martín and F. Giacalone, *Fullerene Polymers: Synthesis, Properties and Applications*, Weinheim: Wiley-VCH Verlag GmbH & Co. KGaA, 2009.

[145] S. a Krasnikov, S.I. Bozhko, K. Radican, O. Lübben, B.E. Murphy, S.-R. Vadapoo, H.-C. Wu, M. Abid, V.N. Semenov, and I.V. Shvets, "Self-assembly and ordering of C60 on the WO2/W(110) surface," *Nano Research*, vol. 4, Dec. 2011, pp. 194-203.

[146] T. Hashizume, K. Motai, X. Wang, H. Shinohara, Y. Saito, Y. Maruyama, K. Ohno, Y. Kawazoe, Y. Nishina, H. Pickering, Y. Kuk, and T. Sakurai, "Intramolecular structures of C60 molecules adsorbed on the Cu (111)-(1x1) surface," *Physical review letters*, vol. 71, 1993, p. 2959–2962.

[147] E.I. Altman and R.J. Colton, "Nucleation, growth, and structure of fullerene films on Au (111)," *Surface Science*, vol. 279, 1992, p. 49–67.

[148] C. Rogero, J.I. Pascual, J. Gómez-Herrero, and a M. Baró, "Resolution of site-specific bonding properties of C60 adsorbed on Au(111)," *The Journal of Chemical Physics*, vol. 116, 2002, p. 832.

[149] E. Altman and R. Colton, "The interaction of C60 with noble metal surfaces," *Surface Science*, vol. 295, Sep. 1993, pp. 13-33.

[150] W. Krätschmer, L.D. Lamb, K. Fostiropoulos, and D.R. Huffman, "Solid C60: a new form of carbon," *Nature*, vol. 347, 1990, pp. 354-358.

[151] F. Loske, R. Bechstein, J. Schütte, F. Ostendorf, M. Reichling, and A. Kühnle, "Growth of ordered C60 islands on TiO2(110).," *Nanotechnology*, vol. 20, Feb. 2009, p. 065606.

[152] L.J. Terminello, D.K. Shuh, F.J. Himpsel, D. a Lapiano-Smith, J. Stöhr, D.S. Bethune, and G. Meijer, "Unfilled orbitals of C60 and C70 from carbon K-shell X-ray absorption fine structure," *Chemical Physics Letters*, vol. 182, Aug. 1991, pp. 491-496.

[153] G.G. Otero, J. Méndez, and J.A. Martín-Gago, "STM Study Of C60 Overlayers On Pt(111) Surfaces," *Vacuum*, p. In press.

[154] G.G. Otero, "Ciclodeshidrogenazión catalizada por superficies: Fullerenos a partir de precursores aromaticos," 2010.

[155] R. Fasel, P. Aebi, R.G. Agostino, D. Naumović, J. Osterwalder, a Santaniello, and L. Schlapbach, "Orientation of adsorbed C60 molecules determined via x-ray photoelectron diffraction.," *Physical review letters*, vol. 76, Jun. 1996, pp. 4733-4736.

[156] C.S. Yannoni, R.D. Johnson, G. Meijer, D.S. Bethune, and J.R. Salem, "13C NMR Study of the C60 Cluster in the Solid State: Molecular Motion and Carbon Chemical Shift Anisotropy," *Journal of Physical Chemistry*, vol. 95, Mar. 1991, p. 9.

[157] H. Sun, "COMPASS: An ab Initio Force-Field Optimized for Condensed-Phase ApplicationsOverview with Details on Alkane and Benzene Compounds," *The Journal of Physical Chemistry B*, vol. 102, Sep. 1998, pp. 7338-7364.

[158] M.L. Sushko, A.Y. Gal, and A.L. Shluger, "Interaction of organic molecules with the TiO2 (110) surface: ab inito calculations and classical force fields.," *The journal of physical chemistry B*, vol. 110, Mar. 2006, pp. 4853-62.

[159] "www.accelrys.com."

[160] H.C. Andersen, "Molecular dynamics simulations at constant pressure and/or temperature," *The Journal of Chemical Physics*, vol. 72, 1980, p. 2384.

[161] C.D. Dimitrakopoulos and P.R.L. Malenfant, "Organic Thin Film Transistors for Large Area Electronics," *Advanced Materials*, vol. 14, Jan. 2002, pp. 99-117.

[162] M. Kitamura and Y. Arakawa, "Pentacene-based organic field-effect transistors," *Journal of Physics: Condensed Matter*, vol. 20, May. 2008, p. 184011.

[163] S. Yoo, B. Domercq, and B. Kippelen, "Efficient thin-film organic solar cells based on pentacene/C[sub 60] heterojunctions," *Applied Physics Letters*, vol. 85, 2004, p. 5427.

[164] A.C. Mayer, M.T. Lloyd, D.J. Herman, T.G. Kasen, and G.G. Malliaras, "Postfabrication annealing of pentacene-based photovoltaic cells," *Applied Physics Letters*, vol. 85, 2004, p. 6272.

[165] A.K. Pandey, S. Dabos-Seignon, and J.-M. Nunzi, “Pentacene: PTCDI-C13H27 molecular blends efficiently harvest light for solar cell applications,” *Applied Physics Letters*, vol. 89, 2006, p. 113506.

[166] C.C. Mattheus, a B. Dros, J. Baas, a Meetsma, J.L. de Boer, and T.T. Palstra, “Polymorphism in pentacene.,” *Acta crystallographica. Section C, Crystal structure communications*, vol. 57, Aug. 2001, pp. 939-41.

[167] R. Ruiz, D. Choudhary, B. Nickel, T. Toccoli, K.-C. Chang, A.C. Mayer, P. Clancy, J.M. Blakely, R.L. Headrick, S. Iannotta, and G.G. Malliaras, “Pentacene Thin Film Growth,” *Chemistry of Materials*, vol. 16, Nov. 2004, pp. 4497-4508.

[168] C.B. France, P.G. Schroeder, and B. a Parkinson, “Direct Observation of a Widely Spaced Periodic Row Structure at the Pentacene/Au(111) Interface Using Scanning Tunneling Microscopy,” *Nano Letters*, vol. 2, Jul. 2002, pp. 693-696.

[169] G. Bavdek, A. Cossaro, D. Cvetko, C. Africh, C. Blasetti, F. Esch, A. Morgante, and L. Floreano, “Pentacene nanorails on Au(110).,” *Langmuir*, vol. 24, Feb. 2008, pp. 767-72.

[170] S. Söhnchen, S. Lukas, and G. Witte, “Epitaxial growth of pentacene films on Cu (110).,” *The Journal of chemical physics*, vol. 121, Jul. 2004, pp. 525-34.

[171] M. Alagia, C. Baldacchini, M.G. Betti, F. Bussolotti, V. Carravetta, U. Ekström, C. Mariani, and S. Stranges, “Core-shell photoabsorption and photoelectron spectra of gas-phase pentacene: experiment and theory.,” *The Journal of chemical physics*, vol. 122, Mar. 2005, p. 124305.

[172] J. Zhou, S. Dag, S. Senanayake, B. Hathorn, S. Kalinin, V. Meunier, D. Mullins, S. Overbury, and A. Baddorf, “Adsorption, desorption, and dissociation of benzene on TiO2(110) and Pd/TiO2(110): Experimental characterization and first-principles calculations,” *Physical Review B*, vol. 74, Sep. 2006, p. 125318.

[173] S. Reiß, H. Krumm, A. Niklewski, V. Staemmler, and C. Wöll, “The adsorption of acenes on rutile TiO2 (110): A multi-technique investigation,” *The Journal of Chemical Physics*, vol. 116, 2002, p. 7704.

[174] L. Gross, F. Mohn, N. Moll, P. Liljeroth, and G. Meyer, "The chemical structure of a molecule resolved by atomic force microscopy.," *Science*, vol. 325, Aug. 2009, pp. 1110-4.

[175] G.A. Jeffrey, *An Introduction to Hydrogen Bonding*, Oxford: Oxford University Press, 1997.

[176] C. Kolczewski, R. Püttner, M. Martins, a S. Schlachter, G. Snell, M.M. Sant'anna, K. Hermann, and G. Kaindl, "Spectroscopic analysis of small organic molecules: a comprehensive near-edge x-ray-absorption fine-structure study of C6-ring-containing molecules.," *The Journal of chemical physics*, vol. 124, Jan. 2006, p. 034302.

[177] M. Chiodi, L. Gavioli, M. Beccari, V. Di Castro, A. Cossaro, L. Floreano, A. Morgante, A. Kanjilal, C. Mariani, and M. Betti, "Interaction strength and molecular orientation of a single layer of pentacene in organic-metal interface and organic-organic heterostructure," *Physical Review B*, vol. 77, Mar. 2008, p. 115321.

[178] Z. Jia, V. Lee, I. Kymissis, L. Floreano, A. Verdini, A. Cossaro, and A. Morgante, "In situ study of pentacene interaction with archetypal hybrid contacts: Fluorinated versus alkane thiols on gold," *Physical Review B*, vol. 82, Sep. 2010, p. 125457.

[179] S. Prato, L. Floreano, D. Cvetko, V.D. Renzi, A. Morgante, S. Modesti, F. Biscarini, R. Zamboni, and C. Taliani, "Anisotropic Ordered Planar Growth of α-Sexithienyl Thin Films," *The Journal of Physical Chemistry B*, vol. 103, Sep. 1999, pp. 7788-7795.

[180] L. Huang, D. Rocca, S. Baroni, K.E. Gubbins, and M.B. Nardelli, "Molecular design of photoactive acenes for organic photovoltaics.," *The Journal of chemical physics*, vol. 130, May. 2009, p. 194701.

[181] I. Kymissis, C.D. Dimitrakopoulos, and S. Purushothaman, "High-performance bottom electrode organic thin-film transistors," *IEEE Transactions on Electronics Devices*, vol. 48, 2001, pp. 1060-1064.

[182] H. Sirringhaus, P.J. Brown, R.H. Friend, M.M. Nielsen, K. Bechgaard, B.M.W. Langeveld-Voss, A.J.H. Spiering, R.A.J. Janssen, E.W. Meijer, P. HErwig, and D.M. de Leeuw, "Two-dimensional charge transport in self-organized, high-mobility conjugated polymers," *Nature*, vol. 401, 1999, pp. 685-688.

[183] A.R. Murphy and J.M.J. Frechet, “Organic semiconducting oligomers for use in thin film transistors,” *Chem. Rev*, vol. 107, 2007, p. 1066–1096.

[184] L.A. Majewski, R. Schroeder, and M. Grell, “Low-Voltage, High-Performance Organic Field-Effect Transistors with an Ultra-Thin TiO2 Layer as Gate Insulator,” *Advanced Functional Materials*, vol. 15, Jun. 2005, pp. 1017-1022.

[185] L. Floreano, A. Cossaro, D. Cvetko, G. Bavdek, and A. Morgante, “Phase diagram of pentacene growth on Au(110).,” *The Journal of Physical Chemistry B*, vol. 110, Mar. 2006, pp. 4908-13.

[186] J.A. Merlo, C.R. Newman, C.P. Gerlach, T.W. Kelley, D.V. Muyres, S.E. Fritz, M.F. Toney, and C.D. Frisbie, “p-Channel Organic Semiconductors Based on Hybrid Acene−Thiophene Molecules for Thin-Film Transistor Applications,” *Journal of the American Chemical Society*, vol. 127, Mar. 2005, pp. 3997-4009.

[187] J. Wintterlin and M.-L. Bocquet, “Graphene on metal surfaces,” *Surface Science*, vol. 603, Jun. 2009, pp. 1841-1852.

[188] J.B. Howard, J.T. McKinnon, M.E. Johnson, Y. Makarovsky, and A.L. Lafleur, “Production of C60 and C70 fullerenes in benzene-oxygen flames,” *The Journal of Physical Chemistry*, vol. 96, Aug. 1992, pp. 6657-6662.

[189] J.F. Anacleto, H. Perreault, R.K. Boyd, S. Pleasance, M.A. Quilliam, P.G. Sim, J.B. Howard, Y. Makarovsky, and A.L. Lafleur, “C60 and C70 fullerene isomers generated in flames. Detection and verification by liquid chromatography/mass spectrometry analyses.,” *Rapid Commun. Mass Spectrom.*, vol. 6, 1992, pp. 214-220.

[190] L.T. Scott, “Methods for the chemical synthesis of fullerenes.,” *Angewandte Chemie International Ed.*, vol. 43, Sep. 2004, pp. 4994-5007.

[191] M.M. Boorum, Y.V. Vasil’ev, T. Drewello, and L.T. Scott, “Groundwork for a rational synthesis of C60: cyclodehydrogenation of a C60H30 polyarene.,” *Science*, vol. 294, Oct. 2001, pp. 828-31.

[192] L.T. Scott, M.M. Boorum, B.J. McMahon, S. Hagen, J. Mack, J. Blank, H. Wegner, and A. de Meijere, "A rational chemical synthesis of C60.," *Science*, vol. 295, Feb. 2002, pp. 1500-3.

[193] G.G. Otero, G. Biddau, C. Sánchez-Sánchez, R. Caillard, M.F. López, C. Rogero, F.J. Palomares, N. Cabello, M. a Basanta, J. Ortega, J. Méndez, A.M. Echavarren, R. Pérez, B. Gómez-Lor, and J. a Martín-Gago, "Fullerenes from aromatic precursors by surface-catalysed cyclodehydrogenation.," *Nature*, vol. 454, Aug. 2008, pp. 865-8.

[194] K. Amsharov, N. Abdurakhmanova, S. Stepanow, S. Rauschenbach, M. Jansen, and K. Kern, "Towards the Isomer-Specific Synthesis of Higher Fullerenes and Buckybowls by the Surface-Catalyzed Cyclodehydrogenation of Aromatic Precursors.," *Angewandte Chemie International Ed.*, vol. 49, Oct. 2010, pp. 9392 -9396.

[195] J. Kikuma, K. Yoneyama, M. Nomura, T. Konishi, T. Hashimoto, R. Mitsumoto, Y. Ohuchi, and K. Seki, "Surface analysis of CVD carbon using NEXAFS, XPS and TEM," *Journal of Electron Spectroscopy and Related Phenomena*, vol. 88-91, Mar. 1998, pp. 919-925.

[196] K.-H. Ernst, M. Neuber, M. Grunze, and U. Ellerbeck, "NEXAFS Study on the Orientation of Chiral P-Heptahelicene on Ni(100)," *Journal of the American Chemical Society*, vol. 123, Jan. 2001, pp. 493-495.

[197] H. Oji, R. Mitsumoto, E. Ito, H. Ishii, Y. Ouchi, K. Seki, T. Yokoyama, T. Ohta, and N. Kosugi, "Core hole effect in NEXAFS spectroscopy of polycyclic aromatic hydrocarbons: Benzene, chrysene, perylene, and coronene," *The Journal of Chemical Physics*, vol. 109, 1998, p. 10409.

[198] C.L. Perkins and M. a Henderson, "Photodesorption and Trapping of Molecular Oxygen at the TiO2 (110) -Water Ice Interface," *Journal of Physical Chemistry B*, vol. 2, 2001, pp. 3856-3863.

[199] M. a Henderson, "The interaction of water with solid surfaces: fundamental aspects revisited," *Surface Science Reports*, vol. 46, May. 2002, pp. 1-308.

[200] P.A. Thiel and T.E. Madey, "THE INTERACTION OF WATER WITH SOLID SURFACES : FUNDAMENTAL ASPECTS," *Surface Science Reports*, vol. 7, 1987, pp. 211-385.

[201] R. Hopkins, a Tivanski, B. Marten, and M. Gilles, “Chemical bonding and structure of black carbon reference materials and individual carbonaceous atmospheric aerosols,” *Journal of Aerosol Science*, vol. 38, Jun. 2007, pp. 573-591.

[202] J.I. Pascual, J. Gómez-Herrero, C. Rogero, A.M. Baró, D. Sánchez-Portal, E. Artacho, P. Ordejón, and J.M. Soler, “Seeing molecular orbitals,” *Chemical Physics Letters*, vol. 321, Apr. 2000, p. 78–82.

[203] C. Joachim, J.K. Gimzewski, and A. Aviram, “Electronics using hybrid-molecular and mono-molecular devices.,” *Nature*, vol. 408, Nov. 2000, pp. 541-8.

[204] J. Heath and M. Ratner, “Molecular Electronics,” *Physics Today*, 2003, pp. 43-49.

[205] A.H. Flood, J.F. Stoddart, D.W. Steuerman, and J.R. Heath, “Whence molecular electronics?,” *Science*, vol. 306, Dec. 2004, pp. 2055-6.

[206] S. Barlow, “Complex organic molecules at metal surfaces: bonding, organisation and chirality,” *Surface Science Reports*, vol. 50, Aug. 2003, pp. 201-341.

[207] X. Zhu, “Electronic structure and electron dynamics at molecule-metal interfaces: implications for molecule-based electronics,” *Surface Science Reports*, vol. 56, Nov. 2004, pp. 1-83.

[208] R.A. Wolkow, “CONTROLLED MOLECULAR ADSORPTION ON SILICON: Laying a Foundation for Molecular Devices,” *Annual Review of Physical Chemistry*, vol. 50, 1999, p. 413.

[209] H. Li, X. Wang, and W. Ding, “Electron attenuation lengths in fullerene and fullerides,” *Journal of Electron Spectroscopy and Related Phenomena*, vol. 153, Oct. 2006, pp. 96-101.

[210] R.R. Sahoo and A. Patnaik, “Binding of fullerene C60 to gold surface functionalized by self-assembled monolayers of 8-amino-1-octane thiol: a structure elucidation,” *Journal of Colloid and Interface Science*, vol. 268, Dec. 2003, pp. 43-49.

[211] N. Swami, H. He, and B. Koel, "Polymerization and decomposition of C60 on Pt(111) surfaces," *Physical Review B*, vol. 59, Mar. 1999, pp. 8283-8291.

[212] C.-T. Tzeng, W.S. Lo, J.Y. Yuh, R.Y. Chu, and K.-D. Tsuei, "Photoemission, near-edge x-ray-absorption spectroscopy, and low-energy electron-diffraction study of C60 on Au (111) surfaces," *Physical Review B*, vol. 61, 2000, p. 2263–2272.

[213] K.-D. Tsuei, J.-Y. Yuh, C.-T. Tzeng, R.-Y. Chu, S.-C. Chung, and K.-L. Tsang, "Photoemission and photoabsorption study of C60 adsorption on Cu(111) surfaces," *Physical Review B*, vol. 56, Dec. 1997, pp. 15412-15420.

[214] C. Enkvist, S. Lunell, B. Sjögren, S. Svensson, P. Brühwiler, A. Nilsson, A. Maxwell, and N. Mårtensson, "C 1s shakeup spectrum of C60: global charge-transfer satellites and their relation to the x-ray threshold singularities in macroscopic systems," *Physical Review B*, vol. 48, 1993, p. 14629.

[215] D.G. de Oteyza, Y. Wakayama, X. Liu, W. Yang, P.L. Cook, F.J. Himpsel, and J.E. Ortega, "Effect of fluorination on the molecule–substrate interactions of pentacene/Cu(100) interfaces," *Chemical Physics Letters*, vol. 490, Apr. 2010, pp. 54-57.

[216] C. Baldacchini, F. Allegretti, R. Gunnella, and M. Betti, "Molecule–metal interaction of pentacene on copper vicinal surfaces," *Surface Science*, vol. 601, Jul. 2007, pp. 2603-2606.

[217] H. Fukagawa, H. Yamane, T. Kataoka, S. Kera, M. Nakamura, K. Kudo, and N. Ueno, "Origin of the highest occupied band position in pentacene films from ultraviolet photoelectron spectroscopy: Hole stabilization versus band dispersion," *Physical Review B*, vol. 73, Jun. 2006, p. 245310.

[218] S. Kang, Y. Yi, C. Kim, S. Cho, M. Noh, K. Jeong, and C. Whang, "Energy level diagrams of C60/pentacene/Au and pentacene/C60/Au," *Synthetic Metals*, vol. 156, Jan. 2006, pp. 32-37.

[219] P.G. Schroeder, C.B. France, J.B. Park, and B. a Parkinson, "Orbital Alignment and Morphology of Pentacene Deposited on Au(111) and SnS2 Studied Using Photoemission Spectroscopy," *The Journal of Physical Chemistry B*, vol. 107, Mar. 2003, pp. 2253-2261.

[220] A. Linsebigler, G. Lu, and J.T. Yates, “CO chemisorption on TiO2(110): Oxygen vacancy site influence on CO adsorption,” *The Journal of Chemical Physics*, vol. 103, 1995, p. 9438.

[221] M. Henderson, “Evidence for bicarbonate formation on vacuum annealed TiO2(110) resulting from a precursor-mediated interaction between CO2 and H2O,” *Surface Science*, vol. 400, Mar. 1998, pp. 203-219.

[222] C.D. Wagner, W.M. Riggs, L.E. Davis, J.F. Moulder, and G.E. Mullenberg, *Handbook of X-ray Photoelectron Spectroscopy*, Eden Prairie: Perkin-Elmer Corp., 1979.

[223] R. González-Moreno, C. Sánchez-Sánchez, M. Trelka, R. Otero, A. Cossaro, A. Verdini, L. Floreano, M. Ruiz-bermejo, A. García-Lekue, J.A. Martín-Gago, and C. Rogero, “Following the metalation process of protoporphyrin IX with metal substrate atoms at room temperature,” *Journal of Physical Chemistry C*, p. In press.

[224] I. Takahashi, D.J. Payne, R.G. Palgrave, and R.G. Egdell, “High resolution X-ray photoemission study of nitrogen doped TiO2 rutile single crystals,” *Chemical Physics Letters*, vol. 454, Mar. 2008, pp. 314-317.

[225] A. Rienzo, L.C. Mayor, G. Magnano, C.J. Satterley, E. Ataman, J. Schnadt, K. Schulte, and J.N. O’Shea, “X-ray absorption and photoemission spectroscopy of zinc protoporphyrin adsorbed on rutile TiO2(110) prepared by in situ electrospray deposition.,” *The Journal of chemical physics*, vol. 132, Feb. 2010, p. 084703.

[226] G. Gonella, S. Terreni, D. Cvetko, A. Cossaro, L. Mattera, O. Cavalleri, R. Rolandi, A. Morgante, L. Floreano, and M. Canepa, “Ultrahigh vacuum deposition of L-cysteine on Au(110) studied by high-resolution X-ray photoemission: from early stages of adsorption to molecular organization.,” *The Journal of Physical Chemistry B*, vol. 109, Sep. 2005, pp. 18003-9.

[227] P. Krüger, J. Jupille, S. Bourgeois, B. Domenichini, C. Sánchez-Sánchez, A. Verdini, L. Floreano, and A. Morgante, “Unified picture of the excess electrons at rutile surfaces,” *Science*, p. To be submitted.

[228] E. Asari, “Atomic structures of TiO2(110) surface between p(1×1) and p(1×2) studied by scanning tunneling microscopy,” *Applied Surface Science*, vol. 193, Jun. 2002, pp. 70-76.

[229] H. Onishi and Y. Iwasawa, “Dynamic visualization of a metal-oxide-surface/gas-phase reaction: Time-resolved observation by scanning tunneling microscopy at 800 K.,” *Physical review letters*, vol. 76, Jan. 1996, pp. 791-794.

[230] R.A. Bennett, P. Stone, and M. Bowker, “Scanning tunnelling microscopy studies of the reactivity of the TiO2(110) surface: Re-oxidation and the thermal treatment of metal nanoparticles,” *Faraday Discussions*, vol. 114, 1999, pp. 267-277.

[231] E. Asari, W. Hayami, and R. Souda, “Transitional structures of the TiO2(110) surface from p(1×1) to p(1×2) studied by impact collision ion scattering spectroscopy,” *Applied Surface Science*, vol. 167, Oct. 2000, pp. 169-176.

[232] C. Polop, C. Rojas, J.A. Martín-Gago, R. Fasel, J. Hayoz, D. Naumović, and P. Aebi, “Structure of Si atomic chains grown on the Si/Cu(110) c(2×2) surface alloy,” *Physical Review B*, vol. 63, Mar. 2001, p. 115414.

[233] A.F. Santander-Syro, O. Copie, T. Kondo, F. Fortuna, S. Pailhès, R. Weht, X.G. Qiu, F. Bertran, A. Nicolaou, A. Taleb-Ibrahimi, P. Le Fèvre, G. Herranz, M. Bibes, N. Reyren, Y. Apertet, P. Lecoeur, A. Barthélémy, and M.J. Rozenberg, “Two-dimensional electron gas with universal subbands at the surface of SrTiO3,” *Nature*, vol. 469, Jan. 2011, pp. 189-193.

[234] C. Sánchez-Sánchez, C. González, P. Jelinek, J. Méndez, P.L. de Andres, J.A. Martín-Gago, and M.F. López, “Understanding atomic-resolved STM images on TiO2(110)-(1x1) surface by DFT calculations.,” *Nanotechnology*, vol. 21, Oct. 2010, p. 405702.

[235] M. Nolan, S. Elliott, J. Mulley, R.A. Bennett, M. Basham, and P. Mulheran, “Electronic structure of point defects in controlled self-doping of the TiO2 (110) surface: Combined photoemission spectroscopy and density functional theory study,” *Physical Review B*, vol. 77, Jun. 2008, p. 235424.

[236] M. Ganduglia-Pirovano, A. Hofmann, and J. Sauer, “Oxygen vacancies in transition metal and rare earth oxides: Current state of understanding

and remaining challenges," *Surface Science Reports*, vol. 62, Jun. 2007, pp. 219-270.

[237] R. Patel, Q. Guo, I. Cocks, E.M. Williams, E. Román, and J.L. De Segovia, "The defective nature of the TiO2 (110)-(1x2) surface," *JOURNAL OF VACUUM SCIENCE & TECHNOLOGY A*, vol. 15, 1997, pp. 2553-2556.

[238] J. Abad, "Growth of subnanometer-thin Si overlayer on TiO2 (110)-(1x2) surface," *Applied Surface Science*, vol. 234, Jul. 2004, pp. 497-502.

[239] J. Osterwalder, T. Greber, P. Aebi, R. Fasel, and L. Schlapbach, "Final-state scattering in angle-resolved ultraviolet photoemission from copper.," *Physical review. B, Condensed matter*, vol. 53, Apr. 1996, pp. 10209-10216.

[240] D.J. Dwyer, J.L. Robbins, S.D. Cameron, N. Dudash, and J. Hardenbergh, *Chemisorption and Catalysis over TiO2-Modified Pt Surfaces*, ACS Symposium Series, 1986.

[241] A. Berkó, G. Menesi, and F. Solymosi, "STM study of rhodium deposition on the TiO2(110)-(1x2) surface," *Surface Science*, vol. 372, Feb. 1997, pp. 202-210.

[242] A. Berkó and F. Solymosi, "Method for independent control of particle size and distance in rhodium epitaxy on TiO2(110)-(1×2) surface: An STM study," *Surface Science*, vol. 400, 1998, pp. 281-289.

[243] A. Berkó, "Fabrication of Ir/TiO2(110) Planar Catalysts with Tailored Particle Size and Distribution," *Journal of Catalysis*, vol. 182, Mar. 1999, pp. 511-514.

[244] A. Berkó, "CO-induced changes of Ir nanoparticles supported on TiO2 (110)-(1×2) surface," *Surface Science*, vol. 411, Aug. 1998, p. L900-L903.

[245] S. Gan, Y. Liang, D.R. Baer, M.R. Sievers, G.S. Herman, and C.H.F. Peden, "Effect of Platinum Nanocluster Size and Titania Surface Structure upon CO Surface Chemistry on Platinum-Supported TiO2 (110)," *The Journal of Physical Chemistry B*, vol. 105, Mar. 2001, pp. 2412-2416.

[246] V. Çelik, H. Ünal, E. Mete, and Ş. Ellialtıoğlu, “Theoretical analysis of small Pt particles on rutile TiO2(110) surfaces,” *Physical Review B*, vol. 82, Nov. 2010, p. 205113.

[247] S. Fischer, J.A. Martín-Gago, E. Román, K.D. Schierbaum, and J.L. De Segovia, “The valence-band electronic structure of clean and Pt-covered TiO2 (110) surfaces studied with photoemission spectroscopy,” *Journal of Electron Spectroscopy and Related Phenomena*, vol. 83, 1997, pp. 217-225.

International Publications (S. C. I.) and Patents

Published Papers in ISI Journals

G. Otero, G. Biddau, **C. Sánchez-Sánchez**, R. Caillard, M. F. López, C. Rogero, M. A. Basanta, J. Ortega, J. Méndez, A. M. Echevarren, R. Pérez, B. Gómez-Lor y J. A. Martín-Gago. *"Fullerenes from aromatic precursors by surface-catalysed cyclodehydrogenation"*, **Nature**, 454 (2008) 865

C. Sánchez-Sánchez, C. González, P. Jelinek, J. Méndez, P. L. de Andrés, J. A. Martín-Gago y M. F. López. *"Understanding atomic-resolved STM images on TiO_2(110)-(1x1) surface by DFT"*, **Nanotechnology**, 21 (2010) 405702.

Lanzilotto, Valeria; **Sánchez-Sánchez, Carlos**; Bavdek, Gregor; Cvetko, Dean; Lopez, Maria; Martin-Gago, Jose; Floreano, Luca. *"Planar Growth of Pentacene on the Dielectric TiO_2 (110) Surface"*, **Journal of Physical Chemistry C**, In Press (2011)

J. Abad, **C. Sánchez-Sánchez**, P. Vilmercati, A. Goldoni, M. F. López and J.A. Martin-Gago. *"Thermal behaviour of the O_2/TiO_2 (110)-(1x2) surface"*, **Vacuum**, In Press (2011)

Gonzalez-Moreno, Ruben; **Sánchez-Sánchez, Carlos**; Trelka, Marta; Otero, Roberto; Cossaro, Albano; Verdini, Alberto; Floreano, Luca; Ruiz-Bermejo, Marta; Garcia-Lekue, Aran; Martin-Gago, Jose; Rogero, Celia. *"Following the*

Metalation Process of Protoporphyrin IX with Metal Substrate Atoms at Room Temperature ", **Journal of Physical Chemistry C**, In Press (2011)

Papers to be submitted shortly

C. Sánchez-Sánchez, M. G. Garnier, P. Aebi, M. Blanco-Rey, P. de Andrés, J. A. Martin-Gago and M. F. López. *"Valence band electronic structure characterization of the rutile TiO_2 (110) - (1x2) reconstructed surface"* (2011)

C. Sánchez-Sánchez, M. Blanco-Rey, P. de Andres, J. A. Martín-Gago and M. F. López. *"Small Pt nanoparticles on the TiO_2 (110) - (1x2) surface"* (2011)

P. Krüger, J. Jupille, S. Bourgeois, B. Domenichini, **C. Sánchez-Sánchez**, A. Verdini, L. Floreano, and A. Morgante. *"Unified picture of the excess electrons at rutile surfaces"* (2011)

Carlos Sánchez-Sánchez, Valeria Lanzilotto, Cesar González, Alberto Verdini, Pedro de Andrés, Luca Floreano, María F. López and José Ángel Martín-Gago "Spinning of C_{60} molecules on TiO_2 (110) surfaces" (2011).

Patents

Inventor: G. Otero, **C. Sánchez-Sánchez**, R. Caillard, M. F. López, J. Méndez, J. A. Echevarren, B. Gómez-Lor, C. Rogero y J. A. Martín-Gago,

Title: *Procedure for the synthesis of fullerenes*

Request number: PCT/ES2009/070238 Country: España Date: 18-06-2008

Organism: CSIC-INTA-CQT.